

DISS. ETH NO. 20965

**EXPERIMENTAL CHARACTERIZATION OF
QUANTUM MICROWAVE RADIATION AND ITS
ENTANGLEMENT WITH A SUPERCONDUCTING QUBIT**

A dissertation submitted to

ETH ZURICH

for the degree of

Doctor of Sciences

presented by

Christopher Eichler

Dipl.-Phys., JWGU Frankfurt am Main

born December 19th, 1983

citizen of Germany

accepted on the recommendation of

Prof. Dr. Andreas Wallraff, examiner

Prof. Dr. Ataç İmamoğlu, co-examiner

2013

Zusammenfassung

Die Verwendung von Josephson-Tunnelkontakten als künstliche Atome und deren starke Kopplung an einzelne Mikrowellenphotonen haben es während der letzten zehn Jahre ermöglicht, einzelne Energiequanten in nichtlinearen Schaltkreisen zu kontrollieren. Obwohl die Präparation und Manipulation von quantenmechanischen Zuständen auf einzelnen Mikrochips mittlerweile mit hoher Präzision möglich sind, stellt es nach wie vor eine große Herausforderung dar, einzelne propagierende Mikrowellenphotonen mit ähnlich hoher Effizienz zu detektieren. Entsprechende physikalische Methoden könnten den Weg für eine mikrowellen-basierte Quantenkommunikation ebnen.

Statt Photonen mit Hilfe von Einzelphoton-Detektoren zu messen, werden im Bereich der Mikrowellenstrahlung bislang meist lineare, transistor-basierte Verstärker im Messprozess verwendet, die ein hohes Maß an Rauschen zum detektierten Signal hinzufügen. Vor allem durch dieses Rauschen bedingt, existierten bis vor kurzem keine Experimente zur Messung der Photonstatistik und der Kohärenzeigenschaften von propagierenden Mikrowellenfeldern jenseits der Gauss'schen Eigenschaften.

In der vorliegenden Arbeit beschreibe ich die Charakterisierung von Mikrowellenfeldern mittels linearer Detektion und deren quantenmechanische Verschränkung mit einem stationären Zwei-Niveau-System. Wir haben unterschiedlichste Typen von quantenmechanischen Feldern erzeugt, die von Fock-Zuständen, über gequetschte Strahlung bis hin zu räumlich verschränkten Zuständen zweier Photonen reichen. Allgemeine Konzepte und Methoden wurden ausgearbeitet, um die Quanteneigenschaften dieser Felder auch mit kommerziell verfügbaren linearen Verstärkern zu messen. Darüber hinaus haben wir quantenlimitierte Verstärker entwickelt, die zu einer wesentlichen Verbesserung der Detektionseffizienz führen und die Messung von Feldkorrelationen höherer Ordnung experimentell zugänglich machen. Basierend auf diesen Erkenntnissen und Entwicklungen waren wir erstmals in der Lage die Verschränkung einzelner Photonen mit einem supraleitenden künstlichen Atom zu beobachten.

Die beschriebenen Resultate weisen in eine vielversprechende Richtung für zukünftige Experimente, in denen Mikrowellenphotonen als Quanteninformationsträger makroskopische Distanzen überwinden. Insbesondere die Möglichkeit Verschränkungskorrelationen zwischen stationären Zwei-Niveau-Systemen und einzelnen sich ausbreitenden Mikrowellenphotonen zu generieren, zu lenken und zu detektieren, rückt die Realisierung von Quantennetzwerken mit supraleitenden Schaltkreisen in erreichbare Nähe.

Abstract

Josephson junction based artificial atoms and their strong coupling to single microwave photons have enabled a variety of quantum control experiments in nonlinear electronic circuits during the past decade. While the on-demand generation and the processing of quantum states on a chip can now be achieved with high fidelity, it remains challenging to detect and to characterize single quanta of propagating microwave fields with equally high efficiency. Bridging this gap would open a novel quantum communication channel based on superconducting circuits and microwave radiation.

Instead of detecting individual photons one by one, microwave fields are most commonly measured using transistor-based linear amplifiers, which add a significant amount of noise during the amplification. Mainly due to this added noise, measurements of photon statistics and coherence properties beyond the Gaussian level did not exist in this frequency range until recently.

In this thesis, I report the use of linear detection schemes for the characterization of itinerant microwave radiation and its entanglement with a stationary qubit. We have generated various types of quantum fields, ranging from on-demand single- and two-photon Fock states, over squeezed radiation, to N00N-type entangled fields, which propagate in two spatially separated paths. A detailed theoretical framework has been developed to measure the statistical properties of these fields efficiently in the presence of noise added during detection. We have also realized quantum-limited parametric amplifiers, which significantly increase the detection efficiency and enable us to access higher order field correlations. Based on these achievements we have been able to observe entanglement between a superconducting artificial atom and single propagating microwave photons, for the first time.

Our results point in a promising direction for future experiments, in which propagating microwave fields carry quantum information over macroscopic distances. Particularly, the ability to synthesize, guide and detect entanglement correlations between itinerant photons and stationary qubits put the realization of microwave based quantum networks within reach.

These then are some illustrations of things that are happening in modern times – the transistor, the laser, and now these junctions, whose ultimate practical applications are still not known. The quantum mechanics which was discovered in 1926 has had nearly 40 years of development, and rather suddenly it has begun to be exploited in many practical and real ways. We are really getting control of nature on a very delicate and beautiful level.

— Richard P. Feynman (1963) —

Contents

Abstract	iii
1 Introduction: Probing quantum physics in superconducting circuits	1
1.1 Historical overview	1
1.2 A decade of quantum optics in superconducting circuits	2
1.3 Outline of the thesis: A guide to the reader	3
2 Concepts of circuit quantum electrodynamics	7
2.1 Dissipationless nonlinear electronic circuits	7
2.1.1 Requirements for the implementation of quantum physics in engineered systems	7
2.1.2 Lumped elements and collective degrees of freedom	9
2.1.3 The Josephson junction and the Cooper pair box	11
2.2 Relevant circuit QED building blocks	13
2.2.1 The transmon qubit	13
2.2.2 Transmission line resonator	15
2.2.3 Coupling to the electromagnetic environment	18
2.3 Coupling a qubit to a resonator: The Jaynes-Cummings model	22
2.3.1 Dispersive regime	24
2.3.2 Dynamics at qubit-cavity resonance	26
2.4 General aspects of the experimental setup	27
2.4.1 Fabricating and probing superconducting circuit devices	27
2.4.2 Electromagnetic control lines	30
2.4.3 Linear detection chain: Amplification and noise	33

3	Characterizing quantum microwave radiation with linear detectors	37
3.1	Generating single microwave photons	38
3.1.1	Sample characterization	38
3.1.2	Vacuum Rabi oscillations	41
3.1.3	Mapping an arbitrary qubit state onto a single photon state	42
3.2	Experimental photon state tomography for single microwave photons	44
3.2.1	Quadrature detection and its optical analog	44
3.2.2	Temporal mode matching	47
3.2.3	Data acquisition: Generating quadrature histograms	50
3.3	Interpretation and analysis of quadrature histograms	51
3.3.1	Phase space distributions	52
3.3.2	Identifying measured histograms with phase space distributions	53
3.3.3	Determination of normally ordered moments	55
3.3.4	Special classes of states and the Fock space density matrix	56
3.3.5	Reconstruction of single photon states	57
3.4	Maximum likelihood state estimation	60
3.4.1	Maximum-likelihood procedure based on measured moments	60
3.4.2	Iterative maximum-likelihood procedure based on measured histograms	62
3.5	Two channel detection and the positive P distribution	66
3.5.1	Two-channel detection	66
3.5.2	The positive P function	68
3.5.3	Two channel detection as a measurement of the positive P function	68
3.6	Hong-Ou-Mandel interference: Reconstruction of two-photon NOON states	69
3.6.1	Two-photon interference at a beam splitter	69
3.6.2	State reconstruction based on 4D histograms	71
3.6.3	Measurement results and interpretation	72
4	Parametric amplification and vacuum noise squeezing	77
4.1	Principles of parametric amplification	78
4.1.1	Parametric processes at optical and microwave frequencies	78
4.1.2	A circuit QED implementation of a parametric amplifier	79
4.1.3	Regimes of a driven nonlinear oscillator	81
4.2	Input-Output relations for the Parametric amplifier	82
4.2.1	Classical nonlinear response	82
4.2.2	Linearized response for additional weak (quantum) signal fields	85
4.2.3	Gain, bandwidth, noise and dynamic range	87

4.3	Effective system parameters from distributed circuit model	90
4.3.1	Resonator mode structure in the linear regime	90
4.3.2	Kerr nonlinear terms and effective Hamiltonian	93
4.3.3	Josephson junction arrays	95
4.3.4	Decay rate and resonance frequency correction for low Q resonators	97
4.4	Experimental characterization of parametric amplifiers	98
4.4.1	Tunability and (non-)linear response	98
4.4.2	Gain measurements	101
4.4.3	Phase-sensitive and phase-insensitive mode of operation . .	105
4.5	Observation of two-mode squeezing in the microwave frequency domain	109
4.5.1	Experimental Setup and system noise calibration	110
4.5.2	Measuring correlations between signal and idler noise . . .	111
5	Entanglement between a superconducting qubit and propagating microwave fields	117
5.1	Entanglement with single microwave photons	117
5.1.1	Experimental setup and generation of photon/qubit entanglement	118
5.1.2	Parametric amplification and detection	120
5.1.3	Measurement of photon-qubit correlations	121
5.1.4	Analysis of entanglement correlations and state reconstruction	123
5.1.5	Time-resolved correlations based on single shot qubit readout	126
5.2	Two-photon entangled states	127
5.2.1	Mapping the f -level onto a two-photon state	128
5.2.2	State reconstruction of a two-photon entangled state	129
5.3	Coherent state Entanglement based on dispersive interaction	130
5.3.1	Motivation	130
5.3.2	Master equation and input-output relation	131
5.3.3	Criterion for quantum coherence	132
5.3.4	Calculation of qubit - field correlations	133
5.3.5	Experimental aspects	135
6	Outlook	137
A	Appendices	141
A.1	Characteristic functions, moments and cumulants	141
A.2	Probability distribution for two channel complex envelopes	143
A.2.1	Thermal noise	144
A.2.2	Equivalence to canonical positive P function	145
A.3	Relation between POVM and quasi-probability distribution	146

A.4	Joint Tomography Scheme for a Qubit - Photon Field System	146
A.4.1	Qubit state tomography	146
A.4.2	Joint tomography	147
A.4.3	POVM operators and maximum-likelihood state estimation .	148
A.5	Parametric amplifier calibration and pump tone cancelation	149
A.6	System noise and dynamic range	151
A.7	Simulation of capacitances for interdigitated finger capacitors	153

Bibliography	155
---------------------	------------

List of publications	175
-----------------------------	------------

Credits	177
----------------	------------

Curriculum Vitae	179
-------------------------	------------

Introduction: Probing quantum physics in superconducting circuits

1.1 Historical overview

The quantum character of electromagnetism naturally becomes observable when the dynamics of single charged particles such as electrons in an atom are studied. After the first experimental indications for a quantum-mechanical energy level discretization [Planck01, Bohr13, Einstein05] and the general theoretical formulation of quantum electrodynamics (QED) [Dirac27, Feynman50, Dyson49], the quantum nature of radiation and matter has been explored during a century of atomic physics and quantum optics research. Today, this allows for generating and processing quantum states of single atoms and photons with remarkable control.

In addition to its consequences for the behavior of single particles, quantum theory imposes an exchange symmetry to the wave function of many-particle systems [Pauli40]. This global symmetry can lead to the formation of collective matter states in which a macroscopic number of particles is described by an effective single particle wave function. With the emergence of collective phenomena such as Bose-Einstein condensation [Anderson95, Davis95] and superconductivity [Bardeen57], the question arose whether the associated collective excitations may possess coherent quantum dynamics similar to those obeyed by single elementary particles.

In the case of superconductivity, the phase drop across the tunnel barrier between two superconductors can be interpreted as such a collective variable. First evidence for the coherent dynamics of this macroscopic phase variable has been given by the measurement of quantum tunneling in a current biased Josephson junction [Voss81, Devoret85, Martinis87], which initiated the development of tunnel barrier based

artificial atoms [Nakamura97, Bouchiat98, Nakamura99, Mooij99, Vion02] and their controlled coupling to microwave radiation in superconducting circuits [Wallraff04, Chiorescu04, Schoelkopf08].

One of the central motivations for this research field is the realization of quantum information processing platforms. The strong connection between information theory and quantum physics fascinates researchers since the 1980's [Feynman82, Deutsch85, Shor94, Grover96, Chuang98] and since then drives scientists to realize physical implementations, which bring the control and processing of quantum information into reality. Besides successful approaches with optical photons [O'Brien09], nuclear spins [Vandersypen04], trapped ions [Blatt08], ultracold atoms in optical lattices [Bloch08] and quantum dots [Hanson08], the search for appropriate solid state systems is actively pursued. In this context, Josephson junction based electrical circuits offer flexible conditions in the design and fabrication of engineered quantum systems. Because of their natural coupling to microwave radiation they also benefit from a powerful signal processing toolbox in this frequency range.

1.2 A decade of quantum optics in superconducting circuits

During the last ten years significant progress has been made with superconducting circuits in exploring microwave quantum optics, in realizing quantum algorithms, and by more recent attempts to simulate many-particle physics. All these experiments crucially rely on the possibility to create and measure coherent superposition states and entanglement between different macroscopic degrees of freedom. Based on the ground breaking experiment by Nakamura *et al.* [Nakamura99] and related proposals [Buisson01, Makhlin01, Marquardt01, Al-Saidi01, Plastina03, Yang03, Blais04] how to realize cavity QED experiments [Haroche89, Mabuchi02, Miller05, Walther06] on superconducting chips, an important achievement was made in 2004 by demonstrating the strong coupling of a superconducting qubit to a coplanar microwave resonator [Wallraff04]. In the years after, similar devices were intensely characterized experimentally in the resonant [Deppe08, Fink08, Bishop09a] as well as the dispersive regime [Schuster05, Schuster07, Fragner08, Johnson10]. They repeatedly confirmed that Josephson junction based electrical circuits can be well represented as single artificial atoms – often approximated as two-level systems - which interact strongly with photons in a cavity.

The implementation of quantum algorithms in superconducting circuits was pushed forward by the realization of cavity mediated inter-qubit coupling [Steffen06, Majer07, Sillanpää07]. The development of efficient control and state tomography techniques [Filipp09] allowed for preparing and characterizing entanglement of up to three qubits

on a chip [DiCarlo10]. Soon after, both the concatenation of single and two-qubit gates [DiCarlo09] as well as collective interactions [Mlynek12] have been investigated to realize basic quantum algorithms [Mariantoni11b, Fedorov12, Lucero12] and error correction [Reed12]. At the the same time the quantum nature of resonator fields were explored, by generating arbitrary superposition states of a single resonator mode [Hofheinz08, Hofheinz09] and entanglement between two different modes [Wang11, Nguyen12]. The experimental progress also inspired researchers to constantly improve the coherence times over the years by modifying the qubit and circuit topologies [Koch07, Paik11, Rigetti12].

A major difference between superconducting circuits and most other quantum control platforms is their natural coupling to microwave instead of optical photons. Although microwave frequency quantum fields confined in cavities have earlier been generated and characterized with remarkable control using Rydberg atoms [Haroche06, Deleglise08], until recently only a few experiments existed which investigated propagating microwave fields. This is partly due to the difficulty in detecting single microwave photons, which have a 10^5 times smaller energy compared to their optical counterparts. It thus is challenging to build detectors with high quantum efficiency in this frequency range and to develop methods for characterizing quantum microwave radiation in the presence of significant detector noise [Menzel10, Bozyigit11, Eichler11b, Lang11, Eichler12a, Menzel12]. The possibility to analyze photon statistics and the coherence of microwaves is not only of particular interest in the context of quantum communication and networking with superconducting circuits, but offers a powerful tool to study various kinds of devices [Frey12, Puebla-Hellmann12], which can emit radiation in the microwave frequency range.

While progress has also been made in the development of microwave photon counters [Chen11, Romero09, Peropadre11, Poudel12], the research of efficient field detection was mainly focused on linear amplifiers. Following the ideas by Yurke *et al.* from the 1980's [Yurke88, Yurke06], a revival of parametric amplifier technologies took place [Siddiqi04, Castellanos-Beltran08, Yamamoto08, Tholén09, Bergeal10a, Eichler11a, Hatridge11, Ho Eom12], which recently turned into application for the real-time monitoring of superconducting qubits [Vijay11] in feedback experiments [Vijay12, Ristè12a], as well as the measurement of microwave photon statistics and quantum correlations [Mallet11, Eichler12b].

1.3 Outline of the thesis: A guide to the reader

In this thesis, I demonstrate the use of linear detection schemes for measuring photon statistics and coherences of various types of quantum microwave fields and their

entanglement correlations with a superconducting qubit. I discuss the experimental state tomography of single itinerant microwave photons in the presence of significant amplifier noise [Eichler11b]. For this purpose, we have developed general quantum state reconstruction methods, which are based on the measurement of field quadrature histograms and take the effect of limited detection efficiency into account [Eichler12a]. I also report the experimental realization of a degenerate parametric amplifier and demonstrate its near quantum limited operation in a phase-preserving mode, by measuring quantum correlations between the emitted signal and idler frequency noise [Eichler11a]. These correlations provide a major resource for the realization of continuous variable quantum information protocols. Finally, I report the first observation of entanglement between a superconducting qubit and single propagating microwave photons. Using low noise parametric amplification, we are able to resolve all relevant quantum correlations between the propagating field and the superconducting qubit to demonstrate entanglement with high fidelity [Eichler12b].

In order to give the present thesis an additional benefit over the underlying research articles, I aim for discussing the different research topics in a more general context. I have included the relevant introductory elements and cover the material in a self-contained way, to make it accessible also to non-expert readers. On the other hand, detailed background information about the technical and theoretical aspects is provided for interested researchers.

A brief introduction to superconducting circuit elements including the Cooper pair box and the transmission line resonator is presented in Chapter 2. I keep the derivations short but motivate the specific model descriptions from first principles. Furthermore, the concept of open quantum systems is discussed in the context of electrical circuits. I review only those elements which are relevant for the following discussion instead of giving a general introduction to the field. Those readers which are familiar with superconducting circuits can skip the introductory chapter without missing important information necessary for understanding the following parts.

In Chapter 3, I describe the tomographic state reconstruction of microwave radiation using linear detection. I explain the optical analogue of typical microwave detection schemes and discuss the influence of added amplifier noise on the measurement outcome. Measurements of photon statistics for an on-demand single photon source are presented and compared with the statistics of classical coherent fields. I also discuss more advanced reconstruction techniques including a maximum likelihood approach, which takes the full measurement record into account. Finally, I discuss two-channel detection schemes using microwave beamsplitters and demonstrate their application in a two-photon interference experiment.

In order to improve the detection efficiency of our linear detection chain we have developed a parametric amplifier which operates close to the quantum limit. The

goal of Chapter 4 is to establish the relation between design parameters of the device and amplifier properties such as bandwidth, gain and dynamic range. This chapter is particularly interesting for readers which search for a guide to build and operate a Josephson parametric amplifier. In addition to this presentation of technically relevant material, I discuss experiments in which we have measured squeezing correlations between signal and idler photons generated out of vacuum fluctuations. The quantum origin of these correlations shows that the device operates close to the quantum limit.

In Chapter 5, the on-demand generation and detection of entanglement between a superconducting qubit and single itinerant photons is discussed. The measurement of all relevant quantum correlations is efficiently realized by using a parametric amplifier. In addition to the preparation of single-photon entangled states, I present a scheme to prepare two-photon states on demand by making use of the third energy level of the superconducting artificial atom. In the context of qubit-field entanglement, we have also theoretically investigated quantum correlations between the output field of a coherently driven cavity and a dispersively coupled qubit. Our results give new insight into the measurement process during dispersive readout schemes. Finally, I discuss prospects of the presented work in Chapter 6.

Concepts of circuit quantum electrodynamics

2.1 Dissipationless nonlinear electronic circuits

Microscale quantum devices provide a high level of flexibility in the design of system parameters and are thus promising to realize platforms for the study of control, manipulation and measurement of quantum correlations. Knowledge about general requirements on appropriately engineered systems helps to understand key aspects and advantages of superconducting circuits, as well as challenges in this field of research.

2.1.1 Requirements for the implementation of quantum physics in engineered systems

Here, I formulate a set of requirements which has to be obeyed by a physical system to enable quantum control experiments. They are related to the DiVincenzo criteria for quantum computation [Di Vincenzo95] but less stringent, since we allow for a wider range of experimental purposes. Note that alternative sets of criteria may be formulated as well. However, the following requirements are the important ones in the context of superconducting circuits and cavity QED systems in general.

For a successful implementation of quantum-mechanical operations it is, at first, necessary to initialize the system in a well defined state with no thermally induced statistical uncertainty. Formally, this is equivalent to the preparation of a pure state of the system, which guarantees that all statistical properties of the measurement outcomes are of purely quantum mechanical origin. Typically, this pure initial state is the ground state, which is reached by cooling the relevant degrees of freedom

far below the characteristic temperature scale associated with the typical energy level separation in the system. Cooling can either be realized with refrigerative techniques reaching temperatures down to $T \lesssim 10$ mK [Pobell06] or with system-specific active cooling methods such as sideband cooling [Wineland79, Schliesser08, Park09, Leibrandt09, Teufel11]. Alternatively, initializing of the system in a pure state can be achieved by performing a high fidelity quantum non-demolition measurement which leaves the system in a well-known state determined by the measurement result [Braginski96, Ristè12c].

A second condition is the presence of a quantum nonlinearity which makes the energy levels anharmonic without opening a channel for dissipation. This enables the individual addressing of transitions between selected energy levels. If in contrast, the system is purely linear, a classical control signal applied to the input of the system always leads to a classical output, independent of what has happened in between. Prominent examples for intrinsically anharmonic systems are spin half particles in a magnetic field, which have only one accessible level above the ground state, and single atoms. For this reason, also engineered macroscopic objects with an anharmonic level spectrum are often called 'artificial atoms'.

Once an anharmonic system is under control, it needs to obey coherent dynamics. On the one hand, this requires that energy relaxation times are longer than the time necessary for performing an experimental sequence, i.e. the time between system preparation and detection. On the other hand, all relevant energy levels have to be stable in time such that the dynamical phases acquired during time-evolution do not randomize. Understanding the origins of decoherence and its suppression is one of the major challenges in the development of quantum systems built of microscale devices [Wellstood04, Ithier05, DiVincenzo06, Koch07, Lenander11, Anton12, Catelani12]. Note that dissipation – if engineered properly – can also be useful for the generation of entanglement or the stabilization of arbitrary pure states [Krauter11, Murch12].

Finally, the realization of quantum control experiments requires the efficient coupling of the system to the classical world. It needs precise and individual control knobs to manipulate the physical objects with classical control fields. Furthermore, since the measurement process and its backaction play an important role in quantum mechanics [Wiseman10], we need efficient detectors – transforming the quantum into a classical information – with well-characterized properties .

All these criteria can be satisfied in electrical circuits at microwave frequencies when cooled down to millikelvin temperatures. As discussed below, the crucial element for making these systems nonlinear is the Josephson junction. The high degree of flexibility in designing electrical circuits on a chip in combination with advanced signal generation and processing technologies at microwave frequencies have made superconducting circuits one of the most rapidly advancing systems in experimental

quantum science.

2.1.2 Lumped elements and collective degrees of freedom

A useful concept for designing and modeling engineered quantum systems are collective degrees of freedom, which allow for the description of the dynamics of a macroscopic number of particles by a single variable. It not only reduces the description of engineered solid state systems to single or few degree of freedom problems but also simplifies the intuitive assembly of different subsystems to form more complicated structures. As a consequence, the effective device properties can be understood without considering the full microscopic model each time a new system is engineered. Here, I discuss this concept of system modelling for electrical circuitry, which plays a central role in circuit QED. Interestingly, it turns out that in many cases it is possible to go directly from a lumped circuit model to the relevant Schrödinger equation for the collective degrees of freedom [Devoret97, Nigg12]. There is, however, a vivid discussion if this procedure is still valid in a limit where many-body effects become relevant [Nataf10, Viehmann11].

We consider the system shown in Figure 2.1(a), which consists of two metallic islands connected by a wire. For simplicity, we assume that there is no resistive loss in the metal¹ and that the surrounding dielectric medium is the vacuum. From Maxwell's first equation $\nabla \cdot \mathbf{E} = \rho/\epsilon_0$ it follows that a net charge difference $2Q$ between the two objects leads to an electrical field \mathbf{E} . If we prohibit, for the moment, a flow from one to the other island the charges on each side will arrange on the surface such that the metal stays free of electrical field inside. In this static situation, the energy required for moving one charge through the electrical field from one to the other side is path-independent and therefore it is convenient to define the position independent voltage V as this energy per unit charge. The voltage V is proportional to the charge difference $2Q$ between the two islands $V = Q/C$, where C is the constant capacitance between the islands, which only depends on the shape and geometrical arrangement of the two objects as well as the dielectric medium in between. In this static situation the total energy stored in the electrical field is thus given by $E_{el} = Q^2/2C$.

The time required for relaxing into a quasi-static field configuration for an object of characteristic size d is typically on the order of $\tau \sim d/c$ where c is the speed of light in the relevant dielectric medium. If τ is much smaller than the timescale on which the total charge $Q(t)$ on the object changes, the spatial charge configuration as well as the electrical field lines can follow quasi-instantaneously. If this is the case, the finite extent of the object is fully captured by the single parameter C . The object can thus be represented by a pointlike – or lumped – effective element. As long as $Q(t)$ changes

¹The modeling of damping is discussed in Section 2.2.3.

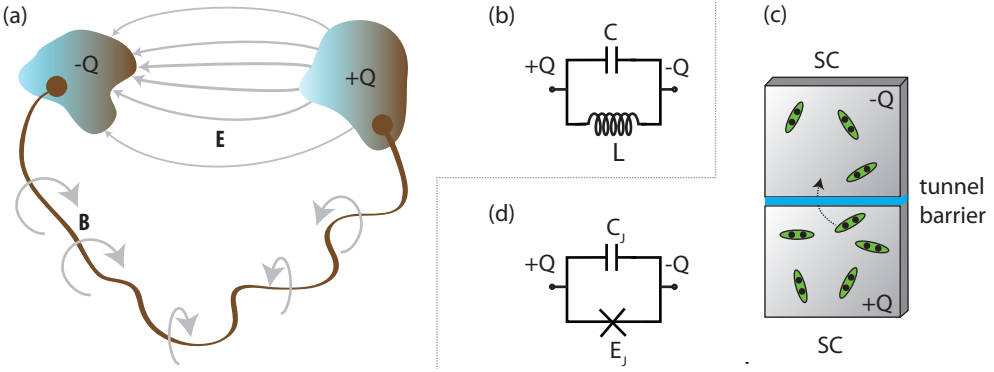


Figure 2.1: (a) Two metallic islands connected by a conducting wire. In a lumped element regime the total energy in the electric field \mathbf{E} and the magnetic field \mathbf{B} only depends on the total charge Q and the magnetic flux variable Φ . (b) Equivalent circuit model with effective inductance L and capacitance C . (c) Schematic of a Josephson junction. Two superconducting (SC) islands are separated by a thin barrier of insulating material (blue), such that their superconducting wave functions overlap and Cooper pairs (green) can tunnel from one to the other island. (d) Effective circuit model of the Josephson junction. The energy associated with Cooper pair tunneling is equivalent to a magnetic energy stored in a nonlinear inductor, which is represented by a cross in circuit schematics. The electrostatic energy between the two islands is represented by the capacitive element C_J .

on timescales much larger than τ we have $E_{\text{el}}(t) = Q(t)^2/2C$ at all times. Note that for typical metals the inverse plasma frequency of the electron gas density is also very small such that waves of the electron gas density do not get excited at the frequencies we are interested in [Girvin11].

If charge carriers can flow from one to the other object through the wire, the associated current density \mathbf{j} produces a magnetic field \mathbf{B} according to $\nabla \times \mathbf{B} = \mu_0 \mathbf{j}$ (see Figure 2.1). Assuming that the wire is short compared to the characteristic wavelength of the system, the current I is constant along the wire and given by the change of charges on the islands $I = \dot{Q}$. Similarly to the electrical field case, there is a constant proportionality between the square of the current and the energy stored in the magnetic field $E_{\text{mag}} = L\dot{Q}^2/2$. The inductance L is an effective parameter which is constant and determined by the geometry of the wire and the surrounding magnetic susceptibility. The total energy $E_{\text{tot}} = Q^2/2C + L\dot{Q}^2/2$ stored in the magnetic and electric fields only depends on the dynamics of the single charge variable Q , which can therefore be interpreted as a collective variable representing the effective dynamics of all the involved charge carriers. Note that the kinetic energy contribution of the moving charge carriers is typically very small compared to the energy stored in the magnetic field and is therefore negligible. However, for thin superconducting wires of nanoscale

size this additional kinetic energy becomes relevant and has to be accounted for by introducing the effective kinetic inductance [Yoshida92].

Since the expression for the total energy E_{tot} in terms of the variable Q is formally equivalent to that of an harmonic oscillator with resonance frequency $\omega = 1/\sqrt{LC}$, the equivalent Hamilton function turns out to be

$$H = \Phi^2/2L + Q^2/2C \quad (2.1)$$

with the conjugate flux variable $\Phi = L\dot{Q}$. In the quantum regime, charge and magnetic flux variable have to be interpreted as non-commuting operators $[\Phi, Q] = \hbar/i$ [Yurke84, Devoret97] and it is convenient to write the Hamiltonian as $H = \hbar\omega(a^\dagger a + \frac{1}{2})$, where

$$a \equiv i \frac{\Phi}{\sqrt{2L\hbar\omega}} + \frac{Q}{\sqrt{2C\hbar\omega}} \quad \text{and} \quad a^\dagger = -i \frac{\Phi}{\sqrt{2L\hbar\omega}} + \frac{Q}{\sqrt{2C\hbar\omega}} \quad (2.2)$$

are operators which annihilate and create the fundamental excitations in the system. Due to the underlying electromagnetic field they are photons with frequency ω .

As mentioned above, this quantization method, which starts from a lumped element circuit model and treats charge Q and magnetic flux Φ as conjugate non-commuting variables can be generalized to systems with more degrees of freedom as well [Yurke84, Devoret97]. An example, for this general procedure is discussed in Section 4.3 in the context of parametric amplifiers. Note, that in the above single mode description of the field we have neglected the emission of electromagnetic radiation into the surrounding environment. I discuss this important point later in Section 2.2.3 in the context of open transmission lines.

2.1.3 The Josephson junction and the Cooper pair box

In a system which is solely composed of inductive and capacitive elements the total Hamiltonian can always be written as a sum of harmonic oscillators $H = \sum_i \hbar\omega_i(a_i^\dagger a_i + 1/2)$, each representing one of its normal modes, see for example Ref. [Nigg12]. Consequently, the response to a classical control signal is purely linear and can generally be described within a classical picture. In other words, it is possible to replace the operators a_i by complex numbers α_i [Glauber63] and describe the dynamics based on classical equations of motion. Note that in this regime, the presence of vacuum fluctuations only affects the temperature dependence of the Johnson noise power, which in the limit of $k_B T/\hbar\omega \rightarrow 0$ saturates at the vacuum noise level instead of going to zero [Devoret97, Mariani10].

In order to experimentally study the quantum regime of electrical circuits, it is essential to have a nonlinear element in the system which causes effective photon-photon interactions. In conventional cavity QED and quantum optics systems, this

nonlinearity is typically realized either as a medium with nonlinear refractive index [Lee11] or as an ensemble of atoms interacting with the intra-cavity radiation field [Thompson92, Walther06]. Both break the linearity due to their intrinsically anharmonic level structure. For on-chip electrical circuits the most successful nonlinear element has so far been the Josephson junction [Josephson62, Tinkham96]. Compared to other solid state elements, it is not only advantageous since it features flexible design and fabrication parameters but moreover due to its ideally lossless behavior. All experiments presented in this thesis rely on the Josephson junction as a nonlinear element. As we will see in the following chapters, the wide range of accessible junction parameters allows for the realization of system Hamiltonians with very different properties.

The Josephson junction consists of two superconducting islands, which are separated by a thin insulating layer, see Figure 2.1(c). If both islands are in the superconducting groundstate all degrees of freedom are frozen out by the energy gap of the superconductor, except the tunneling of Cooper pairs through the barrier. The energy change associated with a tunnel process is captured by the following hopping Hamiltonian [Büttiker87, Makhlin01]

$$H_{\text{tunnel}} = -\frac{E_J}{2} \sum_{N=-\infty}^{\infty} |N\rangle\langle N+1| + |N+1\rangle\langle N|, \quad (2.3)$$

where $\{|N\rangle\}$ label the charge basis states with N tunneled Cooper pairs relative to equilibrium. The energy E_J is the Josephson energy which depends on the tunnel barrier properties and is a measure of the energy associated with a tunnel process of a Cooper pair from one to the other island. The discreteness of the number of Cooper pairs is implicitly taken into account in this description. The tunneling Hamiltonian is diagonal in the phase basis $|\phi\rangle \propto \sum_N e^{iN\phi}|N\rangle$ with resulting eigenenergies

$$H_{\text{tunnel}}|\phi\rangle = -E_J \cos \phi|\phi\rangle. \quad (2.4)$$

The phase ϕ has the compact property $|\phi\rangle = |\phi + 2\pi\rangle$ and is identical to the phase difference between the two superconducting wavefunctions [Girvin11].

In addition to the tunneling energy, a finite capacitance C_J between the two superconducting islands gives rise to an electrostatic energy $Q^2/2C_J$, where Q is the charge operator $Q = 2e \sum N|N\rangle\langle N|$. The total Hamiltonian, including both the tunneling and the electrostatic energy, is thus given by

$$H = \frac{Q^2}{2C_J} - E_J \cos \phi \quad (2.5)$$

Comparing this Hamiltonian with the one for the LC circuit in Eq. (2.1) we find that

the electrostatic terms are equal but the magnetic energy $\Phi^2/2L$ is replaced by the tunneling energy $-E_J \cos \phi$. It is thus natural to interpret the phase ϕ as a magnetic flux in units of the reduced magnetic flux quantum $\varphi_0 = \hbar/2e$. The essential difference between the tunneling energy and a magnetic energy contribution is the non-quadratic dependence on ϕ . This leads to an anharmonic level spectrum, which is exactly what we were aiming for. Due to the analogy between the phase variable ϕ and the magnetic flux Φ we can treat the Josephson tunnel barrier as a nonlinear inductor, which in a circuit diagram is typically represented by a cross as illustrated in Figure 2.1(d). Note that the equivalence between phase ϕ and magnetic flux is also reflected in the second Josephson equation $V = \varphi_0 \dot{\phi}$ [Tinkham96], which states that the time derivative of the phase $\dot{\phi}$ is proportional to the voltage drop V across the barrier, similarly as for a magnetic flux variable.

2.2 Relevant circuit QED building blocks

Superconducting tunnel barriers in combination with inductive and capacitive elements form the fundamental toolbox for designing on-chip quantum systems with characteristic frequencies in the microwave domain. The wide range of experimentally accessible Josephson energies (E_J/h from GHz to THz range in our lab) allows us to form objects with different characteristic properties ranging from effective two-level system [Devoret04] to oscillators with a weak nonlinearity [Castellanos-Beltran07]. In this section, I introduce the main building blocks of the devices used in our experiments. I discuss the transmon qubit, the transmission line resonator, as well as the modeling of resistive elements and open transmission lines.

2.2.1 The transmon qubit

The Josephson junction Hamiltonian, as introduced in Eq. (2.5), describes in itself a non-linear oscillator. However, the transition frequencies of the Cooper pair box are very sensitive to non-integer offset charges n_g between tunneled Cooper pairs on the two islands. If such offset charges are induced by environmental stray fields or tunneled quasi-particles, this leads to unwanted dephasing. The offset charge can also be controlled using an external voltage bias. In the presence of offset charges, the Cooper pair box Hamiltonian becomes [Büttiker87, Makhlin01, Koch07]

$$H_{\text{CPB}} = 4E_C(N - n_g)^2 - E_J \cos \phi, \quad (2.6)$$

where N is the number operator of tunneled Cooper pairs and n_g is the offset charge in units of $2e$. Furthermore, we have expressed the total box capacitance C_J in terms of the charging energy $E_C = e^2/2C_J$. If we interpret N and ϕ analogues to momentum

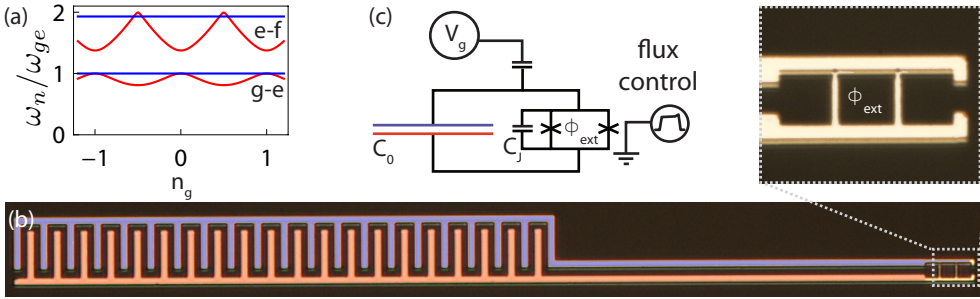


Figure 2.2: (a) First two transition energies of the transmon qubit as a function of offset charge n_g for the ratios $E_J/E_C = 5$ (red) and $E_J/E_C = 40$ (blue). (b) False color micrograph of a transmon qubit. The two superconducting aluminium islands (blue) and (red) are evaporated on a sapphire substrate (black). The Josephson junctions of the SQUID loop (enlarged picture) connect the two islands via a thin barrier of aluminium oxide. The flux control line allows for tuning the transition energies. For the shown device the charging energy is $E_C = 350$ MHz. (c) Equivalent circuit diagram of the transmon. The additional voltage source V_g models all controlled and uncontrolled sources of offset charges n_g .

and position variables, n_g plays the role of an additional vector potential. The Cooper pair box Hamiltonian can be diagonalized analytically, e.g. [Koch07], where we label the eigenstates as $\{|g\rangle, |e\rangle, |f\rangle, \dots\}$ and the associated nondegenerate transition energies as $\{\hbar\omega_{ge}, \hbar\omega_{ef}, \dots\}$.

For a typical Cooper pair box the ratio between Josephson and charging energy E_J/E_C is on the order of 1 and in this regime the transition energies strongly depend on the gate charge n_g . This unwanted energy dispersion due to offset charges can be exponentially suppressed by increasing the ratio E_J/E_C [Koch07, Schreier08], see Figure 2.2(a). Experimentally this is achieved by shunting the Josephson junction with an additional large capacitor C_0 such that the total charging energy decreases to $E_C = e^2/2(C_J + C_0)$.² The increased E_J/E_C ratio not only reduces the sensitivity to charge noise but also the anharmonicity $\alpha \equiv \omega_{ef} - \omega_{ge}$. However, the charge dispersion decreases exponentially with $\sim e^{-E_J/E_C}$, while the anharmonicity scales approximately linearly in E_C . It is thus possible to keep a sufficient amount of anharmonicity for using the device as an effective two-level system and at the same time suppress the charge dispersion to a degree where it is not limiting the dephasing time anymore. A detailed discussion about the capacitively shunted Cooper pair box including an analysis of the complete capacitance network and noise properties can be found in Ref. [Koch07].

An optical micrograph of a capacitively shunted Cooper pair box – called transmon

²In practice, the effective charging energy has to be determined from the full capacitive network as described in Refs. [Koch07, Burkhard12].

– is shown in Figure 2.2(b) with an equivalent circuit model in Figure 2.2(c). The interdigitated capacitor on the left forms the large shunting capacitance C_0 . Both islands are connected with a pair of Josephson junctions in a superconducting quantum interference device (SQUID) configuration. For our purposes it is sufficient to consider the SQUID loop as an effective single Josephson junction with tunable Josephson energy. If both junction have the same Josephson energy $E_J/2$, the total effective Josephson energy $E_{J,\text{tot}} = E_J |\cos(\Phi_{\text{ext}}/\varphi_0)|$ can be varied by changing the magnetic flux Φ_{ext} enclosed by the SQUID loop. Since the transition energy between the ground and first excited state ω_{ge} is given by $\hbar\omega_{ge} \approx \sqrt{8E_C E_{J,\text{tot}}} - E_C$, the tunable Josephson energy thus results in a tunable qubit frequency.

The tunability is desirable for two reasons: First, the Josephson energy of a tunnel barrier depends exponentially on the barrier thickness, which underlies small variations during the fabrication process. Therefore, even though the fabricated Josephson energy might slightly differ from the designed one, the tunability allows for biasing the qubit at a desired frequency. Second, the magnetic flux through the loop can be varied on nanosecond timescales using on-chip fluxlines [Majer07]. This fast tuning enables us to turn on and off the effective interaction with other circuit components for well-defined times. A potential drawback of this tunability is that the qubit frequency is sensitive to magnetic flux noise, especially far away from the 'sweet spot' [Vion02] at $\Phi_{\text{ext}} = 0$, where the gradient $|\partial\omega_{ge}/\partial\Phi_{\text{ext}}|$ is large.

The capacitive shunting of the Cooper pair box is only one possible modification to achieve noise resilient qubits. Various other superconducting devices have been fabricated based on current biased [Martinis02] or inductively shunted Josephson junctions [Friedman00, Chiorescu03, Manucharyan09], which can be operated with different control, coupling and readout mechanisms. However, the fundamental element of all these devices is always the Josephson junction with its anharmonic $\cos(\phi)$ - potential.

2.2.2 Transmission line resonator

A second building block of circuit QED devices are harmonic oscillators, which play the role of cavities in conventional cavity QED systems. They can be realized either as lumped element LC circuits [Geerlings12], as 3D cavities [Paik11, Rigetti12] or as distributed coplanar waveguide resonators [Wallraff04]. In our experiments we use the latter ones, which I therefore introduce in this section.

The coplanar waveguide resonator can be understood as the on-chip version of a finite length coaxial cable with two open ends. The inner conductor of this transmission line is formed by a thin stripe of metal with length d , while the outer conductor is realized as a large ground plane, see Figure 2.3a. In order to minimize resistive and dielectric losses, both parts are made of superconducting niobium evaporated on a

mono-crystalline sapphire substrate. Since its characteristic size d turns out to be comparable to the wavelengths of resonating modes, we have to treat the object as a distributed element, in which the voltage $V(x)$ with respect to ground and the current $I(x)$ flowing through the inner conductor are position dependent. The magnetic flux variable Φ thus becomes a continuous field, $\Phi \rightarrow \Phi(x)$, which is related to local voltage and current by [Yurke84]

$$V(x) = \dot{\Phi}(x) \quad , \quad I(x) = \frac{1}{l} \partial_x \Phi(x). \quad (2.7)$$

Here, we have introduced l as the self-inductance per unit length of the line. It is proportional to the vacuum permeability $l = g\mu_0$ in non-magnetic insulators. The dimensionless prefactor $g = g(s, w)$ is a function of the geometry parameters s and w of the line, compare Figure 2.3(b). For the specific parameters used in our devices the geometry factor is $g(w = 10 \mu\text{m}, s = 4.5 \mu\text{m}) = 0.318$ [Göppl08, Simons01].

To derive the Hamiltonian of the transmission line resonator we start from the total Lagrange function $\mathcal{L} = T - U$ and perform a Legendre transformation. In terms of the magnetic flux field $\Phi(x)$, the kinetic part T is given by the electric energy while the potential U is given by the magnetic energy. Integrating over the whole field results in the Lagrange function

$$\mathcal{L} = \int_0^d dx \left\{ \frac{c}{2} (\dot{\Phi}(x))^2 - \frac{1}{2l} (\partial_x \Phi(x))^2 \right\}, \quad (2.8)$$

where c is the capacitance per unit length of the line. It is proportional to the effective permittivity $c = g^{-1} \epsilon_{\text{eff}} \epsilon_0$, where the effective relative permittivity is found to be $\epsilon_{\text{eff}} \approx 5.5$ for sapphire substrates of thickness $h = 500 \mu\text{m}$.

Evaluating the Euler-Lagrange equation $\partial_t(\delta\mathcal{L}/\delta\dot{\Phi}) - \delta\mathcal{L}/\delta\Phi = 0$ results in the wave equation

$$v^2 \partial_x^2 \Phi(x) - \ddot{\Phi}(x) = 0, \quad (2.9)$$

where the wave velocity is given by $v = 1/\sqrt{lc} = 1/\sqrt{\epsilon_{\text{eff}} \epsilon_0 \mu_0}$. Note that the geometry factor $g(s, w)$ drops out in this expression such that the wave velocity v and likewise the resulting resonance frequencies are insensitive to small changes in the geometry parameters s and w . Variations in the photo-lithographical fabrication procedure therefore leave the resonance frequency unaffected, which makes their design and fabrication reliable and reproducible.

Taking into account the boundary condition of vanishing currents at the two open ends allows us to write the solution to the wave equation – up to a constant offset – in

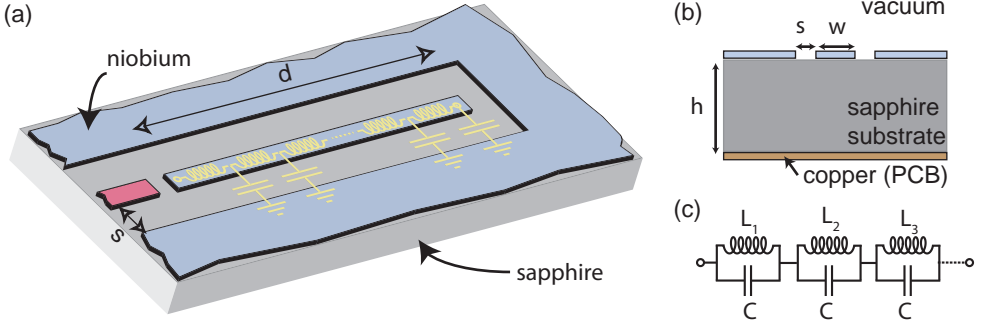


Figure 2.3: (a) Schematic of a coplanar transmission line resonator. A strip of superconducting niobium with length d is separated by a gap s from a ground plane of the same material (blue). Both are evaporated onto a mono-crystalline sapphire substrate (gray). The resonator is coupled with controlled strength to the electromagnetic environment (red) for applying classical drive field and for detection. The length d for typical transmission line resonators in the GHz range is a few millimeters. (b) Vertical cross section through a coplanar transmission line. The geometric factor g is determined by the width w of the inner conductor and its distance s from the ground plane. The thickness h of the dielectric substrate influences the effective dielectric constant ϵ_{eff} . (c) Effective circuit model of the transmission line resonator in the normal mode representation, neglecting the coupling to the electromagnetic environment.

terms of its normal modes

$$\Phi(x) = r \sum_{n=1}^{\infty} \phi_n \cos(k_n x), \quad (2.10)$$

with wave vectors $k_n = n\pi/d$. The dimensionless scaling factor r will be specified below, by requiring that the resonance modes have the correct impedance. In terms of the normal mode flux variables ϕ_n the Lagrange function is diagonal

$$\mathcal{L} = \frac{1}{2} \sum_n C \dot{\phi}_n^2 - \frac{1}{L_n} \phi_n^2 \quad \text{with } C = r^2 \frac{cd}{2}, \quad L_n = \frac{2ld}{r^2 \pi^2 n^2}. \quad (2.11)$$

Introducing the charge variable $q_n = \delta\mathcal{L}/\delta\dot{\phi}_n$ as the conjugate to the magnetic flux variable ϕ_n results in the Hamiltonian

$$\mathcal{H} = \frac{1}{2} \sum_{n=1}^{\infty} \left(\frac{q_n^2}{C} + \frac{\phi_n^2}{L_n} \right). \quad (2.12)$$

Comparing this Hamiltonian with the one in Eq. (2.1) we see that it describes a sum of independent harmonic oscillators with resonance frequencies $\omega_n = 1/\sqrt{L_n C} =$

$\pi n/d \sqrt{lc}$. In the quantum regime, the conjugate magnetic flux and charge are non-commuting operators $[\phi_n, q_m] = \delta_{nm} \hbar/i$ and we can write the Hamiltonian in the familiar form

$$\mathcal{H} = \sum_{n=1}^{\infty} \hbar \omega_n (a_n^\dagger a_n + \frac{1}{2}) \quad \text{with} \quad a_n \equiv \phi_n \frac{i}{\sqrt{2L_n \hbar \omega_n}} + q_n \frac{1}{\sqrt{2C \hbar \omega_n}}. \quad (2.13)$$

with field operators a_n . Although the resulting resonance frequencies ω_n are independent of r , this scaling factor becomes relevant when calculating the coupling rates to an environment (see next section). For this purpose the effective impedances

$$\sqrt{\frac{L_n}{C}} = \frac{2}{r^2 \pi n} \sqrt{\frac{l}{c}}, \quad (2.14)$$

of the resonating modes have to be known, which obviously depend on r . We can fix r by comparing the admittance $Y_n = -i\omega C + i/\omega L_n$ associated with each resonant mode with the admittance $Y_{\text{TL}} = -i \tan(\pi\omega/\omega_1)/Z_0$ of a transmission line of length d and impedance $Z_0 = \sqrt{l/c}$ [Poza93]. This admittance is required to be equal to Y_n in the vicinity of a resonance. Calculating the derivatives with respect to ω and requiring that they are equal $\partial_\omega Y_n|_{\omega=\omega_n} \doteq \partial_\omega Y_{\text{TL}}|_{\omega=\omega_n}$ leads to $r = 1$. In summary, we have found that the transmission line resonator can be expressed as a sum of independent LC oscillators with effective capacitance $C = cd/2$ and inductances $L_n = 2ld/\pi^2 n^2$. An equivalent circuit representation is shown in Figure 2.3(c).

2.2.3 Coupling to the electromagnetic environment

Until now we have assumed that the LC oscillators and the Cooper pair box are completely decoupled from their environment. In practice, however, we have to apply control signals for manipulating the system state and want to extract information from the system. Both require a connection to an electromagnetic environment, see coupling port in Figure 2.3(a). Furthermore, sources of loss and decoherence originate from the coupling to uncontrolled environmental degrees of freedom, such as spurious electromagnetic modes, as well as acoustic and electronic modes in the sample material. To capture these aspects it is necessary to extend the Hamiltonian description by including the environment into the models. This is of particular relevance for the presented experiments, in which the transformation of localized into propagating fields is studied.

For simplicity, we consider only a single mode of the above transmission line resonator $a \equiv a_n$ with associated Hamiltonian H_{sys} , which is capacitively coupled to a bath of environmental modes. Typically, these modes are realized as a transmission line of infinite length, as schematically shown in Figure 2.4(a). They could, however,

also be of completely different physical origin.

We can look at this situation from three different perspectives: First, we can have the viewpoint of an external observer who sends in a signal (quantum or classical) to extract information from the system by measuring the reflected output signal. This approach is captured by input-output-theory [Gardiner85]. Second, we can have the perspective of the system itself and ask how its quantum mechanical time-evolution is affected by the adjacent bath. This results in a master equation formulation of the system dynamics [Walls94]. Third, we can treat the system in an electrical circuit fashion [Poazar93], which is very useful when explicitly calculating decay rates. Instead of providing a formal derivation of these concepts I will lay out the relation between these approaches and discuss their practical relevance.

Input-Output Theory: Since the infinite length transmission line, shown in Figure 2.4(a), is equal to a transmission line resonator in the limit of $d \rightarrow \infty$, its Hamiltonian is given by $H_{\text{bath}} = \hbar \int_{\omega} d\omega \omega b_{\omega}^{\dagger} b_{\omega}$, where we have dropped the constant vacuum contribution $1/2$ for convenience. Furthermore, the coupling capacitance C_{κ} leads to a coupling Hamiltonian modeled by $H_{\text{coupl}} = \hbar \sqrt{\kappa/2\pi} \int_{\omega} d\omega (b_{\omega}^{\dagger} a + b_{\omega} a^{\dagger})$ [Walls94]. The relation between the coupling capacitance C_{κ} and the coupling rate κ is derived below. From the viewpoint of an external observer located at the end of the transmission line it is natural to decompose the bath modes into input $b_{\text{in}}(t)$ and output $b_{\text{out}}(t)$ modes which correspond to fields traveling towards or away from the system and reaching it at time t (compare Figure 2.4(a) and see Refs. [Walls94, Gardiner85] for a formal definition). While the input fields b_{in} could be controlled by for example an external drive field, the output modes b_{out} describe the signal reflected from the system. If we evaluate the Heisenberg equations of motion for the system and the bath modes using the full Hamiltonian $H_{\text{sys}} + H_{\text{bath}} + H_{\text{coupl}}$, we obtain the boundary condition [Gardiner85, Walls94]

$$b_{\text{out}}(t) = \sqrt{\kappa} a(t) - b_{\text{in}}(t) \quad (2.15)$$

between incoming and outgoing field modes. As expected, the output signal has not only a contribution from the input field, but also depends on the system field a . The equation of motion for the system field is given [Gardiner85, Walls94]

$$\dot{a}(t) = -\frac{i}{\hbar} [a, \mathcal{H}_{\text{sys}}] - \frac{\kappa}{2} a(t) + \sqrt{\kappa} b_{\text{in}}(t). \quad (2.16)$$

The first term on the right hand side describes the unitary evolution of the resonator, which is independent of κ . The second term is a damping term, which leads to a decay of the resonator field. The last term acts as an external driving force. Thus, Eq. (2.16) is equivalent to the equation of motion for a driven and damped oscillator. Note that the input modes at different times are independent and satisfy the commutation

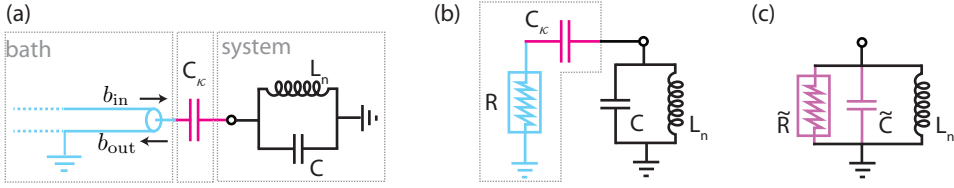


Figure 2.4: (a) Schematic of a single LC oscillator (system) capacitively coupled to the electromagnetic environment (bath) realized as a transmission line of infinite length. (b) The transmission line acts as a perfect absorber (i.e. blackbody) to the system which in electrical circuits is represented by a resistor with real impedance $Z(\omega) = R$. (c) The circuit in (b) can be mapped onto an effective parallel LCR circuit.

relation $[b_{in}(t), b_{in}^\dagger(t')] = \delta(t - t')$. Furthermore they carry at least the vacuum noise to the resonator which will become important in the context of vacuum squeezing (see Section 4.5). The input-output relations in Eq. (2.16) are of particular relevance in the context of spectroscopic measurements, in which the averaged output field $\langle b_{out} \rangle$ is measured while applying a classical drive field $b_{in}(t) \rightarrow \beta e^{-i\omega t}$. The measurement of the resulting reflection coefficient $r \equiv \langle b_{out} \rangle / \langle b_{in} \rangle$, and more generally the scattering matrix for systems with multiple coupling ports, are an important tool for characterizing superconducting circuit devices.

Master equation approach:

While the input-output approach results in a Heisenberg equation of motion for the field operator, it is sometimes desirable to express the system dynamics in terms of a density matrix ρ , since it also captures higher order field correlations. If the input modes are all in thermal equilibrium characterized by $\langle b_{in}(t) \rangle = 0$ and $\langle b_{in}^\dagger(t)b_{in}(t') \rangle = \bar{N}\delta(t - t')$ with thermal occupation number \bar{N} . The bath has two distinct effects on the system. First, it acts as a channel for decay into the transmission line and second, it randomly excites the system if the bath is at non-zero temperature. From the viewpoint of the system the bath presents an ideal blackbody in the sense that all radiation leaking into the bath will never be reflected back but is perfectly absorbed. An extension of the Schrödinger equation for ρ can be found, which accounts for these two effects but is otherwise independent of the bath modes. It results in the master equation [Walls94]

$$\dot{\rho} = \frac{i}{\hbar} [\rho, H_{sys}] + \underbrace{(\bar{N} + 1) \frac{\kappa}{2} (2a\rho a^\dagger - a^\dagger a \rho - \rho a^\dagger a)}_{\text{decay}} + \underbrace{\bar{N} \frac{\kappa}{2} (2a^\dagger \rho a - a a^\dagger \rho - \rho a a^\dagger)}_{\text{spontaneous excitation}}, \quad (2.17)$$

where all modes of the bath are traced out. The first term on the right hand side of Eq. (2.17) expresses the unitary evolution of the density matrix and the last two terms account for the average effect of spontaneous decay and excitation by appropriate

Lindblad terms [Lindblad76]. Note that the two last terms in Eq. (2.16) describe the same two effects, as long as the input modes $b_{\text{in}}(t)$ carry thermal noise. The derivation of the master equation is based on the Markov assumption [Gardiner91] that the input modes $b_{\text{in}}(t)$ are independent of the history of the resonator field a . Equivalently, one can say that the correlation time between system and bath is zero. The specific form of the Lindblad terms in Eq. (2.17) is related to the form of the coupling Hamiltonian H_{coupl} . If the bath couples to the photon number operator $n = a^\dagger a$ instead of the field operator a this leads to Lindblad terms of the type $\frac{1}{2}\gamma_\phi(2n\rho n - n^2\rho - \rho n^2)$, which describe pure dephasing [Gardiner91].

Damping in electrical circuits: From the viewpoint of the system, the open transmission line appears as an ideal one-dimensional blackbody, which on the one hand perfectly absorbs all incident radiation and on the other hand carries thermal and vacuum noise to the system. In an electrical circuit diagram such an ideal absorber – or blackbody – can be represented by a resistor with impedance $Z(\omega) = R = \sqrt{l/c}$, which is frequency independent, real and equal to the ratio between inductance and capacitance per unit length of the transmission line. In order to calculate the coupling rate κ between system and bath it is convenient to represent the transmission line by this resistive circuit element, as shown in Figure 2.4(b), and to use Kirchhoff's and Ohm's laws to derive an appropriate equation of motion for the field stored in the system. To this aim we map the circuit in Figure 2.4(b) onto an equivalent parallel LCR circuit (see Figure 2.4(c)) with effective resistance \tilde{R} and capacitance \tilde{C} given by

$$\begin{aligned}\tilde{C} &= \frac{C_\kappa}{\omega^2 C_\kappa^2 R^2 + 1} + C \approx C_\kappa + C \\ \tilde{R} &= R \left(1 + \frac{1}{\omega^2 C_\kappa^2 R^2}\right) \approx \frac{R}{\omega^2 C_\kappa^2 R^2}.\end{aligned}\quad (2.18)$$

Both approximations hold in the limit where the coupling to the transmission line C_κ is small compared to the effective capacitance C of the resonator mode. Since the sum of all currents through the elements has to vanish, the parallel LCR circuit is described by the following equation of motion for the voltage V across the circuit elements

$$\ddot{V}\tilde{C} + \frac{\dot{V}}{\tilde{R}} + \frac{V}{L_n} = 0. \quad (2.19)$$

This equation describes a damped harmonic oscillation with decay rate

$$\kappa = \frac{1}{\tilde{C}\tilde{R}} \approx \frac{C_\kappa^2 R}{C^2 L_n} \quad (2.20)$$

and resonance frequency

$$\tilde{\omega}_n^2 = \frac{1}{\tilde{C}L_n} - \frac{\kappa^2}{4} = \frac{\omega_n^2}{1 + C_\kappa/C} - \frac{\kappa^2}{4} \approx \frac{\omega_n^2}{1 + C_\kappa/C}. \quad (2.21)$$

The larger the ratio C_κ/C is, the more the resonator is shifted towards lower frequencies. The damping rate κ is the one which has already appeared in the master equation and in the input-output relations. In order to include the additional frequency shift into the Hamiltonian description we have to replace ω_n by $\tilde{\omega}_n$ in Eq. (2.13). This calculation has shown that the basic methods of electrical circuitry are very powerful for calculating decay rates and frequency shifts due to the coupling to an electromagnetic environment and often more easily accessible than Fermi's golden rule based calculations. The same approach is in good approximation also applicable to nonlinear circuits which include Josephson junctions. Eq. (2.20) can thus also be used to calculate the capacitive coupling rates between a transmon qubit and its adjacent flux and gate lines.

Finally, I would like to emphasize that the term 'dissipation' in this context may imply that the radiation is lost. However, in many situation the open transmission line is connected to a detector or other systems and thus the intra-cavity field is not damped in the conventional sense but only transformed into propagating transmission line modes, compare Section 3.2.2.

2.3 Coupling a qubit to a resonator: The Jaynes-Cummings model

In the previous section I have discussed the transmon as an artificial atom and the transmission line resonator as a cavity-like object which allows for storing photons in the microwave frequency range. If the transmon is positioned in the large electrical field of the resonator, it can strongly interact with the photons stored in the resonator. In this situation, the two systems can coherently exchange energy faster than their respective decoherence rates, which is referred to as the strong coupling limit of cavity QED [Haroche06]. In circuit QED large coupling rates are easily accessible, mainly due to the large size of the participating objects and their planar geometry (compare Figure 2.5(a)). Because of the correspondingly small mode volume the effective dipole moment is highly enhanced [Devoret07]. This has first been realized experimentally in 2004 [Wallraff04] and enabled further investigations of interactions between photons and atom-like systems in electrical circuits by adapting the concepts of cavity QED physics, see schematic in Figure 2.5(b).

As for the individual objects, we can find the equivalent Hamilton function of the

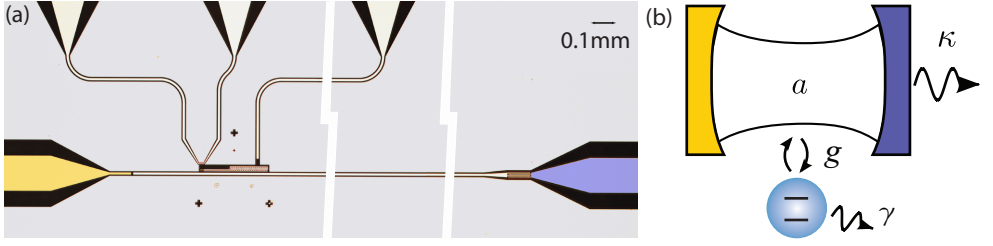


Figure 2.5: (a) False color optical micrograph of a typical circuit QED sample used in our experiments. A single transmon with two individual control lines is coupled to a transmission line resonator with one weakly coupled input port (orange) and one strongly coupled output port (violet). (b) Schematic of an equivalent cavity QED system with a single atom coupled to an optical cavity.

combined transmon-resonator circuit. The detailed procedure how to map the full capacitive network³ to the Hamiltonian is described e.g. in Refs. [Blais04, Koch07, Burkhard12]. For circuit designs similar to the one shown in Figure 2.5, the final Hamiltonian can be written as [Blais04]

$$H_{JC} = \underbrace{4E_C(N - n_g)^2 - E_J \cos \phi}_{=H_{CPB}} + \underbrace{\hbar\omega_{\text{res}}a^\dagger a}_{=H_{\text{res}}} + \underbrace{2\beta eV_{\text{rms}} N(a + a^\dagger)}_{=H_{\text{int}}} \quad (2.22)$$

where $V_{\text{rms}} = \sqrt{\hbar\omega_{\text{res}}/2C}$ is the voltage associated with the vacuum field of the resonator with frequency ω_{res} . The geometry dependent prefactor $\beta < 1$ takes into account that only part of the voltage drop V_{rms} is across the Cooper pair box islands. Since V_{rms} is fixed by the resonator properties, β is the important tuning parameter when designing a specific coupling strength. In Eq. (2.22) we have assumed that only one resonator mode a has a frequency close to the qubit transition frequency ω_{ge} and all the other modes can be neglected. Note that these modes can have a significant effect on the cavity-mediated qubit-qubit interaction [Filipp11]. This is, however, not relevant for the work presented in this thesis, in which the single mode approximation is valid for all experiments.

When the coupling energy is small compared to the qubit and resonator transition frequencies, we can make a rotating wave approximation [Jaynes63] and express the interaction part of the Hamiltonian in the eigenbasis $\{|i\rangle\}$ of the Cooper pair box Hamiltonian [Koch07]

$$H_{\text{int}} = -i\hbar \sum_{i=g,e,f,\dots} g_i |i+1\rangle\langle i| a - \text{h.c.}, \quad \text{with } g_i \equiv 2\beta eV_{\text{rms}}\langle i|N|i+1\rangle, \quad (2.23)$$

³The required simulation of capacitances between all contributing superconducting islands is typically realized with commercially available finite-element software, such as *Ansoft Maxwell*.

where the matrix elements are approximately $\langle i|N|i+1\rangle \approx \sqrt{i+1} (E_J/(32E_C))^{1/4}$. For later convenience, we have also introduced an additional factor $-i$, which corresponds to a local phase rotation of the field operator $a \rightarrow -ia$. Interestingly, the expression for the matrix elements implies that a decreasing charging energy leads to an increase in coupling strength.

Eq. (2.23) describes the interaction part of a generalized Jaynes-Cummings Hamiltonian, which includes all higher transmon levels. Due to the anharmonicity of transmon levels it is often possible to take only the first two lowest lying energy levels $\{|g\rangle, |e\rangle\}$ into consideration and describe the transmon as an effective two-level system. In this case the Hamiltonian reduces to the Jaynes-Cummings Hamiltonian for a qubit

$$H_{\text{int}} = -i\hbar g (\sigma^+ a - \sigma^- a^\dagger), \quad (2.24)$$

where we have set $g \equiv g_g$ and defined $\sigma^+ \equiv |e\rangle\langle g| \equiv (\sigma^-)^\dagger$.

In the following, we describe the dynamics of this system in the two limiting situations where the detuning $\Delta = \omega_{ge} - \omega_{\text{res}}$ between qubit and resonator frequency is either large or small compared to the coupling strength.

2.3.1 Dispersive regime

As discussed above, the transition frequency of the qubit ω_{ge} and thus its detuning Δ from the resonator can be varied by changing the magnetic flux enclosed by the SQUID loop of the transmon. If the qubit is far detuned from the resonator $\Delta \gg g$, the two systems are non-resonantly coupled and interact only dispersively without direct energy exchange. In our experiments, this dispersive interaction is used for reading out the qubit state by applying a coherent microwave field to the resonator [Blais04, Wallraff05] and measuring its qubit state dependent response.

In order to derive the dispersive limit of the transmon-resonator coupling, it is important to take the higher transmon levels into account, since they lead to additional dispersive shifts even if they stay unpopulated. This is due to the relatively weak anharmonicity of the transmon levels compared to the Cooper pair box. Diagonalizing the generalized Hamiltonian in Eq. (2.22) to first order in the small parameters $\lambda_i = g_i/\Delta_i$, where Δ_i is the detuning of the i -th transmon transition frequency from the resonator frequency, results in [Koch07]

$$H_{\text{JC}} \rightarrow e^{-X} H_{\text{JC}} e^{+X} \approx H_{\text{JC}} + [H_{\text{JC}}, X] \approx \hbar\omega'_{\text{res}} a^\dagger a - \frac{\hbar}{2} \omega'_{ge} \sigma_z - \hbar\chi \sigma_z a^\dagger a. \quad (2.25)$$

Here, we have defined $X = i \sum_i (\lambda_i a |i+1\rangle\langle i| + \text{h.c.})$ and $\sigma_z = |g\rangle\langle g| - |e\rangle\langle e|$. The

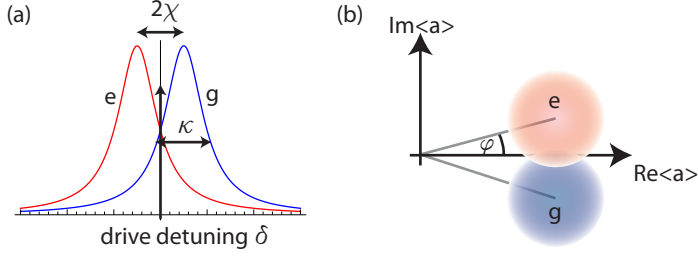


Figure 2.6: (a) Mean photon number in a resonator with linewidth κ when a coherent drive is applied at detuning $\delta = \omega_{\text{drive}} - \omega'_{\text{res}}$ for the qubit in the ground state (blue) and in the excited state (red). (b) When the drive is applied at zero detuning $\delta = 0$, only the phase φ of the output field depends on the qubit state. The measurement of this phase allows us to distinguish between ground and excited state. The colored circles indicate quantum fluctuations and thermal noise added during detection, which requires a minimal measurement strength or averaging over many realizations to distinguish between the two amplitudes.

dispersive energy shift is

$$\hbar\chi \approx -\frac{g^2 E_C}{\Delta(\Delta - E_C/\hbar)}. \quad (2.26)$$

The frequencies ω'_{res} and ω'_{ge} account for the frequency renormalizations due to the dispersive interaction. Since they are typically small, we will in the following not explicitly distinguish between the bare and the renormalized frequencies.

The important term in Eq. (2.25) is $\chi\sigma_z a^\dagger a$, which can be either interpreted as a photon number dependent qubit frequency shift (AC Stark shift) or as a qubit state dependent resonator shift [Blais04]. In the latter interpretation the resonator has a qubit state dependent response to a classical drive, see Figure 2.6(a), which can be measured in the resonator output field for determining the qubit state [Wallraff05, Gambetta06, Bianchetti09]. More specifically, the qubit becomes entangled with the coherent resonator output field such that a measurement performed on the output field projects the qubit onto the corresponding eigenstate. We discuss this aspect in more detail in Section 5.3.

Due to vacuum fluctuations and additional noise added during the detection, the integrated output field has to have a minimal amplitude to distinguish between ground and excited state with high fidelity, compare Figure 2.6(b). This integrated amplitude can either be increased by turning on the measurement tone for a longer time or by increasing its power. Since the measurement time is typically limited by the finite qubit lifetime, one aims for increasing the measurement power. However, when increasing the power to a value where the mean photon number in the resonator exceeds the critical photon number of $n_{\text{crit}} = \Delta^2/4g^2$ [Blais04], the dispersive approximation on the right hand side of Eq. (2.25) breaks down and higher order terms in the expansion

become relevant [Reed10, Boissonneault10, Laflamme12]. While such regimes can still be useful for realizing a high-fidelity qubit readout, the quantum non-demolition (QND) character [Lupaşcu07] of the measurement is then no longer guaranteed. For feedback and post-selection application the QND nature of the measurement is, however, desirable and the alternative way to increase the distinguishability of ground and excited state within the qubit lifetime is to use a better, possibly quantum limited amplifier, see Chapter 4.

2.3.2 Dynamics at qubit-cavity resonance

If the qubit is tuned close to resonance with the cavity, the interaction term H_{int} leads to a hybridization of the two systems and new energy eigenstates are formed. In the two-level approximation of the transmon the corresponding eigenenergies are given by [Haroche06]

$$\hbar\omega_n^\pm = n\hbar\omega_{\text{res}} \pm \frac{\hbar}{2} \sqrt{\Delta^2 + 4ng^2} + \frac{\hbar}{2}\Delta, \quad (2.27)$$

where we have shifted the ground state energy to zero for convenience. On resonance $\Delta = 0$, the corresponding eigenstates are given by $|n\pm\rangle = (|ng\rangle \mp i|n-1e\rangle)/\sqrt{2}$. Each resonator eigenenergy is thus split into two new energies. The splitting scales with the square root of the photon number in the resonator, as indicated in the level diagram in Figure 2.7(a). This \sqrt{n} scaling provides a direct proof for the anharmonic character of the transmon and the quantum nature of the hybridization of the two systems [Fink08, Bishop09b, Fink10b].

If the system is initially in the ground state and is probed with a coherent drive field at frequency ω , transitions into one of the first two excited states are induced when the drive is close to the respective transition frequency $\omega \approx \omega_0^\pm$. Further transitions into higher excited states are suppressed due to the nonlinear scaling of transition energies (compare level diagram Figure 2.7(a)). Because of this blocking of further transitions, only one excitation may enter the system at a time – an effect which is referred to as photon blockade [Imamoğlu97]. This effect shows up in the antibunching of photons in the fluorescent radiation and can thus be used as a continuously driven single microwave photon source [Lang11].

Since the interaction time between qubit and resonator is controllable, the Jaynes-Cummings dynamics can also be used to coherently exchange energy between the two systems. Bringing the qubit initially into its excited state $|e0\rangle$ while it is far detuned from the resonator and then tuning it into resonance for variable time τ , the single qubit excitation oscillates between qubit and resonator according to the time-evolution $\cos(2g\tau)|e0\rangle + \sin(g\tau)|g1\rangle$ of the initial state. Since the cavity field is initially empty these oscillations are called Vacuum Rabi oscillations. In the experiments described below, we make use of these oscillations for preparing single and two photon Fock

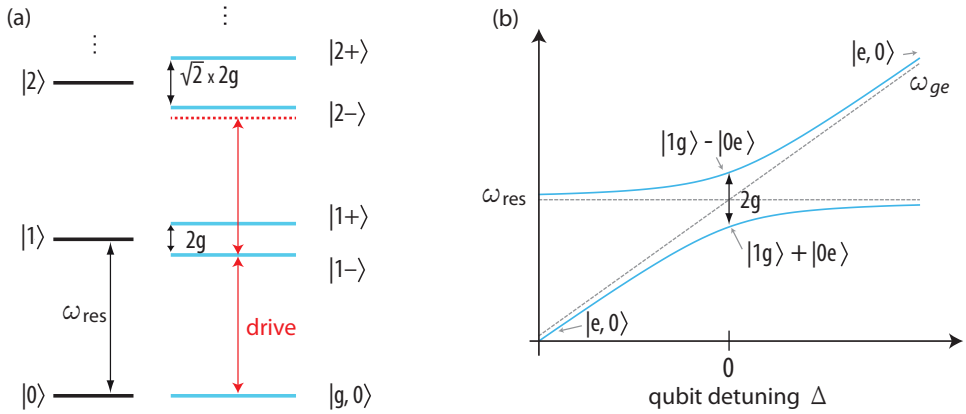


Figure 2.7: (a) Level diagram for the Jaynes-Cummings model at zero detuning $\Delta = 0$. Each level of the harmonic oscillator is split into two new levels due to the hybridization with the qubit. A coherent drive (red), resonant with the transition from the ground to the $|1-\rangle$ state, is off-resonant from the next higher transition. A second photon can not enter the system. (b) Vacuum Rabi splitting vs. qubit-resonator detuning.

states [Hofheinz08, Eichler12a] as well as for entangling the qubit with itinerant single microwave photons [Eichler12b].

2.4 General aspects of the experimental setup

In this section I describe the basic experimental principles for probing superconducting circuits at millikelvin temperatures. I briefly summarize the chip fabrication process, illustrate the cryogenic environment and discuss the implementation of microwave and DC control lines. Finally, the components of the linear microwave detection chain and the data acquisition are presented.

2.4.1 Fabricating and probing superconducting circuit devices

The superconducting circuits, which we use in our experiments, are fabricated in the *FIRST* cleanroom at *ETH* Zurich⁴. Structures which have a feature size of more than a micrometer are fabricated using photolithography. During this process we spin a thin layer of photoresistive material (e.g. PMMA) on a niobium sputtered 4-inch sapphire wafer, align a mask which comprises all the micron size structures on top of the resist, and expose those regions with UV light which are removed afterwards by chemical developing. The parts which are no longer covered by photoresist are then etched

⁴www.first.ethz.ch

away using a reactive ion etcher⁵. Finally, the remaining photoresist is chemically removed using acetone.

After completing the photolithographic procedure, the individual microchip devices are cut out of the 4-inch wafer with a dicing saw⁶. The individual devices are then either used as test chips for measuring basic sample properties such as resonance frequencies and quality factors in a helium bath at $T = 4.2$ K, or they are further processed by writing Josephson junctions and structures with smaller feature size than $1\ \mu\text{m}$ onto the chip. This is done by an electron beam lithography process, which reaches a resolution down to 2 nm. The desired structures are written into a bi-layer of e-beam resist, which acts as a mask for the shadow evaporation of aluminium. Josephson junctions are realized by oxidizing the first aluminium layer in a controlled fashion and evaporating a second layer of aluminium under a different evaporation angle. The thickness of the oxide layer, which is predominantly controlled by the oxidation time, and its area determine the Josephson energy of the junction. For details about the photo- and electron beam lithography procedures realized in our lab we refer the reader to Refs. [Göppl09, Fink10a].

In order to probe the fabricated devices in a standardized well-controlled microwave environment, they are glued with PMMA and mounted into a printed circuit board (PCB), see Figure 2.8(b). Care has to be taken when designing printed circuit boards in order to avoid spurious modes in the relevant frequency range, which can act as uncontrolled decay channels. The transmission lines on the microchip and those on the PCB are attached to each other with aluminium wire bonds. They are placed manually onto the sample using the wire bonder⁷. Wire bonds are also used to contact the ground plain of the chip with the one on the PCB, compare Figure 2.8(a). Parasitic resonances can be avoided by increasing the density of bond wires and by reducing their length, see e.g. Ref [Wenner11]. For the latter reason it can also be advantageous to use photolithographically fabricated airbridges instead of bond wires to contact different parts of the ground plane on the chip. The microwave transmission lines on the PCB are connected to SMP microwave connectors⁸, which provide an interface for connecting standard semi rigid coaxial cables, as shown in Figure 2.8(b). Ideally, all the transmission lines on sample and PCB are designed to have the same effective impedance of $50\ \Omega$ as the attached coaxial cables.

In order to probe the quantum properties of the devices, they are cooled down to millikelvin temperatures, at which thermal excitations are strongly suppressed. This is achieved by mounting the PCB in a sample holder box attached to the base plate of a dilution refrigerator Figure 2.8(c). All parts are made of oxygen free copper

⁵*RIE 76 from Oxford instruments*

⁶*Disco DAD 321*

⁷*Westbond 747677E*

⁸*Rosenberger 19S102-40ME4*

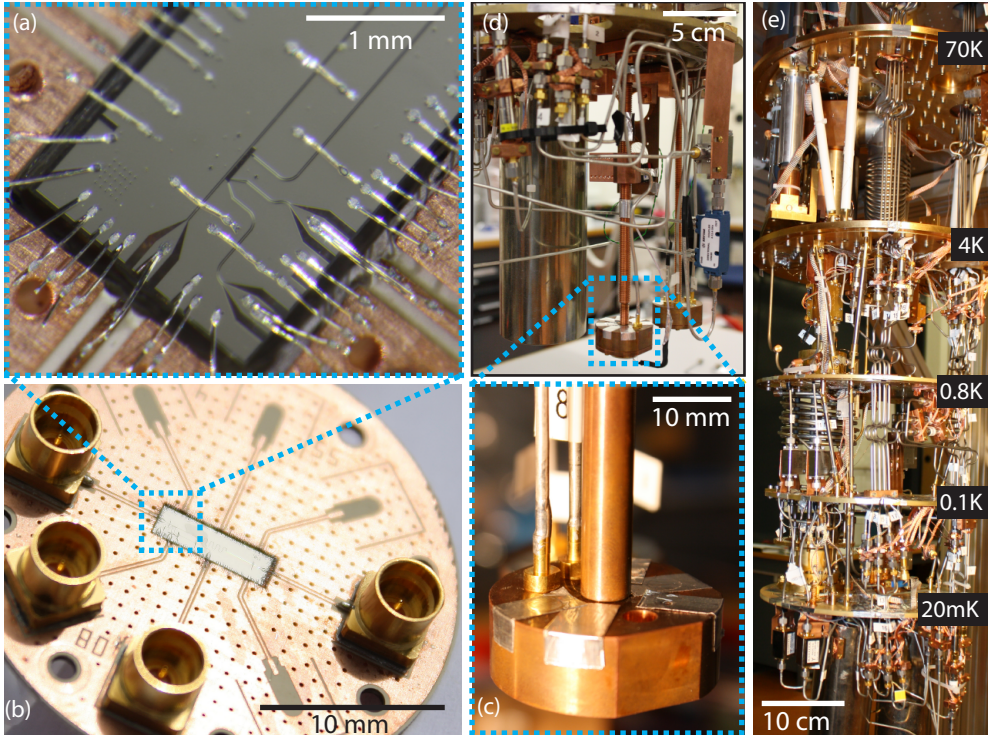


Figure 2.8: (a) Image of a fabricated sample glued into a PCB and connected to it with aluminium bond wires. (b) Full size image of the PCB with SMP connectors. (c) Image of the sample holder box onto which the sample/PCB is mounted. Two semirigid cables are connected to the sample trough the box. (d) Components attached to the base plate of the dilution refrigerator including sample holders, magnetic shields, semirigid cables and various microwave components. (e) Inner part of the dilution refrigerator with indicated temperature stages.

to guarantee fast thermalization between the sample and the base plate. The base temperature is typically at $T = 20$ mK. The holder is surrounded by a cryoperm magnetic shield to reduce stray magnetic fields (Figure 2.8(d)). Controlled magnetic flux bias is applied through a small coil mounted underneath the sample (not visible in the shown pictures).

The dilution refrigerator⁹ (inner part shown in Figure 2.8(e)), relies on two cooling mechanisms [Pobell06]. Pulse tube refrigeration is used for pre-cooling down to $T \approx 4$ K, while the millikelvin temperatures are reached by dilution refrigeration. The pulse tube cooler [Mikulin84] removes heat from the system by periodically pumping

⁹Vericold DR200

He^4 gas into and out of two regenerators filled with porous media. One regenerator is positioned at the upper plate, which is cooled to $T \approx 60$ K. The other one is placed at the 4 K stage underneath (compare Figure 2.8(e)). The heart of the dilution refrigerator is a mixing chamber mounted at the base plate of the cryostat. In the steady state of operation a dilute phase of He^3 floats on top of a pure He^4 phase. The energy required for He^3 atoms to pass through the boundary of the two phases is taken from the environmental heat bath, which causes cooling when He^3 is pumped through the mixture. Heat exchange between the downwards and upwards flowing He is used for gradually cooling down the additional plates from ~ 800 mK down to ~ 20 mK at the base plate. The efficient circulation of He^3 through the dilution unit is enhanced by pumping at a large volume placed at the 800 mK plate (*still*). For details about cryogenic cooling techniques we refer the reader to Ref. [Pobell06].

2.4.2 Electromagnetic control lines

When operating superconducting devices in a quantum regime, not only the relevant modes of the sample itself have to be cooled into their quantum ground state, but also the modes carrying the control signals which are incident to the sample need to be close to the vacuum noise level. Since all these signals are generated at room temperature, they have to be attenuated on the way down to the sample such that the associated thermal noise effectively reaches the vacuum level. On the other hand the cabling has to be chosen such that heat load from the room temperature environment onto the cold plate is minimized. Figure 2.9 schematically shows how the three generic types of control lines are implemented to match these conditions.

A typical microwave control line is shown in Figure 2.9(a). The microwave signals are generated with low phase noise signal generators¹⁰. They output a coherent field with analogous properties as the field produced by a laser at optical frequencies. The continuous signal, which has frequencies up to 20 GHz, can either be gated or modulated in phase and amplitude to generate controlled pulse shapes with a bandwidth above 1 GHz. This is done by multiplying the output of the signal generator at an IQ -mixer with a shaped pulse from an arbitrary waveform generator (AWG). For a detailed discussion about pulse generation, modulation and calibration using AWGs and mixers, see PhD thesis of M. Baur [Baur12].

Since the coherent microwave fields are generated at room temperature they include thermal noise of the source, which is at least as high as the effective Johnson-Nyquist noise at temperature $T_0 \approx 300$ K. The vacuum limit of noise is essentially reached for frequencies $\omega/2\pi \gg k_B T_0/h$. While for radiation at optical frequencies this inequality is satisfied at room temperature, for microwave frequencies the noise is three

¹⁰e.g. Agilent E8257D and Rohde & Schwarz SMF100A

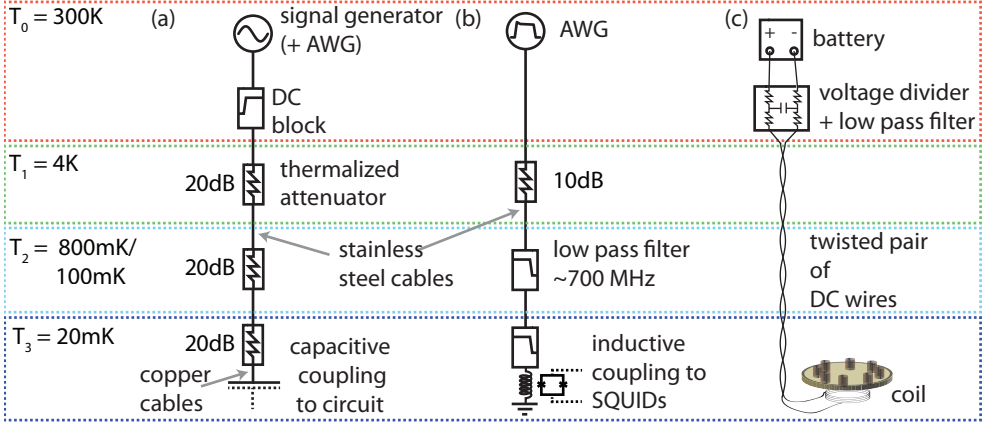


Figure 2.9: (a) Microwave control line. (b) Flux control line. (c) DC flux bias line. For details see discussion in the main text.

orders of magnitude above the vacuum limit. To attenuate these additional thermal fluctuations, the signal is sent through a chain of attenuators, which are thermalized at the various temperature stages of the cryostat (compare Figure 2.9(a)). An attenuator with attenuation constant $A = -20 \text{ dB} = 0.01$, thermalized at temperature T , can be interpreted as a beamsplitter with transmission coefficient A , which transmits only 1% of the incident power, while adding 99% of blackbody radiation from a resistor at temperature T . The effective noise temperature T_{eff} of radiation after a chain of equal attenuators, which are thermalized at temperatures $T_0, T_1, T_2, T_3, \dots$ can thus be estimated as $k_B T_{\text{eff}} \approx \hbar \omega / \ln(n_{\text{eff}}^{-1} + 1)$, where

$$n_{\text{eff}} \stackrel{A \ll 1}{\approx} \dots n_3 + A(n_2 + A(n_1 + An_0)) \dots \quad (2.28)$$

is the effective number of noise photons determined by the Bose-Einstein distribution $n_i = 1/(e^{\hbar \omega / k_B T_i} - 1)$. For the sequence of temperature stages as denoted in Figure 2.9(a), this results in $T_{\text{eff}} \approx 55 \text{ mK}$ at frequency $\omega / 2\pi = 7 \text{ GHz}$ and thus leads to an effective cooling of incoming radiation to the vacuum noise level. As long as the microwave source has sufficient output power, the attenuation of the coherent part of the signal can be compensated by increasing the power of the signal generator and/or the AWG accordingly.

In order to reduce the heat load onto the base plate all microwave cables which pass through different temperature stages and are used for control, are made of stainless steel¹¹. Compared to copper cables their heat conductivity is at least two orders

¹¹UT85-SS-SS

of magnitude lower depending on the specific temperature and the exact material [Fink10a]. The higher amount of attenuation in stainless steel cables is not a problem since the signals are anyway strongly attenuated on the way to the sample. The residual heat load through the cables can be reasonably distributed among the different temperature stages of the cryostat by appropriately adjusting the distances between thermalizing contacts attached to the cables [Fink10a].

While the microwave radiation couples capacitively to the on-chip circuit, the effective Josephson energies of SQUID loops are controlled by applying magnetic fluxes. A typical flux control line is schematically shown in Figure 2.9(b). For the generation of flux pulses we use arbitrary waveform generators¹² with a sampling rate of 1.2 G samples per second. This high bandwidth allows us to manipulate the transmon transition frequencies on timescales faster than their typical interaction time with the resonator. Finite thermal noise on flux control fields does not necessarily limit the stability of transition frequencies. By reducing the mutual inductance (i.e. coupling strength) between the flux control line and the SQUID loop, the effective noise on transition frequencies can in principle be reduced to a level where the frequency stability is limited by other effects. Strong attenuation of DC currents would also cause unwanted heating. The flux lines are therefore not as strongly attenuated as the microwave transmission lines. All the high frequency components which are not relevant for shaping the flux control pulse are filtered out using cold low pass filters¹³ with typical cutoff frequencies between 500 – 1000 MHz. Due to finite impedance mismatches and frequency dependent attenuation in the flux line, its actual response function deviates from that of the bare low pass filters. In order to account for these additional filter effects we measure the response function of the flux line when the cryostat is warm and correct the generated AWG output such that the pulse incident on the sample agrees best with the desired pulse shape. For details about this inversion of the flux response function, see Ref. [Baur12].

Finally, I would like to stress that it is important to minimize particularly the low frequency noise incident on the flux line. Consequently, one has to avoid ground loops between the instruments and the cryostat. In our setup we have achieved this by grounding the cryostat only via the fluxline, which is connected to the AWG. Furthermore, one could add a DC block to the input of the flux line such that frequency components below a few kHz are filtered out. This, however, may require a more involved signal shaping, which takes into account the additional filter effect in combination with the finite repetition rate of applied flux pulses.

In addition to the flux control lines we use small coils mounted below the sample to apply a constant magnetic flux bias to the SQUIDs (Figure 2.9(c)). Using coils

¹²Tektronix 5014 AWG

¹³Mini-Circuits VLF series

instead of on-chip flux lines for DC bias avoids a steady current flow onto the PCB, which can lead to significant heating. The coils are fed through a twisted pair of DC wires powered by a voltage source¹⁴ providing a maximum voltage of ± 20 V and a resolution of 1 mV. Above the 4 K temperature stage the wires are made of copper, while below the 4 K stage superconducting NbTi wires are used to avoid heating. The wires are thermalized at each temperature stage by twisting them around a copper heat sink. Current noise through the coil is reduced by adding a high impedance low pass filter at room temperature and shielding the cables outside the cryostat.

2.4.3 Linear detection chain: Amplification and noise

In all experiments presented in this thesis, we measure the microwave radiation emitted from the sample under investigation, after applying a sequence of control fields or while continuously driving the system. In many cases one exclusively measures the classical part of these output fields, which carries information about the sample properties. However, more recently we have developed methods to investigate the non-classical features of the emitted microwave radiation by measuring higher order photon correlations [Bozyigit11, Eichler11b, Eichler12a]. Because of the much smaller energy of microwave photons compared to their optical counterpart it is challenging to measure microwave fields with high efficiency. In particular, photon counters in the relevant frequency range are still under development [Chen11] and the detection of microwave radiation is most commonly realized with linear amplifiers and analog-to-digital converters (ADCs) instead. A detailed discussion of the components in our detection chain is presented in this section. A comparison with optical homodyne detection and a formal description of the measured quantities is provided in the context of photon state tomography in Chapter 3.

The detection chain used in our experiments is schematically shown in Figure 2.10(a) with all of its individual components. To visualize the effect of amplification and down-conversion, we consider the evolution of a signal emitted from the sample. The signal is centered around a carrier frequency f_{RF} with some finite bandwidth. The corresponding power spectral density S_f of this output field is schematically depicted in Figure 2.10(b). The radiation is sent into a high electron mobility transistor (HEMT) amplifier which is thermalized at the 4 K plate. Two isolators between the source and the HEMT amplifier provide directionality in the propagation of radiation. While they efficiently attenuate thermal noise which propagates backwards from the 4 K stage to the sample, they are – in the ideal case – perfectly transmitting in forward direction¹⁵. In practice, however, they impose additional attenuation and insertion loss also in forward direction, which together with the

¹⁴SIM928 from *Stanford Research Systems*

¹⁵Note that the development of on-chip circulators is an active field of research [Kamal11]

cable losses lead to a total attenuation $A < 1$ between sample and HEMT amplifier. In the relevant frequency range around 7 GHz the best available HEMT amplifiers add $N_{\text{HEMT}} \approx 6 - 10$ noise photons per Hz per second to the signal at the input. The noise number is related to the noise temperature T_{HEMT} by the Bose-Einstein distribution $N_{\text{HEMT}} \equiv 1/(e^{hf/k_B T_{\text{HEMT}}} - 1)$ where f is the frequency at which the noise power is evaluated. Including the damping before amplification, this leads to the following effective noise offset in the power spectral density [Poza93]

$$N_{\text{noise}} + 1 = \frac{1}{A} + \frac{N_{\text{HEMT}}}{A} + \dots \quad (2.29)$$

at the output of the HEMT amplifier. The additional contribution $' + 1'$ accounts for the fact that even in the ideal case where $N_{\text{HEMT}} = 0$ and $A = 1$ there are at least amplified vacuum fluctuations present in the output field of a phase-insensitive amplifier (compare Figure 2.10(c) and e.g. Ref. [Clerk10]). We will discuss this point in more detail in the context of parametric amplification. In the limit where the gain of the HEMT amplifier is much larger than the added noise photon number of the following low noise (LN) amplifier $G_{\text{HEMT}} \gg N_{\text{LN}}$ all noise contributions due to amplification and attenuation at later stages can be neglected. If this is not the case, we have to add more terms to Eq. (2.29) according to Friis formula [Poza93]. Note that all the additional amplification stages are necessary to amplify the electrical field to a value to which the ADC is sensitive enough. Due to the finite resolution of the ADC (14 bit in our setup), it is important to properly adjust the total amount of gain to optimally use the range of the ADC without clipping the sampled signal. A typical voltage range of the ADCs used in our setups is ± 1 V.

The first two amplification stages at room temperature are followed by an analog down-conversion. During this process the signal is multiplied at an IQ -mixer with the coherent field of a local oscillator (LO). The frequency of the LO field is offset by an IF frequency of 25 MHz from the center frequency of the detected band. Due to this multiplication of frequency components, the frequency component which was before at f_{RF} is shifted down to 25 MHz [Poza93], see Figure 2.10(d). Since we do not detect the radiation at the second output port of the mixer the noise level is effectively increased by a factor of two [Lang09]. This is due to the backfolding of noise at frequencies which had a positive detuning from the local oscillator. Despite the increase in noise, the advantage of this heterodyne detection scheme is that no calibration of relative phases and amplitudes of the mixer outputs is required. Furthermore, the backfolding effect is drastically reduced in the case where the most significant noise contribution originates from a narrow-band amplifier which has small gain at the backfolded frequency components. This is for example the case for the parametric amplifiers discussed in Chapter 4. For typical values of loss $A = 3\text{dB} \approx 0.5$

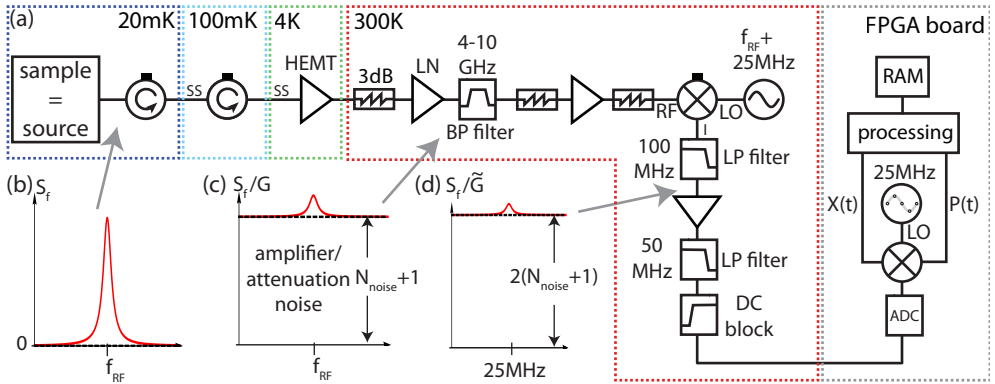


Figure 2.10: (a) Linear detection chain for measuring field quadratures X and P . (b)-(d) Power spectral densities in units of *photons per Hz per second* at different points in the detection chain rescaled by the total gain (including attenuation) at the respective stage. See main text for details.

and amplifier noise $N_{\text{HEMT}} = 10$ the total noise offset becomes ~ 45 . This value can either be reduced by improving the first amplification stage (Chapter 4) or by minimizing cable losses between sample and HEMT amplifier using superconducting semirigid cables. They provide reduced radiation loss while being thermally isolating.

Before sampling the signal with a 100 MHz ADC (i.e. 10 ns sampling time) the frequency components above 50 MHz and below a few kHz are filtered out using a low pass filter and a DC block. This is necessary to avoid backfolding of frequency components above 50 MHz during the second digital down-conversion step realized with field programmable gate array (FPGA) electronics¹⁶. The digital down-conversion returns two quadrature components $X(t)$ and $P(t)$, which are related to the amplitude A and phase ϕ of the detected field by $X + iP = Ae^{i\phi}$. They can be further processed on the FPGA by performing operations such as filtering, averaging, Fourier transformation or histogramming [Lang09, Bozyigit10]. The result after these operations is stored in a RAM on the FPGA board and finally transferred to the host computer via PCI. All instruments which are used for generation and detection of microwave fields are phase-locked to each other by a Rubidium based 10 MHz reference clock¹⁷.

¹⁶Xilinx Virtex 4

¹⁷Stanford Research FS725

Characterizing quantum microwave radiation with linear detectors

Microwave frequency quantum fields confined in cavities have been generated and characterized with remarkable control using Rydberg atoms and superconducting qubits for state preparation and readout. These experiments have illuminated fundamental principles of quantum physics, e.g. by exploring the coherent superposition of quantum states [Deleglise08, Hofheinz09] and their decoherence [Brune96, Deleglise08, Wang09], the entanglement between multiple modes [Wang11] and the stabilization of Fock states using quantum feedback [Sayrin11]. More recently, progress has also been made in the characterization of propagating quantized microwave fields. They have so far been prepared in squeezed [Castellanos-Beltran08] and single photon states [Houck07, Astafiev10] and fully characterized using time-correlation measurements [Bozyigit11, Lang11] and quantum state tomography methods [Mallet11, Eichler11b, Menzel10, Eichler11a, Flurin12]. These developments have also benefited from advances in the efficient detection of microwave fields. Both quantum limited linear amplifiers [Yurke06, Yurke87, Castellanos-Beltran08, Bergeal10a, Kinion08, Hatridge11] and photon counters [Chen11, Romero09] significantly extend the range of potential quantum optics experiments using microwave photons interacting with superconducting qubits, nanomechanical resonators, quantum dots [Frey12, Delbecq11], spin ensembles [Schuster10, Kubo10] and Rydberg atoms [Hogan12].

The use of itinerant microwave photons in quantum optics experiments requires efficient field characterization methods. A detailed understanding of microwave and optical field detection schemes allows for adapting existing quantum optics concepts to the special requirements of microwave fields. I therefore discuss field quadrature

detection schemes at microwave frequencies, their optical analogue and their use for determining the quantum state of a single mode of a radiation field. In general, the quantum state of any field mode a is characterized by its density matrix ρ_a or an equivalent quasi-probability distribution such as the Wigner, the Husimi Q or the Glauber-Sudarshan P function [Gerry05, Carmichael99]. Less widely appreciated, the mode a is also equivalently specified by the infinite set of its moments $\langle (a^\dagger)^n a^m \rangle$ [Bužek96].

In this chapter, I present experiments in which we measure such field moments to characterize single photon states and their superposition with the vacuum. I discuss the relation between measurement results of single-channel detection schemes and quasiprobability distributions. New insight into microwave state tomography is given by developing a method to reconstruct the maximally likely Fock-space density matrix directly from the measured quadrature histograms. Furthermore, I present state tomography experiments in which quantum states beyond the single-photon level have been prepared and reconstructed. I also show that two-channel microwave detection can be interpreted as a positive P function measurement [Agarwal94] even in the presence of added classical detection noise. Finally, I demonstrate full two-mode tomography for a Hong-Ou-Mandel type experiment using similar ideas¹.

3.1 Generating single microwave photons

Sources which emit exactly one photon at a time are essential components for the implementation of linear optics quantum computation schemes [Knill01, O’Brien09] and have a wide range of applications in quantum communication. Although such radiation sources exist for a long time at optical frequencies [Diedrich87, Lounis05] they have only recently been realized in the microwave frequency range [Houck08, Bozyigit11]. Here, I discuss the implementation of such an on-demand single photon source using a superconducting quantum circuit.

3.1.1 Sample characterization

For the preparation of single photons, we use a device which consists of a single transmission line resonator and a strongly coupled transmon qubit, see Figure 2.5(a). The transmission line resonator has one weakly coupled input port used for coherent driving and one strongly coupled output port into which the largest part of the stored radiation is emitted. The transmon qubit is equipped with two individual control lines: One microwave line for driving transitions between individual energy levels and one flux line for tuning the qubit transition frequency on nanosecond timescales.

¹The Hong-Ou-Mandel experiment has been realized in collaboration with C. Lang.

We characterize the device properties by first probing the vacuum Rabi mode splitting as discussed in Section 2.3. While tuning the qubit frequency with a time-varying magnetic flux, we measure the resonator transmission of a coherent drive field applied at frequency $\omega/2\pi$ (Figure 3.1(a)). The resulting resonance peaks are fitted to the model in Eq. (2.27) to extract the coupling constant $g/2\pi \approx 65$ MHz and the resonator frequency $\omega_{\text{res}}/2\pi \approx 7.135$ GHz. In a second experiment we perform qubit spectroscopy to find the qubit transition frequency $\omega_{ge}/2\pi$ chosen far away from the resonator. While probing the resonator transmission at a fixed frequency we apply an additional drive tone to the qubit of which we vary the frequency Figure 3.1(b). Due to the dispersive shift discussed in Section 2.3.1 the transmission through the resonator changes when the drive tone is resonant with the qubit transition. For low drive powers we observe one resonance peak, which corresponds to the transition from the ground to the first excited state ω_{ge} . When increasing the drive power, a second peak shows up which corresponds to a two-photon transition from the ground state into the f -level of the transmon. From the center frequencies of the two spectroscopy peaks, we extract $\omega_{ge}/2\pi \approx 6.44$ GHz and the anharmonicity $\alpha = (\omega_{ge} - \omega_{ef})/2\pi \approx -405$ MHz. Based on the theoretical transmon model [Koch07] we find the charging energy $E_C/h = 350$ MHz.

From the determined values of g, ω_{ge} and E_C we calculate the dispersive shift $\chi/2\pi \approx -2.05$ MHz at the chosen qubit frequency using Eq. (2.26). In order to confirm this value experimentally, we measure the resonator frequency shift due to the dispersive interaction with the qubit, see Figure 3.1(c). During one measurement we leave the qubit in the ground state and during a second one we saturate the qubit transition such that it is in the ground or excited state with equal probability. While in the first case the resonator is shifted by $-\chi/2\pi$, in the second measurement the shift is zero [Wallraff05, Bianchetti10a]. By fitting the measured transmission spectra to Lorentzian lines we find agreement with the calculated dispersive shift. From the same fit we extract a resonator decay rate of $\kappa/2\pi \approx 6.35$ MHz.

We then employ time-resolved measurements to determine the qubit decay and dephasing times (T_1, T_2^*). In a Rabi type experiment we apply a 10 ns long coherent pulse resonant with the qubit transition frequency $\omega_{ge}/2\pi$ via the qubit charge line. Further excitations into higher transmon levels are avoided by using a calibrated DRAG pulse shape [Motzoi09, Gambetta11], which is designed exactly for this purpose. A detailed discussion of DRAG pulse calibration can be found in [Baur12].

By varying the amplitude of the pulse we drive Rabi oscillations between ground and excited state. The state evolution of an initial ground state is $|g\rangle \rightarrow \cos\theta|g\rangle + e^{i\phi}\sin\theta|e\rangle$. The effective Rabi angle θ is proportional to the drive amplitude, the pulse length and the coupling capacitance between qubit and gate line. The phase ϕ is controlled by the phase of the drive field. For $\theta = \pi/2$ the qubit state is brought into the

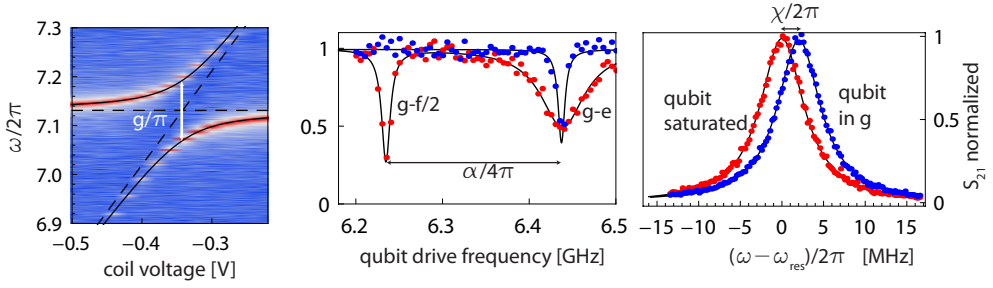


Figure 3.1: Spectroscopic sample characterization. (a) Measurement and fit of the vacuum Rabi mode splitting. (b) Transmon spectroscopy for two different drive powers. For weak drive (blue) only the ω_{ge} transition (g-e) is visible, while for larger drive powers (red) a two-photon transition into the f -level is also possible (g-f/2). Solid lines are fits to Lorentzian functions. (c) Measured transmission S_{21} through the resonator for varying probe frequency when the qubit is in the ground state (blue) and when it is driven into saturation (red). The two curves are separated by the dispersive shift $\chi/2\pi$ and fitted by Lorentzian lines (solid lines).

equal superposition state $(|g\rangle + e^{i\phi}|e\rangle)/\sqrt{2}$ while for $\theta = \pi$ the qubit is prepared in the excited state. Further increase of the pulse amplitude drives the system back into the ground state, as can be seen from the measurement data shown in Figure 3.2(a). During this experiment the qubit population is measured using a pulsed dispersive readout [Wallraff05]. After completing the qubit operation, we apply a coherent readout field to the dispersively coupled resonator, see insets of Figure 3.2, which changes its response depending on the qubit state. The average output field is described by so-called cavity Bloch equations and is used to determine the average qubit population [Bianchetti09].

Using the pulse amplitudes for π and $\pi/2$ rotations extracted from the Rabi experiment, we measure the qubit relaxation time T_1 . We bring the qubit from the ground into the excited state and vary the delay time τ between preparation and readout. For increasing τ the qubit is more likely to be found in the ground state, see Figure 3.2(b). By fitting the experimental data to an exponentially decaying function we extract the qubit relaxation time $T_1 = 1.1 \mu\text{s}$. The dephasing time of the qubit T_2^* is measured in a Ramsey type experiment. By applying a $\pi/2$ pulse, the qubit is first prepared in an equal superposition state and then left under free evolution for variable time τ . In a frame rotating with the drive frequency $\omega_d/2\pi$, the superposition state acquires a dynamical phase $(\omega_{ge} - \omega_d)\tau$ during this evolution, which is measured by applying a second $\pi/2$ pulse and reading out the excited state population. In the ideal case, in which the transition frequency ω_{ge} is perfectly stable over time the decay time of the observed fringes (compare Figure 3.2(c)) is given by the relaxation time $T_2^* = 2T_1$. In contrast, if the transition frequency $\omega_{ge}/2\pi$ is subject to fluctuations,

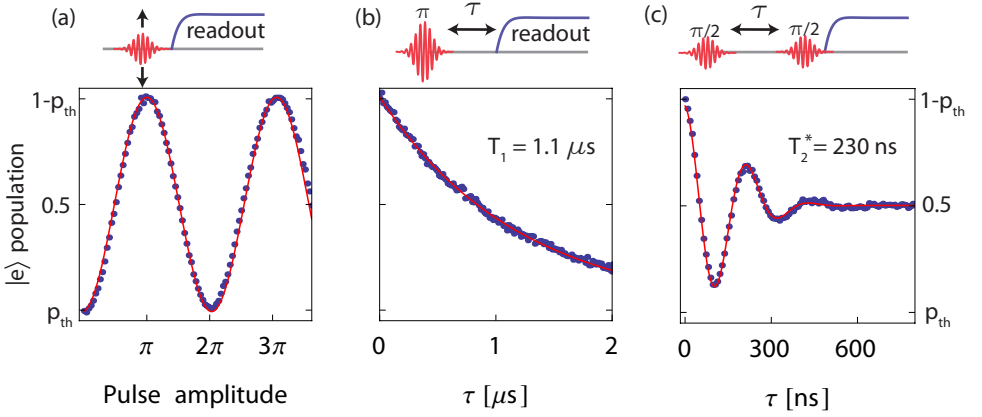


Figure 3.2: (a) Measurement and fit of Rabi oscillations. p_{th} indicates the small residual excited state occupation in the steady state, compare Section 5.1.5. The amplitude of the pulse is varied for fixed pulse length. (b) The qubit relaxation time T_1 is measured by varying the delay between preparation and readout pulse. (c) Result of a Ramsey experiment from which the dephasing time T_2^* is determined. The data is fitted to a Gaussian envelop function.

the acquired phase is different in each experimental run and the fringes are washed out on average. The decay of the fringes in a Ramsey experiment is not necessarily exponential but depends on the spectral density of the noise. If the dominating contribution is from $1/f$ noise [Koch07], the Ramsey fringes decay with a Gaussian function $\propto e^{-(\tau/T_2^*)^2}$ [Ithier05, Bylander11]. For the described experiments, the qubit was biased far away from the sweet spot, where it is expected to be very sensitive to flux noise through the SQUID loop. When fitting the Gaussian model to the measured fringes we find a dephasing time of $T_2^* \approx 230$ ns.

3.1.2 Vacuum Rabi oscillations

The tunability of qubit transition frequencies on nanosecond timescales with magnetic flux pulses can be used to let the qubit interact resonantly with the resonator for a controllable amount of time. This allows us to map a qubit excitation coherently into the resonator. We consider the situation where the qubit is initially far detuned from the resonator. After preparing the qubit in the excited state $|e\rangle$, we apply a flux pulse which tunes the qubit transition frequency into resonance with the resonator. The flux pulse has a rise time shorter than the vacuum Rabi period π/g such that we can assume that the change in qubit frequency is quasi-instantaneous compared to the timescale of interaction. The system therefore stays in its initial state $|e0\rangle$ before it starts to resonantly interact with the cavity. According to the interaction $H_{int}/\hbar = -ig(a\sigma^+ - h.c.)$ the initial state evolves as $\cos(gt)|e0\rangle + \sin(gt)|g1\rangle$ such that

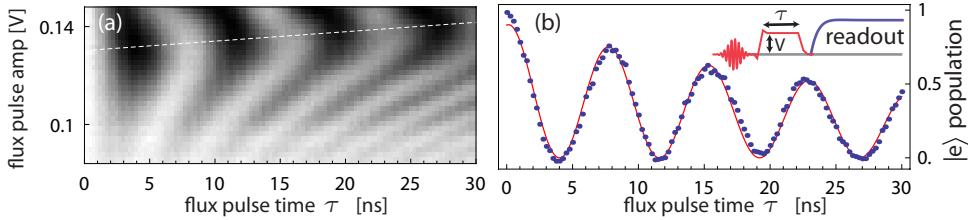


Figure 3.3: Time-resolved vacuum Rabi oscillations. The slight tilt is due to imperfect calibration of the flux pulse. (a) Final excited state population of a qubit initially in state $|e\rangle$ after applying a flux pulse of varying amplitude and length. (b) Cut through the data shown in (a) along the dashed white line and fit to an exponentially decaying sinusoidal oscillation.

the single initial excitation will sinusoidally oscillate between qubit and resonator. When the qubit is tuned back to its initial frequency after time τ , the final qubit excitation is $p_e = \langle |e\rangle \langle e| \rangle = (1 + \cos(g\tau)) / 2$ while the remaining excitation is left in the resonator as a photon.

In Figure 3.3(a) we show the results of an experiment in which the final qubit excitation has been probed after applying a flux pulse with variable voltage for time τ . The qubit detuning Δ from the resonator, which is approximately proportional to the voltage of the flux pulse, reaches zero at $\sim 0.135\text{V}$. For this amplitude the qubit excitation can be fully transferred into the resonator. At finite detuning the oscillation frequency becomes faster due to the larger energy separation between the two relevant eigenstates (compare Eq. (2.27)), while the contrast of the oscillations decreases. The qubit excitation is only fully swapped into the resonator when tuned into resonance. A cut through the data along the dashed white line is shown in Figure 3.3(b) and corresponds to the dynamics of the qubit population at resonance. The oscillations have a periodicity of 7.6 ns which is close to the expected value $\pi/g \approx 7.7$ ns, where $g/2\pi \approx 65$ MHz is known from the spectroscopic measurement of the vacuum Rabi mode splitting. The sinusoidal oscillations decay exponentially, mostly due to the decay of the resonator field into the transmission line and partially due to the intrinsic qubit decay. The decay time extracted from the fit to the data is 42 ns $\approx (T_1 + 1/\kappa)/2$, which is consistent with the spectroscopic measurement of κ and the individually measured T_1 time.

3.1.3 Mapping an arbitrary qubit state onto a single photon state

From the measured vacuum Rabi oscillations we determine the flux pulse parameters for which the qubit excitation is fully transferred into the resonator. According to the Jaynes-Cummings dynamics we expect that for this specific interaction time any initial qubit state $c_0 |g\rangle + c_1 |e\rangle$ is mapped onto the equivalent resonator state $c_0 |0\rangle + c_1 |1\rangle$.

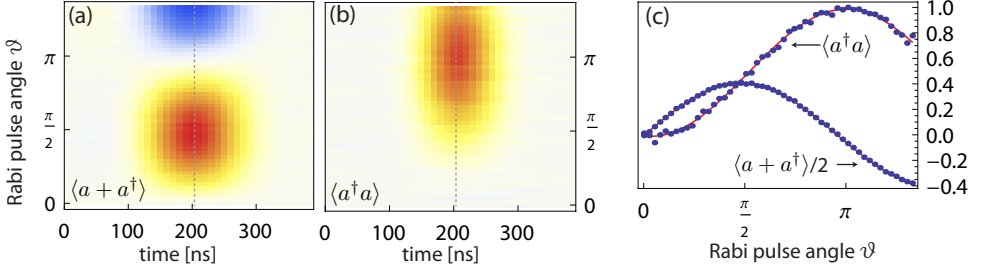


Figure 3.4: Mapping an arbitrary qubit state onto a propagating photon. (a) Average of the filtered resonator output field for varying initial qubit pulses after a swap with the resonator. (b) Same as in (a) but averaging the photon number instead of the field amplitude. (c) Vertical cuts through the data in (a) and (b) along the indicated lines and sinusoidal fits.

Not only the qubit population is thus mapped onto the mean number of photons in the resonator $|e\rangle\langle e| \rightarrow \langle a^\dagger a \rangle$, but moreover any initial qubit coherence translates into a coherence of the final photon state $\langle \sigma^- \rangle \rightarrow \langle a \rangle$. These photon states then decay exponentially into a propagating transmission line mode, where we detect them using the linear detection chain described in Section 2.4.3 [Houck08, Bozyigit11, Eichler11b].

After applying a Rabi pulse with amplitude θ to the qubit and after mapping the qubit state onto the resonator, we record filtered time-traces of the resonator output field similarly as in Ref. [Bozyigit11]. The average over 5000 repetitions of such measurements are shown in Figure 3.4(a). If the output field was detected with a bandwidth much larger than the decay rate κ , the averaged time-traces would resemble the temporal envelope of the photon field. This has a fast rise time on the order of π/g and then decays exponentially with decay time $2/\kappa$ [Bozyigit11]. For the measurements in Figure 3.4, however, we have chosen a filter function which is matched to the temporal profile of the photon pulse. Such a filter broadens the fast rise-time but makes the photon detection more efficient. This relation between the chosen filter function and detection efficiency is discussed in Section 3.2.2 in more detail.

In addition to the mean amplitude $\langle a \rangle$ of the field, we also measure the average emitted photon number $\langle a^\dagger a \rangle$. This is done in real-time on the FPGA by squaring individual time-traces before averaging them [Bozyigit10]. The result of this measurement is shown in Figure 3.4(b), where the constant noise offset originating from added amplifier noise is subtracted from the data. While for a classical coherent state we would expect the average photon number to be the square of the mean amplitude, the two quantities behave differently for the generated single photon states. In Figure 3.4(c) we compare the measured mean amplitude with the mean photon number for

different Rabi angles θ . The mean amplitude $|\langle a \rangle|$ reaches its maximum for an applied $\pi/2$ pulse, while the mean photon number $\langle a^\dagger a \rangle$ is maximal for $\theta = \pi$. As expected, the mean photon number is equal to the initial excited state population $\langle |e\rangle \langle e| \rangle$ and the mean amplitude is proportional to the qubit coherence $\langle \sigma^- \rangle$. This set of measurements thus indicates that the state of the transmon qubit can be efficiently mapped onto a flying photonic qubit [Houck08, Bozyigit11].

3.2 Experimental photon state tomography for single microwave photons

In order to ultimately verify that the emitted radiation has single photon character one has to show that the expectation value $\langle (a^\dagger)^2 a^2 \rangle$ vanishes. For the presented on-demand microwave single photon source this has been first realized in our lab by measuring time-correlation functions [Bozyigit11] and quadrature histograms [Eichler11b]. In the following, I describe the latter approach, which allows us to access all higher order field-correlations of type $\langle (a^\dagger)^n a^m \rangle$ systematically. This turns out very useful in the context of quantum state tomography beyond the single channel and single photon level. For the detection of the single microwave photons we use a state-of-the-art linear detection chain, see Figure 2.10. A major challenge was to develop appropriate state reconstruction methods, which allow for the measurement and interpretation of the relevant quantum correlations in the presence of significant added classical noise.

3.2.1 Quadrature detection and its optical analog

We first derive a formal relation between the output field of the photon source (i.e. transmission line resonator) and the measured quadratures X and P . Analogies between the microwave case and equivalent optical detection schemes enable us to adapt existing concepts from quantum optics for our purposes. We consider both the measurement of a single field quadrature and the simultaneous detection of two canonically conjugate quadratures. The radiation field of interest is described as a single bosonic mode a reaching the detector within a specific window in time. The single mode a can be isolated from the continuum of modes by performing temporal mode matching, i.e. integrating the continuous signal over the temporal profile of the photon pulse which is to be characterized [Carmichael08, Eichler11b]. We discuss ideal temporal mode matching for an exponentially decaying cavity field in the next Section 3.2.2.

For a full reconstruction of the quantum state of the field, both the photon number statistics and all coherences between the different contributing Fock states have to be experimentally determined. This can be achieved by measuring generalized field quadrature components $\hat{X}_\phi \equiv \frac{1}{2}(ae^{-i\phi} + a^\dagger e^{i\phi})$, which naturally allows for the

exploration of the full phase space, i.e. the off-diagonal elements of the density matrix in the number state basis [Lvovsky09]. In optical systems, where photon number statistics are naturally obtained using photon counters, such a field quadrature measurement can be realized using homodyne detection schemes [Scully97]. In this approach, the field of interest is combined on a beam splitter with a strong coherent field of a local oscillator, such that the difference of the photocurrents at the two beam splitter outputs is proportional to a specific field quadrature \hat{X}_ϕ of the input field (Figure 3.5(a)). The quadrature phase ϕ can be tuned by changing the local oscillator phase. Instead, microwave field quadratures are usually measured by down-converting the field with a local oscillator tone using a microwave frequency mixer and sampling the electrical field directly using analog to digital converters (ADC). However, these ADCs are only sensitive enough to detect large amplitude fields which contain a macroscopic number of photons per sampling time ($\sim 10^{10}$), such that a linear amplification stage is required in the process of detection, as shown in Figure 3.5(c). The noise added during this amplification process is typically the main limitation for the detection efficiency of microwave fields as discussed below.

Instead of measuring a single field quadrature for different phases ϕ , two conjugate field quadratures can be simultaneously measured to get all the information required for a complete quantum state reconstruction [Arthurs65, Braunstein91, Caves94, Welsch99, Yuen80]. One possible realization of such a measurement uses a beam splitter and two quadrature detectors at each output [Noh91] (Figure 3.5(b)). The beam splitter necessarily introduces an additional mode h through its open port. This mode adds [at least] the vacuum noise to the signal with which the simultaneous detection of conjugate variables preserves Heisenberg's uncertainty principle. Taking the beam splitter transformations $a \rightarrow (a + h)/\sqrt{2}$ and $h \rightarrow (a - h)/\sqrt{2}$ into account², the two detected field quadratures at the beam splitter outputs correspond to real \hat{X} and imaginary \hat{P} part of the complex amplitude $a + h^\dagger$. This holds for both the optical and the microwave case. However, for microwaves we still have to consider the transformation of the signal mode due to the linear amplification stage. A generic phase-insensitive linear amplifier transformation can be modeled as [Haus62, Caves82, Clerk10]

$$a \rightarrow \sqrt{G}a + \sqrt{G-1}h_{\text{amp}}^\dagger \quad (3.1)$$

where h_{amp} is an additional bosonic mode accounting for the noise added by the amplifier. Again, in the ideal (i.e. quantum limited) case h_{amp} is in the vacuum state, and for a more realistic scenario in a thermal state. Combining the amplification transformation with the beamsplitting at the mixing stage (compare Figure 3.5(c)) and

²Depending on the specific realization of the beam splitter, additional relative phase factors appear in the beamsplitting transformation, see for example Section 3.6. This is, however, not relevant for the following general discussion and we have chosen this specific beam splitter transformation.

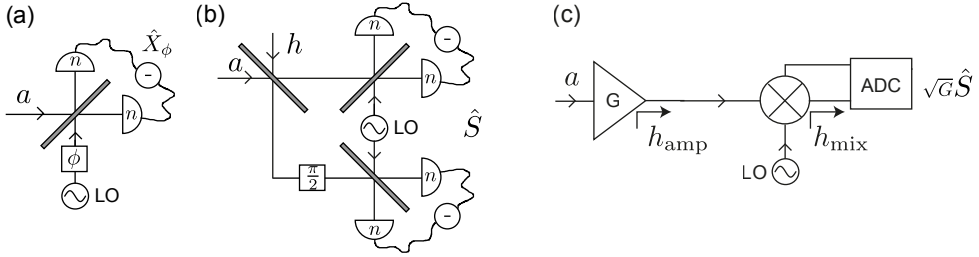


Figure 3.5: Field quadrature detection schemes for optical and microwave fields. (a) Schematic of balanced optical homodyne detection. The signal field a is combined with a coherent local oscillator (LO) field with controlled phase ϕ at a beam splitter and the quadrature amplitude \hat{X}_ϕ is detected with photon counters (n) in the two output arms. (b) Double homodyne detection scheme. The signal field a is split into two parts at a beam splitter while introducing an additional vacuum mode h . Placing a homodyne detector as described in (a) at each of the two beam splitter outputs allows for measuring two conjugate quadratures (i.e. the complex amplitude \hat{S}). (c) Measurement of the complex amplitude at microwave frequencies. The signal mode is amplified with a phase-insensitive linear amplifier introducing an additional noise mode h_{amp} . The amplified output is split into two parts at a microwave frequency mixer, while adding the mode h_{mix} , and multiplied with a coherent local oscillator field. The down-converted electrical field is sampled with analog to digital converters (ADC).

dividing by $\sqrt{G/2}$ we find the relation [daSilva10]

$$\hat{S} \equiv a + h^\dagger = \hat{X} + i\hat{P}. \quad (3.2)$$

with the total noise mode $h = \sqrt{\frac{G-1}{G}}h_{\text{amp}} + \sqrt{\frac{1}{G}}h_{\text{mix}}$. Here, we have defined the complex amplitude operator \hat{S} representing the two conjugate quadratures as a single complex number. In the limit of large gain $G \gg 1$ the total noise is dominated by the amplifier noise $h \approx h_{\text{amp}}$ and the following noise contributions can be neglected [Leonhardt94]. Furthermore, we notice that once we amplify the field phase-insensitively at least the vacuum noise is added independently of whether we detect only one quadrature or two conjugate quadrature components. Once the signal is amplified it is thus natural to detect 2 conjugate quadratures since the signal-to-noise ratio is unaffected by the necessary splitting of the signal.

It is important to mention that there is a detection scheme using linear amplifiers, which is ideally noiseless for one quadrature component. This is achieved by using a phase-sensitive amplifier instead of a phase-insensitive one which can – in the quantum limit – be modeled by the squeezing transformation [Caves82, Loudon00, Yurke06]

$$a \rightarrow \sqrt{G}e^{-i\phi}a + \sqrt{G-1}e^{i\phi}a^\dagger \quad (3.3)$$

with the tunable phase ϕ . Amplifiers described by this transformation have recently been built and are working close to the quantum limit [Yurke87, Castellanos-Beltran08, Eichler11a, Hatridge11]. The quadrature \hat{X}_ϕ is noiselessly amplified while its conjugate quadrature is deamplified. The detection scheme is thus equivalent to an optical homodyne detection [Caves94, Lvovsky09, Mallet11, Filippov11]. In Section 4.4.3 we show how to operate a degenerate parametric amplifier in either a phase-sensitive or a phase-insensitive mode.

We note that while for optical fields the simultaneous detection of two conjugate quadratures requires a more complicated setup than for photon number detection it is the natural measurement observable for microwave fields. In the following, we will therefore focus on this type of measurement in the context of quantum state reconstruction.

3.2.2 Temporal mode matching

Throughout the previous section we have described the photon field, which is to be characterized, by a single *time-independent* mode a . Here, we discuss the relation between this single mode a and the *time-dependent* field $a_{\text{out}}(t)$ which is continuously sampled in an experiment. The link between the two is given by a mode-matching relation

$$a = \int dt f(t) a_{\text{out}}(t) \quad (3.4)$$

where the normalization condition $\int dt |f(t)|^2 = 1$ of the temporal profile function $f(t)$ guarantees that $[a, a^\dagger] = 1$ is satisfied. Experimentally, the function $f(t)$ is realized as an appropriate digital filter, as discussed in more detail below. The best choice of $f(t)$ depends on the temporal shape of the field, i.e. the properties of the coupling between radiation source and the transmission line under observation. In the following we discuss optimal temporal mode matching for a single-sided cavity acting as the radiation source (Figure 3.6).

We represent the cavity mode for the following calculation by the annihilation operator $A(t)$ to distinguish it from the detected output mode a . Note, that we work in a Heisenberg picture, where the operator $A(t)$ is time-dependent. We assume that at time $t = 0$ the cavity is prepared in a specific state described by the statistics of $A(0)$ and then left under free evolution [Walls94]

$$A(t) = e^{-\frac{\kappa t}{2}} A(0) + \sqrt{\kappa} e^{-\frac{\kappa t}{2}} \int_0^t d\tau e^{\frac{\kappa \tau}{2}} a_{\text{in}}(\tau). \quad (3.5)$$

From input-output theory [Gardiner85], we know that the cavity field decays with rate

κ into the output modes according to

$$a_{\text{out}}(t) = \sqrt{\kappa}A(t) - a_{\text{in}}(t). \quad (3.6)$$

The input modes $a_{\text{in}}(t)$ can be understood as a continuous stream of independent modes each reaching the resonator at time t and ideally carrying only the vacuum noise.

By inserting the above expressions into the definition of a we obtain only one term

$$A(0) \sqrt{\kappa} \int_0^\infty dt e^{-\frac{\kappa}{2}t} f(t)$$

depending on the cavity field. In order to maximize the efficiency in detecting the state prepared at time $t = 0$ we have to find $f(t)$ which maximizes this term. The choice $f(t) = \sqrt{\kappa}e^{-\frac{\kappa t}{2}}\Theta(t)$ does so, where $\Theta(t)$ is the Heaviside step function. The total expression for Eq. (3.4) then reduces to

$$a = A(0)\kappa \int_0^\infty dt e^{-\kappa t} - \kappa^{1/2} \int_0^\infty e^{-\frac{\kappa t}{2}} a_{\text{in}}(t) dt + \kappa^{3/2} \int_0^\infty e^{-\kappa t} \int_0^t e^{\frac{\kappa \tau}{2}} a_{\text{in}}(\tau) d\tau dt, \quad (3.7)$$

which due to the identity

$$\begin{aligned} \kappa^{3/2} \int_0^\infty e^{-\kappa t} \int_0^t e^{\frac{\kappa \tau}{2}} a_{\text{in}}(\tau) d\tau dt &= \kappa^{3/2} \int_0^\infty \left(\int_0^\infty \Theta(t - \tau) e^{-\kappa t} dt \right) e^{\frac{\kappa \tau}{2}} a_{\text{in}}(\tau) d\tau \\ &= \kappa^{1/2} \int_0^\infty e^{-\frac{\kappa \tau}{2}} a_{\text{in}}(\tau) d\tau \end{aligned} \quad (3.8)$$

simplifies to

$$a = A(0). \quad (3.9)$$

By proper choice of $f(t)$ we can thus recover the state of the source field $A(0)$ with unit efficiency in the transmission line. Note that a finite mode matching efficiency only reduces the total detection efficiency but does not affect the statistical properties of a . This is due to the identity

$$\langle (a^\dagger)^n a^m \rangle = \eta_F^{(n+m)/2} \langle (A(0)^\dagger)^n A(0)^m \rangle,$$

where $\sqrt{\eta_F} \equiv \sqrt{\kappa} \int_0^\infty dt e^{-\frac{\kappa}{2}t} f(t)$. For perfect mode matching $\eta_F = 1$, while for imperfect filtering $\eta_F < 1$. In the latter case, η_F can be interpreted as an attenuation constant equivalent to a loss in detection efficiency.

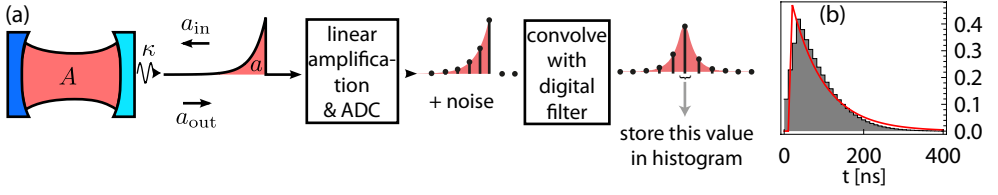


Figure 3.6: (a) An optical analog of the photon source realized in our experiments is shown as a single sided cavity with one highly reflective and one partially transmitting mirror. A single photon is generated in the cavity and then emitted at a rate κ into output modes $a_{\text{out}}(t)$ resulting in an exponentially decaying envelope of the single photon pulse while the modes $a_{\text{in}}(t)$ remain in the vacuum state. The signal is amplified, down-converted, and digitized with an analog-to-digital converter. The digitized signal is then convolved with mode matching filter coefficients and the resulting quadrature pair $\{X, P\}$ is stored in a 2D histogram. (b) Comparison between the filter coefficients (gray bars) and the exponential decay of the cavity (red solid line) used in the experiments for Ref. [Eichler11b].

We experimentally realize mode matching by implementing an appropriate digital filter function in the FPGA. The goal of this mode matching procedure is to extract a single value S from the continuous stream of sampled quadratures, which corresponds to the measurement result of the complex amplitude operator $\hat{S} = a + h^\dagger$. All detection inefficiencies due to cable losses, added amplifier noise and mode matching inefficiency are lumped into the state of the single effective noise mode h .

The digital down-conversion (DDC) outputs a continuous stream of quadrature pairs $\{X_t, P_t\}$, which we write for convenience as the single complex envelope $S_t = X_t + iP_t$. The index t labels the discrete time-steps in units of the sampling time 10 ns. As long as the effective detection bandwidth $B = 50$ MHz is large compared to $\kappa/2\pi$, we can interpret S_t as a discretized version of the unfiltered time-resolved signal $a_{\text{out}}(t) + h_{\text{out}}^\dagger(t)$. The measurement record S_t is further processed by convolving it with filter coefficients f_t

$$S_t \rightarrow \sum_{\tau}^{N_{\text{coeff}}} S_{t+\tau} f_{\tau}, \quad (3.10)$$

where $N_{\text{coeff}} = 40$ is the number of filter coefficients. The number of available filter coefficients depends on the specific FPGA application and is limited due to the finite number of multiplications, which can be performed on the FPGA board in realtime. To achieve temporal mode matching we chose filter coefficients f_t , which resemble the exponential decay of the resonator output field. In practice, the implemented filter coefficients are slightly different from the ideal ones, since the filter is also designed to eliminate other frequency components, originating e.g. from finite DC offsets at the ADC or from coherent pump fields present when operating a parametric amplifier.

The filter coefficients used in the experiments for Ref. [Eichler11b] are shown in Figure 3.6(b) in comparison with the resonator exponential decay. The integrated overlap between the two is $\eta_F = 90\%$.

3.2.3 Data acquisition: Generating quadrature histograms

From the filtered measurement record we determine a single value $S = X + iP$ (Figure 3.6), which corresponds to a measurement result of \hat{S} and is finally stored in a histogram. In order to find the optimal sample point, for which the filter function and photon pulse have maximal overlap, we first record a time-trace of the average filtered photon number (Figure 3.4(b)) and identify the time at which it becomes maximal. By adjusting an appropriate trigger delay, we can specify this optimal sample point after analyzing the full time-resolved measurement data³. From the selected quadrature pair $\{X, P\}$ and an additional bit which specifies whether the source had been turned *ON* or *OFF*, we construct a 21-bit address. In each trial of an experimental run the measurement result is used to increment the memory value, to which this address points. In this way we accumulate 2D histograms of measured $\{X, P\}$ pairs for the two cases in which the source is turned *ON* and *OFF*, respectively. Given the 10-bit discretization of the X and P values, the memory capacity on the FPGA board used in these experiments limits the maximal number of counts per histogram bin to $2^{16} = 65536$.

We can also construct the addresses, which specify the different histogram bins, from more than two independent quadrature values. This enables us to record multi-dimensional histograms in a similar fashion. We use such 3D and 4D histograms to measure qubit-photon entanglement or correlations between two different field modes as discussed in Section 5.1 and Section 3.6, respectively.

After this general discussion about the data acquisition we turn to a specific experiment. For a pulsed single photon source similar to the one described in Section 3.1, we have measured such 2D histograms of quadrature pairs X, P . To extract the properties of mode a alone we perform two measurements. One in which the signal mode a is left in the vacuum (*OFF*), serving as a reference measurement for the noise, and a second one, in which the state of interest $|\psi\rangle$, such as a Fock state $|1\rangle$, is prepared (*ON*). In practice both histograms are accumulated in an interleaved fashion, changing between the two cases every $25 \mu\text{s}$ to avoid systematic errors due to drifts. Since the number of effectively added noise photons turns out to be $N_0 \approx 64$ in the experiments presented here, the measured histograms for both vacuum $D^{[|0\rangle\langle 0|]}$ and for a Fock state $D^{[|1\rangle\langle 1|]}$ are dominated by the noise added during detection, see Figure 3.7(a) and (b). However,

³The trigger delays in the FPGA *histogrammer* applications are aligned to those in the application which is used for recording averaged time traces, such that the first point appearing in the time trace corresponds to the value, which is written into the histogram.

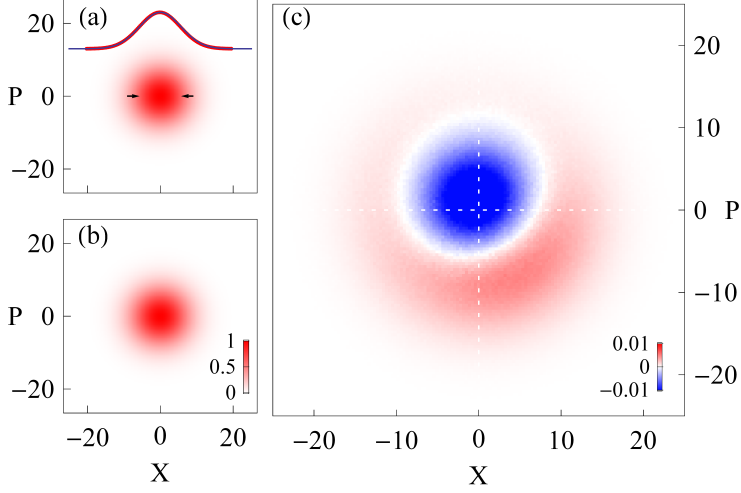


Figure 3.7: (a) Measured quadrature histogram $D^{[0]\langle 0|]}(S)$ for a in the vacuum (*OFF*) where $S = (X + iP)$. The inset shows a horizontal cut through the histogram (red). The distribution is well described by a normal distribution (blue) with width $\sigma = 5.7$ (indicated by black arrows) corresponding to a system noise number of $N_0 \approx 64$. (b) Quadrature histogram $D^{[1]\langle 1|]}(S)$ for preparation of single photon Fock states. (c) Difference of $D^{[1]\langle 1|]}(S)$ and $D^{[0]\langle 0|]}(S)$. Note the two different color scales, both given in units of $D^{[1]\langle 1|]}(0)$, indicating the small difference between the two histograms.

when calculating the numerical difference of both histograms, see Figure 3.7(c), we already clearly observe the circular symmetric character of the single photon phase space distribution. The small deviation from an ideal circular symmetry is due to a slight coherent admixture of the vacuum $|0\rangle$ to the single photon Fock state $|1\rangle$ caused by small errors in the state preparation.

3.3 Interpretation and analysis of quadrature histograms

To be able to further analyze the histogram data shown in Figure 3.7, it is useful to review the concept of phase space distributions used in quantum optics. As explained in the following, we can identify the two measured histograms as specific phase space representations of the quantum states ρ_a and ρ_h of the signal mode a and the noise mode h , respectively. Based on these relations we are able to systematically extract the single photon character of radiation in mode a , even in the presence of significant added amplifier noise.

3.3.1 Phase space distributions

Due to the non-orthogonality of coherent states $\langle\alpha|\beta\rangle = e^{-\frac{1}{2}|\alpha|^2 - \frac{1}{2}|\beta|^2} e^{\alpha^*\beta}$ an arbitrary density matrix ρ_a can be expanded as a linear combination of projectors $|\alpha\rangle\langle\alpha|$ onto coherent states

$$\rho_a = \int_{\alpha} P_a(\alpha) |\alpha\rangle\langle\alpha|. \quad (3.11)$$

Here, we have defined $\int_{\alpha} \equiv \int_{\mathbb{C}} d^2\alpha$ for integrals over the complex plane and $P_a(\alpha)$ as the Glauber-Sudarshan P function [Glauber63, Carmichael99], which uniquely represents the density matrix as a distribution in phase space. $P_a(\alpha)$ is always real-valued but can be negative and can contain singularities proportional to derivatives of the Dirac δ distribution to all orders [Carmichael99]. As can be seen from its definition in Eq. (3.11), the P function reduces to a two-dimensional Dirac distribution $P_a(\alpha) = \delta^{(2)}(\alpha - \beta)$ for coherent states $|\beta\rangle$. Coherent states thus appear as single points in phase space with no statistical spread similar to their classical counterparts. For this reason and due to its possible negative values the P function does not directly describe the statistics of measurements. However, it is very useful since its statistical moments directly correspond to the normally ordered moments

$$\langle\langle (a^\dagger)^m a^n \rangle\rangle = \int_{\alpha} (\alpha^*)^m \alpha^n P_a(\alpha) \quad (3.12)$$

of the field operator a and because of its analogy to probability distributions of classical fields.

A second distribution, which is of particular relevance for the following discussion, is the Husimi- Q function

$$Q_a(\alpha) = \frac{1}{\pi} \langle\alpha|\rho_a|\alpha\rangle, \quad (3.13)$$

since it generates the anti-normally ordered moments

$$\langle a^n (a^\dagger)^m \rangle = \int_{\alpha} (\alpha^*)^m \alpha^n Q_a(\alpha). \quad (3.14)$$

Substituting Eq. (3.11) into the definition of the Q function, we note that it is related to the P function by a Gaussian convolution. For coherent states $Q_a(\alpha)$ becomes a two-dimensional Gaussian distribution with variance 1 centered around the coherent state amplitude. Half of these fluctuations describe the intrinsic vacuum fluctuations of the quantum field, the other half describe the minimal added uncertainty when directly measuring a Q function, which requires the simultaneous detection of two conjugate field quadratures.

Both distributions are special cases of the s -parametrized quasi-probability distribu-

tion $W_a(\alpha, s)$

$$Q_a(\alpha) = W_a(\alpha, -1) \quad (3.15)$$

$$P_a(\alpha) = W_a(\alpha, 1). \quad (3.16)$$

which has been introduced by Cahill and Glauber [Cahill69a] as a generalized phase space representation of the density matrix where the parameter $s \in (-\infty, +1]$. For different values of s the quasi probability distributions are related to each other by a Gaussian convolution [Cahill69a]

$$W_a(\alpha, s) = \frac{2\pi^{-1}}{t-s} \int_{\beta} \exp\left(-\frac{2|\alpha-\beta|^2}{t-s}\right) W_a(\beta, t) \quad (3.17)$$

where $t > s$.

An intuitive interpretation of the parameter s relates to the amount of fluctuations which are contained in the distribution in units of half photons. For $s = 0$ we obtain the Wigner function $W_a(\alpha) \equiv W_a(\alpha, 0)$ which include the intrinsic vacuum fluctuations but no additional noise due to measurement. In the case $s = 1$ we identify the P function where even the vacuum fluctuations are not represented. On the other hand, for $s = -1$ the quasi probability distribution corresponds to the Q function where both the vacuum fluctuations and the minimal added detection noise are embedded. As discussed below, additional classical detection noise leads to $s < -1$ when identifying measured distributions with a generalized quasi probability distribution.

3.3.2 Identifying measured histograms with phase space distributions

In order to understand the relation between generalized quasi probability distributions and the measured histograms shown in Figure 3.7, we interpret $D^{[|0\rangle\langle 0|]}$, $D^{[|1\rangle\langle 1|]}$ as estimates for the probability of measuring the observable $\hat{S} = a + h^\dagger$ with outcome S . From such measured distributions all statistical moments in \hat{S} can be numerically evaluated as

$$\langle (\hat{S}^\dagger)^n \hat{S}^m \rangle_{\rho_a} = \int_S (S^*)^n S^m D^{[\rho_a]}(S). \quad (3.18)$$

If the noise added by the detection chain is independent of the signal generated by the photon source, the signal mode a and the noise mode h are uncorrelated $\rho = \rho_a \otimes \rho_h$. Under this assumption the moments of the measured distribution can be decomposed

into products of signal and noise moments

$$\langle (\hat{S}^\dagger)^n \hat{S}^m \rangle_{\rho_a} = \sum_{i,j=0}^{m,n} \binom{n}{j} \binom{m}{i} \langle (h^\dagger)^i h^j \rangle \langle a^{m-i} (a^\dagger)^{n-j} \rangle, \quad (3.19)$$

Here, we have chosen an operator ordering where the signal moments $\langle a^m (a^\dagger)^n \rangle$ appear anti-normally ordered and the noise moments $\langle (h^\dagger)^m h^n \rangle$ normally ordered. Note that since \hat{S} is a normal operator $[\hat{S}, \hat{S}^\dagger] = 0$, one can express Eq. (3.19) also with opposite ordering, as shown in Eq. (3.23) later in the text.

The probability distribution for the sum of two independent random variables $a + h^\dagger$ is identical to the convolution of the individual distributions for a and h^\dagger . As a result, one possible representation of the probability distribution $D^{[\rho_a]}(S)$ is given by the convolution [Kim97]

$$D^{[\rho_a]}(S) = \int_{\alpha} P_h(S^* - \alpha^*) Q_a(\alpha). \quad (3.20)$$

In the following we discuss special cases of Eq. (3.20). At optical frequencies the measurement of \hat{S} can be realized using a double homodyne or heterodyne detection and the noise mode h is nearly in the vacuum state for which $P_h(\beta) = \delta^{(2)}(\beta)$ resulting in

$$D^{[\rho_a]}(S) = Q_a(S). \quad (3.21)$$

Thus, for ideal heterodyne detection the measured distribution corresponds to the Q function. In contrast, for microwave fields the noise mode h is often in a thermal state with mean photon number N_0 ranging typically from 0.5 to 10 if parametric or SQUID amplifiers are used [Mallet11, Vijay11, Kinion08] or between 30 and 200 if the first amplification is performed by a transistor based amplifier [Bozyigit11, Eichler11b, Eichler11a, Lang11]. In this case $P_h(\alpha) = e^{-|\alpha|^2/N_0}/\pi N_0$ acts as a Gaussian filter and by comparing with Eq. (3.17) we obtain the broadened quasi probability distribution

$$D^{[\rho_a]}(S) = W_a(S, -1 - 2N_0). \quad (3.22)$$

Note that finite thermal noise in h can be equivalently interpreted as optical homodyne detection with finite detection efficiency η for which the measured distribution is given by $D^{[\rho_a]}(S) = W_a(S, 1 - 2\eta^{-1})$ [Leonhardt93]. Added noise can thus be understood as a reduced detection efficiency $\eta = 1/(1 + N_0)$.

We conclude that under the experimentally verified assumption [Eichler11b, Menzel10] of h being in a thermal state not correlated with a the measured distribution of \hat{S} is a direct measurement of the generalized quasi probability distribution and

therefore contains all information required to reconstruct the density matrix ρ_a of the state of interest or to test its nonclassical properties [Vogel00, Kiesel11]. In contrast to other reconstruction schemes only a single observable \hat{S} needs to be measured.

However, in many experiments the mean photon number of the noise field is larger than the mean photon number of the signal field $N_0 > \langle a^\dagger a \rangle$ and consequently the features of measured probability distributions are on first sight dominated by the noise distribution. Therefore the goal is to systematically extract the information contained about mode a in the measured quasi probability distribution and represent it in a form, which allows for a direct estimation of the properties of the state, such as the fidelity with respect to an expected density matrix.

3.3.3 Determination of normally ordered moments

One way of quantifying the properties of a quantum state is to analyze the statistical moments $\langle (a^\dagger)^n a^m \rangle$ of the field operator [Bužek96, Menzel10], since quantities such as the mean amplitude, the mean photon number and the variance in the photon number can be extracted immediately. In this section we discuss the approach developed in Ref. [Eichler11b] to extract these moments from the measured distributions in the presence of significant amplifier noise N_0 . The basic idea is to deconvolve the quasi probability distributions for the field operators a and h order by order.

Rewriting Eq. (3.19) with a different choice of operator ordering

$$\langle (\hat{S}^\dagger)^n \hat{S}^m \rangle_{\rho_a} = \sum_{i,j=0}^{n,m} \binom{m}{j} \binom{n}{i} \langle (a^\dagger)^i a^j \rangle \langle h^{n-i} (h^\dagger)^{m-j} \rangle, \quad (3.23)$$

we find that once the anti-normally ordered moments of the noise mode $\langle h^n (h^\dagger)^m \rangle$ are known, the set of linear equations can be solved for $\langle (a^\dagger)^n a^m \rangle$. A systematic method to solve this system of equations analytically is provided in Appendix A.1. From Eq. (3.18) we note that a reference measurement $D^{|0\rangle\langle 0|}(S)$, for which a is prepared in the vacuum, gives direct access to the moments $\langle h^n (h^\dagger)^m \rangle$, since all normally ordered moments in a with $n, m \neq 0$ are then $\langle (a^\dagger)^n a^m \rangle = 0$ and Eq. (3.23) reduces to

$$\langle (\hat{S}^\dagger)^n \hat{S}^m \rangle_{|0\rangle\langle 0|} = \langle h^n (h^\dagger)^m \rangle. \quad (3.24)$$

In cryogenic setups such a reference measurement with a in the vacuum can typically be performed by cooling the source of radiation into the ground state or very close to it [Fink10b]. The identity in Eq. (3.24) can be understood as follows: The situation with a in the vacuum state corresponds to an ideal Q function measurement for the noise mode h and the moments generated by this distribution are exactly the anti-normally

ordered ones appearing in Eq. (3.24). We finally invert Eq. (3.23) to extract the desired moments $\langle (a^\dagger)^n a^m \rangle$ of the mode to be characterized.

In principle, the moments of the measured histograms can be evaluated to arbitrary order. However, there are limitations in the accuracy with which the moments $\langle (a^\dagger)^n a^m \rangle$ can be determined depending on the integration time and the detection efficiency. As investigated theoretically in Ref. [daSilva10], the statistical error of the moments increases with increasing order. The result shows that the number of measurements which are necessary to extract a moment of order M with a given precision scales with $(1 + N_0)^M$. The measurement time necessary to determine higher order moments with a fixed precision thus scales exponentially with increasing order.

The state of a single mode of the radiation field has an infinite number of degrees of freedom, i.e. an infinite dimensional Hilbert space. This makes it in principle impossible to exactly reconstruct a state, because an infinite amount of information is to be acquired. However, the measurement of a finite set of moments often allows for a controlled reduction of the relevant state space [Bužek96].

3.3.4 Special classes of states and the Fock space density matrix

One class of states which is characterized by a finite set of moments comprises coherent, thermal and squeezed (i.e. Gaussian) states, for which the statistical moments up to second order

$$\{\langle a \rangle, \langle a^\dagger a \rangle, \langle a^2 \rangle\}. \quad (3.25)$$

determine all higher order moments. In order to analyze how close the reconstructed state really is to a Gaussian, one has to measure the third order cumulants and evaluate their deviations from zero (for the relation between cumulants and moments see Appendix A.1).

A second class of states which can be reconstructed using a finite set of measured moments includes those with finite photon number contributions satisfying $\langle n | \rho_a | m \rangle = 0$ for $m, n \geq N$ in the Fock basis $\{|n\rangle\}$. For these states the normally ordered moments

$$\langle (a^\dagger)^n a^m \rangle = 0 \quad m \text{ or } n \geq N \quad (3.26)$$

vanish and the state is completely determined by the finite set of moments

$$\{\langle (a^\dagger)^n a^m \rangle\} \quad m \text{ and } n \leq N. \quad (3.27)$$

It is important to note that it necessarily follows from $\langle (a^\dagger)^N a^N \rangle = 0$ that there are no Fock states $|n\rangle$ with $n \geq N$ contributing to the density matrix. If $\langle (a^\dagger)^N a^N \rangle < \epsilon$ can be

verified experimentally one knows an upper bound

$$\epsilon > \langle (a^\dagger)^N a^N \rangle = \sum_{n \geq N} \langle n | \rho_a | n \rangle \frac{n!}{(n-N)!} \geq \sum_{n \geq N} \langle n | \rho_a | n \rangle \quad (3.28)$$

for the sum of higher order Fock state populations. The approximation made when truncating the Hilbert space is thus well-controlled.

If such a truncation is possible the moments can be mapped to a density matrix in Fock representation by evaluating the sum [Herzog96]

$$\begin{aligned} \langle m | \rho_a | n \rangle &= \frac{1}{\sqrt{n!m!}} \sum_{l=0}^{\infty} \frac{(-1)^l}{l!} \langle (a^\dagger)^{n+l} a^{m+l} \rangle \\ &\equiv \mathcal{M}(\langle (a^\dagger)^n a^m \rangle) \end{aligned} \quad (3.29)$$

up to terms of order $2N$.

The described procedure is very efficient since the evaluation of moments from the measured distributions as well as finding the solution of Eq. (3.23) requires only small computational effort. Furthermore the moment representation provides a very intuitive picture to extract fundamental properties of the quantum state.

3.3.5 Reconstruction of single photon states

Based on the theoretical insights gained in the last two sections we are able to evaluate the moments $\langle (\hat{S}^\dagger)^n \hat{S}^m \rangle_{\rho_a}$ and $\langle (\hat{S}^\dagger)^n \hat{S}^m \rangle_{|0\rangle\langle 0|}$ from the measured histograms shown in Figure 3.7(a)-(b) and use them to determine the normally ordered signal moments $\langle (a^\dagger)^n a^m \rangle$ up to the desired order, four in this case, as shown in Figure 3.8(a). We note that the quadrature histograms are normalized such that the zeroth order moments are always unity for all prepared states. The off diagonal elements in the moment matrix express coherences between different photon number states. They vanish for states with circular symmetric phase space distributions such as pure Fock states or thermal states. For the Fock state $|1\rangle$ (Figure 3.8(a)), we observe that all off diagonal moments are close to zero. In addition, we note that the fourth order moment $\langle (a^\dagger)^2 a^2 \rangle$ is also close to 0 indicating antibunching of the prepared single photon states [Bozyigit11]. In contrast, a thermal state with the same mean photon number would display vanishing off diagonal moments but finite diagonal 4th order moments. Experimentally, for the single photon Fock state, the aforementioned residual coherent admixture of the vacuum state leads to a non-vanishing small mean amplitude $|\langle a \rangle| = 0.044$ and a slightly reduced mean photon number $\langle a^\dagger a \rangle = 0.91$. For an integration time of 12 hours for each state, we find errors of the 4th order moments to be approximately ± 0.1 where the statistical error in the moments is known to increase exponentially with

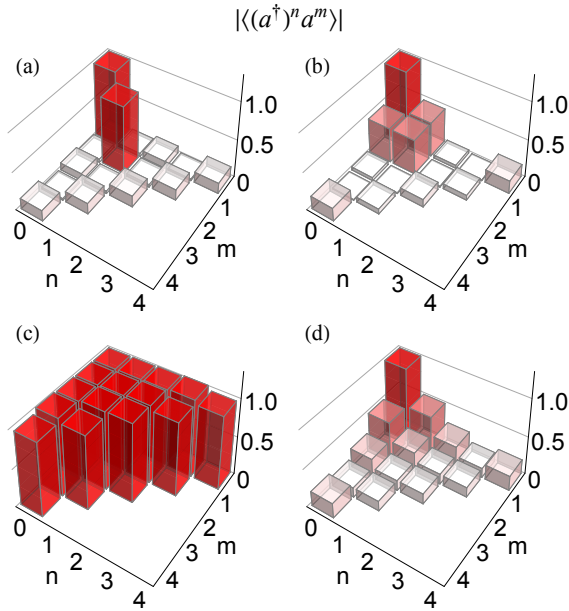


Figure 3.8: Absolute value of the normally ordered moments $|\langle (a^\dagger)^n a^m \rangle|$ up to 4th order for (a) a single photon Fock state, (b) a superposition state $(|0\rangle - |1\rangle)/\sqrt{2}$, and two coherent states with amplitude (c) $\alpha = 1$, and (d) $\alpha = 0.5$.

increasing order [daSilva10]. In comparison, the estimated statistical errors for the first, second and third order moments are approximately 1.5×10^{-3} , 4.5×10^{-3} , and 1.5×10^{-2} , respectively. The errors have been estimated from the standard deviation of the moments acquired in repeated measurements of the distributions.

We have also prepared and analyzed superposition states of the type $(|0\rangle + e^{i\phi}|1\rangle)/\sqrt{2}$, see Figure 3.8(b). The relative phase ϕ is controlled by the phase of the corresponding qubit state that is mapped into the resonator. For this class of states, the mean amplitude ideally equals the mean photon number $\langle a \rangle = \langle a^\dagger a \rangle = 0.5$. The first equality remains approximately valid even if the state is slightly mixed with the vacuum. We have been able to use this property to determine the effective gain of our amplifier chain because first and second order moments have a different characteristic scaling with the gain. This allowed us to scale X and P axes of the histograms (Figure 3.7) such that they correspond to the real and imaginary part of $a + h^\dagger$. From our measurement data, we extract $|\langle a \rangle| = 0.466$ which is close to the expected value. Note that this determination of the effective gain is equivalent to a calibration of the system noise N_0 , which is often realized using a blackbody radiation source with variable temperature [Mallet11, Flurin12].

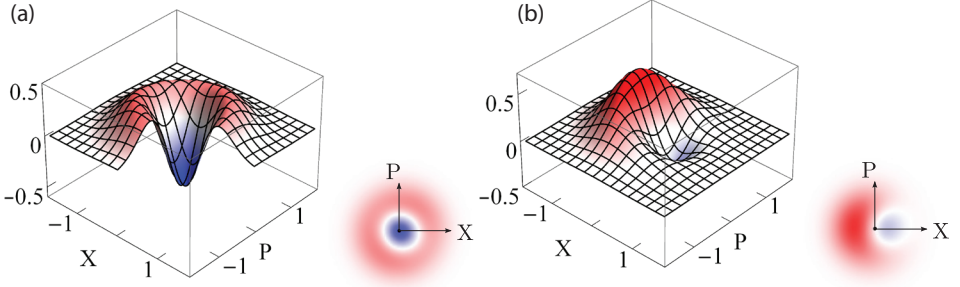


Figure 3.9: Wigner function $W(\alpha = X + iP)$ for (a) a single photon Fock state and (b) a superposition state both reconstructed from the measured moments shown in Figure 3.8.

To further confirm the validity of our scheme, we have generated coherent states $|\alpha\rangle$ with amplitude $\alpha = 1$ and $\alpha = 0.5$ by applying 10 ns square coherent pulses with controlled amplitude to the weakly coupled input port of the resonator. The moments of coherent states are given by $\langle (a^\dagger)^n a^m \rangle = (\alpha^*)^n \alpha^m$. For $\alpha = 1$ all moments are observed to be close to 1 (Figure 3.8(c)), as expected. This also demonstrates that systematic errors in the detection chain, such as small nonlinearities, are negligible since all moments take their expected values. For $\alpha = 0.5$ (Figure 3.8(d)), the measured moments decay exponentially with $\langle (a^\dagger)^n a^m \rangle = 0.5^{n+m}$, as expected. The fourth order moments appear larger than the third order ones, due to their larger statistical error.

From the measured moments we have reconstructed the Wigner function $W(\alpha)$ for a single photon Fock state and its superposition with the vacuum (Figure 3.9). It is sufficient to evaluate [Haroche06]

$$W(\alpha) = \sum_{n,m} \int d^2\lambda \frac{\langle (a^\dagger)^n a^m \rangle (-\lambda^*)^m \lambda^n}{\pi^2 n! m!} e^{-\frac{1}{2}|\lambda|^2 + \alpha\lambda^* - \alpha^*\lambda}$$

up to order $n + m = 3$ because $\langle (a^\dagger)^2 a^2 \rangle \sim 0$. In general, all higher order moments with $n + m \geq 2N - 1$ have to be zero if one diagonal moment $\langle (a^\dagger)^N a^N \rangle$ vanishes, which follows from the fact that diagonal moments $\langle k | (a^\dagger)^n a^n | k \rangle$ with $n > k$ are zero for Fock states $|k\rangle$.

The Wigner function of the single photon Fock state (Figure 3.9(a)) shows clear negative values which indicate the quantum character of the observed state. The slight shift of $\langle a \rangle = 0.044$ from the phase space origin that we already observed in the raw measurement data (Figure 3.7(c)) of the $|1\rangle$ state is also apparent in the reconstructed Wigner function. The superposition state $(|0\rangle - |1\rangle) / \sqrt{2}$ displayed in Figure 3.9(b) has a finite mean amplitude which leads to the finite center of mass of the distribution. Still, negative values in the distribution persist, illustrating the quantum coherence between

the $|0\rangle$ and $|1\rangle$ state. We have also varied the relative phase ϕ of the superposition states and have observed the expected rotation of the Wigner function.

3.4 Maximum likelihood state estimation

Due to the unavoidable statistical imprecision in expectation values extracted from a finite number of measurements, a direct mapping from the measurement data to the desired state representation does not in general result in a completely positive density matrix. Maximum-likelihood state estimation [Hradil04] aims to correct for that. In this section we discuss two different maximum-likelihood procedures applicable to complex amplitude detection schemes as relevant for the circuit QED experiments under consideration. The first method is based on the experimentally determined finite set of moments $\langle (a^\dagger)^n a^m \rangle$ together with their respective standard deviations $\delta_{n,m}$. The second one estimates the density matrix directly from the measured probability distributions.

3.4.1 Maximum-likelihood procedure based on measured moments

In order to find the most likely density matrix given a set of measured moments and their respective standard deviations $\delta_{n,m}$, we maximize the log-likelihood function (see e.g. supplementary material of Ref. [Chow12])

$$\mathcal{L}_{\text{Log}} = - \sum_{n,m} \frac{1}{\delta_{n,m}^2} |\langle (a^\dagger)^n a^m \rangle - \text{Tr}[\rho_a (a^\dagger)^n a^m]|^2 \quad (3.30)$$

with respect to the elements of the density matrix ρ_a . The properties $\rho_a \geq 0$ and $\text{Tr}\rho_a = 1$ of the density matrix are included as constraints in the maximization of Eq. (3.30). The standard deviations $\delta_{n,m}$ appear in the denominator of each term, such that moments which are determined with low accuracy contribute to the log-likelihood function with less weight.

This maximization problem can be formulated as a semi-definite program, for which efficient numerical solutions exist [Vandenberghe96, Chow12]. Note that this maximum likelihood scheme is particularly efficient for states which contain only few photons since in this case only a finite set of moments is non-zero.

We have tested the described maximum-likelihood procedure based on experimental data sets obtained in a circuit QED experiment. In addition to the generation of single photon states [Eichler11b] we have prepared two photon Fock states and their coherent superposition with the vacuum. The setup employed for these experiments and details about the generation of the two-photon state generation are discussed in Section 5.2. Note that for the reconstruction of two-photon states it is necessary to measure photon

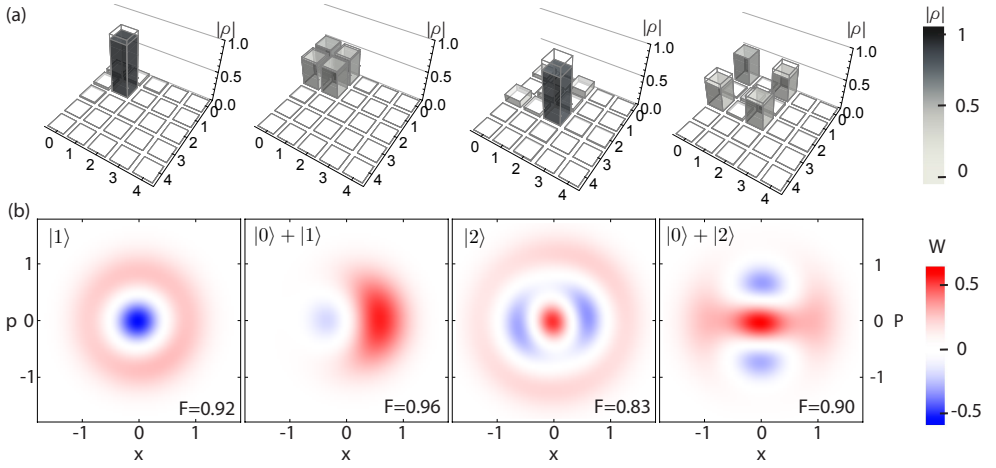


Figure 3.10: (a) Absolute value of the experimentally reconstructed density matrices (grayscale) in comparison with the ideal ones (wireframes) for the four indicated quantum states. (b) Measured density matrices transformed into their corresponding Wigner functions $W(x, p)$. The fidelities between ideal states $|\psi\rangle$ and measured density matrices are evaluated as $F = \langle \psi | \rho | \psi \rangle$.

correlations including moments up to sixth order. The accurate measurement of $\langle (a^\dagger)^3 a^3 \rangle$ – compared to previous measurements in which $\langle (a^\dagger)^2 a^2 \rangle$ had been the highest order measured moment [Bozyigit11, Eichler11b, Lang11] – was enabled by a Josephson parametric amplifier used as the first amplifier in the detection chain [Castellanos-Beltran08, Eichler12b].

Based on the measured moments and their respective standard deviations up to order $n + m = 8$ we reconstruct each density matrix by maximizing Eq. (3.30). In order to demonstrate that higher order photon number populations are not relevant for the description of the state if one of the diagonal moments $\langle (a^\dagger)^N a^N \rangle$ is measured to be close to zero (compare Eq. (3.28)), we have chosen a Hilbert space with up to four photon Fock states. The results (Figure 3.10(a)) show that only the zero, one and two photon Fock states contribute to the reconstructed density matrices while the higher Fock states stay unpopulated. A compromise between the size of the Hilbert space and the likelihood of the reconstructed state may be found by applying the Akaike or Bayesian information criterion [Guta12] to reduce the complexity of the model used for reconstructing the state. In order to illustrate the quantum character of the reconstructed states we have transformed the density matrices into their corresponding Wigner functions [Eichler11b], which show negative values in all four cases (Figure 3.10(b)).

We estimate the statistical error in the fidelities of the reconstructed density matrices

by repeating the likelihood maximization for resampled sets of moments [Řeháček08, Chow12]. The resulting standard deviations of the resampled fidelities are below 2% for all reconstructed states. The small statistical errors are due to the high overall microwave detection efficiency of $\eta = 0.19$ of our setup in combination with the large number of measurements exceeding 10^8 for all the shown density matrices. Since high repetition rates of up to 10 MHz [Bozyigit11] are possible for circuit QED experiments we believe that the maximum likelihood approach is well suited in this context. However, in experiments for which only a small number of samples is available alternative methods such as the Bayesian approach [Audenaert09, Dobek11] may be advantageous compared to maximum likelihood procedures.

3.4.2 Iterative maximum-likelihood procedure based on measured histograms

In addition to the moments based maximum likelihood scheme we formulate an iterative procedure which estimates the density matrix directly from the measured histograms. This reconstruction method is useful for photon states which contain a large number of contributing Fock states and consequently a large number of non-vanishing moments. In addition to this practical relevance it gives insight into the interpretation of the measured probability distribution.

The measurement of a quantum observable can be described by a set of positive operator valued measures (POVM) $\hat{\Pi}_j$ [Nielsen00], which have the property that the probability p_j for getting the respective measurement result is given by $p_j = \text{Tr}[\rho \hat{\Pi}_j]$. The operators $\hat{\Pi}_j$ need to be positive and hermitian but not necessarily projectors. In the ideal case they form a decomposition of the Hilbert space $\sum_j \hat{\Pi}_j = \mathbb{1}$. Preparing and measuring a system in state ρ repeatedly will return each of the possible results f_j times. The most likely state ρ_{ML} given this set of data is the one which maximizes the likelihood function

$$\mathcal{L} = \prod_j \text{Tr}[\rho \hat{\Pi}_j]^{f_j}. \quad (3.31)$$

Note that in order to find a unique global maximum of \mathcal{L} , it is a necessary condition that an arbitrary density matrix can be constructed as a linear combination of $\hat{\Pi}_j$. As a counterexample, if the POVM are given by a complete orthogonal set of projectors $\hat{\Pi}_j = |j\rangle\langle j|$ the ML function \mathcal{L} is independent of the off-diagonal elements of ρ expressed in the $|j\rangle$ basis. The maximization of \mathcal{L} can thus only identify the most likely diagonal density matrix elements $\langle j|\rho|j\rangle$.

It is computationally demanding to directly determine ρ_{ML} for high-dimensional Hilbert spaces. However, the density matrix ρ_{ML} can be found using iterative methods [Hradil04, Lvovsky04, Řeháček07, Lvovsky09]. In order to formulate the ML

iteration procedure we define the operator

$$\hat{R}(\rho) = \sum_j \frac{f_j}{\text{Tr}[\rho \hat{\Pi}_j]} \hat{\Pi}_j. \quad (3.32)$$

The iterative method for updating the density matrix [Hradil04, Hradil97]

$$\rho_{k+1} = \mathcal{N} \hat{R}(\rho_k) \rho_k \hat{R}(\rho_k) \quad (3.33)$$

with renormalization constant \mathcal{N} , has shown good convergence towards ρ_{ML} [Lvovsky09]. As an initial condition for the iteration procedure one either chooses the maximally mixed state $\rho_0 = 1/d$, where d is the dimension of the reconstructed Hilbert space, or constructs a more realistic initial condition by taking into account the measured moments.

In a practical implementation where the phase space is discretized and the Hilbert space is truncated to finite dimensions we might also be faced with the situation that the POVM operators do not sum to the identity operator $\sum_j \hat{\Pi}_j = \hat{G} \neq 1$. In this situation the iteration procedure can be modified as

$$\rho_{k+1} = \mathcal{N} \hat{G}^{-1} \hat{R}(\rho_k) \rho_k \hat{R}(\rho_k) \hat{G}^{-1} \quad (3.34)$$

to guarantee convergence towards the most likely density matrix [Hradil06, Mogilevtsev07].

Iterative method for ideal complex amplitude detection

The method described above has been adapted to optical homodyne detection by Lvovsky [Lvovsky04] in 2004 and is frequently used in experiments based on optical homodyne tomography [Babichev04, Tipsmark11, Usuga10]. Here we adapt the method to measurements of the complex amplitude operator \hat{S} . We start with the case of ideal detection, i.e. for the noise mode h being in the vacuum state.

As discussed in Section 3.3.2 the measured probability distribution in this case is the Q function $D^{[\rho_a]}(S) = Q_a(S)$. The underlying set of POVMs $\hat{\Pi}_S$ is thus defined by the condition

$$Q_a(S) \doteq \text{Tr}[\rho_a \hat{\Pi}_S]. \quad (3.35)$$

Since the Q function can be written as the expectation value $Q_a(\alpha) = \frac{1}{\pi} \langle \alpha | \rho_a | \alpha \rangle$ with respect to coherent states $|\alpha\rangle$ we identify the well-known result [Helstrom76]

$$\hat{\Pi}_{S=\alpha} \equiv \hat{\Pi}_\alpha = \frac{1}{\pi} |\alpha\rangle \langle \alpha|. \quad (3.36)$$

Here and in the following we have labeled the possible measurement results of \hat{S} by α to emphasize their relation to coherent states.

The coherent state projectors $\hat{\Pi}_\alpha$ have both the desired properties: They sum up to the identity operator $\int_\alpha \hat{\Pi}_\alpha = \mathbb{1}$ and they allow for the construction of an arbitrary density matrix as a linear combination of projectors

$$\rho_a = \pi \int_\alpha P_a(\alpha) \hat{\Pi}_\alpha, \quad (3.37)$$

compare with Eq. (3.11). Based on this knowledge we can directly apply the iteration procedure Eq. (3.34).

Full state tomography thus requires the measurement of only a single observable \hat{S} which ideally projects onto coherent states. Due to the properties of coherent states all information about the phase of the field necessary to reconstruct the off-diagonal density matrix elements is contained in this measurement. This is one of the reasons why the discussed detection scheme has great potential in microwave photon field tomography – especially since the advent of nearly quantum-limited amplifiers [Bergeal10a, Castellanos-Beltran08, Eichler11a, Hatridge11].

Iterative method for generalized complex amplitude detection

Due to noise added by amplifiers as well as finite radiation losses in waveguides and microwave components the mode h is typically not described by the vacuum but a thermal state with mean photon number N_0 . In the following we show how to reconstruct the density matrix ρ_a in this situation. We keep the discussion as general as possible and allow for mode h being in an arbitrary state described by ρ_h which can be specified experimentally using a reference measurement.

Preparing the signal mode a in the vacuum state we can measure the Q function of mode h since $D^{[0]\langle 0|}(\alpha) = Q_h(\alpha^*)$. Applying the iterative maximum likelihood scheme for ideal detection we reconstruct the most likely state for the noise mode ρ_h . To account for this noise state in the reconstruction of ρ_a we identify the modified POVM operators $\hat{\Pi}_\alpha^{[\rho_h]}$, which describe the measurement process under the condition that the detection system is in state ρ_h . The result, which can be shown by verifying the identity

$$\text{Tr}[\rho_a \hat{\Pi}_\alpha^{[\rho_h]}] \doteq D^{[\rho_a]}(\alpha) \stackrel{\text{Eq. (3.20)}}{=} \int_\beta P_h(\alpha^* - \beta^*) Q_a(\beta), \quad (3.38)$$

between POVMs and the expected measured distribution (Appendix A.3), is

$$\hat{\Pi}_\alpha^{[\rho_h]} = \frac{1}{\pi} T_h(\alpha) \tilde{\rho}_h T_h^\dagger(\alpha). \quad (3.39)$$

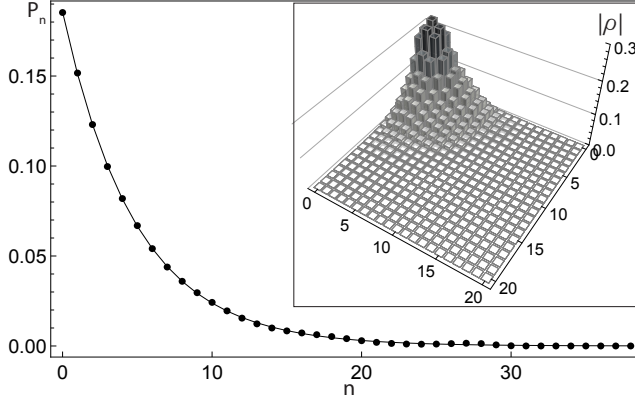


Figure 3.11: Diagonal matrix elements $p_n = \langle n|\tilde{\rho}_h|n\rangle$ of the detector state (dots) obtained with the iterative maximum likelihood method from experimental data. The photon number distribution is well described by a thermal distribution (solid line) with mean photon number $N_0 \approx 4.4$. The inset shows the reconstructed density matrix with fidelity $F = 95\%$ of a coherent state with $\alpha \approx 1.7$.

Here we have defined the displacement operator $T_h(\alpha) \equiv e^{\alpha h^\dagger - \alpha^* h}$ and $\tilde{\rho}_h$ as the most likely density matrix with respect to the reflected histogram $Q_h(-\alpha^*)$. Note that since displaced Fock states are orthonormal and complete [Wunsche91]

$$\int_{\alpha} T(\alpha)|m\rangle\langle n|T^\dagger(\alpha) = \mathbb{1}\delta_{n,m}, \quad (3.40)$$

the relation $\int_{\alpha} \hat{\Pi}_{\alpha}^{[\rho_h]} = \mathbb{1}$ holds for any valid detector state ρ_h . This leads to the remarkable result that the reconstruction method is unbiased for arbitrary detector states. The only two requirements for the method to apply are that the signal and noise modes are uncorrelated $\rho = \rho_a \otimes \rho_h$ and that a can be cooled into the vacuum state or any other known state. Both of these conditions can be realized experimentally to good approximation as discussed before. In order to estimate the density matrix ρ_a we can again apply the iterative method using $\hat{\Pi}_{\alpha}^{[\rho_h]}$ as a set of POVMs.

We have applied the iterative maximum likelihood scheme to the same data sets as presented in Fig.3.10 and found quantitative agreement between the two methods to about 1%. As described in the following, we have tested the iterative method also for a coherent state $|\alpha\rangle$ with mean amplitude $\alpha \approx 1.7$, for which we expect higher photon number states to be occupied. We first apply the iterative procedure to the reference histogram which characterizes the detector state $\tilde{\rho}_h$. Its diagonal elements $p_n = \langle n|\tilde{\rho}_h|n\rangle$ are shown in Figure 3.11 as dots which are very well described by a thermal distribution (solid line) with mean photon number $N_0 \approx 4.4$. The off-diagonal

elements (not shown) are all smaller than $\epsilon = 0.004$. Therefore, the detection noise is very well approximated by thermal noise. Taking into account the estimated detector state $\tilde{\rho}_h$ we construct $\hat{\Pi}_\alpha^{[\rho_h]}$ and iterate the maximum likelihood procedure for the coherent state histogram. The resulting estimated density matrix ρ_a is shown in the inset of Figure 3.11 and has a fidelity of $F = 95\%$ compared to an ideal coherent state. We refer the loss of fidelity to low-frequency phase drifts of the microwave generator during the accumulation of histograms.

Note that in order to reconstruct and express the density matrix of the detector state $\tilde{\rho}_h$ with high accuracy we have to take into account a Hilbert space of a dimension which is approximately 10 times the noise number N_0 . It is therefore numerically challenging to implement the iterative procedure in cases where the noise number is large. If this is the case one may preferably chose to work with the moments based maximum likelihood method presented in the previous section.

3.5 Two channel detection and the positive P distribution

We have already pointed out that field quadrature measurement is the most commonly used detection method for microwave frequency fields. Based on this detection principle it has also been possible to experimentally realize Hanbury Brown Twiss-type setups (Figure 3.12) where two instead of one complex amplitudes are measured [Gabelli04, Menzel10, Mariantoni10, Bozyigit11, Lang11]. The advantage of such a detection scheme is that ideally the system noise in the two detection arms is uncorrelated and only the signal mode a contributes to the cross-correlations between the two output arms. In this section we provide a quantum optics description of a generic two-channel microwave detection chain [Menzel10, Mariantoni10] as shown in Figure 3.12. We formulate the main advantages of such a measurement setup and show that under reasonable assumptions a direct measurement of a positive P distribution [Drummond80] is realized. This relation between the positive P distribution and the two-channel detection scheme gives important insight into the general statistical properties of the obtained measurement results.

3.5.1 Two-channel detection

The main difference between the one- and the two-channel setup depicted in Figure 3.12 is the additional beam splitter which splits the signal mode a into two equal parts while introducing an additional mode v . As a result, the input modes at the two amplifiers are given by $(a \pm v)/\sqrt{2}$ and the total measured complex amplitudes \hat{S}_1 and

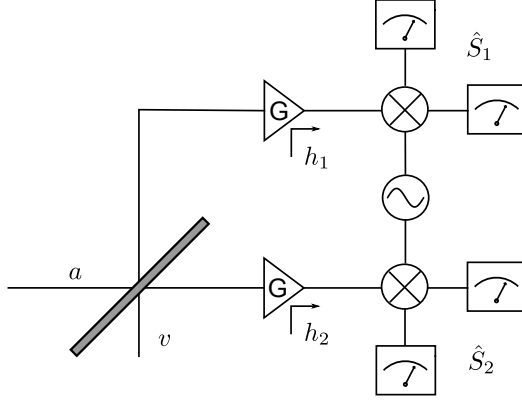


Figure 3.12: Two channel detector with radiation incident from input mode a . Each of the beam splitter outputs has an individual amplification stage adding noise in modes h_1 and h_2 . In both channels the complex amplitude is measured [daSilva10, Bozyigit11].

\hat{S}_2 can be expressed as

$$\begin{aligned}\hat{S}_1 &= a + v + \sqrt{2}h_1^\dagger, \\ \hat{S}_2 &= a - v + \sqrt{2}h_2^\dagger,\end{aligned}\quad (3.41)$$

where h_1 and h_2 are the modes accounting for the system noise of the two detection chains. Under the assumptions justified below that (i) the mode v is in the vacuum state, that (ii) all other modes are uncorrelated $\rho = \rho_a \otimes \rho_{h_1} \otimes \rho_{h_2}$, and that (iii) the noise has no phase-coherence $\langle h_2^m \rangle = 0 = \langle h_1^m \rangle$, $\forall m > 0$ we find the following cross-correlations [daSilva10]

$$\langle (\hat{S}_1^\dagger)^m \hat{S}_2^n \rangle = \langle (a^\dagger)^m a^n \rangle. \quad (3.42)$$

The above assumptions require that (i) the open beam splitter port is connected to a bath of zero temperature, that (ii) the signal is not correlated with the two completely independent amplifier chains, and that (iii) the noise does not depend on the phase defined by the reference local oscillator, all of which can in good approximation be realized experimentally [Bozyigit11, Lang11].

This result is remarkable since under realistic conditions the above cross-correlations completely describe the state of mode a independent of the detector noise modes. This means that the scheme is largely independent of the choice of amplifiers and noise sources, even if the noise constitutes the majority of the power in the signals S_1, S_2 . As we show in the following these properties can be understood in terms of the positive P function representation [Drummond80].

3.5.2 The positive P function

The positive P function was introduced by Drummond and Gardiner [Drummond80] as a theoretical concept for the solution of Fokker-Planck equations. In contrast to the Wigner function and Glauber-Sudarshan P function it is completely positive and has all properties of a genuine probability distribution. The positive P function $P(\alpha, \beta^*)$ is defined as a non-diagonal expansion of the density matrix in the coherent state basis

$$\rho_a = \int_{\alpha, \beta} P(\alpha, \beta) \frac{|\alpha\rangle \langle \beta|}{\langle \beta | \alpha \rangle}. \quad (3.43)$$

Like the P function it generates the normally ordered moments of the field operator

$$\langle (a^\dagger)^m a^n \rangle = \int_{\alpha, \beta} P(\alpha, \beta) \alpha^n (\beta^*)^m. \quad (3.44)$$

Furthermore this four-dimensional probability distribution $P(\alpha, \beta^*)$ can be shown to be positive, not unique and to exist for any quantum state [Drummond80]. To resolve the problem of uniqueness one can resort to the *canonical choice* [Braunstein91] of the positive P function which is given by

$$P_{\text{can}}(\alpha, \beta) = \frac{1}{4\pi} \exp\left(-\frac{|\alpha - \beta|^2}{4}\right) Q_a\left(\frac{\alpha + \beta}{2}\right). \quad (3.45)$$

While the positive P function is often considered artificial and only of theoretical relevance, Braunstein *et al.* have shown that it can be interpreted as the probability distribution for the simultaneous measurement of four quadrature variables [Braunstein91]. A scheme for an optical experiment was proposed by Agarwal [Agarwal94] based on fourfold balanced homodyne detection. To our knowledge this scheme has so far not been implemented, probably due to the significant experimental effort necessary at optical frequencies.

3.5.3 Two channel detection as a measurement of the positive P function

The scheme by Agarwal and the two channel microwave detection scheme in Figure 3.12 are equivalent up to the presence of the amplifier noise. Furthermore under the assumptions made above about the noise, the observables \hat{S}_1, \hat{S}_2 generate the normally ordered moments in the same way as the positive P function. It is thus natural to assume that the probability distribution of the measurement data $P(S_1, S_2)$ is a positive P-representation of the input mode a . In appendix Appendix A.2 we

calculate this distribution and find

$$P(S_1, S_2) = \frac{1}{4} \int_{\beta} P_a(\beta) Q_1\left(\frac{S_1^* - \beta^*}{\sqrt{2}}\right) Q_2\left(\frac{S_2^* - \beta^*}{\sqrt{2}}\right). \quad (3.46)$$

where $Q_{1,2}(\alpha)$ are the Q functions of the system noise modes h_1, h_2 . When the noise added to both channels is in a thermal state with mean photon number N_0 Eq. (3.46) simplifies to

$$P(S_1, S_2) = \frac{\exp\left(-\frac{|S_1 - S_2|^2}{4(N_0 + 1)}\right)}{4\pi(N_0 + 1)} W_a\left(\frac{S_1 + S_2}{2}, -1 - 2N_0\right) \quad (3.47)$$

and for quantum limited detection, i.e. $N_0 = 0$, to

$$P(S_1, S_2) = \frac{1}{4\pi} \exp\left(-\frac{|S_1 - S_2|^2}{4}\right) Q_a\left(\frac{S_1 + S_2}{2}\right) \quad (3.48)$$

$$= P_{\text{can}}(S_1, S_2). \quad (3.49)$$

The compelling result is that for quantum limited detection the measurement data distribution corresponds to the canonical choice of the positive P -representation $P_{\text{can}}(\alpha, \beta)$. Moreover, we show in Appendix A.2.2 that the measured distribution is always a positive P distribution

$$\frac{1}{\pi} \int_{S_1, S_2} P(S_1, S_2) \frac{\langle \alpha | S_1 \rangle \langle S_2 | \alpha \rangle}{\langle S_2 | S_1 \rangle} = Q_a(\alpha) \quad (3.50)$$

for any thermal populations N_1, N_2 in the detector noise modes. As a consequence, the density matrix can be directly evaluated from the measured $P(S_1, S_2)$ using Eq. (3.43) even in the presence of significant thermal noise of unequal powers in the detection chains. These results suggest that the measurement of a positive P distribution is possible with current microwave frequency quadrature detection setups.

3.6 Hong-Ou-Mandel interference: Reconstruction of two-photon NOON states

3.6.1 Two-photon interference at a beam splitter

When two identical single photons simultaneously impinge at the two input ports of a beam splitter, they perfectly bunch together and leave the beam splitter as a pair in either one or the other output port. This interference effect results from the bosonic nature of photons and has first been observed experimentally by Hong, Ou and

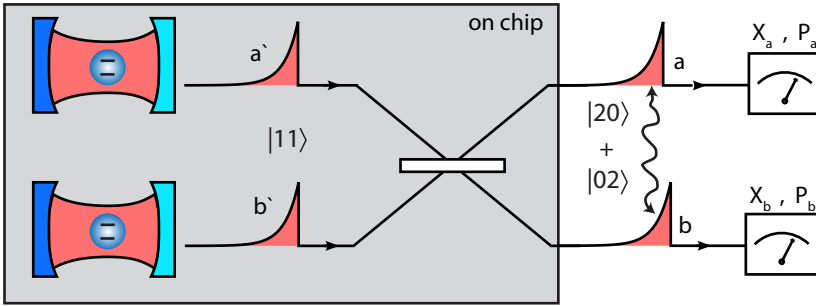


Figure 3.13: Schematic of the experimental setup used for a two-photon interference experiment. Two transmon-resonator systems, shown as their optical analog, are used to create single photons on demand. The photons propagate in modes a' and b' towards a beam splitter which is on the same chip as the two sources (gray area). Radiation in modes a and b at the beam splitter output is linearly amplified, to measure the complex amplitudes $S_a = X_a + iP_a$ and $S_b = X_b + iP_b$ in both channels.

Mandel in 1987 [Hong87]. Because of the absence of any classical analog, two-photon interference is a fundamental manifestation of the quantum nature of electromagnetic radiation.

Since the bunching of photons relies on their indistinguishability, two-photon interference has been experimentally studied in a variety of systems [Riedmatten03, Kaltenbaek06, Beugnon06, Flagg10, Lettow10], to test the reliability and frequency stability of single-photon sources. Interference at a beam splitter is also important in the context of quantum information science. It provides a major building block in linear optics quantum computation schemes [Knill01], and enables the realization of quantum repeater nodes as well as the distribution of entanglement between spatially separated atoms [Duan01, Moehring07, Hofmann12].

All existing two-photon interference experiments have thus far been realized with photons at optical frequencies. Using a superconducting circuit setup, we have been able to observe Hong-Ou-Mandel interference, for the first time, also with microwave photons [Lang13]. The sample used for these experiments consists of two on-demand single-photon sources and a microwave beam splitter. All components are fabricated on a single chip, as schematically shown in Figure 3.13. Each single-photon source is realized as a transmon-resonator system, similar to the one described in Section 3.1, while the beam splitter is implemented as a 90° hybrid [Poazar93, Bozyigit11].

The single photons incident to the beam splitter are generated on-demand and have an exponentially decaying temporal envelop. The methods used for generating these photons are described in Section 3.1. They propagate towards the beam splitter in modes a' and b' , respectively, such that the state incident to the beam splitter can be

written as

$$|\psi_{in}\rangle = |11\rangle = a'^{\dagger} b'^{\dagger} |00\rangle.$$

The beam splitter transformation [Poza93]

$$\begin{aligned} a' &= \frac{1}{\sqrt{2}}(-ia - b) \\ b' &= \frac{1}{\sqrt{2}}(-a - ib) \end{aligned} \quad (3.51)$$

relates the input modes a' and b' to the output modes a and b . Using this relation, we find the output state vector

$$\begin{aligned} |\psi_{out}\rangle &= \frac{1}{2}(-ia - b)^{\dagger}(-a - ib)^{\dagger} |00\rangle = \frac{-i}{2} \left((a^{\dagger})^2 + (b^{\dagger})^2 \right) |00\rangle \\ &\propto \frac{1}{\sqrt{2}}(|20\rangle + |02\rangle), \end{aligned} \quad (3.52)$$

where we have dropped the irrelevant global phase factor i in the second line. The photon fields are thus in a superposition state of two photons in one arm and two photons in the other arm of the beam splitter output. An entangled state of this type is called a two-photon *NOON* state [Kok02]. In its general form $\frac{1}{\sqrt{2}}(|N0\rangle + |0N\rangle)$ it describes a superposition state, for which all N photons are either in one *or* the other mode.

3.6.2 State reconstruction based on 4D histograms

Here, I discuss the experimental characterization of two-photon interference using quantum state tomography. Combining the methods presented in Section 3.5 and Section 3.3 we are able to measure all moments of type $\langle (a^{\dagger})^n a^m (b^{\dagger})^k b^l \rangle$ for the described experiment. These moments contain complete information about the relevant photon statistics and correlations between the two spatially separated microwave fields. They also enable a reconstruction of the joint density matrix ρ of the two mode state.

The tomography experiment is based on the measurement of four-dimensional histograms in the field quadratures $\{X_a, P_a, X_b, P_b\}$. Note, that we use temporal mode matching (Section 3.2.2) during the detection, in order to measure the field quadratures with optimal efficiency. Each set $\{X_a, P_a, X_b, P_b\}$ corresponds to an individual measurement outcome of the observables

$$\hat{S}_a \equiv \hat{X}_a + i\hat{P}_a = a + h_a^{\dagger} \quad \text{and} \quad \hat{S}_b \equiv \hat{X}_b + i\hat{P}_b = b + h_b^{\dagger}, \quad (3.53)$$

Here, h_a and h_b are independent modes accounting for the effective noise added in the

two detection channels.

Because of the limited memory storage of our FPGA board, the histograms are discretized into 16 bins per field quadrature. We record two histograms: One for which the state of interest $|\psi_{\text{out}}\rangle$ is prepared $D^{[|\psi_{\text{out}}\rangle\langle\psi_{\text{out}}|]}$, and one for which we leave the photon sources turned off $D^{[|00\rangle\langle 00|]}$. The second measurement acts as a reference measurement for the noise in modes h_a and h_b . Based on these measured histograms, we determine all relevant statistical moments by numerically evaluating the following integrals

$$\langle (\hat{S}_a^\dagger)^n \hat{S}_a^m (\hat{S}_b^\dagger)^k \hat{S}_b^l \rangle_\rho = \int_{S_a, S_b} D^{[\rho]} (S_a^*)^n S_a^m (S_b^*)^k S_b^l \quad (3.54)$$

where $D^{[\rho]}$ are the measured histograms. In practice, the integration is realized as a summation over all histogram bins. Taking into account that the fields a and b are not correlated with the added noise in h_a and h_b , we decompose the statistical moments in products of the following operator expectation values

$$\langle (\hat{S}_a^\dagger)^n \hat{S}_a^m (\hat{S}_b^\dagger)^k \hat{S}_b^l \rangle_\rho = \sum_{w,x,y,z} \binom{n}{w} \binom{m}{x} \binom{k}{y} \binom{l}{z} \langle (a^\dagger)^w a^x (b^\dagger)^y b^z \rangle \langle h_a^{n-w} (h_a^\dagger)^{m-x} h_b^{k-y} (h_b^\dagger)^{l-z} \rangle. \quad (3.55)$$

Based on this equation and using an equivalent procedure as described in Section 3.3, we can determine $\langle h_a^n (h_a^\dagger)^m h_b^k (h_b^\dagger)^l \rangle$ and $\langle (a^\dagger)^n a^m (b^\dagger)^k b^l \rangle$ from the measured statistical moments $\langle (\hat{S}_a^\dagger)^n \hat{S}_a^m (\hat{S}_b^\dagger)^k \hat{S}_b^l \rangle_{[|\psi_{\text{out}}\rangle\langle\psi_{\text{out}}|]}$ and $\langle (\hat{S}_a^\dagger)^n \hat{S}_a^m (\hat{S}_b^\dagger)^k \hat{S}_b^l \rangle_{[|00\rangle\langle 00|]}$. Details about the efficient inversion of Eq. (3.55) are discussed in Appendix A.1.

3.6.3 Measurement results and interpretation

In a first experimental sequence we prepare two-photon *NOON* states by simultaneously generating pairs of single photon Fock states in the two cavities. The photon generation is repeated every 600 ns, which allows us to record histograms from $\sim 3 \times 10^{10}$ individual measurement results within approximately 10 hours. The data points are stored in 32 different histograms to be able to determine also the standard deviation of the extracted moments. Using the procedure described above, we evaluate the moments $\langle (a^\dagger)^n a^m (b^\dagger)^k b^l \rangle$ up to order $n, m, k, l \in \{0, 1, 2\}$. During the analysis we take a residual thermal steady-state population of 0.03 in modes a and b into account. The total gain of the detection chain is calibrated by preparing an equal superposition state in only one mode, for which we expect half a photon in mode a' .

From the measurement data, shown in Figure 3.14(a), we find both mean amplitudes, $\langle a \rangle$ and $\langle b \rangle$, close to zero. This is expected, since each beam splitter output mode is in

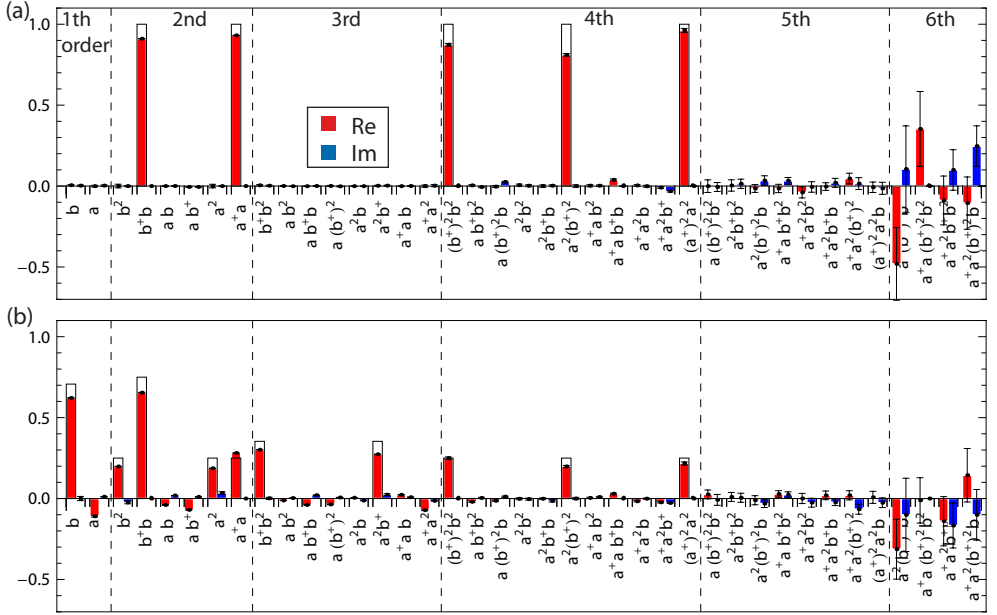


Figure 3.14: Measured (colored bars) and ideal (wireframes) moments $\langle\langle (a^\dagger)^n a^m (b^\dagger)^k b^l \rangle\rangle$ for the prepared states $\frac{1}{\sqrt{2}}(|02\rangle + |20\rangle)$ in (a) and $\frac{1}{2}|00\rangle + \frac{1}{\sqrt{2}}|01\rangle + \frac{1}{\sqrt{8}}(|20\rangle + |02\rangle)$ in (b).

a statistical mixture of either zero or two photons when analyzed individually. This is also reflected in the second order moments, where we find the average photon number in both channels close to one. The bunching of photons into pairs is explained by the finite values of $\langle\langle (a^\dagger)^2 a^2 \rangle\rangle$ and $\langle\langle (b^\dagger)^2 b^2 \rangle\rangle$. Both would be zero, if there was only a single photon in each output channel. The fact that $\langle a^\dagger a b^\dagger b \rangle$ is close to zero, shows that there is never a photon in mode a , if there is one in b (and vice versa). Most importantly, our experiment also demonstrates the quantum coherence of the prepared state. Finding $\langle a^2 (b^\dagger)^2 \rangle$ close to the ideal value one, clearly verifies that we have created a superposition of $|02\rangle$ and $|20\rangle$ instead of a mere statistical mixture between the two states.

In a second experiment, we demonstrate that we can also prepare and detect coherences in the individual channels. To this aim we prepare the beam splitter input field

$$|\psi_{\text{in}}\rangle = \frac{1}{2}(|0\rangle - |1\rangle) \otimes (|0\rangle - i|1\rangle) = \frac{1}{2}(1 - a^\dagger)(1 - ib^\dagger)|00\rangle \quad (3.56)$$

Using the beam splitter transformation in Eq. (3.51) we find

$$\begin{aligned}
 |\psi_{\text{out}}\rangle &= \frac{1}{4}(\sqrt{2} - ia^\dagger + b^\dagger)(\sqrt{2} + ia^\dagger + b^\dagger)|00\rangle \\
 &= \frac{1}{2}|00\rangle + \frac{1}{\sqrt{2}}|01\rangle + \frac{1}{\sqrt{8}}(|20\rangle + |02\rangle),
 \end{aligned} \tag{3.57}$$

for the expected output state. Also for this prepared state, the measured moments are in good agreement with the expected ones, as shown in Figure 3.14(b). We note that the output fields are no longer symmetric in modes a and b . For the specific relative phase between the input superposition states, photons leave the beam splitter predominantly in mode b . Ideally, 0.75 average photons leave the beam splitter in mode b and only 0.25 average photons in mode a . Furthermore, the mean amplitude $\langle b \rangle$ is finite, while $\langle a \rangle$ is ideally zero. The finite measured value of $\langle a \rangle$ is explained by relative phase drifts during the measurement time of a few hours. The agreement between theory and experiment in the third and fourth order terms, shows that our measurement scheme is able to accurately detect all types of coherences between different Fock states.

We have also reconstructed the most likely density matrix ρ for the two mode state from our measurement data. In analogy to Eq. (3.29), we find the following relation between the moments and the density matrix in the Fock basis

$$\langle ml|\rho|nk\rangle = \sum_{j,i=0} (-1)^{i+j} \frac{\langle (a^\dagger)^{n+j} a^{m+j} (b^\dagger)^{k+i} b^{l+i} \rangle}{\sqrt{n!m!k!l!j!i!}} \tag{3.58}$$

Since we have verified the single-photon character of each individual source, we can to very good approximation neglect potential 3-photon contributions in the measured fields. Based on this assumption, we reconstruct the density matrix in the finite two-photon Hilbert space $\{|0\rangle, |1\rangle, |2\rangle\}^{\otimes 2}$. The density matrix in this finite-dimensional Hilbert space is completely determined by the moments $\langle (a^\dagger)^n a^m (b^\dagger)^k b^l \rangle$ up to order $n, m, k, l \in \{0, 1, 2\}$. Based on the linear map in Eq. (3.58), we maximize the log-likelihood function in Eq. (3.30) to find the most likely density matrix, given the measured moments and their respective standard deviations. The real part of the resulting density matrices is shown in Figure 3.15 for both prepared states. The imaginary density matrix elements are all smaller than 0.03. Both states have a fidelity of $F = \langle \psi_{\text{out}}|\rho|\psi_{\text{out}}\rangle \approx 85\%$ compared to the ideal ones. As a measure of entanglement between the two fields we have also evaluated the negativity [Vidal02]. We find $\mathcal{N}(\rho) = 0.39$ for the reconstructed two-photon N00N state, which has to be compared to $\mathcal{N} = 0$ for unentangled states and $\mathcal{N} = 0.5$ for maximally entangled states.

In summary, we have demonstrated a detailed characterization of microwave two-

3.6 Hong-Ou-Mandel interference: Reconstruction of two-photon NOON states

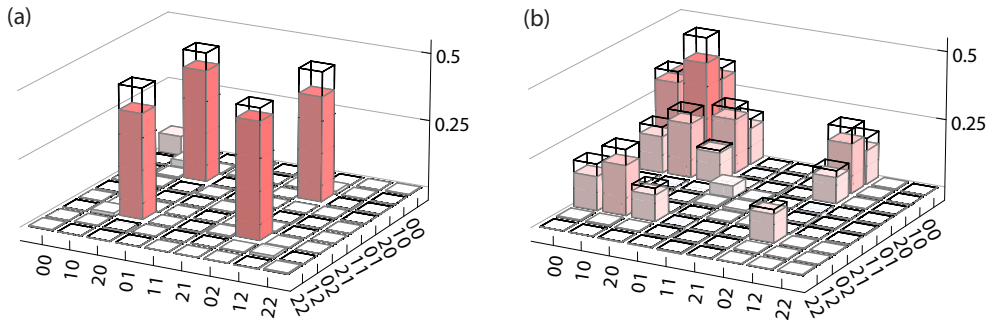


Figure 3.15: Measured (colored bars) and ideal (wireframes) density matrix ρ for the prepared states $\frac{1}{\sqrt{2}}(|02\rangle + |20\rangle)$ in (a) and $\frac{1}{2}|00\rangle + \frac{1}{\sqrt{2}}|01\rangle + \frac{1}{\sqrt{8}}(|20\rangle + |02\rangle)$ in (b). The fidelity of both reconstructed states is $F \approx 85\%$.

photon interference using linear detection methods. Our results imply that we can generate single photons and their superposition with the vacuum with high frequency stability. The demonstration of entanglement between the two spatially separated propagating fields may turn useful in future quantum communication experiments with microwaves.

Chapter 4

Parametric amplification and vacuum noise squeezing

The main limitation for the performance of the measurements presented in the previous chapter was the noise added during amplification, which reduced the effective detection efficiency to a few percent. While we have developed sensitive methods to characterize quantum microwave radiation with high accuracy even in the presence of this added noise, it is still desirable to have detectors which work closer to the quantum limit. This is not only essential for accessing higher order field correlations, as demonstrated in Section 3.4.1, but moreover a requirement for quantum feedback and post-selection based experiments [Wiseman10, Vijay12, Johnson12, Ristè12c]. More generally, an improved amplifier increases the signal-to-noise ratio and is thus highly desirable in a variety of experimental situations. As an example, a significant enhancement of the measurement precision using quantum-limited amplifiers have recently been demonstrated in the context of nanomechanical resonators [Teufel11] and in magnetometry [Hatridge11].

The most successful quantum limited detectors which have so far been realized in the microwave frequency range are based on the principle of parametric amplification [Louisell61, Gordon63, Mollow67, Clerk10]. This amplification process has been used also in quantum optics to generate entangled photon pairs [Burnham70] and squeezed states [Slusher85, Wu86] and was first investigated in electrical circuits operating at microwave frequencies by Yurke *et al.* [Yurke87, Yurke88]. Due to the rapidly evolving field of superconducting circuits the interest in low-noise amplifiers has dramatically increased recently and has lead to a revival of Josephson junction based amplifiers in the past years [Yurke06, Castellanos-Beltran07, Tholén07, Yamamoto08, Castellanos-Beltran08, Kamal09, Bergeal10b, Hatridge11, Eichler11a, Abdo13].

Here, I describe the development of such a parametric amplifier in our lab at ETH Zurich for the use in circuit QED applications. After a discussion of basic concepts, I derive all relevant relations between microscopic system parameters and characteristic amplifier properties. The present chapter shall also act as a guide for building and operating a parametric amplifier with good gain characteristics. We characterize the parametric amplifier experimentally, and demonstrate its near quantum limited performance by measuring entanglement correlations between the signal and idler noise emitted from the device. These squeezing correlation could also act as a resource for future continuous variable quantum optics experiments [Braunstein05].

4.1 Principles of parametric amplification

4.1.1 Parametric processes at optical and microwave frequencies

In quantum optics the term 'parametric' is used for processes in which a nonlinear refractive medium is employed for mixing different frequency components of light. Such processes are parametric in the sense that a coherent pump field, applied to a nonlinear medium, modulates its refractive index, which appears as a *parameter* in a semi-classical treatment. This time-varying parameter is affecting modes which are detuned from the pump and can stimulate their population with photons. The energy for creating these photons is provided by the pump field.

Predominantly, the frequency conversion is either realized as a three-wave mixing process in media with $\chi^{(2)}$ nonlinearity or as a four-wave mixing process in media with $\chi^{(3)}$ nonlinearity. In a three-wave mixing process one pump photon with frequency ω_p is converted into a pair of signal ω_s and idler ω_i photons obeying energy conservation $\omega_p = \omega_i + \omega_s$. Four-wave mixing describes the conversion of two pump photons into a pair of signal and idler photons $2\omega_p = \omega_s + \omega_i$. If the signal and idler modes are initially in the vacuum state such processes are called spontaneous parametric down-conversion and spontaneous four wave mixing [Burnham70]. This phenomenon is abundantly used for creating heralded single photons, i.e. single photons conditioned on a photon counting event.

In order to enhance the production rate of signal and idler pairs one can place the nonlinear medium inside a cavity to form an optical parametric oscillator [Slusher85]. The emitted signal and idler photons are perfectly correlated which results in squeezing. Since the conversion from pump photons into signal and idler pairs is stimulated by already existing fields the described phenomenon is an amplifying process, which we call parametric amplification.

The refractive index in optics is equivalent to the impedance of electrical circuits. In order to realize parametric processes at microwave frequencies we therefore have to modulate an effective impedance. This can be achieved by varying either a capacitive

or an inductive element in time. Although there have been early proposals for fast time-varying capacitances [Louisell60], it nowadays seems more convenient to make use of dissipationless Josephson junctions for this purpose. In a regime in which the current I flowing through a Josephson junction is much smaller than its critical current $I_C \equiv 2eE_J/\hbar$ its associated inductance is approximately $L \approx L_J(1 + \frac{1}{6}(I(t)/I_C)^2)$. Applying an AC current through the junction using appropriate microwave drive fields therefore leads to the desired time-varying impedance. Because of the proportionality of the inductance L to the square of the current $I^2(t)$, such a drive results in a four-wave mixing process.

The effective impedance can alternatively be modulated by varying the magnetic flux enclosed by a SQUID loop [Yamamoto08] such that the effective inductance is approximately modulated proportionally to the AC current $I(t)$ in the loop, $L \approx L_J(1 + I(t)/I_0)$. The quantity I_0 in this expression depends on the DC flux bias point of the SQUID loop. Since the relation between current and inductance is in this case linear, the magnetic flux drive results in a three-wave mixing process.

In order to enhance parametric amplification in a well-controlled frequency band while suppressing it for frequencies out of this band, one can place the modulated Josephson inductance inside a resonator. This is the simplest way to control the band in which parametric amplification occurs. A number of variations of this basic idea are now explored. The circuit topology has recently been modified to achieve a spatial separation of signal and idler modes [Bergeal10a, Bergeal10b, Bergeal12, Roch12, Flurin12] and to build traveling wave amplifiers, in which a field is amplified while propagating in forward direction coaxially with a pump field [Ho Eom12]. Various drive mechanisms ranging from single and double pumps [Kamal09] to magnetic flux drives [Yamamoto08, Wilson11] have been explored¹. Being aware of this variety of possible approaches, we focus on the specific implementation we have chosen in the following. It is the realization of a single mode parametric amplifier driven with one pump tone.

4.1.2 A circuit QED implementation of a parametric amplifier

Our parametric amplifier consists of a $\lambda/4$ transmission line resonator shunted by an array of SQUIDs (Figure 4.1(a)). The use of SQUIDs instead of single junctions provides us with tunability of the resonance frequency as already discussed in the context of the transmon qubit. Since parametric amplifiers typically provide amplification in a narrow band only, tunability is highly desirable to match the band of amplification with the frequency of the signal to be amplified. The Josephson energy per SQUID is approximately a thousand times larger (0.5 – 5 THz in units of the

¹Note that there is a close analogy between parametric amplification and the dynamical Casimir effect [Johansson09, Wilson11].

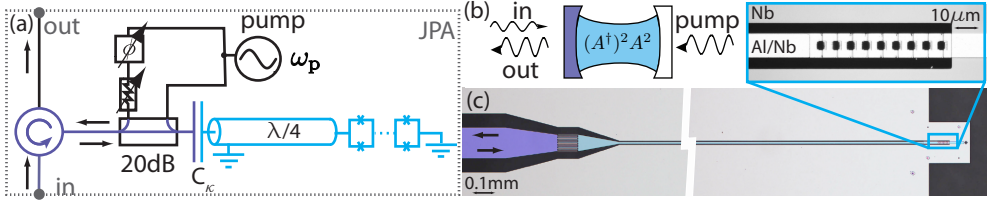


Figure 4.1: (a) Circuit schematic of the parametric amplifier. For details see text. (b) Optical analog of the system. (c) False colored optical micrograph of the sample with an enlarged picture of the SQUID array.

Planck constant h) compared to that of typical transmon junctions. Consequently, the effective anharmonicity of the parametric amplifier is much smaller and we can account for it by adding a small Kerr nonlinear term to the system Hamiltonian, as indicated in Figure 4.1(b). A *weak* nonlinearity is advantageous when aiming for parametric amplification with high dynamic range, as discussed in Section 4.2.3.

The ground plane and inner conductor of the resonator are made of niobium (Nb) while the SQUIDs are fabricated with aluminium (Al), see Figure 4.1(c). The overlap areas between the most left and right SQUIDs and the inner conductor and ground plane, respectively, are chosen sufficiently large ($700\mu\text{m}^2$) in order to avoid effects due to finite capacitances at the aluminium/niobium interface. As a consequence, the associated contact impedance is effectively zero at the relevant microwave frequencies even if there is no DC contact between aluminium and niobium.

The resonator is coupled with capacitance C_k to a transmission line where input and output modes are spatially separated using a circulator (Figure 4.1(a)). A 20 dB directional coupler between the $\lambda/4$ -resonator and the circulator is used to feed in the pump field required for modulating the SQUID inductance. The second port of the directional coupler is used to cancel out the pump tone reflected from the sample interferometrically (for details about the cancellation method see Appendix A.5). The capacitance C_k determines the quality factor of the resonator and with it the band in which parametric amplification occurs².

An optical analog of the setup is shown in Figure 4.1(b). The Kerr nonlinearity represents the effective nonlinear 'refractive index' of the medium inside the cavity with an effective $\chi^{(3)}$ nonlinearity. When driving this nonlinearity with a coherent pump field, we achieve a conversion of pump photons into fields detuned from the pump. All parametric effects we consider here are captured by this nonlinear oscillator model.

²Capacitances have been simulated with the finite element software *Ansoft Maxwell* as described in Appendix A.7.

4.1.3 Regimes of a driven nonlinear oscillator

The relevant part of the Hamiltonian which describes the parametric amplifier considered here can be written as

$$H_{\text{JPA}} = \hbar\tilde{\omega}_0 A^\dagger A + \hbar\frac{K}{2}(A^\dagger)^2 A^2, \quad (4.1)$$

where the subscript JPA stands for 'Josephson parametric amplifier' [Yurke87] and A labels the annihilation operator of the intra-resonator field. Expressions for the resonance frequency $\tilde{\omega}_0/2\pi$ and the effective Kerr nonlinearity K are derived in Section 4.3 based on the full circuit model. Our devices are designed to have typical nonlinearities on the order of $K/\tilde{\omega}_0 \approx 10^{-6}$ or smaller. In the following section we analytically study the dynamics of this system using input-output formalism. Before going into the mathematical derivations, I qualitatively describe different dynamical regimes of this nonlinear oscillator and explain the mechanism which leads to amplification. Many of the important device properties can be understood from its classical response to a coherent drive field.

If we assume for the moment that the amplifier has no internal losses, all the incident power has to be reflected from the device and the classical response is completely specified by the phase φ of the reflected field. We can directly measure this phase, for example with a network analyzer. In contrast to a linear system, where φ only depends on the probe frequency $\omega/2\pi$, it also depends on the power of the probe field in the case of a nonlinear oscillator. In Figure 4.2(a), the theoretically expected value of φ is plotted as a function of the probe amplitude for two characteristic drive frequencies (blue and red). While for low drive powers the phase is constant (quasi-linear response) the phase changes significantly for increased drive power. Depending on the probe frequency we either get into a bistable regime (red) where two stable solutions exist [Dykman80, Marthaler06] or into a regime where the phase has a unique solution (blue). In both cases the phase significantly depends on the input power. The bistable response can for example be used to build a bifurcation amplifier [Siddiqi04, Vijay09] and for nonlinear dispersive readout [Mallet09], which has been intensely studied in the context of circuit QED.

Since we are particularly interested in *linear* amplification the following discussion is focused on the regime, in which the response has a unique solution (blue). The mechanism of amplification can be understood qualitatively in the following way. If we imagine that the device is constantly driven at a frequency and power at which the reflected phase φ depends sensitively on power (see gray circle in Figure 4.2(a)), the system will strongly react to small perturbations. Such perturbations, which could e.g. be caused by an additional small signal field, are therefore translated into a large change of the system response.

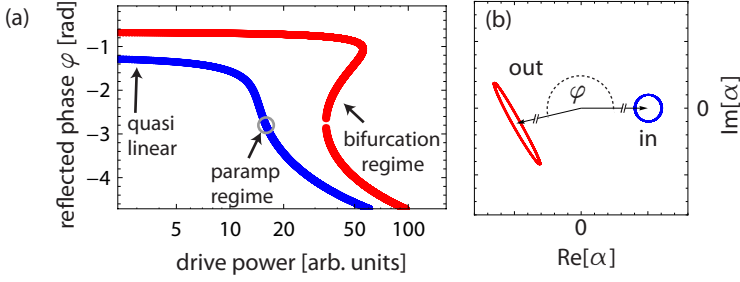


Figure 4.2: (a) Phase of the reflected probe signal for varying drive powers and two characteristic drive frequencies (blue and red). (b) Illustration of the nonlinear oscillator response in the quadrature plane. The blue circle describes various input field configurations close to the one indicated by the gray circle in (a). Due to the nonlinear response of the resonator they result in the output fields indicated by the red ellipse.

We illustrate this amplifying effect by plotting the device response in the quadrature plane to input fields with slightly varying amplitude and phase. In Figure 4.2(b) we indicate these different input fields as a blue circle around their mean value (arrow). The small differences in amplitude of the input fields translate into a large change in φ of the output field (red ellipse). If we interpret the arrow in Figure 4.2(b) as a constant pump and its difference to the points on the blue circle as an additional signal, the signal is either amplified or deamplified depending on its phase relative to the pump.

The mechanism of amplification can thus already be understood by investigating the nonlinear response to a monochromatic drive field. In order to characterize the exact behavior of input fields with finite bandwidth we have to analyze the response in more detail. This also allows us to understand how to use the parametric amplifier in a phase-insensitive mode where both quadratures of an input signal are amplified equally, independent of the relative phase to the pump tone.

4.2 Input-Output relations for the Parametric amplifier

4.2.1 Classical nonlinear response

Here, we employ the input-output formalism [Gardiner85, Walls94] to calculate the nonlinear resonator response, which has already been discussed qualitatively in the previous section. The derivation is along the lines of Ref. [Yurke06]. A schematic of the input output model is shown in Figure 4.3. Based on Eq. (2.16) and the parametric amplifier Hamiltonian in Eq. (4.1) we obtain the following equation of motion for the

intra-resonator field

$$\dot{A} = -i\omega_0 A - iKA^\dagger AA - \frac{\kappa + \gamma}{2} A + \sqrt{\kappa} A_{\text{in}}(t) + \sqrt{\gamma} b_{\text{in}}(t). \quad (4.2)$$

In addition to the coupling to transmission line modes $A_{\text{in}}(t)$ with rate κ we account for potential radiation loss mechanisms by introducing the coupling to modes $b_{\text{in}}(t)$ with loss rate γ (compare Figure 4.3(a)). A boundary condition equivalent to

$$A_{\text{out}}(t) = \sqrt{\kappa} A(t) - A_{\text{in}}(t), \quad (4.3)$$

also holds for the loss modes. When operating the device as a parametric amplifier, the input field A_{in} is typically a sum of a strong coherent pump field and an additional weak signal field. Since this signal carries at least the vacuum noise to the resonator we have to treat it as a quantum field. We account for this particular situation in this formalism by decomposing the total field modes into sums of a classical part and a quantum part

$$\begin{aligned} A_{\text{in}}(t) &= (a_{\text{in}}(t) + \alpha_{\text{in}}) e^{-i\omega_p t}, & A_{\text{out}}(t) &= (a_{\text{out}}(t) + \alpha_{\text{out}}) e^{-i\omega_p t}, \\ A(t) &= (a(t) + \alpha) e^{-i\omega_p t} \end{aligned} \quad (4.4)$$

where α , α_{in} , α_{out} represent the classical parts of the field which are associated with the pump, while a , a_{in} , a_{out} account for the additional signal fields. Since all α 's are complex numbers the modes a satisfy the same bosonic commutation relations as modes A do. By multiplying the field modes defined in Eq. (4.4) with the additional exponential factor $e^{-i\omega_p t}$ we chose to work in a frame rotating at the pump frequency ω_p . Our strategy is to first solve the classical response for the pump field α exactly and then linearize the equation of motion for the weak quantum field a in the presence of the pump. Finally, this leads to a scattering relation between input modes a_{in} and reflected modes a_{out} .

The steady state solution for the coherent pump field is determined by

$$\left((i(\tilde{\omega}_0 - \omega_p) + \frac{\kappa + \gamma}{2}) \alpha + iK\alpha^2\alpha^* \right) = \sqrt{\kappa}\alpha_{\text{in}}, \quad (4.5)$$

which follows immediately by substituting Eq. (4.4) into Eq. (4.2) and collecting only the c-number terms. By multiplying both sides with their complex conjugate we get the equation

$$\left(\left(\frac{\omega_p - \tilde{\omega}_0}{\kappa + \gamma} \right)^2 + \frac{1}{4} \right) |\alpha|^2 - \frac{2(\omega_p - \tilde{\omega}_0)K}{(\kappa + \gamma)^2} |\alpha|^4 + \left(\frac{K}{\kappa + \gamma} \right)^2 |\alpha|^6 = \frac{\kappa}{(\kappa + \gamma)^2} |\alpha_{\text{in}}|^2, \quad (4.6)$$

which determines the average number of pump photons $|\alpha|^2$ in the resonator. Eq. (4.6) reduces to

$$1 = \left(\delta^2 + \frac{1}{4}\right)n - 2\delta\xi n^2 + \xi^2 n^3, \quad (4.7)$$

by defining the scale invariant quantities

$$\delta \equiv \frac{\omega_p - \tilde{\omega}_0}{\kappa + \gamma}, \quad \tilde{\alpha}_{\text{in}} \equiv \frac{\sqrt{\kappa}\alpha_{\text{in}}}{\kappa + \gamma}, \quad \xi \equiv \frac{|\tilde{\alpha}_{\text{in}}|^2 K}{\kappa + \gamma}, \quad n \equiv \frac{|\alpha^2|}{|\tilde{\alpha}_{\text{in}}|^2}. \quad (4.8)$$

δ represents the detuning between pump and resonator frequency in units of the total resonator linewidth, $\tilde{\alpha}_{\text{in}}$ is the dimensionless drive amplitude, and ξ is the product of drive power and nonlinearity, also expressed in dimensionless units. Finally, n represents the mean number of pump photons in the resonator relative to the incident pump power. As an important consequence, we notice from Eq. (4.8) that only the product of drive power and nonlinearity influences the dynamics but not each quantity itself. A small nonlinearity can therefore always be compensated by increasing the drive power. Properties such as the gain-bandwidth product are therefore independent of the strength of the nonlinearity³. Furthermore, the solutions to Eq. (4.8) for negative ξ values are identical to those for positive ξ up to a sign change in δ . Since ξ is negative for the Josephson parametric amplifier, we focus on this particular case.

Eq. (4.7) is a cubic equation in n and can therefore be solved analytically. We do not write down the lengthy solutions here explicitly, but assume in the following that we have an explicit analytical expression for n in terms of δ and ξ . In Figure 4.3(b) we plot n for various parameters ξ as a function of δ . At the critical value $\xi_{\text{crit}} = -1/\sqrt{27}$ the derivative $\partial n/\partial\delta$ diverges and thus the response of the parametric amplifier becomes extremely sensitive to small changes. For even stronger effective drive powers $\xi/\xi_{\text{crit}} > 1$ the cubic equation in Eq. (4.7) has three real solutions. The high and low solutions to the photon number are stable while the intermediate one is unstable. The system bifurcates in this regime as mentioned earlier. The critical detuning below which the system can become bistable is $\delta_{\text{crit}} = -\sqrt{3}/2$. The critical point $(\xi_{\text{crit}}, \delta_{\text{crit}})$ is the one at which both $\partial\delta/\partial n$ and $\partial^2\delta/\partial^2 n$ vanish. In the scale invariant units the maximal value of n is always 4, which is reached at the detuning $\delta = 4\xi$.

Experimentally, the device properties are characterized by measuring the complex reflection coefficient $\Gamma \equiv \alpha_{\text{out}}/\alpha_{\text{in}}$. Based on the input-output relation $\alpha_{\text{out}} = \sqrt{\kappa}\alpha - \alpha_{\text{in}}$ and Eq. (4.5) we can evaluate this reflection coefficient as

$$S_{11} \equiv \Gamma = \frac{\kappa}{\kappa + \gamma} \frac{1}{\frac{1}{2} - i\delta + i\xi n} - 1. \quad (4.9)$$

³Note that there are practical limitations, such as heating in the setup or upper limits in the fabrication of Josephson junctions sizes, which also affect the choice of parameters

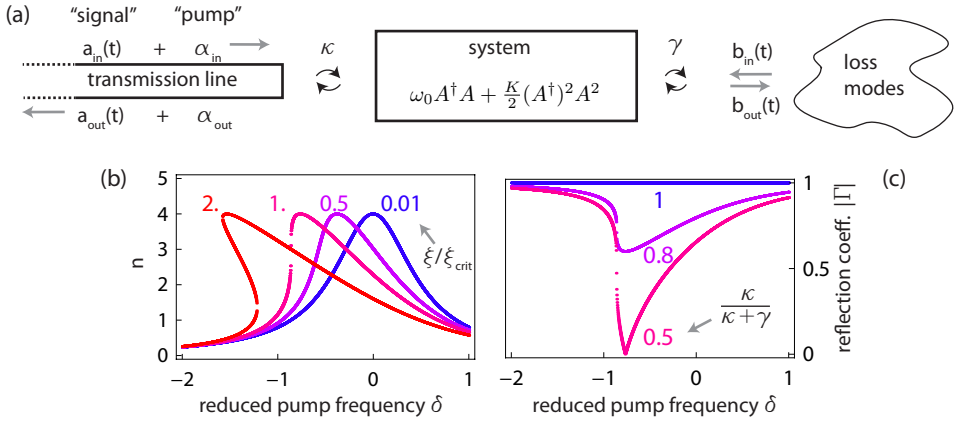


Figure 4.3: (a) Schematic of the input output model used for calculating the response of the parametric amplifier in the presence of additional loss modes. (b) Normalized pump photon number n in the resonator as a function of reduced pump frequency δ for effective drive strengths $\xi/\xi_{\text{crit}} = 0.01, 0.5, 1, 2$, where $\xi_{\text{crit}} = -1/\sqrt{27}$. (c) Absolute value of the reflection coefficient $|\Gamma|$ for different coupling ratios $\kappa/(\kappa + \gamma) = 1, 0.8, 0.5$.

with absolute square

$$|\Gamma|^2 = \frac{\left(\frac{\kappa}{\kappa + \gamma} - \frac{1}{2}\right)^2 + (\delta - \xi n)^2}{\frac{1}{4} + (\delta - \xi n)^2}. \quad (4.10)$$

In Figure 4.3(c) we plot the expected reflection coefficient at $\xi = \xi_{\text{crit}}$ for various loss rates γ . For vanishing losses $\gamma = 0$ all the incident drive power is reflected from the device and $|\Gamma| = 1$. Note that also in this case the resonance is clearly visible in the phase of the reflected signal (not shown here). When the loss rate γ becomes similar to the external coupling rate κ part of the radiation is dissipated into the loss modes. In the case of critical coupling $\gamma = \kappa$ all the coherent power is transmitted into the loss modes at resonance. This is equivalent to the case of a symmetrically coupled $\lambda/2$ resonator, for which the transmission coefficient is also one at resonance [Göppl08].

4.2.2 Linearized response for additional weak (quantum) signal fields

Under the assumption that the photon flux associated with the signal $\langle a_{\text{in}}^\dagger a_{\text{in}} \rangle$ is much smaller than the photon flux of the pump $|\alpha_{\text{in}}|^2$, we can drop terms such as $Ka^\dagger \alpha \alpha$, because they are small compared to the leading terms $Ka^\dagger \alpha \alpha$ and $Ka \alpha \alpha^*$. It is thus valid to linearize the equation of motion for a in the presence of the pump field. By substituting Eq. (4.4) into Eq. (4.2) and keeping only terms which are linear in a we

get

$$\dot{a}(t) = i\left(\omega_p - \tilde{\omega}_0 - 2K|\alpha|^2 + i\frac{\kappa + \gamma}{2}\right)a(t) - iK\alpha^2 a^\dagger(t) + \sqrt{\kappa}a_{\text{in}}(t) + \sqrt{\gamma}b_{\text{in}}(t). \quad (4.11)$$

Since Eq. (4.11) is linear, we can solve it by decomposing all modes into their Fourier components

$$a(t) \equiv \sqrt{\frac{\kappa + \gamma}{2\pi}} \int_{-\infty}^{\infty} d\Delta e^{-i\Delta(\kappa + \gamma)t} a_\Delta \quad (4.12)$$

and equivalently for $a_{\text{in},\Delta}$ and $b_{\text{in},\Delta}$. Note that Δ , the detuning between signal frequencies and the pump frequency, is expressed here in units of the linewidth $\kappa + \gamma$. It is thus dimensionless equivalently to δ . Substituting the Fourier decompositions into Eq. (4.11) and comparing the coefficients of different harmonics, results in

$$0 = \left(i(\delta - 2\xi n + \Delta) - \frac{1}{2}\right)a_\Delta - i\xi n e^{2i\phi} a_{-\Delta}^\dagger + \tilde{c}_{\text{in},\Delta}, \quad (4.13)$$

where

$$\tilde{c}_{\text{in},\Delta} \equiv \frac{\sqrt{\kappa}a_{\text{in},\Delta}}{\kappa + \gamma} + \frac{\sqrt{\gamma}b_{\text{in},\Delta}}{\kappa + \gamma} \quad (4.14)$$

describes the sum of all field modes incident on the resonator. Furthermore, ϕ in Eq. (4.13) is the phase of the intra-resonator pump field, defined by $\alpha = |\alpha|e^{i\phi}$. The fact that Eq. (4.13) couples modes a_Δ and $a_{-\Delta}^\dagger$ can be interpreted as a wave mixing process. In order to express a_Δ in terms of the input fields $c_{\text{in},\Delta}$ we rewrite Eq. (4.13) as a matrix equation

$$\begin{pmatrix} \tilde{c}_{\text{in},\Delta} \\ \tilde{c}_{\text{in},-\Delta}^\dagger \end{pmatrix} = \begin{pmatrix} i(-\delta + 2\xi n - \Delta) + \frac{1}{2} & i\xi n e^{i2\phi} \\ -i\xi n e^{i2\phi} & i(\delta - 2\xi n - \Delta) + \frac{1}{2} \end{pmatrix} \begin{pmatrix} a_\Delta \\ a_{-\Delta}^\dagger \end{pmatrix}. \quad (4.15)$$

By inverting the matrix on the right hand side we can express the fluctuating parts of the intra-resonator field a_Δ in terms of the incoming fields $\tilde{c}_{\text{in},\Delta}$

$$a_\Delta = \frac{i(\delta - 2\xi n - \Delta) + \frac{1}{2}}{(i\Delta - \lambda_-)(i\Delta - \lambda_+)} \tilde{c}_{\text{in},\Delta} + \frac{-i\xi n e^{2i\phi}}{(i\Delta - \lambda_-)(i\Delta - \lambda_+)} \tilde{c}_{\text{in},-\Delta}^\dagger \quad (4.16)$$

with

$$\lambda_\pm = \frac{1}{2} \pm \sqrt{(\xi n)^2 - (\delta - 2\xi n)^2}. \quad (4.17)$$

Using Eq. (4.3), we identify the final transformation between input and output modes

$$a_{\text{out},\Delta} = g_{S,\Delta}a_{\text{in},\Delta} + g_I a_{\text{in},-\Delta}^\dagger + \sqrt{\frac{\gamma}{\kappa}}(g_{S,\Delta} + 1)b_{\text{in},\Delta} + \sqrt{\frac{\gamma}{\kappa}}g_{I,\Delta}b_{\text{in},-\Delta}^\dagger \quad (4.18a)$$

$$\stackrel{\gamma/\kappa \rightarrow 0}{=} g_{S,\Delta}a_{\text{in},\Delta} + g_I a_{\text{in},-\Delta}^\dagger \quad (4.18b)$$

where we have defined

$$\begin{aligned} g_{S,\Delta} &= -1 + \frac{\kappa}{\kappa + \gamma} \frac{i(\delta - 2\xi n - \Delta) + \frac{1}{2}}{(i\Delta - \lambda_-)(i\Delta - \lambda_+)} \\ g_{I,\Delta} &= \frac{\kappa}{\kappa + \gamma} \frac{-i\xi n e^{2i\phi}}{(i\Delta - \lambda_-)(i\Delta - \lambda_+)}. \end{aligned} \quad (4.19)$$

Eq. (4.18b) represents the central results of this calculation. It says that the output field at detuning Δ from the pump frequency is a sum of the input fields at frequencies Δ and $-\Delta$ multiplied with the factors $g_{S,\Delta}$ and $g_{I,\Delta}$, respectively. The additional noise contributions introduced via the loss modes $b_{\text{in},\Delta}$ vanish in the limit $\gamma/\kappa \rightarrow 0$. In this ideal case $\gamma = 0$, the coefficients $g_{S,\Delta}$ and $g_{I,\Delta}$ satisfy the relation

$$G_\Delta \equiv |g_{S,\Delta}|^2 = |g_{I,\Delta}|^2 + 1 \quad (4.20)$$

and Eq. (4.18b) is identical to a two-mode squeezing transformation [Braunstein05, Clerk10] with gain G_Δ . The two-mode squeezing transformation describes a phase-insensitive linear amplifier in its minimal form (compare Eq. (3.1) and Refs. [Caves82]), of which we discuss characteristic properties in the following section.

4.2.3 Gain, bandwidth, noise and dynamic range

For simplicity we consider the case of no losses $\gamma = 0$, for which the parametric amplifier response is described by Eq. (4.18b). The output field at detuning Δ from the pump $a_{\text{out},\Delta}$ is a sum of the fields at frequencies Δ and $-\Delta$ at the input. Both parts are scaled by the frequency dependent complex factors $g_{S,\Delta}$ and $g_{I,\Delta}$, respectively. An incoming signal at detuning Δ is thus amplified by the power gain $G_\Delta = |g_{S,\Delta}|^2$ and mixed with the frequency components at the opposite detuning from the pump. Characteristic properties of the parametric amplifier, such as the maximal gain and the bandwidth, are thus encoded in the quantity $g_{S,\Delta}$ as a function of pump-resonator detuning δ , effective drive strength ξ and detuning between signal and pump Δ .

In Figure 4.4(a) we plot the gain G_0 for zero signal detuning $\Delta = 0$ as a function of δ and ξ . We find that the maximal gain increases with increasing drive strength

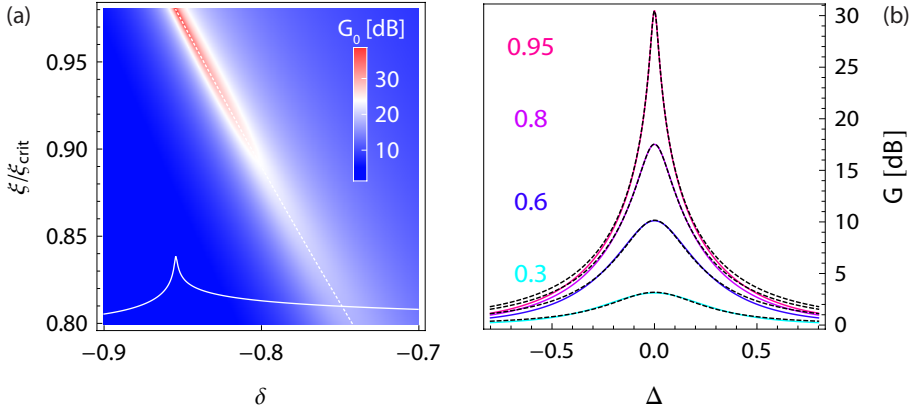


Figure 4.4: (a) Parametric amplifier gain $G = |g_{S,\Delta}|^2$ vs. pump tone detuning δ and drive strength ξ at zero signal detuning Δ and for $\kappa = \gamma$. For increasing drive strength ξ the detuning for maximum gain is indicated by the dashed white line. A cut through the data for the highest value $\xi = 0.98\xi_{\text{crit}}$ is shown as the solid white line in the bottom part. (b) Gain as a function of signal detuning Δ for the indicated drives strengths ξ/ξ_{crit} and optimal pump detuning. The exact gain curves (solid lines) are well approximated by Lorentzian lines (black dashed lines).

ξ while the optimal value for δ at which this gain is reached, shifts approximately linearly with increasing ξ . The optimal values for δ are indicated as a dashed white line in Figure 4.4(a). Mathematically, the gain diverges when ξ approaches the critical value ξ_{crit} . In practice, the gain is limited to finite values due to the breakdown of the stiff pump approximation (see discussion below).

By changing the pump parameters ξ and δ we can adjust the gain G_0 to any desirable value up to typically more than 30 dB. Note that the gain can become smaller than one, in the presence of finite internal losses $\gamma > 0$. Once the pump parameters are fixed we can characterize the bandwidth of the amplifier by analyzing the gain as a function of the signal detuning Δ . In Figure 4.4(b) we plot the gain as a function of Δ for the indicated values of ξ/ξ_{crit} and the corresponding optimal pump detunings δ (compare dashed white line in (a)). When the gain is increased, the band of amplification becomes narrower. This is quantitatively expressed by the gain bandwidth relation $\sqrt{G_0}B \approx 1$, where B is the detuning Δ for which the gain reaches half of its maximal value. Remember that Δ is defined in units of the resonator linewidth $\kappa + \gamma$, which means that the amplifier bandwidth equals approximately the resonator linewidth divided by the square root of the gain. The gain curves are well approximated by Lorentzian lines as indicated by the dashed black lines in Figure 4.4(b). This Lorentzian approximation becomes better with increasing gain.

The gain-bandwidth relation suggests that the amplifier bandwidth can be increased

by lowering the total quality factor of the resonator. There are, however, several technical challenges to overcome when increasing the bandwidth. One of them is closely related to the dynamic range of the amplifier. In the derivation made in the previous sections we have assumed that the solution of the classical drive field is unaffected by the additional signal and quantum fluctuations at the input. This is called the stiff pump approximation [Kamal09], which assumes that the pump power at the output is equal to the pump power at the input. This is of course an approximation, since the pump field provides the energy which is necessary for amplifying the additional signal. As a rule of thumb, the stiff pump approximation is valid as long as the pump power is more than 20 dB larger than the total output power of all amplified (quantum) signals [Castellanos-Beltran08]. The minimum amount of energy transfer from the pump field into other modes is set by the amplification of vacuum noise within the band of amplification. According to Eq. (4.18b) the integrated photon flux at the output of the paramp is equal to

$$P_{\text{out}} \stackrel{\gamma=0}{=} \hbar\omega_p\kappa \int d\Delta \langle a_{\text{out},\Delta}^\dagger a_{\text{out},\Delta} \rangle = \hbar\omega_p\kappa \int d\Delta (G_\Delta - 1), \quad (4.21)$$

when only vacuum fluctuations are incident at the sample. As an example, the realistic parameter configuration $\{\tilde{\omega}_0/2\pi, \kappa/2\pi, G_0\} = \{7 \text{ GHz}, 100 \text{ MHz}, 20\text{dB}\}$ corresponds to a power of amplified vacuum noise of about -100 dBm . If we want the pump power to be 20dB higher than this value, the Kerr nonlinearity $|K|/2\pi$ needs to be smaller than $\sim 10 \text{ kHz}$, which is calculated using Eq. (4.8). Consequently, the larger the amplifier bandwidth, the smaller the nonlinearity has to be.

When using the device as an amplifier, we also have to understand its behavior in terms of added noise. In the ideal case where the loss rate is zero ($\gamma = 0$), the input-output relation of the parametric amplifier in Eq. (4.18b) has the minimal form of a scattering mode amplifier [Clerk10]. The amplification process reaches the vacuum limit as long as the input modes are cooled into the vacuum. In practice, however, the device may have finite loss γ which increases the effectively added noise by a factor of $(\kappa + \gamma)/\kappa$. This is due to the additional amplified noise, which originates from the modes $b_{\text{in},\Delta}$ and contributes to the output field $a_{\text{out},\Delta}$ (compare Eq. (4.18b)). Another potential source of noise is related to the stability of the resonance frequency of the parametric amplifier. Magnetic flux noise in the SQUID loop may lead to a fluctuating resonance frequency and thus a fluctuating effective gain. In order to avoid such effects, one has to sufficiently reduce the coupling of the SQUID loop to the external flux.

4.3 Effective system parameters from distributed circuit model

In the previous section we have analyzed the model of a nonlinear resonator with resonance frequency $\tilde{\omega}_0$, Kerr nonlinearity K and decay rate κ . Here, we explicitly derive this effective Hamiltonian from the full circuit model of a $\lambda/4$ - transmission line resonator, which is terminated by a SQUID loop at the short-circuited end and coupled capacitively to a transmission line, see Figure 4.1(a). These calculations not only allow us to determine $\tilde{\omega}_0, K, \kappa$ from the distributed circuit parameters but give also insight into potential limitations of our effective model.

4.3.1 Resonator mode structure in the linear regime

In order to find the normal mode structure of our system we first neglect its capacitive coupling to the transmission line as indicated in Figure 4.5. Decay effects due the environment will be discussed separately in Section 4.3.4. The total Lagrangian of the system has – in addition to the transmission line part (compare Eq. (2.8)) – a term which describes the SQUID at position $x = d$, see Figure 4.5(a)-(c) and Ref. [Wallquist06].

$$\begin{aligned} \mathcal{L} = & \int_0^d dx \left\{ \frac{c}{2} (\partial_t \Phi(x))^2 - \frac{1}{2l} (\partial_x \Phi(x))^2 \right\} \\ & + E_J \cos \left(\frac{\Phi(d)}{\varphi_0} \right) \end{aligned} \quad (4.22)$$

Since we work in a limit where the Josephson energy is much larger than the charging energy we can neglect the capacitive contribution. The SQUID is furthermore described as a single junction with tunable effective Josephson energy E_J .

We first investigate the linear regime of the system, in which the cosine potential of the SQUID can be approximated as a quadratic potential.

$$E_J \cos \left(\frac{\Phi(d)}{\varphi_0} \right) \approx \text{const} - \frac{1}{2} \left(\frac{\Phi(d)}{\varphi_0} \right)^2 \quad (4.23)$$

Due to the spatial derivative appearing in the Lagrangian in Eq. (4.22) all local fields in the chain are coupled to their next neighbors and we have to find the normal mode structure by solving the Euler-Lagrange equation $\partial_t(\delta\mathcal{L}/\delta\dot{\Phi}) - \delta\mathcal{L}/\delta\Phi = 0$ of the

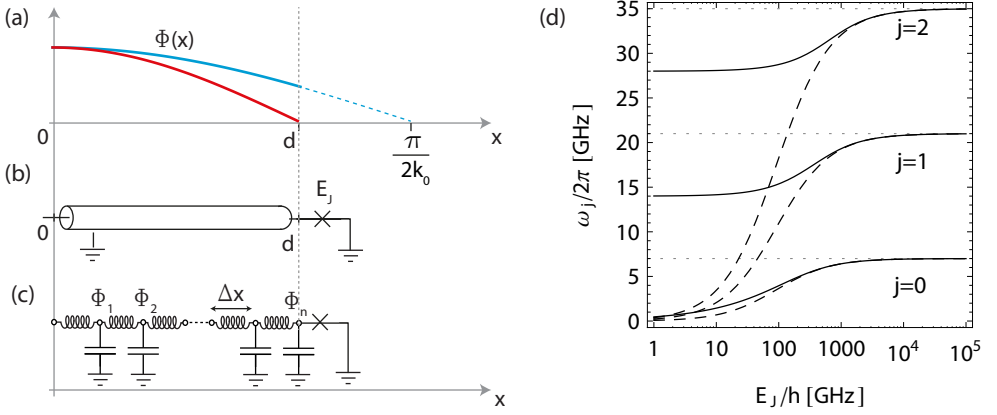


Figure 4.5: (a) Distribution of the magnetic flux field $\Phi(x)$ along the $\lambda/4$ -resonator for the fundamental resonator mode $j = 0$, without (red) and with (blue) a Josephson junction. The additional Josephson inductance changes the boundary condition such that neither the current nor the voltage is zero at position $x = d$. The resulting increase in the effective wavelength $\pi/(2k_0)$ is indicated by the dashed blue line. (b) Transmission line resonator of length d with a Josephson junction at the grounded end. (c) Lumped element representation with indicated discretized magnetic flux field Φ_j as used in Eq. (4.22). (d) Resonance frequencies of the first three modes as a function of Josephson energy. The solid line results from the exact numerical solution of Eq. (4.28) while the dashed line shows the linearized solution in Eq. (4.30). The bare resonance frequency is chosen to be 7 GHz and the impedance of the transmission line resonator 50 Ω .

transmission line resonator. This results in the wave equation⁴

$$v^2 \partial_x^2 \Phi(x) - \partial_t^2 \Phi(x) = 0, \quad (4.24)$$

with the phase velocity $v = 1/\sqrt{cl}$, of which the general solution can be written as a sum of normal modes

$$\Phi(x) = \sum_{j=0}^{\infty} \phi_j \cos(k_j x). \quad (4.25)$$

Up to here the solution is equivalent to the one for the open $\lambda/2$ transmission line resonator presented in Section 2.2.2. The difference between the two cases is due to their respective boundary conditions, which determine the valid wavevectors k_j . The open end at $x = 0$ requires that the current $\partial_x \Phi(x)/l$ vanishes, which is implicitly satisfied by choosing the cosine ansatz in Eq. (4.25). On the shorted end the boundary

⁴Note that for functional derivatives the identity $\frac{\delta}{\delta \Phi} \int dx (\partial_x \Phi(x))^2 = -2 \partial_x^2 \Phi(x)$ holds.

condition is modified by the presence of the Josephson junction. In order to determine this boundary condition, we have to evaluate the Euler-Lagrange equation at position $x = d$. For this purpose it is convenient to write the Lagrangian in a discretized form, see Figure 4.5(c) and compare Ref. [Wallquist06]:

$$\mathcal{L} = \lim_{n \rightarrow \infty} \sum_{j=1}^n \Delta x \left\{ \frac{c}{2} (\partial_t \Phi_j)^2 - \frac{1}{l} \frac{(\Phi_j - \Phi_{j-1})^2}{\Delta x^2} \right\} - \frac{1}{2} E_J \left(\frac{\Phi_n}{\varphi_0} \right)^2 \quad (4.26)$$

where $\Phi_n = \Phi(x = d)$ and $\Delta x = d/n$. Evaluating $\partial_t(\partial \mathcal{L} / \partial \dot{\Phi}_n) - \partial \mathcal{L} / \partial \Phi_n = 0$ leads to the equation

$$\frac{1}{l} \partial_x \Phi(d) + E_J \frac{\Phi(d)}{\varphi_0^2} = 0. \quad (4.27)$$

Substituting the normal ansatz Eq. (4.25) into this equation and comparing the resulting coefficients in front of the independent variables ϕ_j , results in the transcendental equation

$$k_j d \tan(k_j d) = l d \frac{E_J}{\varphi_0^2} \equiv \frac{l d}{L_J}. \quad (4.28)$$

Here, we have defined the Josephson inductance $L_J = \varphi_0^2 / E_J$. The infinite set of solutions k_j of this equation determines the normal modes structure of the system in the linear regime. In the limit where the SQUID inductance L_J vanishes, Eq. (4.28) is solved by the poles of $\tan(k_j d)$, and we recover the normal modes of the $\lambda/4$ resonator

$$k_j^{(0)} d = \frac{\pi}{2} (1 + 2j) \quad \text{with } j \in \{0, 1, 2, 3, \dots\}. \quad (4.29)$$

As a first order correction to this result in the limit of $L_J / l d \ll 1$, we expand Eq. (4.28) to first order in $(k_j^{(0)} - k_j) d$ and find $k_j L_J / l d = (k_j^{(0)} - k_j)$ or equivalently

$$k_j \approx \frac{k_j^{(0)}}{1 + L_J / l d}. \quad (4.30)$$

For the fundamental mode with $j = 0$ this linearized approximation is typically accurate even for inductance ratios up to $L_J / l d \approx 0.5$, whereas for the higher harmonic modes the linearized equation breaks down for much smaller values of $L_J / l d$. A comparison between the exact solution based on Eq. (4.28) and the approximate solution in Eq. (4.30) is shown in Figure 4.5(d) for the first three resonant modes.

When higher harmonics are expected to be relevant one should solve Eq. (4.28) numerically in order to determine the exact wave numbers k_j .

4.3.2 Kerr nonlinear terms and effective Hamiltonian

Using the normal mode decomposition in Eq. (4.25) we can reexpress the Lagrangian in Eq. (4.22) as a sum of oscillators which are only coupled via the boundary condition imposed by the SQUID. For our purposes the phase drop across the junction is typically small, $\Phi_n/\varphi_0 \ll 1$ (i.e. the current flowing through the Josephson junction is small compared to its critical current). We can therefore expand the SQUID cosine potential and take into account only the first non-quadratic correction

$$E_J \cos\left(\frac{\Phi_n}{\varphi_0}\right)^2 = \text{const} - \frac{1}{2}E_J\left(\frac{\Phi_n}{\varphi_0}\right)^2 + \frac{1}{24}E_J\left(\frac{\Phi_n}{\varphi_0}\right)^4 + \dots \quad (4.31)$$

Below we discuss under which circumstances such an approximation may break down. Substituting the normal mode decomposition Eq. (4.25) into the Taylor expansion of the Lagrangian results in

$$\mathcal{L} = \frac{1}{2} \sum_{i=1}^{\infty} \{\dot{\phi}_i C_i \dot{\phi}_i - \phi_i L_i^{-1} \phi_i\} + \sum_{j,i,k,l=1}^{\infty} N_{ijkl} \phi_i \phi_j \phi_k \phi_l \quad (4.32)$$

with the effective capacitances and inductances [Wallquist06]

$$\begin{aligned} C_i &= c \int_0^d dx \cos^2(k_i x) = \frac{cd}{2} \left(1 + \frac{\sin(2k_i d)}{2k_i d}\right), \\ L_i^{-1} &= L_J^{-1} \cos^2(k_i d) + \frac{k_i^2}{l} \int_0^d dx \sin^2(k_i x) \\ &\stackrel{4.28}{=} \frac{(k_i d)^2}{2ld} \left(1 + \frac{\sin(2k_i d)}{2k_i d}\right) \end{aligned} \quad (4.33)$$

and the nonlinearity coefficients

$$N_{ijkl} = \frac{1}{24} E_J \varphi_0^{-4} \prod_{m \in \{i,j,k,l\}} \cos(k_m d). \quad (4.34)$$

As expected the linear part of the Lagrangian is diagonal in the normal mode basis. It describes a set of uncoupled LC oscillators for which the effective resonance frequencies coincide with the product of phase velocity and wave vector $\omega_j = k_j v = 1/\sqrt{L_j C_j}$.

In the limit of vanishing Josephson inductance the effective capacitance is constant for all harmonic modes (compare pg. 275 of Ref. [Pozar93])

$$C_j \stackrel{L_j=0}{=} \frac{cd}{2} = \frac{\pi}{4Z_0\omega_{\text{TL}}}, \quad (4.35)$$

while the effective inductance reduces to

$$L_j \stackrel{L_j=0}{=} \frac{8ld}{\pi^2(1+2j)^2} = \frac{4Z_0}{\pi\omega_{\text{TL}}(1+2j)^2}. \quad (4.36)$$

Here, Z_0 is the impedance of the transmission line, which is typically 50Ω , and $\omega_{\text{TL}} = vk_0^{(0)}$ is the bare resonance frequency of the $\lambda/4$ transmission line resonator. The effective impedance of mode j is given by $\sqrt{L_j/C_j} = 2Z_0/\pi(1+2j)$.

Based on the Lagrange function in Eq. (4.32) we derive the Hamiltonian by introducing the conjugate charge variables $q_i = \delta\mathcal{L}/\delta\dot{\phi}_i = C_i\dot{\phi}_i$. Performing a Legendre transformation and taking only self-interactions and two-mode interactions into account, results in the Hamiltonian

$$\mathcal{H} = \frac{1}{2} \sum_{i=1}^{\infty} \{q_i C_i^{-1} q_i + \phi_i L_i^{-1} \phi_i\} - 3 \sum_{j \neq i}^{\infty} N_{ijj} \phi_i^2 \phi_j^2 - \sum_i^{\infty} N_{iii} \phi_i^4. \quad (4.37)$$

In a quantum regime q_i and ϕ_i are operators which satisfy the commutation relation $[\phi_j, q_i] = \delta_{ij}\hbar/i$ and it is convenient to write the Hamiltonian in terms of normal mode annihilation and creation operators

$$\phi_j = i\phi_{\text{zpf},j}(a_j^\dagger - a_j), \quad q_j = q_{\text{zpf},j}(a_j + a_j^\dagger) \quad (4.38)$$

with

$$q_{\text{zpf},i} = \sqrt{\frac{\hbar\omega_i C_i}{2}}, \quad \phi_{\text{zpf},i} = \sqrt{\frac{\hbar}{2\omega_i C_i}}. \quad (4.39)$$

The abbreviation zpf stands for zero point fluctuations. With the above definitions, the mode operators a_i obey bosonic commutation relations $[a_i, a_j^\dagger] = \delta_{i,j}$. Performing a rotating wave approximation (i.e. removing all terms with an unequal number of creation and annihilation operators), and neglecting the small photon number independent frequency shifts due to the nonlinear terms (i.e. Lamb shifts) we arrive at

$$\mathcal{H} = \hbar \sum_{i=1}^{\infty} \omega_i a_i^\dagger a_i + \frac{K_i}{2} a_i^\dagger a_i^\dagger a_i a_i + \sum_{j \neq i}^{\infty} \hbar K_{ij} a_i^\dagger a_i a_j^\dagger a_j. \quad (4.40)$$

with

$$\begin{aligned} K_i &= K_{ii} = -\frac{E_J}{2\hbar} \left(\frac{\phi_{zpf}}{\varphi_0} \right)^4 \cos^4(k_i d) \stackrel{4.30}{\approx} -\frac{E_J}{2\hbar} \left(\frac{\phi_{zpf}}{\varphi_0} \right)^4 \left(\frac{L_J}{ld} \right)^4 \propto E_J^{-3} \\ K_{ij} &= -\frac{E_J}{2\hbar} \left(\frac{\phi_{zpf}}{\varphi_0} \right)^4 \cos^2(k_i d) \cos^2(k_j d) \end{aligned} \quad (4.41)$$

The quantity $K = K_0$ is the Kerr nonlinearity of the fundamental mode, which is used for the parametric amplification process. The terms proportional to K_{ij} with unequal $i \neq j$ are cross Kerr interaction terms which couple different modes to each other. Such an interaction can for example be used for counting the number of photons in one mode by probing another one with a coherent field [Imoto85, Sanders89, Santamore04, Buks06, Helmer09, Johnson10, Suchoi10], similarly to a dispersive qubit measurement. Note that the values resulting from Eq. (4.41) have to be divided by the square of the number of SQUIDs, if an array is used instead of a single SQUID, as discussed in the following section.

4.3.3 Josephson junction arrays

For deriving the Hamiltonian in Eq. (4.40) we have expanded the SQUID cosine potential to quartic order in the dimensionless flux variable Φ_n/φ_0 where $\Phi_n \equiv \Phi(x = d)$. To guarantee that this approximation holds when we operate the device in the parametric amplification regime, we have to guarantee that Φ_n/φ_0 is small even close to the bifurcation point. Equivalently, we can ask, whether the current flowing through the SQUID loop at corresponding drive powers is small compared to the critical current.

To characterize the validity of the low order expansion of the cosine potential we define the critical coherent field inside the resonator α_{crit} as the one for which $\Phi_n \stackrel{!}{=} \varphi_0$. According to Eq. (4.38) and Eq. (4.25) a coherent field α in mode j leads to an maximal amplitude of $\Phi_n = \phi_{zpf,j} 2\alpha \cos(k_j d)$ across the junction, based on which we define the critical amplitude as

$$\alpha_{\text{crit},j} = \frac{\varphi_0}{\phi_{zpf,j}} \frac{1}{2 \cos(k_j d)} = \frac{\varphi_0}{\phi_{zpf,j}} \frac{ld}{2L_J k_j d \sin(k_j d)}. \quad (4.42)$$

The low order expansion of the SQUID cosine potential is only valid if the field inside the resonator α is always much smaller than this critical amplitude $\alpha \ll \alpha_{\text{crit}}$.

In Section 4.2.1 about the parametric amplifier response we have found that the photon number in a resonator mode at the bifurcation point is $N_{\text{bf}} = (\kappa + \gamma) / \sqrt{3}K$. The ratio between N_{bf} and the critical photon number $N_{\text{crit},j} \equiv |\alpha_{\text{crit},j}|^2$, which we would

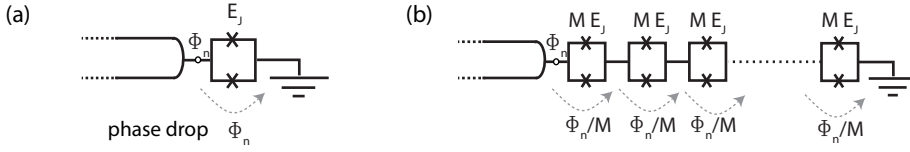


Figure 4.6: (a) The phase drop across a single SQUID junction is proportional to the node flux Φ_n (indicated by the circle) at the end of the transmission line. (b) If we replace the single junction by an serial array of M junctions with M times larger Josephson energy, the phase drop across each junction is by a factor of M smaller while the total effective Josephson inductance stays the same.

like to keep small, is given by

$$\begin{aligned} \frac{N_{\text{bf}}}{N_{\text{crit},j}} &= \frac{8\kappa}{\sqrt{3}} \frac{\hbar}{E_J \cos^2(k_j d)} \left(\frac{\varphi_0}{\phi_{\text{zpf}}} \right)^2 \\ &\approx \frac{8}{\sqrt{3}} Q^{-1} \frac{ld}{L_J}. \end{aligned} \quad (4.43)$$

The second line holds in the limit of small ratios $L_J \ll ld$. As we have pointed out earlier, the dynamic range of the parametric amplifier increases when the Kerr nonlinearity becomes smaller. Unfortunately this requires a large Josephson energy (i.e. small Josephson inductance) which increases the ratio $N_{\text{bf}}/N_{\text{crit}}$. Furthermore, $N_{\text{bf}}/N_{\text{crit}}$ increases linearly with κ , which makes it challenging to build a parametric amplifier with large bandwidth and high dynamic range at the same time using just a single SQUID.

However, by replacing the single SQUID with a serial array of M SQUIDs of M -times larger Josephson energy per SQUID (Figure 4.6), we can keep $N_{\text{bf}}/N_{\text{crit}}$ constant while decreasing the nonlinearity and thus increasing the dynamic range of the amplifier. For simplicity we assume that all SQUIDs in the array have the same effective Josephson energy ME_J . Since the spatial extent of the junction is still small compared to typical resonance wavelengths, we can treat the array as a lumped element. Let us investigate how the different terms in the Lagrangian scale with M .

Assuming that the phase drop from the flux node at the end of the transmission line resonator to the ground is homogeneously distributed over the array, we have the same phase drop Φ_n/M across each SQUID, see Figure 4.6. As a result the quadratic term in the Lagrangian scales as

$$\frac{E_J}{2} \Phi_n^2 \xrightarrow{1 \rightarrow M} \sum_{i=1}^M \frac{ME_J}{2} \left(\frac{\Phi_n}{M} \right)^2 = \frac{E_J}{2} \Phi_n^2 \quad (4.44)$$

and thus remains constant. This agrees with our expectation, since the total linear Josephson inductance has not been changed. However, the quartic term scales like

$$\frac{E_J}{24} \Phi_n^4 \xrightarrow{1 \rightarrow M} \sum_{i=1}^M \frac{ME_J}{24} \left(\frac{\Phi_n}{M} \right)^4 = \frac{1}{M^2} \frac{E_J}{24} \Phi_n^4, \quad (4.45)$$

which leads to a quadratic decrease in the effective Kerr nonlinearity and thus a quadratic increase in $N_{\text{bf}} \propto M^2$. Furthermore, the critical photon number scales also as $N_{\text{crit},j} \propto M^2$ since the critical current of each junction is larger by a factor of M . In other words, the ratio $N_{\text{bf}}/N_{\text{crit}}$ only depends on the total Josephson inductance whereas the bifurcation power increases quadratically in M . For parametric amplifier purposes we can thus conclude that it is advantageous to use an array of SQUIDS instead of a single SQUID.

In practice, the Josephson energies in the array are not all equal due to inhomogeneous coupling to the external magnetic flux. A quantitative analysis of the influence of such variations of Josephson energies on the parametric amplifier characteristics could be an interesting task for future studies. This would help to quantify limitations in the accessible tuning range of the parametric amplifier and a realistic understanding of the breakdown of the expansion of the cosine potential. For such an approach the methods used in Ref. [Ferguson13] could turn out to be useful.

4.3.4 Decay rate and resonance frequency correction for low Q resonators

Since the parametric amplifier bandwidth is proportional to the decay rate κ , typical devices are designed to have a low external quality factor, which is achieved by increasing the coupling capacitance C_κ between transmission line and resonator (Figure 4.1). As calculated in Section 2.2.3 the coupling of an oscillator to the environment shifts its resonance frequency $\omega_j \rightarrow \tilde{\omega}_j$ [Göppl08], which can be significant if the coupling rate is large. When designing parametric amplifier devices, it is therefore necessary to take these shifts into account. Based on the effective inductance and capacitances calculated in Eq. (4.33) and the formulas in Section 2.2.3 we find the approximate expressions

$$\tilde{\omega}_j^2 \approx \frac{\omega_j^2}{1 + C_\kappa/C_j} = \frac{1}{(C_j + C_\kappa)L_j} \quad \text{and} \quad \kappa_j \approx \frac{\tilde{\omega}_j^2 C_\kappa^2 R}{C_\kappa + C_j} \quad (4.46)$$

for resonance frequency and decay rate of the j 'th mode of the parametric amplifier device. The external quality factor is given by $Q_j \equiv \tilde{\omega}_j/\kappa_j$.

In summary, we have explicitly calculated the Kerr nonlinearity K , the resonance frequency $\tilde{\omega}_0$ and the decay rate κ for the specific circuit topology of a Josephson

parametric amplifier. We have established a model for the parametric amplifier properties in dependence on designable circuit parameters such as Josephson energy, transmission line length and coupling capacitance. Based on these consideration we have designed, fabricated and and characterized devices, as discussed in the following section.

4.4 Experimental characterization of parametric amplifiers

4.4.1 Tunability and (non-)linear response

We characterize the Josephson parametric amplifier by first measuring the reflection coefficient Γ in the low power regime for varying magnetic flux bias. To this aim we employ the setup in Figure 4.7, which allows for measuring both the absolute value as well as the phase of the reflection coefficient Γ . We thus achieve the performance of a network analyzer using signal generators, FPGA electronics and a *Labview* based measurement software.

When probing the device spectroscopically, the frequency of a probe field is swept within the range of interest, while keeping the local oscillator frequency at a fixed detuning from the probe field. The down-converted signal contains information about magnitude and phase of the signal reflected from the device. Since the phase of our microwave generators changes in a random fashion every time when the frequency is changed, we have to perform individual reference measurements to determine the relative phase between the local oscillator and the probe field. This is done by splitting both microwave fields into two parts. One part goes directly into the detection chain while the other part is transmitted to the device, from which it is reflected before entering the second channel of the detection chain (Figure 4.7). In both channels we sample the complex amplitudes $S_1 = X_1 + iP_1$ and $S_2 = X_2 + iP_2$ as introduced earlier.

Up to small amplitude variations due to frequency dependent attenuations in cables and components, the magnitude of the reference amplitude $|S_1|$ is almost constant over frequency. Since the phase of the probe signal is the same in both channels we can thus cancel it out by multiplying S_1 with the complex conjugate of S_2 before averaging. The remaining part is then proportional to the desired reflection coefficient. The product of S_1 and S_2^* has an additional phase factor, which originates from the relative propagation delay $\tau = \tau_2 - \tau_1$ in the two paths. In our setups this delay time is typically around ~ 20 ns, which corresponds to a 2π winding of the phase after a frequency change of 50 MHz. Since the dispersion relation of electromagnetic radiation in semi-rigid cables is linear, we can easily account for this phase by multiplying the measured $\langle S_1 S_2^* \rangle$ with $e^{i\omega\tau}$. The correct relative delay is either found by visual inspection and

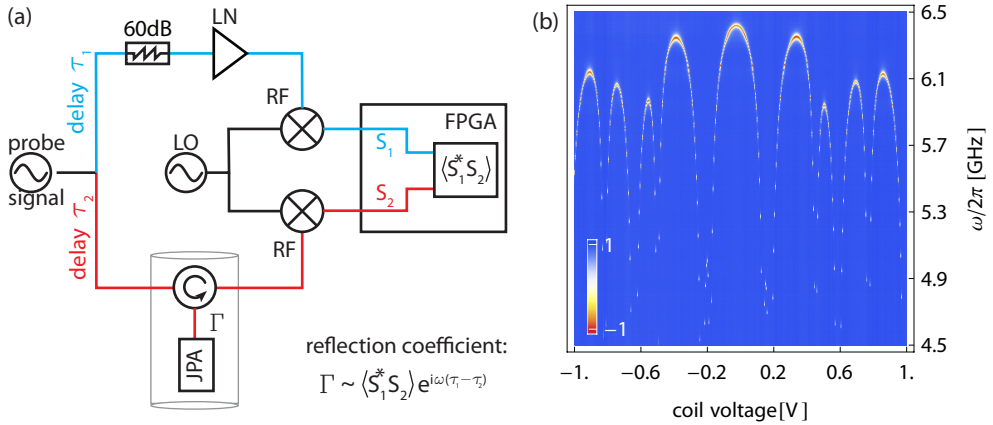


Figure 4.7: (a) Schematic of the measurement setup used for measuring the complex reflection coefficient Γ using microwave signal generators and FPGA electronics. (b) Real part of the measured reflection coefficient Γ for a parametric amplifier device with an array of three SQUIDs.

manual adjustment τ or by an algorithm, which minimizes the variance of the final phase values vs. frequency with respect to τ . Alternatively, we can tune the paramp resonance out of the relevant frequency range and measure a reference trace by which we divide all the other measurement data. This method achieves a cancelation of the phase factor $e^{i\omega\tau}$ and furthermore leads to a normalization of the data.

The result of such a measurement is shown in Figure 4.7(b) for a parametric amplifier device with an array of three SQUIDs. As expected, the resonance frequencies at which we see a strong change in the reflected signal, change with magnetic flux. Due to the inhomogeneous coupling of the SQUID loops to the external magnetic flux, each SQUID has its own periodicity. As a result, the individual periodicities interfere with each other and lead to the specific dependence of the resonance frequency on the applied magnetic field. In order to minimize the inhomogeneity in flux coupling we removed the ground plane in a region close to the resonator in our latest sample designs, see Figure 4.1(c). The cutout in the ground plane also reduces the overall coupling to the external magnetic field due to reduced flux focusing, which is desirable for the parametric amplifier devices, since the SQUID loops are typically much larger than for the small loops used in transmon qubits. A more detailed study of different ground plane geometries could help in further reducing the inhomogeneous flux coupling.

We further analyze the data shown in Figure 4.7(b) by fitting the real and imaginary part of the result to Eq. (4.9) for each B-field value. One example of such a fit is shown in Figure 4.8(a) together with the corresponding data set, from which we extract the resonance frequency $\tilde{\omega}_0 = 6.267$ GHz, the internal $Q_{\text{int}} = \tilde{\omega}_0/\gamma \approx 2500$ and the

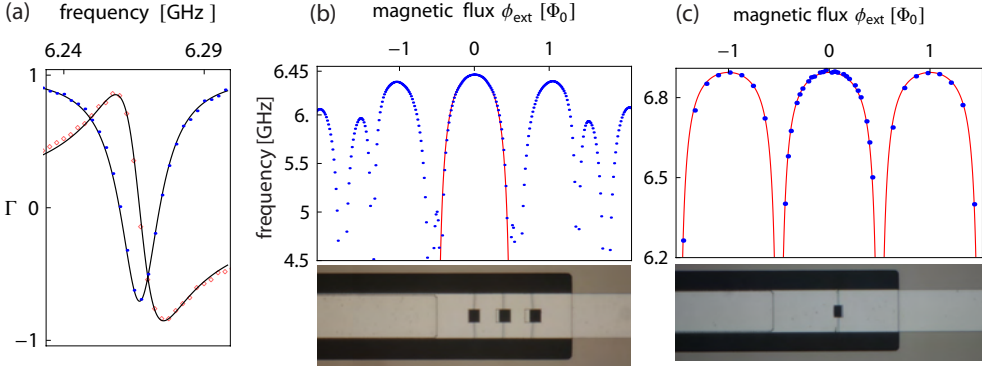


Figure 4.8: (a) Measured real (blue dots) and imaginary (red diamonds) parts of the reflection coefficient Γ in the linear regime for the flux bias $\phi_{\text{ext}} = 0.23$ and fit to theory (lines). (b,c) Extracted resonance frequencies vs. applied magnetic flux for a device with an array of three SQUIDs (b) and for a device with a single SQUID (c). The lines are fits to the theory from which we extract the effective Josephson energy of the SQUID (the SQUID array). Optical micrographs of the SQUIDs of both samples are shown in the bottom part of the figure.

external $Q_{\text{ext}} = \tilde{\omega}_0/\gamma \approx 430$ quality factors at this particular frequency. Performing such a fit for all magnetic flux bias values ϕ_{ext} , we extract the resonance frequency as a function of ϕ_{ext} , see Figure 4.8(b)-(c).

We fit this set of data to the model in Eq. (4.28) to determine the maximal effective Josephson energy $E_{J,\text{max}}$ of the SQUID (or the SQUID array). The transmission line inductance L , which is determined by the length and effective dielectric constant of the transmission line is kept fixed during this fit. For the particular device with an array of three SQUIDs we obtain $E_{J,\text{max}}/h \approx 1.3$ THz. This measured value has to be compared to one third of 5 THz, which was the value for E_J per SQUID we aimed for during the design and fabrication process. Using Eq. (4.41) we can also calculate the nonlinearity $K/\tilde{\omega}_0 \approx -1.1 \times 10^{-6}$ from the extracted effective Josephson energy and the number of SQUIDs in the array. For comparison, we also show the measured flux dependence of the resonance frequency for a single SQUID device in Figure 4.8(c). As expected, the resonance frequency periodically depends on the applied magnetic flux. The effective maximal Josephson energy for this device was extracted to be 4.9 THz.

Once we have characterized the device in the linear regime we tune the resonator to approximately $\sqrt{3}\kappa/2$ above the frequency at which we would like to achieve parametric amplification and probe the nonlinear reflection coefficient. In Figure 4.9(a) we show the measurement results and the fits to Eq. (4.9) for different measurement powers. For powers close to the critical point the effective resonance frequency is shifted to lower frequencies. Furthermore, the gradient of the phase of the reflected

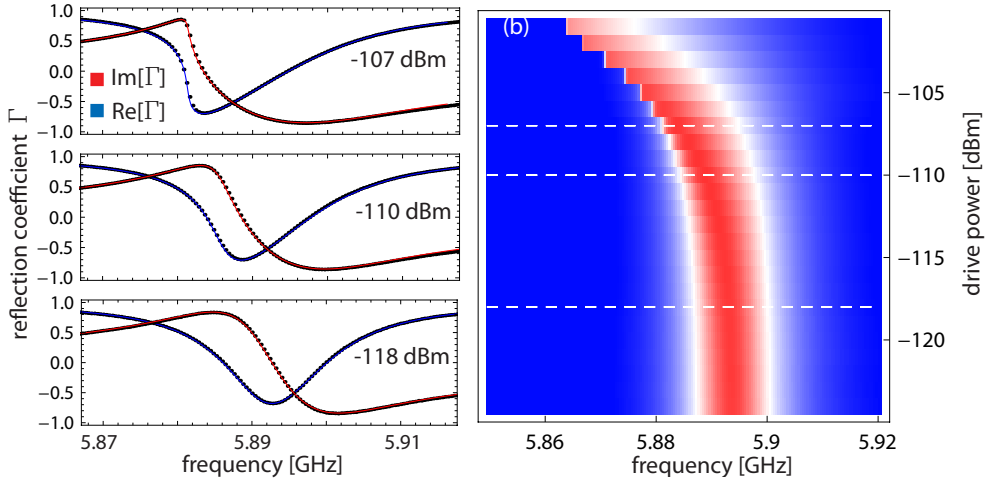


Figure 4.9: (a) Measurement of the reflection coefficient Γ in the nonlinear regime. Data points (black) and fit (solid lines) for real and imaginary part. (b) Real part of the measured reflection coefficient in a 2D color plot for all measured power values. The dashed lines indicate the traces shown in (a).

signal increases with frequency when approaching the critical point. As explained earlier, the device response is very sensitive to small external perturbations at this point, which can be used for their amplification. In Figure 4.9(b) we show the 2D density plot of the real part of Γ for all measured powers. The white dashed lines indicate the three cuts through this set of data which are shown in (a). The determined critical power is approximately $P_{\text{crit}} \approx -105$ dBm, which is in reasonable agreement with the expected value $P_{\text{crit}} = \hbar\omega_p(\kappa + \gamma)^3 / \sqrt{27\kappa|K|} = -107$ dBm, if we take into account the finite accuracy with which we have determined both the cable attenuation between sample and pump source as well as the Kerr nonlinearity K .

Using the sequence of measurements described in this section, we determine all relevant device parameters. The results are in very good agreement with the model presented in the previous sections even close to the bifurcation point where we expect parametric amplification to occur.

4.4.2 Gain measurements

When using the resonator as a parametric amplifier we apply a coherent pump tone, such that the device response becomes highly nonlinear. The frequency and power range in which we expect this to happen is specified by the measurements shown in Figure 4.9. In addition to the pump tone we apply a second coherent field acting as a test signal, which is slightly detuned from the pump and has a much smaller power –

typically 60 dB less than the pump. We detect the output of the parametric amplifier device for this combination of input fields and analyze its relevant frequency components individually, see Figure 4.10(a). From Eq. (4.18b) we expect the small signal power to be amplified by the factor $G_{\Delta} = |g_{S,\Delta}|^2$ and an additional tone with opposite detuning from the pump to be generated. This tone is called idler or intermodulation tone. We schematically visualize the described effects in Figure 4.10(b), by comparing the coherent parts of the power spectral densities at the input and at the output of the device. The energy required for the amplification of the signal and the creation of the idler tone is provided by the pump. The relative change in the pump amplitude is, however, negligible in the limit where the amplified signal power is much smaller than the pump power.

To extract the gain G_{Δ} from the change of the amplitude at the signal frequency we isolate this amplitude from the pump and idler tones. One possibility to do so is to record power spectral densities and to compare the coherent power at the signal frequency for the pump turned on and off. However, when measuring the gain as a function of various parameters (e.g. pump frequency, pump power, signal frequency, signal power, external magnetic flux) we aim for a technique which allows for a fast determination of the amplitude at exactly the signal frequency without evaluating and storing the whole power spectral density.

We achieve this in our experiments by using a specific filtering method, which ensures that both the pump and the idler frequency components drop out in the averaged down-converted signal. For the data acquisition we chose the local oscillator frequency such that the signal tone appears at DC after the down-conversion. We sample the down-converted and digitally filtered signal over $20.48 \mu\text{s}$ and take the time-average over all 2048 sample points. We repeat this measurement sequence every $25 \mu\text{s}$ (trigger time) and average all individual values to get the final complex amplitude, which corresponds to the mean coherent amplitude at the signal frequency. The pump detuning from the signal is chosen 10 kHz above or below a multiple of the inverse trigger time $1/25 \mu\text{s} = 40 \text{ kHz}$. Consequently, the pump tone changes its phase in every measurement trace by $\pi/2$ compared to the trace before. When averaging over many of these traces the pump tone thus cancels out. For the specific signal-pump detuning the idler frequency after down-conversion is 20 kHz detuned from a multiple of the trigger frequency 40 kHz and cancels out as well.

In a first experimental run we measure the maximum gain G_0 as a function of pump power and pump frequency by keeping the signal frequency at a fixed detuning of 10 kHz from the pump frequency. Since for all measured pump configurations this detuning is much smaller than the bandwidth of the parametric amplifier $10 \text{ kHz} \ll \kappa/\sqrt{G_0}$, it is valid to interpret this gain as the maximal one, for which the signal-pump detuning is essentially zero. The results of this measurement are shown in

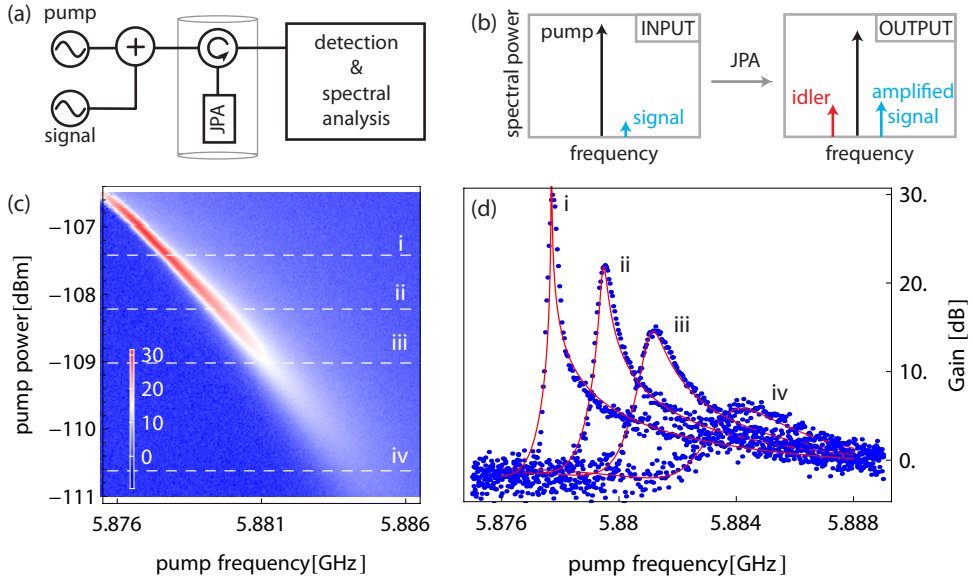


Figure 4.10: (a) Simplified schematic of the experimental setup, which is used for probing the gain properties of the parametric amplifier device. In addition to the pump tone we apply a weak signal field to the device. (b) Schematic of the expected power spectral densities at the input and output of the parametric amplifier shown without the noise contributions. (c) Measurement of the gain G_0 of the amplifier as a function of pump power and pump frequency for a fixed signal detuning of 10 kHz. The dashed white lines indicate the selected traces, which are shown in (d) together with individual fits to the theory. The data shown is measured on the sample with the array of three SQUIDs, see Figure 4.8.

Figure 4.10(c) where the four dashed white lines indicate the individual measurement traces shown in Figure 4.10(d). In agreement with the theoretical expectation we find a small region in parameter space for which amplification with high gain is possible. With increasing pump power the effective resonance frequency of the device shifts to lower frequencies and so does the optimal pump frequency. The fact that the gain can take values below 0 dB is explained by the finite internal losses of about $\gamma/(\kappa + \gamma) \approx 20\%$ for this particular sample.

In most realistic experiments, the signals which are to be amplified are not monochromatic but have a finite bandwidth. It is thus of central importance how the gain depends on the detuning of the signal from the pump. We measure this property by fixing the pump tone at a specific frequency and power, while changing the frequency of the weak signal field. Also in these experiments the detuning between signal and pump is set 10 kHz away from a multiple of the trigger frequency 40 kHz. In Figure 4.11(a) we show measurements of the gain as a function of the signal fre-

quency for three different pump powers. For each power value we have adjusted the pump frequency to achieve maximal gain. Consequently, the maximum of the gain curve, which is reached at minimal detuning from the pump, shifts to lower values with increasing pump power. We find the gain bandwidth product $\sqrt{G_0}B$ equal to the individually measured linewidth of the device, independent of the specific point of operation.

We have also measured the idler (i.e. intermodulation) gain $|g_{I,\Delta}|^2$ of the device by matching the local oscillator frequency to the frequency at which we expect the idler tone to appear. The resulting gain, which is evaluated as the ratio between the output power at the idler frequency and the power of the input signal is shown in Figure 4.11(b). In the limit of high gain, the relative difference between signal and idler gain vanishes and the measured curves appear almost identical. The measurement results are in good agreement with the theoretical prediction, which we have plotted using the same parameters as in (a).

The measurement of the idler gain indicates that signal and idler are strongly correlated. We further investigate these correlations by measuring the sum of signal and idler fields as a function of the phase of the pump tone ϕ . For this experiment we set the analog local oscillator frequency equal to the pump frequency and fix the detuning between signal and pump to 500 kHz. As a result, one of the output ports of the IQ mixer returns the sum of signal and idler fields at the carrier frequency at 500 kHz. The power at this frequency is therefore expected to be proportional to the correlated gain $|g_{S,\Delta}e^{i\phi} + g_{I,-\Delta}^*e^{-i\phi}|^2$. In the limit of large gain this expression is approximately proportional to a cosine function and becomes smaller than one for specific values of the pump phase. The signal is deamplified in this case, which we observe experimentally as shown in Figure 4.11(c). The presence of correlations between signal and idler frequency components can be used for using the device in a phase-sensitive mode where it amplifies one quadrature noiselessly while deamplifying the conjugate quadrature [Caves82]. Furthermore, it implies the possibility to squeeze noise below the vacuum limit [Castellanos-Beltran08, Eichler11a, Flurin12] as long as the input modes incident to the parametric amplifier device are cooled close to the vacuum noise level.

In summary, we have demonstrated a detailed spectroscopic characterization of parametric amplifier devices. Their properties are well-explained by the theory presented in Section 4.2. In the following section we explain how to operate the device either as a phase-sensitive or a phase-insensitive amplifier for (quantum) signals with a finite bandwidth.

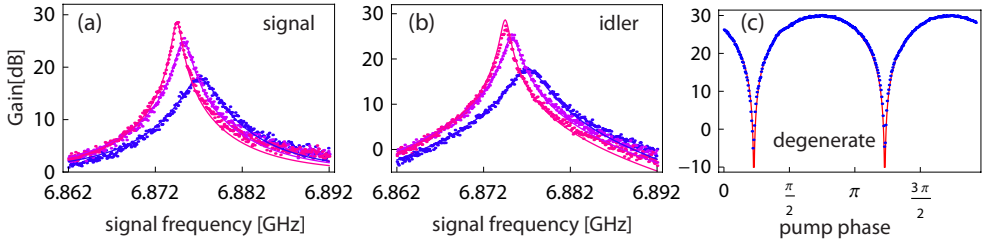


Figure 4.11: (a) Measurement of the signal gain as a function of signal frequency for three different pump configurations $P/P_{\text{crit}} = \{0.65, 0.82, 0.88\}$ and fit to theory (solid lines). (b) Measured and theoretically expected idler (intermodulation) gain for the same three pump configurations. (c) Correlated gain as a function of pump phase and fit to a cosine function.

4.4.3 Phase-sensitive and phase-insensitive mode of operation

The parametric amplification process mixes frequency components which have opposite detuning from the pump frequency. Due to this intermodulating property of the amplification process, we can operate the device in two qualitatively different regimes. The difference between the two is determined by the relative detuning between the pump frequency and the detected frequency window. If the detected frequencies are centered around the pump frequency the amplification is phase-sensitive (i.e. one quadrature of the field is amplified while the other one is deamplified). If we detect only frequency components which have either positive *or* negative detunings from the pump the amplification is phase-insensitive (i.e. phase-preserving). Both cases are schematically depicted in Figure 4.12.

We assume that the radiation, which is to be amplified, is described by the modes $a_{\text{out}}(t)$. The index "out" indicates that it originates from the output of a source, e.g. a single-sided resonator. Since this radiation typically has a finite bandwidth, the sampled output is convolved with a filter function $f(t)$ of appropriate bandwidth and shape to obtain a single pair of quadratures, as discussed in Section 3.2.2. Expressed in frequency domain, this quadrature pair is the result of a measurement performed on the sum of an effective noise mode and the following mode of interest

$$a = \int_{-\infty}^{\infty} d\Delta f_{\Delta} a_{\text{out},\Delta}. \quad (4.47)$$

Here, $a_{\text{out},\Delta}$ is the Fourier transform of output modes $a_{\text{out}}(t)$ as defined in Eq. (4.12) and f_{Δ} is the filter function in frequency domain, which is normalized such that $[a, a^{\dagger}] = 1$. For convenience we specify all frequencies by their detuning Δ from the pump frequency. If we consider the case in which the radiation is sent through a parametric amplifier before it is detected, the observed mode a is modified according

to the parametric amplifier transformation in Eq. (4.18b) to

$$a \xrightarrow{\text{JPA}} a_{\text{amp}} = \int_{-\infty}^{\infty} d\Delta f_{\Delta} \left(g_{S,\Delta} a_{\text{out},\Delta} + g_{I,\Delta} a_{\text{out},-\Delta}^{\dagger} \right), \quad (4.48)$$

For simplicity, we have neglected potential internal losses of the parametric amplifier here ($\gamma = 0$). Although this equation already describes the most general amplifier response, it is instructive to discuss two special choices of the pump frequency relative to the detection window f_{Δ} . In one case the amplifier acts as a phase-sensitive amplifier, while in the other case it acts as a phase-insensitive amplifier.

Phase-sensitive mode of operation: If we chose the detected band f_{Δ} such that it is centered around the pump frequency (compare Figure 4.12(a)) and furthermore chose the filter coefficients to be real $f(t) \in \mathbb{R}$, the identity $f_{\Delta} = f_{-\Delta}^*$ holds and the amplifier output in the detected band writes

$$\begin{aligned} a_{\text{amp}} &= \int_{-\infty}^{\infty} d\Delta \left(f_{\Delta} g_{S,\Delta} a_{\text{out},\Delta} + f_{-\Delta}^* g_{I,\Delta} a_{\text{out},-\Delta}^{\dagger} \right) \\ &= \int_{-\infty}^{\infty} d\Delta f_{\Delta} g_{S,\Delta} a_{\text{out},\Delta} + \left(\int_{-\infty}^{\infty} df_{\Delta} g_{I,-\Delta}^* a_{\text{out},\Delta} \right)^{\dagger}. \end{aligned} \quad (4.49)$$

If we further assume that the bandwidth of the amplifier is large compared to the width of the detected band, we can neglect the frequency dependence of the gain and approximate $g_{S,\Delta} \approx g_{S,0}$ and $g_{I,\Delta} \approx g_{I,0}$. Eq. (4.49) then simplifies to

$$\begin{aligned} a_{\text{amp}} &\approx g_{S,0} \int_{-\infty}^{\infty} d\Delta f_{\Delta} a_{\text{out},\Delta} + g_{I,0} \left(\int_{-\infty}^{\infty} df_{\Delta} a_{\text{out},\Delta} \right)^{\dagger} \\ &= g_{S,0} a + g_{I,0} a^{\dagger} \end{aligned} \quad (4.50)$$

With a proper choice of the pump phase and by dropping a global phase factor this last equation becomes

$$a_{\text{amp}} \approx \sqrt{G_0} a + \sqrt{G_0 - 1} a^{\dagger}, \quad (4.51)$$

which is identical to the generic single mode squeezing transformation, already introduced in Eq. (3.3). While in this mode of operation one quadrature of the field $X = (a + a^{\dagger})/2$ is amplified

$$X \xrightarrow{\text{JPA}} X_{\text{amp}} = \left(\sqrt{G_0} + \sqrt{G_0 - 1} \right) X \quad (4.52)$$

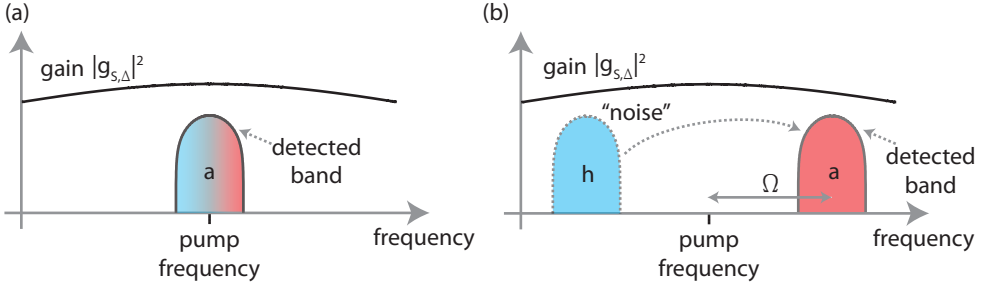


Figure 4.12: (a) Phase-sensitive regime, in which the detected frequencies – described by the filter function f_Δ – are symmetrically distributed around the pump frequency. Intermodulation during the parametric amplification process leads to an interference between frequency components with positive and negative detuning from the pump, which is the origin of the phase-sensitivity. The gain (black line) is assumed to be almost constant within the band of detection. (b) In a phase-insensitive mode of operation the detected frequency band (red area) is detuned from the pump frequency by amount Ω . The field at frequency components with opposite detuning from the pump (blue area), which carries at least the vacuum noise, is added to the field a during the parametric amplification.

the orthogonal quadrature $P = i(a^\dagger - a)/2$ is deamplified

$$P \xrightarrow{\text{JPA}} P_{\text{amp}} = \left(\sqrt{G_0} - \sqrt{G_0 - 1} \right) P. \quad (4.53)$$

The commutation relation is preserved under this transformation $[X_{\text{amp}}, P_{\text{amp}}] = [X, P] = i/2$. Since no additional mode is introduced, the amplification of the X quadrature is noiseless. The phase-sensitivity (i.e. quadrature dependence) of the amplification can be understood as an interference effect. Due to the parametric intermodulation the positive and the negative frequency components are phase correlated such that their sum interferes constructively in one quadrature and destructively in the orthogonal quadrature. Note that by changing the phase of the pump field we can choose any of the generalized quadratures $X_\phi \equiv (a^\dagger e^{i\phi} + a e^{-i\phi})/2$ to be amplified. Noiseless, phase-sensitive amplification schemes are particularly interesting for dispersive qubit readout where the qubit state can be encoded into one quadrature of a coherent readout field [Blais04] and for photon state tomography based on optical tomograms [Mallet11].

Phase-insensitive mode of operation: The photon field characterization methods presented in Chapter 3 were all based on the simultaneous detection of both conjugate field quadratures, which requires a phase-insensitive amplification chain. Also in many instances of practical relevance (e.g. basic sample characterization) it is convenient to operate the parametric amplifier in a regime where it amplifies both quadratures

equally. Although in this mode of operation a minimal amount of noise is added, the corresponding measurement still projects onto pure coherent states in the case of quantum-limited amplification as already discussed in Section 3.4.2. Consequently, this added noise is not necessarily accompanied by a loss of information. The acquired information is still complete in a sense that the post measurement state is pure.

In order to use the parametric amplifier as a phase-insensitive amplifier we chose an operation point at which the pump frequency is far detuned by Ω from the center of the detection band (Figure 4.12(b)). We consider the case indicated in Figure 4.12(b), in which only frequency components with positive detuning from the pump contribute to the detected field. To good approximation we can then write

$$a \approx \int_0^\infty d\Delta f_\Delta a_{\text{out},\Delta}. \quad (4.54)$$

and neglect the frequency components with negative detuning from the pump. Within this approximation the amplified and filtered mode can be expressed as

$$\begin{aligned} a_{\text{amp}} &= \int_0^\infty d\Delta f_\Delta g_{S,\Delta} a_{\text{out},\Delta} + f_\Delta g_{I,\Delta} a_{\text{out},-\Delta}^\dagger \\ &= \int_0^\infty d\Delta f_\Delta g_{S,\Delta} a_{\text{out},\Delta} + \int_{-\infty}^0 d\Delta f_{-\Delta} g_{I,-\Delta} a_{\text{out},\Delta}^\dagger \end{aligned} \quad (4.55)$$

Making again the assumption that the gain is almost constant within the relevant band of detection this further simplifies to

$$\begin{aligned} a_{\text{amp}} &\approx g_{S,\Omega} \int_0^\infty d\Delta f_\Delta a_{\text{out},\Delta} + g_{I,\Omega} \int_{-\infty}^0 d\Delta f_{-\Delta} a_{\text{out},\Delta}^\dagger \\ &= g_{S,\Omega} a + g_{I,\Omega} h^\dagger. \end{aligned} \quad (4.56)$$

with the definition $h = \int_{-\infty}^0 d\Delta f_{-\Delta}^* a_{\text{out},\Delta}$. In the limit of large detuning Ω between pump and detected frequency window, the overlap integral $\int d\Delta f_{-\Delta}^* f_\Delta \approx 0$ vanishes and consequently a and h are independent modes [$a, h^\dagger] \approx 0$. If the signal, which we would like to amplify, lies within the frequency range captured by mode a we can interpret mode h as an independent noise mode, which adds to the signal at the output of the amplifier (Figure 4.12(b)). The transformation in the second line of Eq. (4.56) is a two mode squeezing transformation, which describes a generic phase-insensitive linear amplification process. The additional noise in mode h^\dagger adds to the signal at the output of the amplifier and introduces at least the vacuum noise such that the simultaneous amplification of both quadratures of mode a satisfies Heisenberg's uncertainty relation and preserves the bosonic commutation relation $[a_{\text{amp}}, a_{\text{amp}}^\dagger] = [a, a^\dagger] = 1$.

In both cases we have for simplicity neglected the frequency dependence of the gain. If we relax this condition, all the general statements made above are still valid and the limited parametric amplifier bandwidth can be understood as an additional bandpass filter effect. If we aim for finding an optimal filter function f_Δ for a signal $a_{\text{out},\Delta}$ with known spectral shape we can take into account the frequency dependent gain, as well as the effective noise added during the following amplification stages, to maximize the overall detection efficiency.

4.5 Observation of two-mode squeezing in the microwave frequency domain

The described parametric amplifiers is expected to generate entangled photon pairs of frequencies $\omega_1/2\pi$ and $\omega_2/2\pi$ by annihilating two pump photons $2\omega_p = \omega_1 + \omega_2$. This four-wave mixing process even occurs, if only vacuum fluctuations are present at the input of the parametric amplifier [Castellanos-Beltran08, Mallet11]. The corresponding field modes a_1 and a_2 emitted from the single broadband resonator mode, which are separated in frequency space [Yonezawa07, Kamal09], are then described by a two-mode squeezed state. Alternatively, one can generate two-mode squeezing in two spatially separated modes as has recently been demonstrated [Flurin12, Menzel12]. The entanglement between created photon pairs is revealed in squeezing correlations between the two field modes. The measurement of such continuous variable correlations also provides a direct verification of the quantum limited nature of the parametric amplification process.

Continuous variable entanglement between two modes of a radiation field has until recently mostly been studied at optical frequencies. In this frequency range well-established multi-mode state reconstruction techniques based on single photon counters exist. These have already allowed for a variety of experiments in the context of the EPR paradox [Einstein35, Reid88, Ou92, Babichev04, Vasilyev00] and for the realization of continuous variable quantum computation, cryptography and teleportation experiments [Braunstein05, Furusawa98, Grosshans03].

Here, we apply the state reconstruction methods discussed in Section 3.3 to measure the covariance matrix of a two-mode squeezed state generated in a Josephson parametric amplifier. State tomography for more than a single mode of a radiation field allows to characterize photon sources that display entanglement between propagating photons, see Section 3.6. We first describe the measurement setup, discuss the device parameters, and characterize the system as a phase-insensitive amplifier. We then measure the covariance matrix and reconstruct the Gaussian Wigner function of the four quadrature components [Braunstein05].

4.5.1 Experimental Setup and system noise calibration

For the squeezing experiment we use a parametric amplifier with an array of three SQUIDs, for which we have already presented most of the characterization measurements in the previous sections (Figure 4.13(a)). The SQUID array has an effective Josephson energy of $E_{J,\max}/h \approx 1.3$ THz, which results in a maximal resonator frequency of $\tilde{\omega}_{0,\max}/2\pi \approx 6.4$ GHz. At the chosen flux bias we extract a resonance frequency of $\tilde{\omega}_{0,\max}/2\pi \approx 5.893$ GHz and an external coupling rate of $\kappa/2\pi \approx 15$ MHz which dominates over the internal loss $\gamma/2\pi \approx 2.5$ MHz. We identify the critical point where G_0 takes its largest value [Vijay09] at $\omega_{p,\text{crit}}/2\pi \approx 5.877$ GHz and $P_{p,\text{crit}} \approx -114$ dBm. For pump powers below $P_{p,\text{crit}}$ we are in the stable amplifier regime. A decrease in pump power leads to smaller gain but to larger amplifier bandwidth B . The gain-bandwidth product remains constant according to the relation $\sqrt{G_0}B \propto \kappa$ [Yurke06], which we have verified experimentally. For the following measurements we have fixed the coherent pump at $\omega_p/2\pi = 5.88275$ GHz and $P_p \approx -116.9$ dBm.

The signal frequency dependence of the gain G_Δ for this pump tone is shown in Figure 4.13(b), which is well fitted by the theoretical expectation (black line). To determine the effective system noise relative to the output of the parametric amplifier, we have also measured the noise power spectral density S_Δ [Lang11] and compare it with the gain curve G_Δ . The power spectral density can be decomposed into two contributions

$$S_\Delta \delta(\Delta - \Delta') = \langle h^\dagger(\Delta') h(\Delta) \rangle + \langle a_{\text{out}}(\Delta') a_{\text{out}}^\dagger(\Delta) \rangle. \quad (4.57)$$

The first term on the right hand side describes the system noise part which is dominated by the HEMT amplifier noise. In the relevant frequency range it is almost frequency independent and leads to a constant contribution of N_{noise} noise photons per Hz per second to S_Δ (Figure 4.13(b)). The second term in Eq. (4.57) stands for the noise at the output of the parametric amplifier. Since in the ideal case it can be interpreted as the amplified vacuum noise, the curves for G_Δ and $(S_\Delta - N_{\text{noise}})$ are expected to be close to identical. We can thus extract N_{noise} by scaling the measured power spectral density such that the measured gain curve G_Δ and the measured power spectral density are equal to each other up to the system noise offset N_{noise} . For our measurements, both data sets are well described by the same theoretical curve [Yurke06], see black lines in Figure 4.13(b) from which we determine the system noise number $N_{\text{noise}} \approx 48$. Note that our comparison between gain and power spectral density results in a lower bound for the system noise N_{noise} , because it is based on the assumption that only the minimal amount of noise (vacuum noise) is amplified. Both, finite internal losses and residual thermal noise at the input of the parametric amplifier cause an increase in the spectral power compared to the gain. Taking such imperfections into account

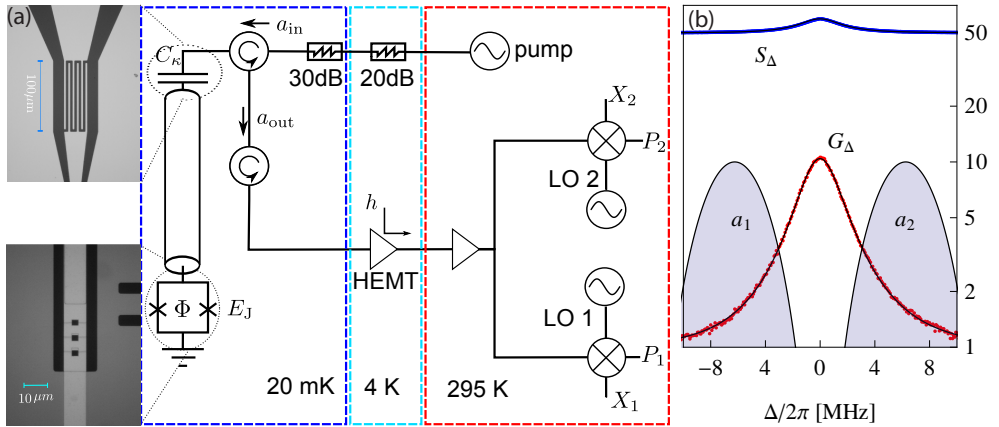


Figure 4.13: (a) Schematic of the experimental setup. The input and output modes of the parametric amplifier are separated using a circulator. Input modes a_{in} are in the vacuum state due to cold attenuators. The output signal is amplified by a cold HEMT amplifier at 4K, introducing the dominant part of additional system noise h . Mixing with two individual local oscillators at room temperature allows for a simultaneous detection of two distinct modes in frequency space. (b) Measured gain G_Δ (red dots) and power spectral density S_Δ (blue dots) for a fixed pump tone as a function of detuning Δ . The 3 dB bandwidth of the gain curve with a maximum gain of 10 dB is $B/2\pi \approx 3.6$ MHz. The Sinc Chebyshev filter functions $f_1(\Delta)$ and $f_2(\Delta)$, defining modes a_1 and a_2 , are shown on a logarithmic scale (arb. units) as the lines enclosing the shaded areas.

would consequently lead to a larger system noise number. Evaluating the following squeezing measurements on the strict lower bound for the system noise $N_{\text{noise}} \approx 48$ therefore guarantees, that the extracted amount of squeezing provides a minimal value.

4.5.2 Measuring correlations between signal and idler noise

Up to now we have characterized our device as a phase-insensitive amplifier. If the input of the parametric amplifier is in the vacuum, the output is amplified vacuum noise. However, due to the parametric nature of this amplification process, where signal and idler photons are always generated in pairs, we expect the signal and idler frequency noise to be strongly correlated. More specifically, the signal and idler output modes should approximately be described by a two-mode squeezed vacuum state. We verify this experimentally by pumping the resonator with the same coherent pump tone as before and recording the quadrature amplitudes in both modes individually.

The resonator output is amplified with the same HEMT amplifier as used for the gain measurements and split into two channels. To separate signal and idler frequency

components from each other (Figure 4.13) we effectively down-convert the microwaves in both channels by mixing them with local oscillator tones at frequencies $\omega_{LO1}/2\pi$ and $\omega_{LO2}/2\pi$ set 6.25 MHz above and below the pump frequency, respectively. The voltages are digitized every 10 ns with an analog to digital converter. Using a field programmable gate array the data is digitally filtered with a Sinc Chebyshev filter function $f(\Delta)$ as shown in Figure 4.13(b). As a result the two detection channels linearly detect photons with frequencies in the windows $f_1(\Delta) = f(\Delta - 2\pi \times 6.25\text{MHz})$ and $f_2(\Delta) = f(\Delta + 2\pi \times 6.25\text{MHz})$, respectively. The filter is designed such that both $f_1(0) = f_2(0) = 0$, rejecting the coherent pump tone.

As a result, the four quadrature components that we extract after the digital data processing correspond to measurement results of the complex valued operators (Section 3.2.1)

$$\hat{X}_{1,2} + i\hat{P}_{1,2} \equiv a_{1,2} + h_{1,2}^\dagger, \quad (4.58)$$

with $a_{1,2} = \int_{-\infty}^{\infty} d\Delta f_{1,2}(\Delta) a_{\text{out}}(\Delta)$ and $h_{1,2}$ equivalently. a_1 and a_2 describe a pair of signal and idler modes at the parametric amplifier output. The system noise modes h_1 and h_2 are in thermal states with mean photon number N_{noise} . We have verified this by measuring 2D quadrature histograms for the noise modes while turning off the pump tone, for which we observe perfectly circular symmetric Gaussian distributions [Eichler11b], see Figure 4.14(a).

According to Eq. (4.18b) we expect a_1 and a_2 to be approximately in a two-mode squeezed vacuum state $\exp\{ra_1a_2 - ra_1^\dagger a_2^\dagger\}|00\rangle$ [Braunstein05]. The relative phase between the two local oscillators has been chosen such that the squeezing parameter r is real and related to the average gain by $\cosh^2(r) \approx \int_{-\infty}^{\infty} d\Delta |f_1(\Delta)|^2 G_\Delta$.

The two-mode squeezed state is characterized by the covariances of the 4 quadrature components $\hat{\xi}_i \in \{\hat{x}_1, \hat{p}_1, \hat{x}_2, \hat{p}_2\}$ of the two modes, defined by $a_{1,2} = \hat{x}_{1,2} + i\hat{p}_{1,2}$. Quantum correlations for this state become most apparent in the relative "position" $\hat{x}_1 - \hat{x}_2$ and the total "momentum" $\hat{p}_1 + \hat{p}_2$ variables, which are squeezed below the standard vacuum limit 1/2 according to $\langle(\hat{x}_1 - \hat{x}_2)^2\rangle = \langle(\hat{p}_1 + \hat{p}_2)^2\rangle = e^{-2r}/2$, while each component itself is amplified $\langle\hat{\xi}_i^2\rangle = \cosh(2r)/4$. Since the two-mode squeezed state belongs to the class of Gaussian states, its Wigner function can be written as a multivariate normal distribution [Braunstein05]

$$W(\alpha) = \frac{1}{4\pi^2 \sqrt{\det \mathbf{V}}} \exp\left\{-\frac{1}{2} \alpha \mathbf{V}^{-1} \alpha^T\right\} \quad (4.59)$$

with the vector of quadrature components $\alpha = (x_1, p_1, x_2, p_2)$ and the quadrature covariance matrix \mathbf{V} with elements $V_{i,j} = \langle\hat{\xi}_i \hat{\xi}_j + \hat{\xi}_j \hat{\xi}_i\rangle/2$ [Braunstein05]. The two-mode phase space distribution is thus fully determined by the 4×4 covariance matrix \mathbf{V} , which describes the joint statistics of the amplitude fluctuations of the two modes.

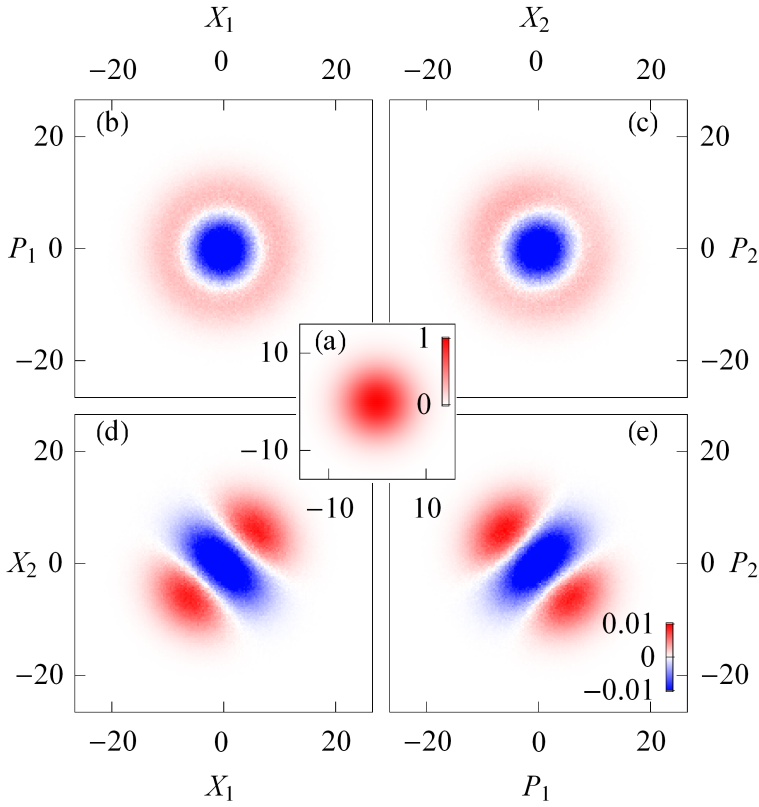


Figure 4.14: (a) Quadrature histogram $\{X_1, P_1\}$ when the pump tone is turned OFF given in units of its maximal value. (b)-(e) Difference between quadrature histograms with pump tone turned ON and OFF for 4 different quadrature pairs in the same units as (a).

To determine the elements of this matrix we detect the four quadrature components as explained above in Eq. (4.58) and store the results in two-dimensional histograms for the six possible pairs $\{X_1, P_1\}$, $\{X_2, P_2\}$, $\{X_1, P_2\}$, $\{X_2, P_1\}$, $\{X_1, X_2\}$, and $\{P_1, P_2\}$. For each pair we first acquire a reference histogram with the pump turned OFF (Figure 4.14(a)), which characterizes the quadrature distribution of the effective noise modes $h_{1,2}$ and a second histogram with the pump turned ON. The differences between such histogram pairs, see Figure 4.14, show a systematic change in the detected quadrature statistics when the resonator output in modes $a_{1,2}$ changes from the vacuum state to the state which is to be characterized. For the single mode histograms $\{X_1, P_1\}$, $\{X_2, P_2\}$ we observe a phase independent increase in the quadrature fluctuations, reflected in the higher probability of measuring larger quadrature values [Figure 4.14(b) and (c)]. Since the increase in fluctuations is circular symmetric it corresponds to a

phase-insensitive amplification in each of the individual modes a_1 and a_2 . However, for the cross-histograms $\{X_1, X_2\}, \{P_1, P_2\}$ we find an increase in the fluctuations along one diagonal axes, indicated by the positive valued regions in the histogram differences [Figure 4.14(d) and (e)], and a decrease in the other direction. Both these observed features are characteristic for a two-mode squeezed state.

The measured data is further analyzed by separating the contributions of noise modes $h_{1,2}$ from those of modes $a_{1,2}$. We calculate all possible expectation values $\langle \hat{X}_i \hat{X}_j \rangle_{\text{ON,OFF}}$ and $\langle \hat{X}_i \hat{P}_j \rangle_{\text{ON,OFF}}$ from the 12 measured pump ON and OFF histograms. Using relations such as $\langle \hat{x}_1^2 \rangle = \langle \hat{X}_1^2 \rangle_{\text{ON}} - \langle \hat{X}_1^2 \rangle_{\text{OFF}} + 1/4$, which follow from Eq. (4.58), we can determine all second order expectation values $V_{i,j}$.

The result for the covariance matrix is shown in Figure 4.15(a). Its diagonal elements express the amplified individual quadrature fluctuations in both modes. Their values are in good agreement with what we expect from the measured gain averaged over the filter function. The non-vanishing off-diagonal elements describe the squeezing correlations between the two modes and are important to demonstrate that the signal and idler photons are entangled. As a criterion for non-classicality we determine the total "momentum" fluctuations $\langle (\hat{p}_1 + \hat{p}_2)^2 \rangle$ and the relative "position" fluctuations $\langle (\hat{x}_1 - \hat{x}_2)^2 \rangle$, where we find both values squeezed below the standard quantum limit by -2.25 ± 0.16 dB and -1.89 ± 0.13 dB, respectively. In addition, we have verified that our measured covariance matrix fulfills the non-separability criterion formulated in [Simon00].

We have further checked the influence of finite thermal fluctuations on the presented results. In independent experiments [Fink10b] we have found $\bar{n} \approx 0.05$ as an upper bound for the thermal noise photon number at the input of the resonator. Evaluating our measurement data, taking this amount of thermal fluctuations into account, results in a reduction of the vacuum squeezing by only 10%. The amount of squeezing, that we have reached after optimizing the pump parameters, is limited by (i) the minimal filter bandwidth that can be implemented to detect the photons, (ii) the uncorrelated noise added by the parametric amplifier due to internal losses, and (iii) the phase-stability, which restricts us to operate the parametric amplifier at a point at which it has relatively small gain [Castellanos-Beltran08].

We evaluate Eq. (4.59) to reconstruct the four-dimensional Wigner function $W(\alpha)$ for the two modes. In Figure 4.15(b) and (d) we show a selection of characteristic projections of $W(\alpha)$ on two-dimensional subspaces. The $\{x_1, p_1\}$ -projection, which describes the individual state of mode a_1 , is amplified vacuum as expected. Compared to the theoretical vacuum Wigner function [Figure 4.15(c)] it has a larger variance, indicating the phase-insensitive amplification of vacuum noise. The $\{x_1, x_2\}$ -projection is squeezed along the diagonal axis, visualizing the 2-mode squeezing correlations between a_1 and a_2 .

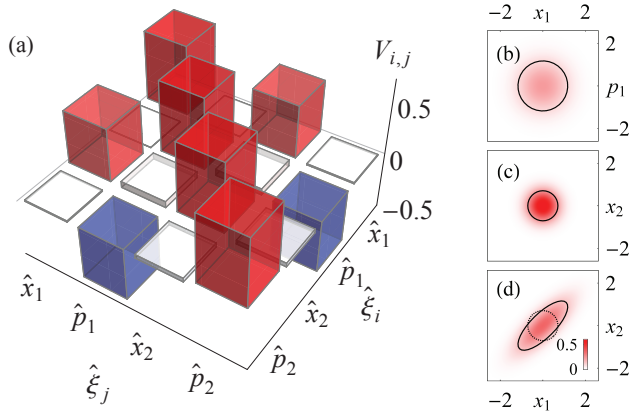


Figure 4.15: (a) Measured quadrature covariance matrix \mathbf{V} of the two-mode squeezed state which allows to reconstruct the four-dimensional Wigner function. (b) and (d) show projections of this function onto two-dimensional subspaces where the ellipses indicate the respective standard deviations. (c) For comparison, we show the theoretical Wigner function of a vacuum state and its corresponding standard deviation as a dashed circle also in (d).

In summary, we have measured the full quadrature covariance matrix of a two-mode squeezed state and observed a reduction of quadrature noise in the variables $\hat{x}_1 - \hat{x}_2$ and $\hat{p}_1 + \hat{p}_2$ by approximately -2 dB below the standard quantum limit. This value can be increased by realizing a parametric amplifier with larger bandwidth, which furthermore allows for using the device as a low noise amplifier in other circuit QED experiments (see Chapter 5). An important step towards future continuous variable quantum computation with propagating microwave photons [Braunstein05] could be a combination of parametric amplifiers with beamsplitters to spatially separate signal and idler modes and create non-local entanglement [Menzel12].

Entanglement between a superconducting qubit and propagating microwave fields

A localized qubit entangled with a propagating quantum field is well suited to study nonlocal aspects of quantum mechanics and may also provide a channel to communicate between spatially separated nodes in a quantum network. Here, we report the on demand generation and characterization of Bell-type entangled states between a superconducting qubit and propagating microwave fields composed of zero, one and two-photon Fock states. Using low noise linear amplification and efficient data acquisition we extract all relevant correlations between the qubit and the photon states and demonstrate entanglement with high fidelity.

5.1 Entanglement with single microwave photons

One of the most fascinating aspects of quantum physics is the entanglement between two spatially separated objects sharing a common nonlocal wave function. Propagating photons are ideal carriers for distributing such entanglement between distant matter systems in a quantum network. Entanglement between photons and stationary qubits has so far been exclusively studied at optical frequencies with single atoms [Blinov04, Volz06, Stute12] and electron spins [Togan10, Gao12, De Greve12], to interface stationary and flying qubits [Wilk07], to implement quantum teleportation [Olmschenk09, Moehring04] and to realize nodes for quantum repeaters [Yuan08] and networks [Ritter12, Kimble08, Moehring07]. Rapid progress in the development

of superconducting circuit based quantum technologies also renders propagating [Houck07, Bozyigit11, Mallet11, Eichler11b, Menzel10, Wilson11, Hoi12, Flurin12] and localized microwave photons [Haroche06, Hofheinz09] an attractive carrier of quantum information. A major obstacle in measuring quantum correlations between superconducting artificial atoms and itinerant photons has so far been the limited detection efficiency at microwave frequencies. Here, we overcome this problem by using a quantum limited parametric amplifier, as presented in Chapter 4, which significantly improves the signal-to-noise ratio in both photon field and qubit measurement. In combination with novel tomography methods, see Chapter 3, this allows us to measure quantum correlations between itinerant microwave radiation and a stationary qubit with high fidelity.

5.1.1 Experimental setup and generation of photon/qubit entanglement

In a first experiment we create entangled states between a superconducting transmon qubit and a single propagating microwave photon. The corresponding field a can be described by two canonically conjugate variables X and P analogous to the position and momentum variables of a mechanical quantum harmonic oscillator, as discussed in Section 3.2.1. In contrast to most experiments performed at optical frequencies, we simultaneously measure both continuous variables X and P rather than the photon number of the field. This enables us to fully characterize quantum fields also beyond the single photon level. In addition to the measurement of photon statistics of the field, we determine the correlations between the measured qubit state and the observed values X and P which clearly demonstrate that the qubit is entangled with the quantum field.

We deterministically prepare 1.25×10^5 Bell states of the form $|\psi\rangle = (|0e\rangle + |1g\rangle) / \sqrt{2}$ per second, in which a single excitation is shared coherently between a qubit and a single propagating mode of a radiation field. Here, $|g\rangle, |e\rangle$ label the qubit basis states and $|0\rangle, |1\rangle, |2\rangle, \dots$ the photon number states. To entangle the qubit and the radiation field we first bring the qubit from the ground state $|0g\rangle$ to the excited state $|0e\rangle$ by applying a 10 ns long π -pulse resonant with its transition frequency $\omega_{ge}/2\pi = 6.442$ GHz. By applying a magnetic flux pulse we then tune the qubit into resonance with a transmission line resonator at frequency $\omega_r/2\pi = 7.133$ GHz, which is strongly coupled to the qubit with rate $g/2\pi = 65$ MHz. After an interaction time of $\tau = \pi/4g \approx 2$ ns we obtain the state $(|0e\rangle + |1g\rangle) / \sqrt{2}$ up to a phase factor which is omitted here for convenience.

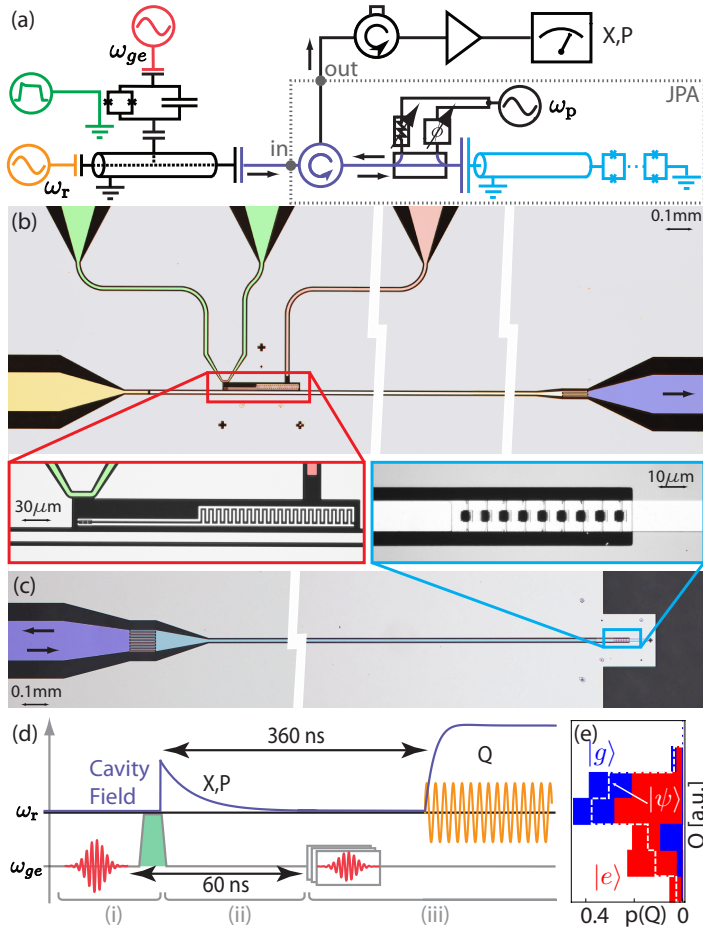


Figure 5.1: Schematic of the experimental setup. (a) A transmon qubit with individual charge drive line (red) at frequency ω_{ge} and flux control line (green) is strongly coupled to a resonator with a weakly coupled input port ($\gamma_{in}/\kappa \approx 0.001$) driven at frequency ω_r for qubit readout (orange). The output field is coupled with rate κ into a transmission line (violet) and amplified with a Josephson parametric amplifier (light blue) pumped at ω_p through a directional coupler with adjustable phase and attenuation for pump tone cancelation. The signal reflected off the parametric amplifier passes through a chain of circulators into a low-noise semiconductor-amplifier after which its two quadratures X, P are detected. (b) False color optical micrograph of the sample. The transmon qubit (enlarged) consists of two capacitively coupled islands connected by a pair of Josephson junctions. (c) False color micrograph of the Josephson parametric amplifier. The array of Josephson junctions (enlarged) at the end of the quarter wavelength resonator (light blue) provides the nonlinearity. (d) Pulse sequence used for the experiment: (i) state preparation, (ii) field measurement and (iii) qubit read-out (see text for details). (e) Measured probability distribution $p(Q)$ of the qubit read-out quadrature Q for prepared ground (blue), excited (red) and Bell (dashed white) states.

The setup employed for this experiment is shown schematically in Figure 5.1(a) with a micrograph of the sample shown in (b) and the experimental sequence in (d). While the qubit on average keeps its excitation during its life time $T_1 = 1.0 \mu s$, the resonator field is emitted during the much shorter cavity decay time of $1/\kappa = 25$ ns. Note that, the interaction time τ during state preparation is small compared to $1/\kappa$, which itself is small compared to the qubit life and coherence times ($T_2^* = 220$ ns). This hierarchy of timescales ($1/g < 1/\kappa < T_1, T_2^*$) guarantees that the entangled state can be coherently prepared, and that the qubit remains in the excited state while the photon is emitted into the propagating transmission line mode a of which both conjugate field quadratures X and P are detected (Figure 5.1(d)). We have thus created a superposition state, in which the single excitation is kept by the qubit and emitted into the transmission line at the same time.

5.1.2 Parametric amplification and detection

We measure the quadratures X and P using a parametric amplifier operating close to the quantum limit [Castellanos-Beltran08]. The amplifier is based on a quarter wave transmission line resonator shunted by an array of Josephson junctions providing the Kerr nonlinearity used in the parametric amplification process (Chapter 4), see Figure 5.1(c). The maximal resonance frequency of the parametric amplifier is $\tilde{\omega}_{0,\max} = 7.5$ GHz and the effective Josephson energy of the array of SQUIDs is $E_{J,\max}/h \approx 520$ GHz. Both values are extract from the measurement data shown in Figure 5.2(a). The quality factor of the device is approximately $Q \approx 30$ in the relevant frequency range, as shown in Figure 5.2(b). Based on the extracted device parameters and the number of SQUIDs in the array, we calculate the approximate Kerr nonlinearity $K/\tilde{\omega}_{0,\max} \approx -2 \times 10^{-6}$ at the maximal resonance frequency.

In our experiment we operate the parametric amplifier in a phase-preserving mode, in which both conjugate field quadratures are amplified equally as discussed in Section 4.4.3. This is achieved by pumping the amplifier at a frequency 12.5 MHz detuned from the center frequency of the detected photon pulse $\omega_r/2\pi$. The measured gain for varying signal detunings from the pump frequency is shown in Figure 5.2(c) for the chosen operation point. To determine the band pass filter effect caused by the parametric amplifier, we have not only measured the absolute value of the gain, but also the phase of the amplified test signal. From this measurement we extract both the real and imaginary part of the gain coefficient $g_{S,\Delta}$, compare Eq. (4.19). At the center frequency of the radiation field to be detected (see dashed line in (c)), the parametric amplifier has a relatively moderate gain of $G(\omega_r) = 16.5$ dB. In this regime, the effective detection efficiency is an order of magnitude higher than for typical setups using transistor based amplifiers only, as discussed in more detail in Appendix A.6.

After amplification, we record the time dependent quadrature amplitudes $\{X(t), P(t)\}$

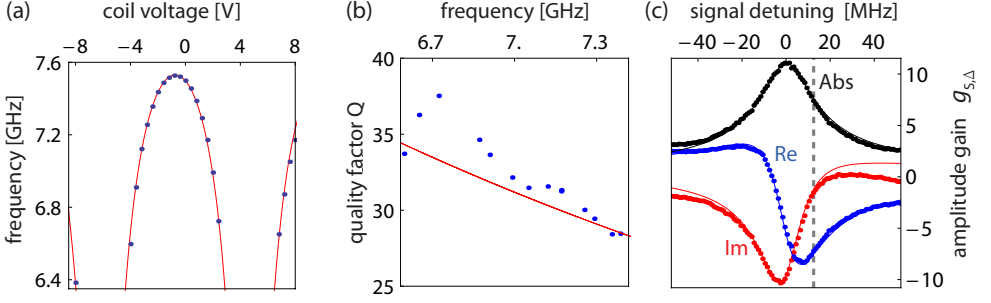


Figure 5.2: (a) Measured resonance frequency of the parametric amplifier for varying magnetic flux bias voltage (blues dots) and fit to theory (red line). (b) Measured quality factor Q as a function of resonance frequency (blue dots) and expectation (red line) based on the extracted Josephson energy $E_{J,\max}$, the simulated coupling capacitance C_κ , and using Eq. (4.46). (c) Measured absolute value, real and imaginary part of the complex amplitude gain $g_{S,\Delta}$ and fit to the theoretical expectation (solids lines) in Eq. (4.19).

of the single photon field in a microwave frequency heterodyne detection setup, see Section 2.4.3. Performing temporal mode matching by convolving $\{X(t), P(t)\}$ with an appropriate filter function (Section 3.2.2), we retain one pair of values $\{X, P\}$ per generated Bell state. After the field detection we perform qubit state tomography (Figure 5.1(d)). We measure the qubit Bloch vector components $\langle\sigma_x\rangle$, $\langle\sigma_y\rangle$ and $\langle\sigma_z\rangle$ by rotating the qubit into the respective eigenbasis and then applying a coherent read-out tone to the resonator. Due to the dispersive resonator frequency shift of $\chi/2\pi = 2.1$ MHz the integrated phase quadrature Q of the transmitted time-dependent signal $Q(t)$ depends on the measured qubit state [Wallraff05, Gambetta07, Bianchetti09], as explained in Section 5.3 in more detail. The probability distribution $p(Q)$ is fitted to a weighted sum of two independently measured reference distributions for the ground and excited state to extract the excited state population in the chosen basis (Figure 5.1(e)). Due to qubit decay during the time required for the measurement of photon field quadratures after preparation of the entangled state, the single-shot qubit readout fidelity making use of the same mode is limited to 37%. In future experiments this aspect could be improved by using separate modes for photon generation and qubit read-out, similar to Ref. [Leek10].

5.1.3 Measurement of photon-qubit correlations

We extract the correlations between qubit and photon in the generated Bell states by recording 3-dimensional histograms of triplets $\{X, P, Q\}$, which count the number of times for which the qubit read-out quadrature Q is measured in combination with photon field quadratures X and P . Within the limitations of the available memory, we

chose to discretize the histograms into 128×128 bins for the measured photon field quadratures times 8 bins for the measured qubit quadrature. Efficient data acquisition and generation of histograms is realized in real-time using field programmable gate array electronics [Bozyigit11]. The resulting data, which is obtained after preparation and detection of $\sim 3 \times 10^8$ Bell states, contains complete information about the photon statistics as well as all relevant qubit-photon correlations. From the measured histograms we extract the qubit population for each quadrature pair $\{X, P\}$ by fitting the histogram columns along the Q axis to the two reference histograms shown in Figure 5.1(e).

Preparing two reference states $|0g\rangle$ and $|0e\rangle$ – for which the photon field is left in the vacuum state and thus is not correlated with the qubit – we find that the qubit population (blue: ground state, red: excited state) is independent of the detected field quadratures X and P (see Figure 5.3(a,b)). This also indicates that there are no correlations of technical origin between the qubit and photon field measurements. The standard deviation of the photon field distribution $\delta_m = 1.84$ is larger than the quantum limit $1/\sqrt{2}$, due to noise added by the amplifiers, losses in the cables and microwave components, as well as finite mode matching efficiency, the combination of which corresponds to an effective detection efficiency of $\eta = 15\%$ (see Section A.6 for details). Individual measurement results with large amplitude values ($\sqrt{X^2 + P^2} \gtrsim 3\delta_m$) are unlikely, which causes the larger statistical uncertainty in the extracted qubit populations at the boundary of the colored regions.

When Bell states $|\psi\rangle = (|0e\rangle + |1g\rangle)/\sqrt{2}$ are prepared we find a clear dependence of the measured qubit Bloch vector on the measured field quadratures $\{X, P\}$ (Figure 5.3(c)-(e)), in stark contrast to the results obtained for separable states. Measuring the qubit in the σ_z basis we find a higher probability to observe the qubit in its ground state at large measured field amplitudes (blue region) and a higher probability to find the qubit in the excited state at small measured field amplitudes (red region in Figure 5.3(c)). This observation is consistent with the expectation to either find the qubit in the ground state when a photon is propagating in mode a or in the excited state when a is in the vacuum state resulting in correspondingly small field amplitudes. The fact that the measured qubit population is circularly symmetric in phase space, i.e. it is independent of the phase of the propagating field, indicates that $|g\rangle$ and $|e\rangle$ are correlated with Fock states – such as the single photon or the vacuum state.

To distinguish the coherent superposition of $|0e\rangle$ and $|1g\rangle$ in the Bell state from a mere statistical mixture, we measure the equatorial components $\langle\sigma_x\rangle$ and $\langle\sigma_y\rangle$ of the qubit Bloch vector by applying $\pi/2$ pulses to the qubit about the corresponding axes and determine their correlations with the measured radiation field. We find that whenever a positive field quadrature $X > 0$ is measured the qubit is more likely to be found in a state with positive $\langle\sigma_x\rangle$ (blue region) and vice versa for negative values

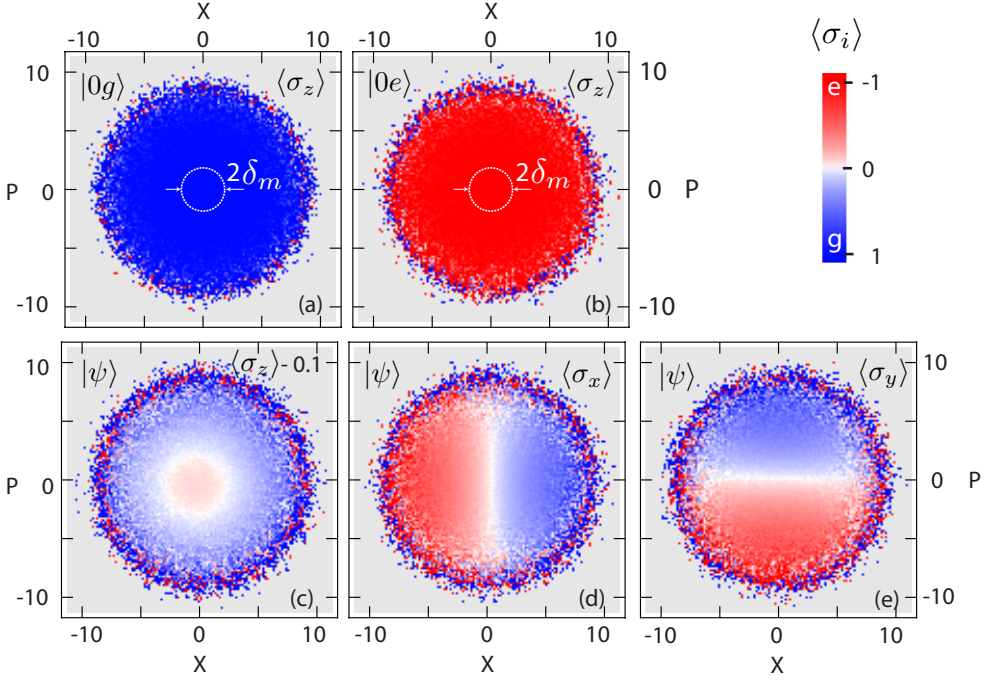


Figure 5.3: Photon-qubit correlations for a prepared Bell state. Qubit state population conditioned on the measured photon field quadratures X and P for the indicated Bloch vector components. $\{X, P\}$ pairs for which no measurement results occurred are shown in gray. White circles indicate the standard deviation of the photon field distribution δ_m . (a)-(c) $\langle\sigma_z\rangle$ for the reference states $|0g\rangle$, $|0e\rangle$ and the Bell state $|\psi\rangle$. For better visibility only, the data in subpanel (c) is offset by its total mean ≈ 0.1 compensating for the qubit decay during photon detection. (d)-(e) $\langle\sigma_x\rangle$ and $\langle\sigma_y\rangle$ for the Bell state $|\psi\rangle$.

(red region in Figure 5.3(d)). This observation can be understood, when rewriting the Bell state $|\psi\rangle = [(|0\rangle + |1\rangle)|g_x\rangle + (|1\rangle - |0\rangle)|e_x\rangle]/2$ in the eigenbasis $\{|g_x\rangle, |e_x\rangle\}$ of the measurement observable σ_x : We note that for the field component $(|0\rangle + |1\rangle)$ we find $\langle X \rangle > 0$ which is correlated with the state $|g_x\rangle$, while $|e_x\rangle$ is correlated with $(|0\rangle - |1\rangle)$ for which $\langle X \rangle < 0$. Equivalently, the $\langle\sigma_y\rangle$ component is correlated with the sign of the P quadrature measurement as shown in Figure 5.3(e).

5.1.4 Analysis of entanglement correlations and state reconstruction

Already in the raw measurement data we clearly observe the expected qubit-photon correlations including their phase coherence. In order to further quantify the properties of the prepared Bell state we evaluate the statistical moments $\langle (a^\dagger)^n a^m \sigma_i \rangle$ from

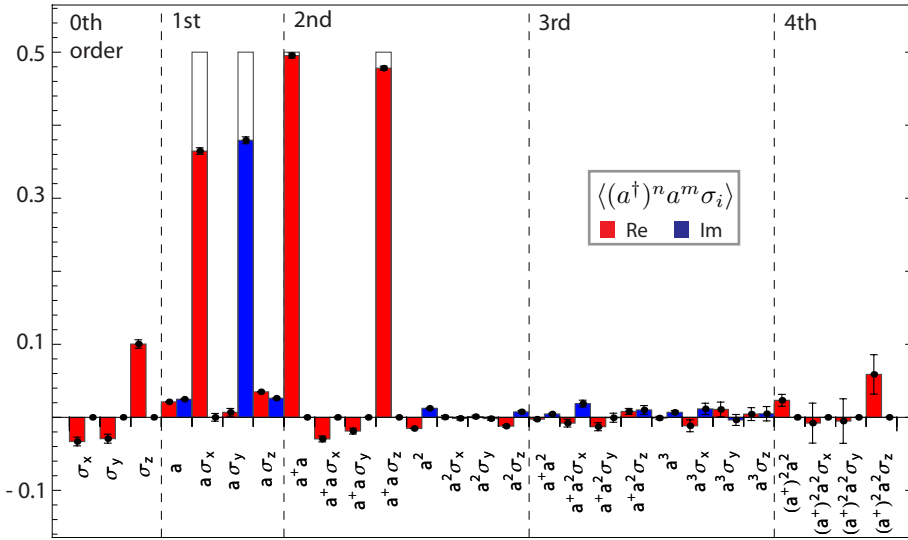


Figure 5.4: Expectation values $\langle (a^\dagger)^n a^m \sigma_i \rangle$ extracted from the qubit-photon field correlations shown in Figure 5.3 and the measured photon field distribution. The real (imaginary) part of these measured moments are shown in red (blue) and compared to the ideal Bell state (wireframe). The error bars are extracted from the standard deviation of repeated measurements.

the measured set of 3-dimensional histograms using the methods presented in Section A.4.1. The resulting measured expectation values (colored bars) of products between the Pauli operators σ_i and photon field operators a, a^\dagger are compared with the theoretical values of an ideal Bell state (wireframes) up to order $n+m=4$ in Figure 5.4. Here we note that in comparison to earlier measurements [Bozyigit11, Eichler11b], the increase in detection efficiency enabled by the parametric amplifier is essential for the measurement of higher order expectation values which now also include products of qubit and photon field operators.

The measured zeroth order moments $\langle \sigma_i \rangle$ represent the Bloch vector of the qubit. Since all values are close to zero the qubit is, as expected, in the maximally mixed state when the photon part of $|\psi\rangle$ is traced out. The small finite value of $\langle \sigma_z \rangle$ is due to qubit decay during the time between state preparation and qubit tomography required for performing photon tomography in the same mode. Finite first order expectation values $\langle a\sigma_i \rangle$ are due to the expected correlations between the equatorial component of the Bloch vector and the phase of the photon field, already observed in the raw measurement data (Figure 5.3(d,e)). The finite second order moments show that the single excitation is shared among qubit and photon field. Since the mean product of excitations $\langle a^\dagger a\sigma_z \rangle$ is close to the mean photon number $\langle a^\dagger a \rangle$ we find that whenever a photon is detected, the qubit is in the ground state for which σ_z takes the value 1.

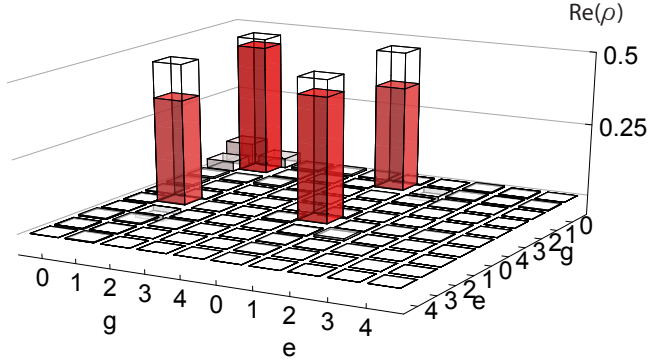


Figure 5.5: Real part of the measured (solid) and ideal (wireframe) density matrix ρ for the Bell state $|\psi\rangle$ with fidelity $F = \langle\psi|\rho|\psi\rangle = 83\%$

We also find that all higher order moments with $n + m = 3, 4$ are close to zero within their statistical errors, indicating that the photon field is a superposition of vacuum and single-photon states only [Eichler12a]. In particular the measured anti-bunching ($\langle\langle a^\dagger \rangle^2 a^2 \rangle = 0.023 \pm 0.008$) shows that there are no contributions of higher photon number states [Bozyigit11]. Moments of higher order can also be determined from the measured histogram data (not shown), albeit with statistical errors which depend exponentially on increasing order [daSilva10].

We have also evaluated the density matrix ρ of the joint qubit-photon state from the measurement data using a direct linear mapping from the moments to the density matrix elements (Section A.4.1). In order to make use of the full measurement data and to guarantee a completely positive density matrix we additionally apply a maximum-likelihood procedure which estimates the most likely density matrix from measured moments and their respective standard deviations up to order $n + m = 8$. This allows for reconstructing the density matrix in a 10-dimensional Hilbert space including photon number states up to $|n\rangle = |4\rangle$. As already expected from the vanishing fourth order moments, we find all number state populations with $n > 1$ close to zero (Figure 5.5). The coherent superposition of the two contributing basis states $|0e\rangle$ and $|1g\rangle$ is reflected in the large off-diagonal elements. Adjusting the overall local oscillator phase, the elements of the imaginary part of the density matrix (not shown) have been minimized to less than 0.023. The total fidelity of the reconstructed state compared to the ideal Bell state $|\psi\rangle$ is $F = \langle\psi|\rho|\psi\rangle = 83\%$. The loss of fidelity is dominantly due to qubit decay and decoherence during the 60 ns period between the state preparation pulse and the final tomography pulse, which determines the time at which the qubit state is characterized. We verify the entanglement between the photon field and the qubit by determining the negativity [Vidal02] of the reconstructed density matrix $\mathcal{N}(\rho) = 0.34$,

which is bounded by zero for unentangled states and 0.5 for ideal Bell states.

5.1.5 Time-resolved correlations based on single shot qubit readout

We have studied qubit-photon correlations also within time-resolved measurements for the prepared Bell state $\frac{1}{\sqrt{2}}(|0e\rangle + |1g\rangle)$. For this experiment, we have operated the parametric amplifier in a phase-sensitive mode by setting the pump frequency equal to the frequency of the readout tone. We repeat the experimental sequence depicted in Figure 5.1(d) and store individual time-traces of the amplified quadrature component X instead of three-dimensional histograms. The parametric amplifier enables us to decide for each trace, whether the qubit is in the ground or the excited state (Figure 5.6(a)). From these single shot measurements we are also able to extract the residual excited state population of the qubit $p_{\text{th}} \lesssim 3\%$. Due to the finite qubit decay during the delay time between state preparation and readout, the qubit may be detected in the ground state although it was initially in the excited state.

Based on the individually measured time-traces we average the power $\langle X^2 \rangle$ in the amplified quadrature X , as shown in Figure 5.6(b). We resolve correlations between the qubit and the photon field by post-selecting those traces for which the qubit is found in a specific state. Averaging only over those time-traces, for which the qubit is found in the excited state, there is no photon flux visible (red). In contrast, if we average conditioned on the qubit being initially in the ground state, we observe the photon flux of a single photon emitted from the resonator (blue). The temporal shape of the photon pulse is determined by the exponential decay of the cavity, the filtering imposed by the parametric amplifier, and the additional digital filtering. The solid line is the expected temporal envelope of the photon pulse based on the individually determined response function. For comparison, we also show the measured photon flux independent of the final qubit state (purple), and find approximately half of the photons on average. These results clearly demonstrate that a photon is only emitted if the qubit is initially in the ground state.

In order to measure the quantum coherence between the photon field and the qubit, we readout the qubit in the σ_x basis by applying a $\pi/2$ rotation and determine the mean quadrature amplitude $\langle X \rangle$ (Figure 5.6(c)). Averaging over all traces, independent of the qubit state, we find the average amplitude close to zero (purple). In contrast, if we select only those traces for which the qubit has been found in the excited state when measuring in the σ_x basis, we observe a finite mean amplitude. This also agrees with the expectation for a Bell state $\frac{1}{\sqrt{2}}(|0e\rangle + |1g\rangle)$, as explained in Section 5.1.3.

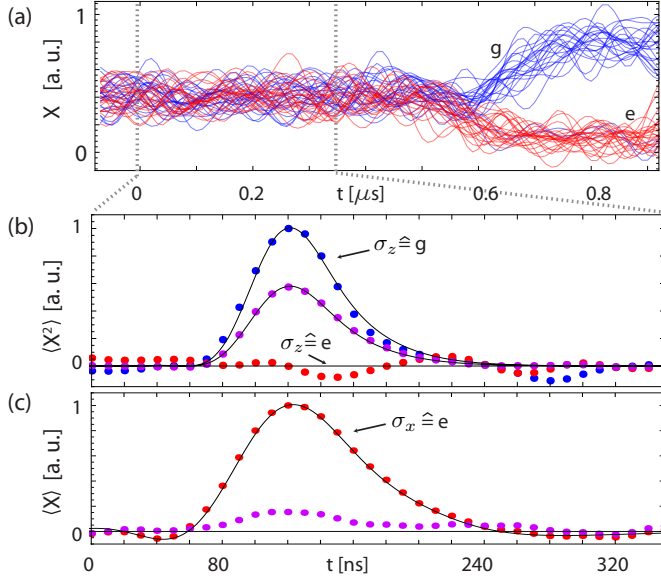


Figure 5.6: Time-resolved measurement of photon-qubit correlations. (a) Individual time-traces of the quadrature X when the qubit is prepared in the ground state (blue) and when the qubit is prepared in the excited state (red). From the prepared excited states we have selected only those traces, for which no spontaneous decay into the ground state has occurred. (b) Average power $\langle X^2 \rangle$ in the amplified quadrature independent of the qubit state (purple dots), conditioned on the qubit in the excited state (red dots), and conditioned on the qubit being initially in the ground state (blue dots). The solid lines show the expected temporal profile of the photon pulse, taking into account the measured parametric amplifier response (Figure 5.2(c)) and the additional digital filtering.

5.2 Two-photon entangled states

To demonstrate the versatility of our state preparation, detection and reconstruction scheme beyond existing experiments we have also prepared entangled states between stationary qubits and multiple propagating photons such as $|\phi\rangle = \frac{1}{2}(|1\rangle + |2\rangle)|g\rangle + \frac{1}{2}(|1\rangle - |2\rangle)|e\rangle$. For the preparation of such states we make use of the third energy level $|f\rangle$ of the transmon [Bianchetti10b]. Using this state preparation scheme, we are also able to generate arbitrary photon superposition states of type $c_g|0\rangle + c_f|2\rangle$, which are disentangled from the qubit. The reconstruction of these states has already been discussed in Section 3.4.1 in the context of photon state tomography. In the following I explain, how these states have been generated.

5.2.1 Mapping the f -level onto a two-photon state

We drive Rabi oscillations between the ground state $|g\rangle$ and the second excited state $|f\rangle$ of the transmon by applying a coherent pulse at frequency $(\omega_{ge} + \omega_{ef})/2$, see inset of Figure 5.7(a). The state evolution of an initial ground state under this drive is $|g\rangle \rightarrow \cos \theta |g\rangle + e^{i\phi} \sin \theta |f\rangle$. The effective Rabi angle θ of this two-photon transition is proportional to the square of the drive amplitude, the pulse length and the coupling capacitance between qubit and gate line. The phase ϕ is controlled by the phase of the drive field. For $\theta = \pi/2$ the qubit state is brought into the equal superposition state $(|g\rangle + e^{i\phi} |f\rangle)/\sqrt{2}$ while for $\theta = \pi$ the qubit is prepared in the $|f\rangle$ state.

By applying a sequence of two flux pulses to the transmon we map an arbitrary initial superposition state $c_g |g\rangle + c_f |f\rangle$ onto the corresponding resonator state $c_g |0\rangle + c_f |2\rangle$. The first flux pulse of amplitude V_1 and length τ_1 brings the ω_{ef} transition into resonance with ω_r , see Figure 5.7(b). According to the interaction $H_{\text{int}}/\hbar = ig_e(a^\dagger |e\rangle \langle f| - h.c.)$ between resonator and the relevant transmon levels (Eq. (2.23)), the initial f -level component evolves as $\cos(g_e \tau_1) |f0\rangle + \sin(g_e t) |e1\rangle$. After interaction time $\tau_1 = \pi/g_e$ the initial state is thus transformed into

$$c_g |0g\rangle + c_f |0f\rangle \rightarrow c_g |0g\rangle + c_f |1e\rangle. \quad (5.1)$$

The second flux pulse of amplitude V_2 and length τ_2 brings the ω_{ge} transition into resonance with ω_r , see Figure 5.7(b). When choosing $\tau_2 = \pi/\sqrt{2}g$ the remaining excited state state population is transferred into the resonator and we are left with the desired state $(c_g |0\rangle + c_f |2\rangle) \otimes |g\rangle$. The total interaction time required for this state preparation is approximately 5 ns and thus still much shorter than the cavity decay time $1/\kappa \approx 25$ ns. The radiation field decays into the transmission line, where we detect it linearly using the parametric amplifier shown in Figure 5.1.

In a first experiment we measure the average photon number of the integrated output field for various initial Rabi pulse amplitudes θ , as shown in Figure 5.7(c). The photon number is proportional to the initial f -level population, as expected for the employed mapping. Note, that all the flux pulse parameters τ_1, τ_2, V_1, V_2 have been calibrated, by maximizing the total emitted photon number. When averaging the mean amplitude, we find $\langle a \rangle$ close to zero for all Rabi angles θ . This is expected for superposition states, which contain only even or only odd number states. We verify the quantum superposition character of the prepared state by measuring the operator average $\langle a^2 \rangle$. While for the Fock state $|2\rangle$ at $\theta = 0$, $\langle a^2 \rangle$ is close to zero it becomes maximal for the equal superposition state $\frac{1}{\sqrt{2}}(|0\rangle + |2\rangle)$. For the specific preparation angles $\theta = \pi/2$ and $\theta = \pi$, we have also performed full quantum state tomography, as shown in Figure 3.10.

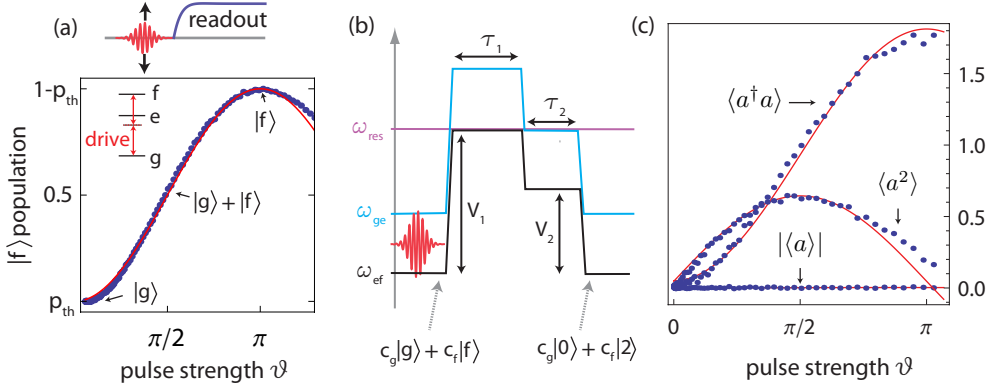


Figure 5.7: (a) Measurement and fit of Rabi oscillations between the ground state $|g\rangle$ and the second excited $|f\rangle$ of the transmon. (b) Schematic of the pulse sequence used to map the f state onto a two-photon state in the cavity. (c) Measurement of the mean amplitude $\langle a \rangle$, the mean photon number $\langle a^\dagger a \rangle$, and the term $\langle a^2 \rangle$ for the integrated field emitted from the cavity after applying the preparation sequence in (b).

5.2.2 State reconstruction of a two-photon entangled state

We have also prepared two-photon states which are maximally entangled with the qubit. For this experiment, we initially bring the system into the $|0f\rangle$ state. We then apply the flux pulse sequence described in Figure 5.7, but chose the length of the second flux pulse by a factor of two shorter, $\tau_2 = \pi / \sqrt{8}g$. The resulting state $\frac{1}{\sqrt{2}}(|1e\rangle + |2g\rangle)$ is then entangled with the qubit, because only half of the e -level population is transferred into the resonator during the second flux pulse. An additional $\pi/2$ pulse applied at the g - e transition frequency creates the state $|\phi\rangle = \frac{1}{2}(|1\rangle + |2\rangle)|g\rangle + \frac{1}{2}(|1\rangle - |2\rangle)|e\rangle$. Note that this state preparation sequence can be interpreted as the generation of the separable state $\frac{1}{2}(|1\rangle + |2\rangle) \otimes (|g\rangle + |e\rangle)$ and an entangling controlled phase gate, which changes the sign of the two photon component $|2\rangle$ only if the qubit is in the excited state. The entanglement between photon field and qubit thus becomes apparent in the negative sign of the $|2e\rangle$ component in $|\phi\rangle$. We characterize the prepared state using the methods described above, which results in a final density matrix with fidelity $F = 80\%$ compared to the ideal one (Figure 5.8). The negativity of $\mathcal{N}(\rho) = 0.33$ determined from the reconstructed density matrix indicates the entanglement of the propagating multi-photon state with the stationary qubit.

In summary, we have demonstrated the generation and detection of entanglement between a superconducting qubit and a propagating microwave field. The development of sensitive detection techniques for the measurement of photon-qubit quantum correlations is an important step towards using itinerant microwave photons as a quantum information carrier, e.g. for connecting spatially separated superconducting circuits or

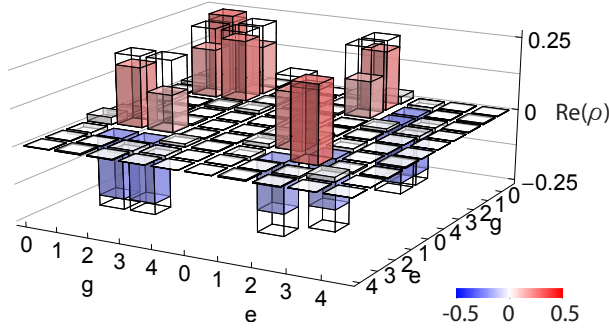


Figure 5.8: Real part of the measured (solid) and ideal (wireframe) density matrix ρ for the state $|\phi\rangle = \frac{1}{2}(|1\rangle + |2\rangle)|g\rangle + \frac{1}{2}(|1\rangle - |2\rangle)|e\rangle$ with fidelity $F = \langle\psi|\rho|\psi\rangle = 80\%$

other systems interacting with microwave photons. The development of microwave photon counters [Chen11] and the high level of control over superconducting circuits put the realization of microwave photon based quantum network experiments within reach.

5.3 Coherent state Entanglement based on dispersive interaction

In the context of qubit-field entanglement we have also theoretically investigated correlations between the qubit and the output field of a cavity for dispersive interaction. These calculations – which are inspired by recent experiments discussed in Ref. [Hatridge13] – give new insight into the dispersive measurement process and could be relevant for quantum networking with continuous variable states. Here, we specifically calculate quantum correlations between the integrated output field of a driven cavity and a dispersively coupled qubit. This investigation allows us to characterize the post-measurement qubit state conditioned on the outcome of a finite-strength dispersive measurement. Our results imply that for any set of parameters an optimal filter function exists, for which the integrated field and the qubit share a pure state.

5.3.1 Motivation

The disturbing effect of a (partial) measurement on a quantum object is in principle known from the observed result, which in case of an ideal detector allows for a perfect determination of the post-measurement state. In general, the determination of this state requires not only monitoring of the full time-resolved measurement record but also knowledge of the intrinsic system dynamics. Jointly, this information can be used

to evaluate the final state by solving the corresponding stochastic master equation [Wiseman10].

In many cases of practical interest (e.g. digital quantum feedback and post-selection) it is more convenient to determine the final system state from the measurement result of a *single* integrated mode instead of the full time record [Korotkov11]. This detection of a narrow band mode does, however, not necessarily preserve the full information about the post-measurement state. For a system composed of a driven cavity and a dispersively coupled qubit, we therefore explicitly calculate quantum correlations between an integrated output field of finite duration and the final qubit state.

These investigations are of particular interest, since they clarify, if the dispersive interaction scheme described below is well suited to create entanglement between a stationary qubit and a flying qubit, similarly to the discussion in Section 5.1 but with coherent fields instead of Fock states. Furthermore, the described problem has recently been studied experimentally in Ref. [Hatridge13], for which the following calculations may provide a theoretical basis to optimize the experimental settings for observing clear features of quantum coherence.

5.3.2 Master equation and input-output relation

We consider a qubit at fixed frequency, which is initially prepared in a superposition state. This qubit interacts dispersively with a coherently driven cavity. Due to the cavity-qubit dynamics it is not obvious if the *integrated* output field contains all information about the final qubit state. In an interaction picture, the evolution of the density matrix for the combined qubit-cavity system is modeled by the following master equation

$$\begin{aligned} \dot{\rho} = \mathcal{L}\rho \equiv & -i[\chi\sigma_z a^\dagger a + \Omega(t)(a^\dagger + a), \rho] \\ & + \kappa(a\rho a^\dagger - \frac{1}{2}\rho a^\dagger a - \frac{1}{2}a^\dagger a\rho), \end{aligned} \quad (5.2)$$

where the first line in Eq. (5.2) describes the unitary evolution under the dispersive interaction χ and the cavity drive $\Omega(t) \in \mathbb{R}$. The second line accounts for the cavity emission κ into a transmission line by an appropriate Lindblad term. Note, that we assume the qubit decay and dephasing rates to be zero.

At time $t = 0$ the qubit is prepared in the state $\frac{1}{\sqrt{2}}(|g\rangle + |e\rangle)$, the cavity is in the vacuum state $|0\rangle$, and a drive $\Omega(t) = \Omega_0$ is turned on for time T and then turned off again (Figure 5.9). During this time a cavity field builds up, which due to the dispersive interaction becomes correlated with the qubit. At the same time the cavity field decays into the transmission line according to the input-output relation [Gardiner85]

$$a_{\text{out}}(t) = \sqrt{\kappa}a(t) - a_{\text{in}}(t) \quad (5.3)$$

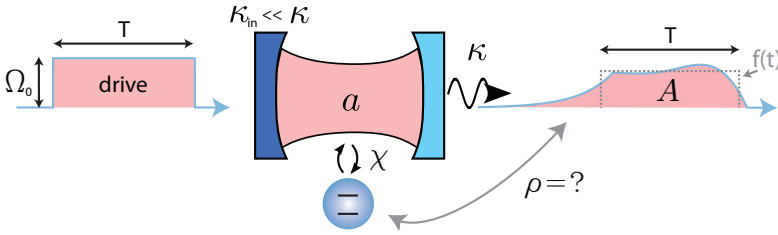


Figure 5.9: Schematic of the dispersive interaction scheme. A coherent drive field of amplitude Ω_0 is applied to the weakly coupled input port of the cavity for time T . The emerging intra-cavity field dispersively interacts with a qubit and decays with rate κ into an integrated transmission line mode A which is detected linearly using an appropriate filter function $f(t)$ for integration.

The single field mode A , which is associated with the radiation pulse leaving the cavity, is now defined as (Section 3.2.2)

$$A \equiv \int dt f(t) a_{\text{out}}(t), \quad (5.4)$$

where $f(t)$ is a normalized filter function in the time-domain which matches the temporal shape of the pulse. Note that a measurement of the integrated output field corresponds to a measurement of the field quadratures of this mode A . In the following the optimal filter function $f(t)$ is determined part of the following investigations.

5.3.3 Criterion for quantum coherence

We are interested in the phase coherence between the integrated field A and the qubit state. In order to make the discussion independent of the specific measurement device (i.e. phase-sensitive or phase-preserving amplifier), we calculate the general quantum state ρ shared between mode A and the qubit at time t_Q when the interaction is completed. The interaction is completed once the photon field has completely left the cavity (Figure 5.9), which is approximately a few cavity decay times after the time T when the drive is turned off. For the numerical calculations discussed below we have set $t_Q = T + 8/\kappa$.

We first derive the most general form of ρ given the dynamics defined by Eq. (5.2). Since the qubit population is a constant of motion $\langle \sigma_z \rangle = 0$, a ground (excited) state at time t_Q has always been a ground (excited) state at earlier times and thus the dynamics in the $|g\rangle$ and $|e\rangle$ subspaces are those of driven harmonic oscillators shifted in frequency by either plus or minus χ . As a result, the output fields associated with the ground and excited states are coherent fields α and β independent of the chosen filter function [Wahyu Utami08]. This drastically reduces the space of possible states

to

$$\rho = (|\alpha g\rangle\langle\alpha g| + |\beta e\rangle\langle\beta e| + C|\alpha g\rangle\langle\beta e| + C^*|\beta e\rangle\langle\alpha g|)/2. \quad (5.5)$$

This state is fully determined by the three parameters α , β and C , which are related to operator expectation values by $2\langle A\sigma_z\rangle = \alpha - \beta$ and $2\langle A\rangle = \alpha + \beta$ and

$$C = 2 \frac{\langle A^\dagger \sigma^-(t_Q) \rangle}{\alpha^* \langle \alpha | \beta \rangle}. \quad (5.6)$$

These identities immediately follow from Eq. (5.5). Note, that σ^- is *not* a constant of motion $\langle \dot{\sigma}^- \rangle \neq 0$, and thus it is important that we evaluate the coherence between mode A and the *final* qubit state at time t_Q .

Once A , $\langle A\sigma_z \rangle$ and the correlator $\langle A^\dagger \sigma^-(t_Q) \rangle$ are determined, we know everything about ρ and thus all the desired correlations between qubit and integrated output field. Furthermore, C is a direct measure of the purity of the state $\text{Tr}[\rho^2] = (1 + |C|^2)/2$, which is 1 for a pure state and 1/2 for the totally incoherent state.

5.3.4 Calculation of qubit - field correlations

In order to evaluate $\langle A^\dagger \sigma^-(t_Q) \rangle$ we express A in terms of the intra-cavity field operator by using Eq. (5.3) and Eq. (5.4)

$$\begin{aligned} \langle A^\dagger \sigma^-(t_Q) \rangle &= \left\langle \int dt f(t) a_{\text{out}}^\dagger(t) \sigma^-(t_Q) \right\rangle \\ &= \sqrt{k} \int dt f(t) \langle a^\dagger(t) \sigma^-(t_Q) \rangle \end{aligned} \quad (5.7)$$

The correlation between the integrated output field and the final qubit state is thus identical to the mode-matched average of the two-time correlator $\langle a^\dagger(t) \sigma^-(t_Q) \rangle$ between the intra-cavity field and the qubit. Based on Eq. (5.2) and the quantum regression formula [Carmichael99]

$$\langle a^\dagger(t) \sigma^-(t_Q) \rangle = \text{tr}\{\sigma^-(0) e^{\mathcal{L}(t_Q-t)} [\rho(t) a^\dagger(0)]\} \quad (5.8)$$

we can evaluate this correlator and therefore the qubit-field coherence C numerically. Similarly, we also calculate correlations between the σ_z - component of the Bloch vector and the cavity field.

In Figure 5.10 we show an example for the simulated correlation dynamics resulting from Eq. (5.8) for both σ_z and σ^- . As expected, the σ_z component of the Bloch vector

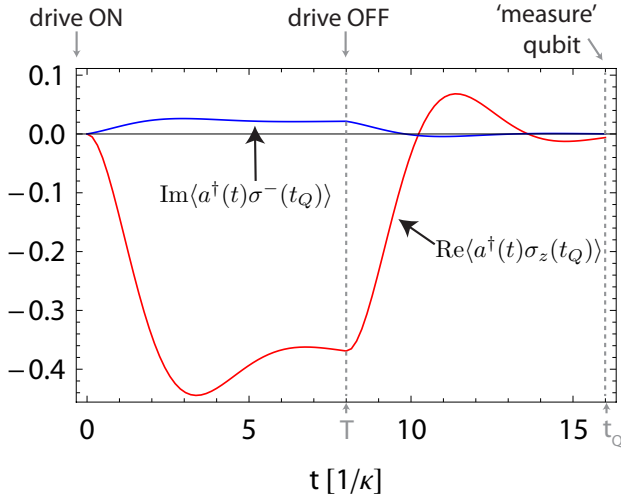


Figure 5.10: Simulated correlation dynamics between the qubit state at time $t_Q = 16/\kappa$ and the cavity field at variable time t for parameters ($\Omega_0 = 0.45\kappa$, $\chi = 0.93\kappa$, $T = 8/\kappa$).

becomes strongly correlated with the cavity field $\langle a^\dagger(t)\sigma_z(t_Q) \rangle$. This correlation is used in dispersive readout schemes to determine the σ_z value of the qubit from a measurement of the output field [Wallraff04, Blais04]. It persists in the limit of long measurements $T \rightarrow \infty$ and grows linearly with increasing drive strength Ω_0 . A finite correlation also remains between the equatorial Bloch vector component and the field, which can be interpreted as a photon number dependent AC Stark shift making the phase of the qubit dependent on the total photon number [Gambetta06].

In the next step we determine the optimal filter function $f(t)$, which maximizes the correlation between the qubit state and mode A given a specific drive pulse (Ω_0 , T). The maximal correlation is reached if the distance between the two coherent amplitudes $|\alpha - \beta|$ is maximized. Since this distance is given by

$$|\alpha - \beta|/2 = \langle A\sigma_z \rangle = \sqrt{\kappa} \int dt f(t) \langle a(t)\sigma_z \rangle \quad (5.9)$$

the choice

$$f(t) \propto \langle a^\dagger(t)\sigma_z \rangle \quad (5.10)$$

maximizes $|\alpha - \beta|$ and thus maximizes the correlation between the integrated field and σ_z . It turns out that this optimal filter function also maximizes the correlation with σ^- , such that $C = 1$ and ρ is pure. In Figure 5.11 we show the simulated coherence C as a function of drive strength Ω_0 for drive time $T = 8/\kappa$. The coherence C is found always at its optimal value 1, even if the mean photon number \bar{n} in the resonator is

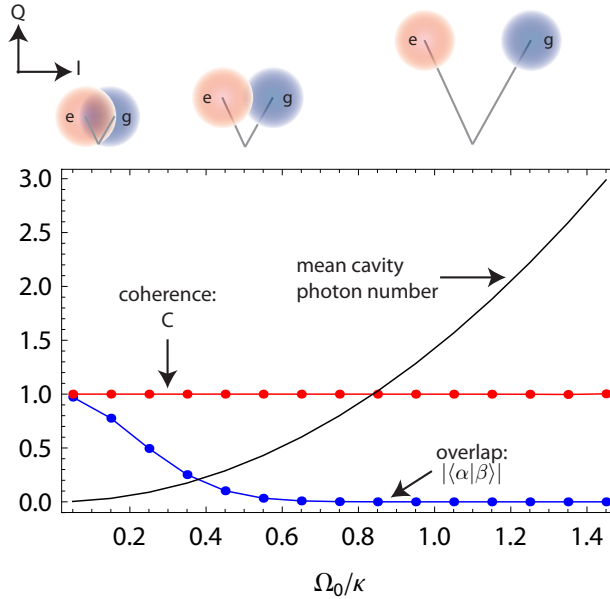


Figure 5.11: Absolute values of the coherence C (red) and the mean photon number stored in the cavity $\bar{n} \approx |\alpha|^2/T$ (black) vs. drive amplitude Ω_0 . The parameters are the same as in Figure 5.10. As indicated by the decreasing overlap $|\langle \alpha | \beta \rangle|$ and the schematic phase space representation in the top panel, the probability for projecting on a final qubit state with equal ground and excited state population decreases with stronger drive.

increased. We have simulated C for different parameter sets $\{\chi, T, \Omega_0\}$ and always found full phase coherence.

5.3.5 Experimental aspects

We finally discuss the experimental accessibility of the quantum coherence C between qubit and integrated field. We have simulated the influence of imperfect filtering and found that the coherence is sensitive to the mode matching efficiency. In an experiment one therefore has to consider the implementation of an optimal filter function. Especially for short drive pulses the deviation between the optimal filter and a square filter is large. Note that in contrast to cases where decay and state preparation are separated in time (compare Section 3.2.2 and Eq. (3.2.2)), here, the non-optimal filtering changes the overall statistical properties (i.e. the ratio between moments of equal order in A is not independent of the filter function).

From the definition of C in Eq. (5.6) we furthermore see that in the ideal case $C = 1$, the measurable expectation value $\langle A^\dagger \sigma^-(t_Q) \rangle$ is proportional to the overlap $\langle \alpha | \beta \rangle$. As a result, the measured quantity becomes exponentially smaller with increasing coherent

state separation (compare top row of Figure 5.11) and it requires more and more sensitivity to resolve the quantum superposition character. This is not surprising, since it is difficult to resolve the coherence of two superimposed "macroscopic" or classical states. Nevertheless, there is an interesting intermediate regime in which the overlap is not too large (i.e. significant entanglement present) but still large enough to detect it with current measurement capabilities and using the methods presented in Section 5.1.4.

In summary, we have calculated the full quantum state shared among the qubit and the traveling photon field A after dispersive interaction. If appropriate temporal mode matching is performed the system is described by a pure superposition state $|\alpha g\rangle + |\beta e\rangle$, independent of the dispersive interaction parameters. This is not obvious and might be rather special for the dispersive system dynamics. It would be interesting to investigate further, which property the system dynamics have to satisfy in general, to construct a single output mode A which shares a pure state with the qubit. Is it the double QND property (i.e. $a^\dagger a \sigma_z$ which commutes with σ_z and with $a^\dagger a$)? What happens if we add a Kerr nonlinear term $(a^\dagger)^2 a^2$ to the Hamiltonian [Lafamme12]? What, if we replace the dispersive interaction by a resonant interaction $a^\dagger \sigma^- + a \sigma^+$? Answering these questions would give new insight into input-output theory of quantum fields and could help in quantifying the post-measurement qubit state for other readout mechanisms.

Chapter 6

Outlook

In the present thesis we have developed a powerful experimental and theoretical toolbox for the control and detection of quantum microwave radiation. The main results of the underlying research are the on-demand generation of various nonclassical fields, the unveiling of their quantum nature [Eichler11b, Eichler11a, Eichler12a], the observation of entanglement between a single photon and a superconducting qubit [Eichler12b], and the tomographic characterization of two-photon interference at a beamsplitter. Our experiments define the current state-of-the-art in quantum control and measurement of propagating microwave fields.

The formulated and implemented concepts for detecting microwave field statistics have a wide range of potential applications and will likely stimulate their further investigations. The developed methods may for example be useful for exploring collective phenomena of artificial atoms coupled to either a common cavity mode [Mlynek12] or a continuum of modes [Astafiev10, Hoi12]. Characteristic features of these systems typically become apparent in the fluorescent radiation. Prominent examples are photon blockade [Imamoğlu97, Lang11] and superradiance of atom clouds [Gross82]. More recently, it has been proposed to study quantum many-body physics in superconducting circuits [Houck12]. An example is the prediction of Majorana modes in parametrically coupled cavity arrays [Bardyn12]. In these settings, the measurement of photon statistics could provide an essential tool for revealing quantum many body correlations.

The accessibility of microwave field correlations beyond the Gaussian level is not limited to circuit QED experiments. Also other systems, such as quantum dots [Frey12], electron spin ensembles [Kubo11, Wu10], molecular electronic devices [Puebla-Hellmann12], and electromechanical systems [Teufel11], naturally interact with radiation in the microwave frequency range. Applying the developed measure-

ment techniques may lead to a better understanding of physical processes also in these systems. Furthermore, the derived statistical methods could prove to be useful in the context of full counting statistics [Lambert10] and in experiments at optical frequencies with finite detection efficiency [Appel07].

The developed on-demand single photon source in combination with on-chip beamsplitters, also put the realization of linear optics based quantum computation [Knill01] with microwave photons within reach. We have experimentally verified desirable properties such as anti-bunching and indistinguishability of the generated photons. To finally achieve a quantum speedup in linear optics based quantum computation, single photon counters are required. While a number of proposals [Romero09, Peropadre11, Poudel12] and a proof-of-principle experiment [Chen11] for the detection of single microwave photons exist, their performance has to be further tested and optimized. Realizing the existing proposals or alternative schemes for microwave photon counting could significantly extend the range of potential quantum optics experiments with microwaves.

A significant part of the doctoral research presented here was dedicated to the development of a Josephson parametric amplifier. We have demonstrated the entanglement between signal and idler photons emitted from this device, which verifies its near quantum limited operation and turns it into a major building block for continuous variable quantum optics [Braunstein05]. Recently, these ideas have been further pursued to demonstrate continuous variable entanglement in spatially separated modes [Flurin12, Menzel12]. Beyond the use of parametric amplifiers for generating squeezed vacuum fields, they are practical devices to improve the efficiency in linear detection schemes. The detailed understanding of relations between amplifier characteristics and circuit design parameters have enabled us to build quantum limited parametric amplifiers which exhibit a high gain-bandwidth product as well as large tunability and dynamic range. In combination with practical hardware and software calibration tools, these devices have recently enabled the realization of quantum feedback [Riste12b, Vijay12] and quantum teleportation experiments in our lab. The number of setups in our laboratory with parametric amplifiers in the detection chain is rapidly increasing.

To date, superconducting circuits are one of the most promising environments for the realization of quantum information processing tasks [Mariantoni11a, Reed12, Fedorov12, Dewes12], which have thus far mainly been investigated on individual devices. Superconducting circuits could, however, also be used for exploring quantum network and communication schemes [Kimble08, Ritter12]. The possibility to synthesize, guide and detect microwave radiation with high efficiency make microwave photons a viable quantum information carrier over intermediate distances. Larger distances between network nodes could be bridged by using a room temperature link

based on coherent conversion from microwave to optical photons or by using sufficiently cold and lossless microwave waveguides. With the observation of photon-qubit entanglement and Hong-Ou-Mandel interference we have realized the main building blocks for the generation of heralded entanglement between different nodes in quantum repeaters and networks [Moehring07, Duan10]. Alternatively, the deterministic generation of entanglement could be explored in future experiments by ideal state transfer [Cirac97, Jahne07] based on resonators with tunable decay rate [Yin13] or stimulated Raman adiabatic passage schemes [Siewert04].

Appendices

A.1 Characteristic functions, moments and cumulants

Here, I discuss the efficient solution of equations of the form

$$\langle (\hat{S}^\dagger)^n \hat{S}^m \rangle = \sum_{i,j=0}^{n,m} \binom{m}{j} \binom{n}{i} \langle (a^\dagger)^i a^j \rangle \langle h^{n-i} (h^\dagger)^{m-j} \rangle. \quad (\text{A.1})$$

We consider the case where both $\langle (\hat{S}^\dagger)^n \hat{S}^m \rangle$ and $\langle h^n (h^\dagger)^m \rangle$ are known and where $\langle (a^\dagger)^i a^j \rangle$ is to be determined. Equivalently, $\langle h^n (h^\dagger)^m \rangle$ can be determined from known $\langle (\hat{S}^\dagger)^n \hat{S}^m \rangle$ and $\langle (a^\dagger)^i a^j \rangle$. Eq. (A.1) is a set of linear equations which could be solved numerically for each specific set of moments. However, the following approach allows us to generate analytical expressions to arbitrary order. We introduce the characteristic functions

$$\begin{aligned} C_S &\equiv \langle e^{\lambda \hat{S}^\dagger} e^{-\lambda^* \hat{S}} \rangle = \sum_{i,j} \frac{(-\lambda^*)^j \lambda^i}{i! j!} \langle (\hat{S}^\dagger)^i \hat{S}^j \rangle \\ C_a &\equiv \langle e^{\lambda a^\dagger} e^{-\lambda^* a} \rangle = \sum_{i,j} \frac{(-\lambda^*)^j \lambda^i}{i! j!} \langle (a^\dagger)^i a^j \rangle \\ C_h &\equiv \langle e^{\lambda h} e^{-\lambda^* h^\dagger} \rangle = \sum_{i,j} \frac{(-\lambda^*)^j \lambda^i}{i! j!} \langle h^i (h^\dagger)^j \rangle, \end{aligned} \quad (\text{A.2})$$

which, by construction, are related to the statistical moments by partial derivatives with respect to λ

$$\langle (a^\dagger)^n a^m \rangle = \partial_\lambda^n \partial_{-\lambda^*}^m C_a \Big|_{\lambda=0}, \quad (\text{A.3})$$

and analogously for moments in \hat{S} and h . Due to the identity

$$C_S = \langle e^{\lambda \hat{S}^\dagger} e^{-\lambda^* \hat{S}} \rangle = \langle e^{\lambda(a+h^\dagger)^\dagger} e^{-\lambda^*(a+h^\dagger)} \rangle = \langle e^{\lambda a^\dagger} e^{-\lambda^* a} \rangle \langle e^{\lambda h} e^{-\lambda^* h^\dagger} \rangle = C_a C_h$$

for uncorrelated a and h , we can explicitly express

$$\begin{aligned} \langle (a^\dagger)^n a^m \rangle &= \partial_\lambda^n \partial_{-\lambda^*}^m \frac{C_S}{C_h} \Big|_{\lambda=0} \\ &= \partial_\lambda^n \partial_{-\lambda^*}^m \frac{\sum_{i,j} \frac{(-\lambda^*)^j \lambda^i}{i! j!} \langle (\hat{S}^\dagger)^i \hat{S}^j \rangle}{\sum_{i,j} \frac{(-\lambda^*)^j \lambda^i}{i! j!} \langle h^i (h^\dagger)^j \rangle} \Big|_{\lambda=0} \end{aligned} \quad (\text{A.4})$$

in terms of $\langle (\hat{S}^\dagger)^n \hat{S}^m \rangle$ and $\langle h^n (h^\dagger)^m \rangle$. The last expression in Eq. (A.4) can be solved with symbolic mathematics software up to a desired order. Note that the summation in the last line of Eq. (A.4) only needs to be evaluated up to the maximal desired order. For example, the moments $\langle (a^\dagger)^n a^m \rangle$ up to order $n, m \in \{0, 1, 2\}$ only depend on moments $\langle (\hat{S}^\dagger)^n \hat{S}^m \rangle$ and $\langle h^n (h^\dagger)^m \rangle$ up to the same order. Note that the same procedure can be extended to extract the moments in the two-channel case from Eq. (3.58).

The derived relation can be reexpressed in an elegant way, by introducing the cumulants as derivatives of the natural logarithm of the characteristic functions, e.g.

$$\langle \langle (a^\dagger)^n a^m \rangle \rangle \equiv \partial_\lambda^n \partial_{-\lambda^*}^m \ln C_a \Big|_{\lambda=0}.$$

With this definition we find

$$\begin{aligned} \langle \langle (a^\dagger)^n a^m \rangle \rangle &= \partial_\lambda^n \partial_{-\lambda^*}^m \ln \left(\frac{C_S}{C_h} \right) \Big|_{\lambda=0} = \partial_\lambda^n \partial_{-\lambda^*}^m (\ln C_S - \ln C_h) \Big|_{\lambda=0} \\ &= \langle \langle (\hat{S}^\dagger)^n \hat{S}^m \rangle \rangle - \langle \langle h^n (h^\dagger)^m \rangle \rangle. \end{aligned} \quad (\text{A.5})$$

As expected, for a sum of two independent random variables $a = S - h^\dagger$, the cumulants are additive.

A.2 Probability distribution for two channel complex envelopes

Here we calculate the joint probability distribution of the complex envelopes in a two channel detection scheme along the lines of Ref. [Agarwal94]. By definition the probability distribution of the measurement data S_1, S_2 is given by the Fourier transform of the characteristic function

$$P(S_1, S_2) = \frac{1}{\pi^4} \int_{z_1, z_2} e^{z_1^* S_1 + z_2^* S_2 - z_1 S_1^* - z_2 S_2^*} \chi_{SS}(z_1, z_2). \quad (\text{A.6})$$

where

$$\chi_{SS}(z_1, z_2) = \left\langle e^{z_1 \hat{S}_1^\dagger + z_2 \hat{S}_2^\dagger} e^{-z_1^* \hat{S}_1 - z_2^* \hat{S}_2} \right\rangle. \quad (\text{A.7})$$

By substituting the operator Eqs. (3.41) for \hat{S}_1 and \hat{S}_2 we find

$$\begin{aligned} \chi_{SS}(z_1, z_2) &= \\ &\chi_a(z_1 + z_2) \chi_v(z_1 - z_2) \chi_{h_1}(-\sqrt{2}z_1^*) \chi_{h_2}(-\sqrt{2}z_2^*) \end{aligned} \quad (\text{A.8})$$

where we introduced the characteristic functions for the four different modes as

$$\chi_a(z) = \langle e^{za^\dagger} e^{-z^*a} \rangle = \int_{\beta} P_a(\beta) e^{z\beta^* - z^*\beta} \quad (\text{A.9})$$

$$\chi_v(z) = \langle e^{zv^\dagger} e^{-z^*v} \rangle \quad (\text{A.10})$$

$$\chi_{h_i}(z) = \langle e^{-z^*h_i} e^{zh_i^\dagger} \rangle = \int_{\beta} Q_i(\beta) e^{z\beta^* - z^*\beta} \quad (\text{A.11})$$

We can simplify these expressions by introducing the following physical assumptions. First, mode v is assumed to be in the vacuum state. In this case its characteristic function is the identity and we have

$$\chi_{SS}(z_1, z_2) = \chi_a(z_1 + z_2) \chi_{h_1}(-\sqrt{2}z_1^*) \chi_{h_2}(-\sqrt{2}z_2^*). \quad (\text{A.12})$$

Substituting this equation and the integral forms of the characteristic functions in the definition of $P(S_1, S_2)$ we get

$$P(S_1, S_2) = \int_{\beta, \eta, \gamma} P_a(\beta) Q_1(\eta) Q_2(\gamma) D, \quad (\text{A.13})$$

where

$$\begin{aligned}
 D &= \pi^{-4} \int_{z_1} \exp(z_1(\sqrt{2}\eta + \beta^* - S_1^*) - \text{c.c.})) \\
 &\quad \int_{z_2} \exp(z_2(\sqrt{2}\gamma + \beta^* - S_2^*) - \text{c.c.})). \\
 &= \frac{1}{4} \delta(\eta^* + \frac{\beta - S_1}{\sqrt{2}}) \delta(\gamma^* + \frac{\beta - S_2}{\sqrt{2}}), \tag{A.14}
 \end{aligned}$$

which reduces Eq. (A.13) to

$$P(S_1, S_2) = \frac{1}{4} \int_{\beta} P_a(\beta) Q_1\left(\frac{S_1^* - \beta^*}{\sqrt{2}}\right) Q_2\left(\frac{S_2^* - \beta^*}{\sqrt{2}}\right). \tag{A.15}$$

A.2.1 Thermal noise

In the next step we assume that the noise modes h_1, h_2 are in thermal states $e^{-|a|^2/N_i+1}/\pi(N_i+1)$ [Cahill69b] with mean photon numbers N_1, N_2 . The probability distribution of the measurement data is then

$$P(S_1, S_2) = \int_{\beta} P_a(\beta) \frac{\exp\left(-\frac{|S_1 - \beta|^2}{2(N_1+1)} - \frac{|S_2 - \beta|^2}{2(N_2+1)}\right)}{4\pi^2(N_1+1)(N_2+1)}. \tag{A.16}$$

Comparing this with the formula for the s-parametrized quasi-probability distribution

$$W_a(\bar{S}, s) = \frac{2\pi^{-1}}{1-s} \int_{\beta} P_a(\beta) \exp\left(-\frac{2|\bar{S} - \beta|^2}{1-s}\right) \tag{A.17}$$

we can identify the relation

$$P(S_1, S_2) = \frac{1}{2\pi N_{\text{tot}}} e^{-\frac{|S_1 - S_2|^2}{2N_{\text{tot}}}} W_a(\bar{S}, s) \tag{A.18}$$

by defining

$$\bar{S} = \frac{N_1+1}{N_{\text{tot}}} S_1 + \frac{N_2+1}{N_{\text{tot}}} S_2, \tag{A.19}$$

$$s = -1 - \frac{4N_1N_2 + 2N_1 + 2N_2}{N_{\text{tot}}}, \tag{A.20}$$

$$N_{\text{tot}} = N_1 + N_2 + 2. \tag{A.21}$$

If we have the same noise level on both channels $N_1 = N_2 = N_0$, we find $s = -1 - 2N_0$ and thus

$$P(S_1, S_2) = \frac{e^{-\frac{|S_1 - S_2|^2}{4(N_0+1)}}}{4\pi(N_0+1)} W_a\left(\frac{S_1 + S_2}{2}, -1 - 2N_0\right) \quad (\text{A.22})$$

In the case of quantum limited detection $N_1 = N_2 = 0$ we have $s = -1$ and the distribution of our measurement data corresponds to the canonical positive P-representation of mode a

$$P(S_1, S_2) = \frac{1}{4\pi} e^{-\frac{|S_1 - S_2|^2}{4}} Q_a\left(\frac{S_1 + S_2}{2}\right). \quad (\text{A.23})$$

A.2.2 Equivalence to canonical positive P function

To prove that Eq. (A.18) is also a positive P function when the thermal noise levels are unequal $N_1 \neq N_2$ we show that [Braunstein91]

$$\frac{1}{\pi} \int_{S_1, S_2} P(S_1, S_2) \frac{\langle \alpha | S_1 \rangle \langle S_2 | \alpha \rangle}{\langle S_2 | S_1 \rangle} \doteq Q(\alpha). \quad (\text{A.24})$$

Using Eq. (A.16), the left hand side of Eq. (A.24) is

$$\int_{\beta, S_1, S_2} P_a(\beta) \frac{\exp\left(-\frac{|S_1 - \beta|^2}{2(N_1+1)} - \frac{|S_2 - \beta|^2}{2(N_2+1)}\right) \langle \alpha | S_1 \rangle \langle S_2 | \alpha \rangle}{4\pi^3(N_1+1)(N_2+1) \langle S_2 | S_1 \rangle} \quad (\text{A.25})$$

This is a multi-dimensional Gaussian integral in the variables S_1, S_2 and can be solved to give

$$\frac{1}{\pi} \int_{\beta} P_a(\beta) e^{-|\beta - \alpha|^2}, \quad (\text{A.26})$$

which is exactly the Q function.

A.3 Relation between POVM and quasi-probability distribution

We verify Eq. (3.38) by the following chain of identities

$$\begin{aligned}
\text{Tr}[\rho_a \hat{\Pi}_\alpha^{[\rho_h]}] &= \text{Tr}\left[\frac{1}{\pi} \rho_a T_\alpha \tilde{\rho}_h T_\alpha^\dagger\right] \\
&= \text{Tr}\left[\frac{1}{\pi} \int_\beta \int_\gamma P_a(\alpha) P_h(-\gamma^*) |\beta\rangle \langle \beta| T_\alpha |\gamma\rangle \langle \gamma| T_\alpha^\dagger\right] \\
&= \text{Tr}\left[\frac{1}{\pi} \int_\beta \int_\gamma P_a(\alpha) P_h(-\gamma^*) |\beta\rangle \langle \beta| |\gamma + \alpha\rangle \langle \gamma + \alpha|\right] \\
&= \frac{1}{\pi} \int_\beta \int_\gamma P_a(\beta) P_h(\alpha^* - \gamma^*) e^{-|\gamma - \beta|^2} \\
&= \frac{1}{\pi} \int_\gamma Q_a(\gamma) P_h(\alpha^* - \gamma^*) \tag{A.27}
\end{aligned}$$

A.4 Joint Tomography Scheme for a Qubit - Photon Field System

A.4.1 Qubit state tomography

In order to describe the joint tomography scheme we first discuss the concepts of qubit tomography. For the reconstruction of the qubit density matrix ρ_σ one measures the Pauli expectation values $\langle \sigma_i \rangle$ along the different spin axes $\sigma_i \in \{\sigma_x, \sigma_y, \sigma_z\}$ which in the measurement basis $\{|g_z\rangle, |e_z\rangle\}$ are represented by the corresponding Pauli matrices. After state preparation the qubit is rotated such that the desired spin component σ_i points along the measurement axis. This rotation is followed by a read-out procedure during which the measurement result is encoded in a classical quantity q [Wallraff05]. In the context of circuit QED single shot read-out [Mallet09, Vijay11] is not always available and q can take a continuous spectrum of values where depending on the qubit state each value has a probability $D_i(q)$ to occur. Here the index $i \in \{x, y, z\}$ specifies the measurement basis.

The distribution $D_i(q)$ obtained after repeating the measurement many times can be fitted to the weighted sum of 2 reference distributions $p_g(q)$ for the ground and $p_e(q)$ for the excited state

$$D_i(q) \doteq \frac{1 - \langle \sigma_i \rangle}{2} p_e(q) + \frac{1 + \langle \sigma_i \rangle}{2} p_g(q) \tag{A.28}$$

to extract the Pauli expectation values $\langle \sigma_i \rangle$. Based on these values the density matrix

can then be determined as $\rho_\sigma = \frac{1}{2}(\mathbb{1} + \sum_i \langle \sigma_i \rangle \sigma_i)$. Note that instead of using Eq. (A.28) the qubit population can also be extracted from the mean values of q [Bianchetti09] as done in many experiments .

A.4.2 Joint tomography

A joint tomography scheme is expected to allow for a full characterization of the system also when photon field and qubit are correlated with each other. The goal is to determine all matrix elements $\langle s, n | \rho_{\sigma,a} | s', m \rangle$ of the joint density matrix $\rho_{\sigma,a}$ where $s, s' \in \{g_z, e_z\}$ label the qubit basis states and n, m the photon field number states. It can be shown that these matrix elements are uniquely determined by the set of moments $\langle (a^\dagger)^n a^m \sigma_i \rangle$ in the following way

$$\begin{aligned} \langle g_z, m | \rho_{\sigma,a} | g_z, n \rangle &= \frac{1}{2} \mathcal{M} \left(\langle (a^\dagger)^n a^m \rangle + \langle (a^\dagger)^n a^m \sigma_z \rangle \right) \\ \langle e_z, m | \rho_{\sigma,a} | e_z, n \rangle &= \frac{1}{2} \mathcal{M} \left(\langle (a^\dagger)^n a^m \rangle - \langle (a^\dagger)^n a^m \sigma_z \rangle \right) \\ \langle e_z, m | \rho_{\sigma,a} | g_z, n \rangle &= \frac{1}{2} \mathcal{M} \left(\langle (a^\dagger)^n a^m (\sigma_x + i\sigma_y) \rangle \right) \end{aligned} \quad (\text{A.29})$$

Here, \mathcal{M} is the linear map from the moments to the density matrix in the number state basis as defined in Eq. (3.29). The scheme described in the following allows to measure all the necessary moments in Eq. (A.29).

We consider the case that in each trial of an experiment both q , characterizing the qubit state, and the complex amplitude \hat{S} , characterizing the photon field, are measured. For each state preparation both numbers are stored in a 3D histogram $D_i(S, q)$ where the index i labels the chosen qubit rotation before measurement. To evaluate the desired expectation values we first determine the Pauli expectation values $\langle \sigma_i \rangle_S$ conditioned on the complex amplitude result S . This is done by fitting each trace of $D_i(S, q)$ along the q axes to the calibration histograms $p_g(q)$ and $p_e(q)$. Based on the knowledge of $\langle \sigma_i \rangle_S$ we determine the photon field distributions conditioned on a specific qubit measurement result as

$$\begin{aligned} D_{g_i}(S) &= \mathcal{N}_g \frac{1 + \langle \sigma_i \rangle_S}{2} \sum_q D_i(S, q) \\ D_{e_i}(S) &= \mathcal{N}_e \frac{1 - \langle \sigma_i \rangle_S}{2} \sum_q D_i(S, q) \end{aligned} \quad (\text{A.30})$$

where \mathcal{N}_g and \mathcal{N}_e are appropriate normalization constants which guarantee that $\int_S D_{g_i}(S) = \int_S D_{e_i}(S) = 1$. For example, $D_{g_x}(S)$ is the photon field distribution under the condition that the qubit is measured with result g in the x -basis.

Given these histograms one can evaluate the conditioned moments $\langle (\hat{S}^\dagger)^n \hat{S}^m \rangle |g_i$ and $\langle (\hat{S}^\dagger)^n \hat{S}^m \rangle |e_i$ using Eq. (3.18). If signal field and qubit are not correlated with the noise $\rho_{\sigma,a} \otimes \rho_h$ we can use the techniques described in Section 3.3.3 to extract the desired quantities $\langle (a^\dagger)^n a^m \sigma_i \rangle$.

A.4.3 POVM operators and maximum-likelihood state estimation

As for photon state tomography, it is desirable to find a set of POVM operators for the described measurement scheme. This allows to construct an iterative maximum-likelihood state estimation procedure and furthermore provides insight into the conditioned histograms introduced in Eq. (A.30).

For a perfect single shot qubit readout with a binary measurement result g or e , the POVMs are given by the projectors onto eigenstates of the Pauli operators, $\hat{\Pi}_{g_i} = |g_i\rangle\langle g_i|$ and $\hat{\Pi}_{e_i} = |e_i\rangle\langle e_i|$. They are complete in the sense that an arbitrary qubit density matrix can be explicitly written as a linear combination of projectors $\rho_\sigma = \frac{1}{2}(\mathbb{1} + \sum_i \langle \sigma_i \rangle (\hat{\Pi}_{g_i} - \hat{\Pi}_{e_i}))$.

Including the photon field measurement (compare Eq. (3.39)) the total set of POVMs is

$$\hat{\Pi}_{\alpha,s_i} = \hat{\Pi}_\alpha^{[\rho_h]} \otimes \hat{\Pi}_{s_i} \quad (\text{A.31})$$

with $s \in \{g, e\}$ and $i \in \{x, y, z\}$ for which the expectation values with respect to the total density matrix are related to the measured histograms by

$$\begin{aligned} \text{Tr}[\rho_{\sigma,a} \hat{\Pi}_{\alpha,g_i}] &\doteq \frac{1 + \langle \sigma_i \rangle}{2} D_{g_i}(\alpha) \\ \text{Tr}[\rho_{\sigma,a} \hat{\Pi}_{\alpha,e_i}] &\doteq \frac{1 - \langle \sigma_i \rangle}{2} D_{e_i}(\alpha) \end{aligned} \quad (\text{A.32})$$

with $\langle \sigma_i \rangle$ being the unconditioned Pauli expectation values. Note that this remains valid for qubit readout with limited single shot fidelity since the storage of the data in 3-dimensional histograms allows for capturing all qubit-photon correlations. By fitting the 3D histogram data along the q -axes to the expected ground and excited state distributions (see Eq. (A.28)) we account for the finite read-out efficiency. Using the set of POVMs given in Eq. (A.31) we are able to use the iterative maximum likelihood procedure described above to estimate the most likely density matrix for the combined system.

A.5 Parametric amplifier calibration and pump tone cancelation

For driving the nonlinear resonator into the parametric regime, a strong pump field is required. This pump field can have two unwanted effects. First, the strong pump tone can partially leak back towards the weak signal source of radiation (a circuit QED system in our case) and cause its constant drive. This is due to finite isolation of the circulators separating the paramp from the signal source (Figure A.1). Second, it can saturate components of the following detection chain, which disturbs the linear character of the measurement scheme. For these reasons, we use the setup shown in Figure A.1 to cancel out most of the reflected pump field before it enters the first circulator.

The pump tone is split up at room temperature into two parts. One part is guided towards the parametric amplifier, while the other part is attenuated and phase-shifted before it couples to the output. In the following, we call this latter part the cancelation tone. Both the phase shifter and the variable attenuator are mechanical components, which are actuated using stepper motors. Using these components we reach a relative step size of $\Delta A \approx 5 \text{ m dB}$ in the attenuation and $\Delta\phi \approx 0.1^\circ$ in the phase. The coupling of the pump field to the input and output modes of the parametric amplifier is achieved using a 20 dB directional coupler. The purpose of this arrangement is to adjust the attenuation A and the phase ϕ , such that the cancelation tone destructively interferes with the pump tone which is reflected from the parametric amplifier. The goal is thus to minimize the total pump power P_{out} propagating towards the circulator, see Figure A.1. While minimizing P_{out} we have to keep the power P_p at a fixed value, which is the pump incident on the parametric amplifier resonator. Remember that for fixed pump frequency and magnetic flux bias, the gain uniquely depends on this power $G = G(P_p)$. If we aim for a specific target gain G_{target} , we have to adjust P_p appropriately.

For an ideal directional coupler the transmission from port 2 into port 3 would be zero (Figure A.1) and thus the power P_p would be completely independent of the cancelation tone (i.e. independent of A and ϕ). However, in reality the directional coupler has a finite directivity, which means that a small fraction of the cancelation tone leaks back towards the parametric amplifier sample. Therefore, by changing A and ϕ we also change P_p and with that the parametric gain G . Note that even small changes in P_p (a few tens of m dB) can significantly change the gain. As a result, we cannot calibrate the pump cancelation independently of the gain but need a calibration algorithm which maximizes a combined objective function $f(G, P_{\text{out}})$ by adaptively changing all three control parameters P_{in}, A and ϕ . In the implemented algorithm, we have chosen an objective function $f(G, P_{\text{out}}) = \log(|G - G_{\text{target}}|) - u \log(P_{\text{out}}/P_s)$,

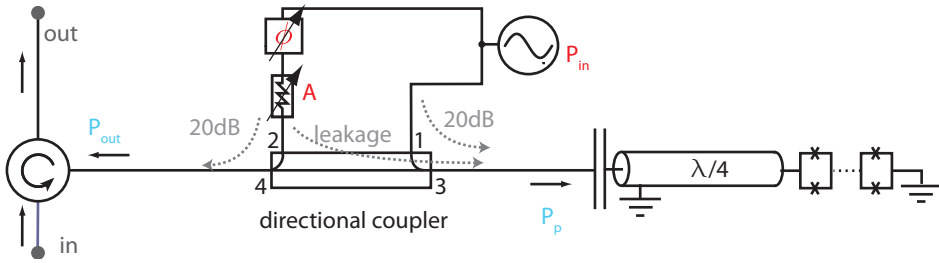


Figure A.1: Schematic of the parametric amplifier setup. The coherent pump power P_{in} is split into two parts at room temperature. One part is guided towards the parametric amplifier sample via the directional coupler port 1. The second part is modified with variable attenuation A and phase shift ϕ to cancel the reflected pump field at the output of port 4. Due to finite directional coupler leakage from port 2 to port 3 a change of A and ϕ also affects the power P_p which reaches the parametric amplifier sample.

where P_s is the power of the amplified test signal used for measuring the gain. The adjustable parameter u allows us to weigh the significance of the gain G compared to the cancellation P_{out} in the objective function. The choice of the function f is not unique. Note that a good choice of u is essential for the success of the optimization procedure. Sometimes it is required to manually change u during the optimization procedure to achieve an acceptable result. In order to find good initial conditions for the optimization procedure, it can help to make an initial coarse-grained sweep over all three control parameters while measuring both G and P_{out} [Heinzle12].

The basic idea of the optimization algorithm is the following [Govenius12]:

1. Measure both G and P_{out}/P_s and evaluate the objective function f .
2. Change one of the control parameters and evaluate f again. Repeat this step until f does no longer increase.
3. Repeat step (2) for the next control parameter.
4. Repeat steps (1) to (3) until f is above a desired threshold

This sequence provides only a simplified picture of the procedure. In practice, the algorithm has to deal with hysteresis effects when stepping the variable attenuator and phase shifter, and has to be robust against noise in the measurements of G and P_{out} . This requires additional features in the control software. The control software also needs input from the user, such as the frequency at which the gain is measured and the step sizes in all three control parameters.

The implemented calibration procedure could be further improved by automating a measurement of the noise, by avoiding hysteresis effects and by optimizing the update

of control parameters. Hysteresis could for example be reduced by approaching the final settings of the attenuator and phase shifter always from the same direction. The implementation of this idea is relatively straightforward. Furthermore, one could replace the mechanical phase shifters and attenuators by electrically controlled ones. This could reduce the total cost, reduce hysteresis effects and make the calibration procedure much faster.

A.6 System noise and dynamic range

In order to determine the effective system noise relative to the output of the cavity, we need a reference signal which is emitted from the cavity with known power. We calibrate such a reference signal using an AC Stark shift measurement. Due to the dispersive interaction between qubit and cavity, the qubit frequency is shifted proportionally to χ and the average photon number \bar{n} in the resonator [Schuster05]. We measure the qubit frequency shift for various drive powers applied to the weakly coupled input port of the cavity (orange port in Figure 5.1(a)), which allows us to translate the externally applied power into the corresponding average photon number \bar{n} , see Figure A.2(a). For a steady state photon number of \bar{n} in the resonator, the coherent output power is $P = \hbar\omega_{\text{res}}\bar{n}_{\text{out}}$ with photon flux $\bar{n}_{\text{out}} = \bar{n}\kappa$ leaving the cavity.

Based on this calibration, we populate the cavity with a known average photon number and measure the power spectral density S_{Δ} after all amplification and down-conversion stages. We perform this measurement for both cases: the parametric amplifier turned on and turned off (Figure A.2(b)). The frequency axis labels the detuning from the pump frequency. When the pump tone is turned off, we observe an almost frequency independent noise offset and an additional coherent peak at 12.5 MHz, which is the detuning of the cavity drive frequency from the pump frequency. The power spectral density S_{Δ} is scaled such that the height of the coherent peak relative to the noise offset is equal to $\bar{n}_{\text{out}}\delta f$, where $\delta f = 100 \text{ MHz}/2048 \approx 49 \text{ kHz}$ is the bin size of our specific power spectral density measurement. For this scaling, we can interpret the power spectral density as the ‘*number of photons emitted from the cavity per Hz and per sec*’. Note that all the attenuation and the noise added at later stages is referred back to the output of the cavity. We extract an effective system noise offset of about $N_0 + 1 \approx 180$ close to the cavity frequency.

We repeat the measurement of the power spectral density with the parametric amplifier turned on and again scale the data such that the coherent peak at 12.5 MHz detuning is equal to $\bar{n}_{\text{out}}\delta f$. Due to the additional parametric amplification, the signal to noise ratio is significantly increased. The noise offset close to the cavity frequency is extracted to be $N_0 + 1 \approx 4$. The deviation from the quantum limit $N_0 = 0$ is due to attenuation in cables and microwave components as well as noise added by the HEMT

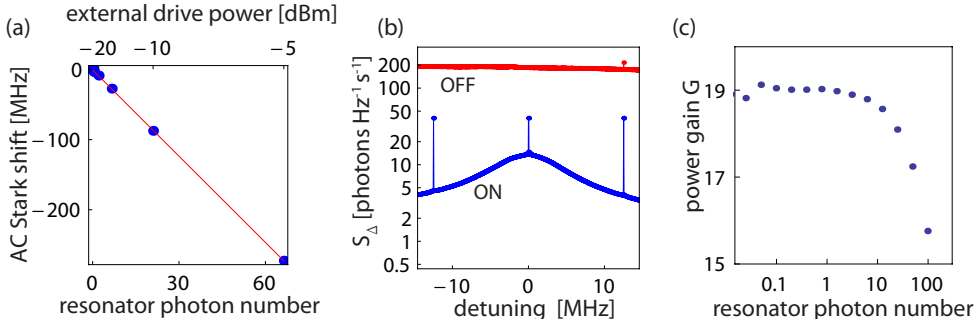


Figure A.2: (a) Measured AC Stark shift of the qubit for varying cavity drive powers. Knowing the dispersive interaction $\chi/2\pi = 2.05$ MHz, we can translate the external drive power into an average photon number inside the cavity. (b) Measured power spectral density S_{Δ} relative to the pump frequency for the parametric amplifier pump turned on (blue) and for the pump turned off (red). Both measured spectra are scaled such that the coherent peak at 12.5 MHz corresponds to the number of photons emitted per Hz and per second from the cavity. (c) Measured gain for various intra-cavity photon numbers. The decrease in gain for increasing photon number is due to saturation of the parametric amplifier.

and parametric amplifier. We believe that the most significant improvement could be achieved by optimizing the cabling between parametric amplifier and cavity. The two additional coherent peaks in the power spectral density measurement originate from the residual pump tone at zero detuning and the idler tone at -12.5 MHz, which is generated during the parametric amplification process.

To estimate the total detection efficiency η in our state tomography experiments we also determine the mode matching efficiency η_F , compare Section 3.2.2. Taking into account the frequency dependence of the complex gain shown in Figure 5.2(c), the implemented digital filter coefficients and the exponential cavity decay, we extract a mode matching efficiency of $\eta_F \approx 50\%$. In combination with the measured system noise, this results in an approximate total detection efficiency of $\eta \approx \eta_F/(N_0 + 1) = 13\%$. This estimate for the detection efficiency does not take into account the frequency dependence of the effectively added noise and cannot account for all analog bandpass filter effects. Furthermore it is subject to inaccuracies in the AC Stark shift calibration. In practice, we therefore determine the total detection efficiency from the preparation and detection of a reference state with well-known properties. We prepare the state $\frac{1}{\sqrt{2}}(|0\rangle + |1\rangle)$ inside the resonator and perform state tomography based on quadrature histogram measurements. The total detection efficiency η , which appears as a parameter in the state tomography procedure, is adjusted such that the measured density matrix has maximal overlap with the one resulting from a master equation simulation. This simulation is based on all independently measured device parameters,

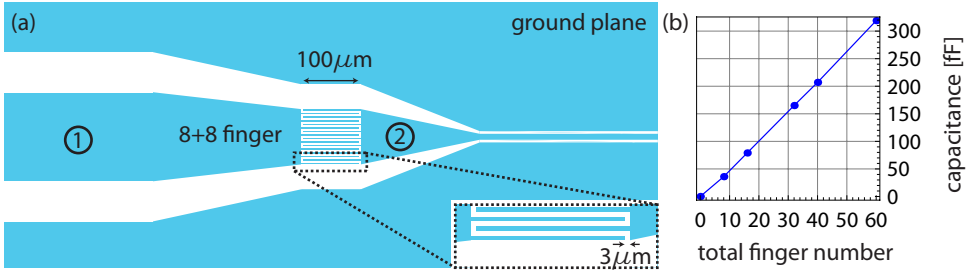


Figure A.3: (a) Design of a interdigitated finger capacitance with 8 + 8 fingers. Superconducting parts are shown in blue. Insulating parts are shown in white. The width of the fingers and the gap between fingers is $3\ \mu\text{m}$. The length of the fingers is $100\ \mu\text{m}$. (b) Simulation results of the capacitances in fF for various numbers of fingers. The simulation results are (36, 79, 165, 207, 319) fF for (8, 16, 32, 40, 60) fingers.

such as qubit decay and dephasing. Based on this procedure, we extract a detection efficiency of $\eta = 15\%$ for the photon-qubit entanglement measurements shown in Chapter 5.

Based on the calibration of the intra-cavity photon number, we can also determine the dynamic range of the parametric amplifier. We measure the parametric amplifier gain for various intra-cavity photon numbers, from which we determine the 1dB compression point at about 25 photons (Figure 5.2(c)). This corresponds to a power of $P = -127\ \text{dBm}$ at the output of the cavity. When amplifying single or few photons decaying from the cavity, the parametric amplifier is thus safely in the linear regime.

A.7 Simulation of capacitances for interdigitated finger capacitors

For the fabrication of parametric amplifier devices with low external quality factors, we have simulated the capacitance of digitated finger capacitors. An example of a designed capacitor is shown in Figure A.3(a), which has 8 + 8 digitated fingers. Based on this design we simulate the capacitance between island 1 and 2 (Figure A.3(a)) using the finite element software¹. For the simulation we model the niobium parts as perfect conductors with thickness 200 nm, which are on top of a $500\ \mu\text{m}$ thick sapphire substrate. The whole object is assumed to be in vacuum. For the simulation we take into account a larger area of the ground plane than the one shown in Figure A.3(a).

The results of the measured capacitances between the inner conductor of the resonator (island 2) and the inner conductor of the launcher (island 1) are shown in

¹Ansoft Maxwell

Figure A.3(b) for various numbers of fingers. For the simulated designs we find an almost linear relation between the capacitance and the number of fingers. When designing capacitors with a different number of fingers we can therefore to good approximation interpolate the expected capacitances. Within the accuracy of the fabrication and the measurement of quality factors, we did not find a systematic deviation between the simulated and the measured capacitances [Göppl08].

Bibliography

- [Abdo13] B. Abdo, A. Kamal & M. Devoret. Nondegenerate three-wave mixing with the Josephson ring modulator. *Phys. Rev. B*, **87** 014508 (2013). Cited on page 77.
- [Agarwal94] G. S. Agarwal & S. Chaturvedi. Scheme to measure the positive P distribution. *Phys. Rev. A*, **49** R665 (1994). Cited on pages 38, 68 and 143.
- [Al-Saidi01] W. A. Al-Saidi & D. Stroud. Eigenstates of a small Josephson junction coupled to a resonant cavity. *Phys. Rev. B*, **65** 014512 (2001). Cited on page 2.
- [Anderson95] M. H. Anderson, J. R. Ensher, M. R. Matthews, C. E. Wieman & E. A. Cornell. Observation of Bose-Einstein condensation in a dilute atomic vapor. *Science*, **269** 198 (1995). Cited on page 1.
- [Anton12] S. M. Anton, C. Müller, J. S. Birenbaum, S. R. O’Kelley, A. D. Fefferman, D. S. Golubev, G. C. Hilton, H.-M. Cho, K. D. Irwin, F. C. Wellstood, G. Schön, A. Shnirman & J. Clarke. Pure dephasing in flux qubits due to flux noise with spectral density scaling as $1/f^\alpha$. *Phys. Rev. B*, **85** 224505 (2012). Cited on page 8.
- [Appel07] J. Appel, D. Hoffman, E. Figueroa & A. I. Lvovsky. Electronic noise in optical homodyne tomography. *Phys. Rev. A*, **75** 035802 (2007). Cited on page 138.
- [Arthurs65] E. Arthurs & J. L. Kelly. unknown. *Bell. Syst. Tech. J.*, **44** 725 (1965). Cited on page 45.
- [Astafiev10] O. Astafiev, A. M. Zagoskin, A. A. Abdumalikov Jr., Y. A. Pashkin, T. Yamamoto, K. Inomata, Y. Nakamura & J. S. Tsai. Resonance fluorescence of a single artificial atom. *Science*, **327** 840 (2010). Cited on pages 37 and 137.
- [Audenaert09] K. M. R. Audenaert & S. Scheel. Quantum tomographic reconstruction with error bars: a Kalman filter approach. *New Journal of Physics*, **11** 023028 (2009). Cited on page 62.
- [Babichev04] S. A. Babichev, J. Appel & A. I. Lvovsky. Homodyne tomography characterization and nonlocality of a dual-mode optical qubit. *Phys. Rev. Lett.*, **92** 193601 (2004). Cited on pages 63 and 109.
- [Bardeen57] J. Bardeen, L. Cooper & J. Schrieffer. Theory of superconductivity. *Phys. Rev.*, **108** 1175 (1957). Cited on page 1.
- [Bardyn12] C.-E. Bardyn & A. İmamoğlu. Majorana-like modes of light in a one-dimensional array of nonlinear cavities. *Phys. Rev. Lett.*, **109** 253606 (2012). Cited on page 137.
- [Baur12] M. Baur. *Realizing quantum gates and algorithms with three superconducting qubits*. Ph.D. thesis, ETH Zurich (2012). Cited on pages 30, 32 and 39.

- [Bergeal10a] N. Bergeal, F. Schackert, M. Metcalfe, R. Vijay, V. E. Manucharyan, L. Frunzio, D. E. Prober, R. J. Schoelkopf, S. M. Girvin & M. H. Devoret. Phase-preserving amplification near the quantum limit with a Josephson ring modulator. *Nature*, **465** 64 (2010). Cited on pages 3, 37, 64 and 79.
- [Bergeal10b] N. Bergeal, R. Vijay, V. E. Manucharyan, I. Siddiqi, R. J. Schoelkopf, S. M. Girvin & M. H. Devoret. Analog information processing at the quantum limit with a Josephson ring modulator. *Nat. Phys.*, **6** 296 (2010). Cited on pages 77 and 79.
- [Bergeal12] N. Bergeal, F. Schackert, L. Frunzio & M. H. Devoret. Two-mode correlation of microwave quantum noise generated by parametric down-conversion. *Phys. Rev. Lett.*, **108** 123902 (2012). Cited on page 79.
- [Beugnon06] J. Beugnon, M. P. A. Jones, J. Dingjan, B. Darquié, G. Messin, A. Browaeys & P. Grangier. Quantum interference between two single photons emitted by independently trapped atoms. *Nature*, **440** 779 (2006). Cited on page 70.
- [Bianchetti09] R. Bianchetti, S. Filipp, M. Baur, J. M. Fink, M. Göppl, P. J. Leek, L. Steffen, A. Blais & A. Wallraff. Dynamics of dispersive single-qubit readout in circuit quantum electrodynamics. *Phys. Rev. A*, **80** 043840 (2009). Cited on pages 25, 40, 121 and 147.
- [Bianchetti10a] R. Bianchetti. *Control and readout of a superconducting artificial atom*. Ph.D. thesis, ETH Zurich (2010). Cited on page 39.
- [Bianchetti10b] R. Bianchetti, S. Filipp, M. Baur, J. M. Fink, C. Lang, L. Steffen, M. Boissonneault, A. Blais & A. Wallraff. Control and tomography of a three level superconducting artificial atom. *Phys. Rev. Lett.*, **105** 223601 (2010). Cited on page 127.
- [Bishop09a] L. S. Bishop, J. M. Chow, J. Koch, A. A. Houck, M. H. Devoret, E. Thuneberg, S. M. Girvin & R. J. Schoelkopf. Nonlinear response of the vacuum Rabi resonance. *Nat. Phys.*, **5** 105 (2009). Cited on page 2.
- [Bishop09b] L. S. Bishop, L. Tornberg, D. Price, E. Ginossar, A. Nunnenkamp, A. A. Houck, J. M. Gambetta, J. Koch, G. Johansson, S. M. Girvin & R. J. Schoelkopf. Proposal for generating and detecting multi-qubit GHZ states in circuit QED. *New J. Phys.*, **11** 073040 (2009). Cited on page 26.
- [Blais04] A. Blais, R.-S. Huang, A. Wallraff, S. M. Girvin & R. J. Schoelkopf. Cavity quantum electrodynamics for superconducting electrical circuits: An architecture for quantum computation. *Physical Review A*, **69** 062320 (2004). Cited on pages 2, 23, 24, 25, 107 and 134.
- [Blatt08] R. Blatt & D. Wineland. Entangled states of trapped atomic ions. *Nature*, **453** 1008 (2008). Cited on page 2.
- [Blinov04] B. B. Blinov, D. L. Moehring, L. M. Duan & C. Monroe. Observation of entanglement between a single trapped atom and a single photon. *Nature*, **428** 153 (2004). Cited on page 117.
- [Bloch08] I. Bloch. Quantum coherence and entanglement with ultracold atoms in optical lattices. *Nature*, **453** 1016 (2008). Cited on page 2.
- [Bohr13] N. Bohr. On the constitution of atoms and molecules. *Philosophical Magazine*, **26** (1913). Cited on page 1.
- [Boissonneault10] M. Boissonneault, J. M. Gambetta & A. Blais. Improved superconducting qubit readout by qubit-induced nonlinearities. *Phys. Rev. Lett.*, **105** 100504 (2010). Cited on page 26.

- [Bouchiat98] V. Bouchiat, D. Vion, P. Joyez, D. Esteve & M. H. Devoret. Quantum coherence with a single Cooper pair. *Phys. Scr.*, **T76** 165 (1998). Cited on page 2.
- [Bozyigit10] D. Bozyigit. *Correlation Function Measurements of a Microwave Frequency Single Photon Source*. Master's thesis, ETH Zurich (2010). Cited on pages 35 and 43.
- [Bozyigit11] D. Bozyigit, C. Lang, L. Steffen, J. M. Fink, C. Eichler, M. Baur, R. Bianchetti, P. J. Leek, S. Filipp, M. P. da Silva, A. Blais & A. Wallraff. Antibunching of microwave-frequency photons observed in correlation measurements using linear detectors. *Nat. Phys.*, **7** 154 (2011). Cited on pages 3, 33, 37, 38, 43, 44, 54, 57, 61, 62, 66, 67, 70, 118, 122, 124 and 125.
- [Braginski96] V. B. Braginski & F. Y. Khalili. Quantum nondemolition measurements: The route from toys to tools. *Rev. Mod. Phys.*, **68** 1 (1996). Cited on page 8.
- [Braunstein91] S. L. Braunstein, C. M. Caves & G. J. Milburn. Interpretation for a positive P representation. *Phys. Rev. A*, **43** 1153 (1991). Cited on pages 45, 68 and 145.
- [Braunstein05] S. L. Braunstein & P. van Loock. Quantum information with continuous variables. *Rev. Mod. Phys.*, **77** 513 (2005). Cited on pages 78, 87, 109, 112, 115 and 138.
- [Brune96] M. Brune, F. Schmidt-Kaler, A. Maali, J. Dreyer, E. Hagley, J. M. Raimond & S. Haroche. Quantum Rabi oscillation: A direct test of field quantization in a cavity. *Phys. Rev. Lett.*, **76** 1800 (1996). Cited on page 37.
- [Buisson01] O. Buisson & F. Hekking. Entangled states in a Josephson charge qubit coupled to a superconducting resonator. In A. D. V., B. Ruggiero & P. Silvestrini, eds., *Macroscopic Quantum Coherence and Quantum Computing*. Kluwer, New York (2001). Cited on page 2.
- [Buks06] E. Buks & B. Yurke. Dephasing due to intermode coupling in superconducting stripline resonators. *Phys. Rev. A*, **73** 023815 (2006). Cited on page 95.
- [Burkhard12] S. Burkhard. *Optimization of transmon design for longer coherence time*. Semester thesis, ETH Zurich (2012). Cited on pages 14 and 23.
- [Burnham70] D. C. Burnham & D. L. Weinberg. Observation of simultaneity in parametric production of optical photon pairs. *Phys. Rev. Lett.*, **25** 84 (1970). Cited on pages 77 and 78.
- [Büttiker87] M. Büttiker. Zero-current persistent potential drop across small-capacitance Josephson junctions. *Phys. Rev. B*, **36** 3548 (1987). Cited on pages 12 and 13.
- [Bužek96] V. Bužek, G. Adam & G. Drobný. Quantum state reconstruction and detection of quantum coherences on different observation levels. *Phys. Rev. A*, **54** 804 (1996). Cited on pages 38, 55 and 56.
- [Bylander11] J. Bylander, S. Gustavsson, F. Yan, F. Yoshihara, K. Harrabi, G. Fitch, D. G. Cory, Y. Nakamura, J.-S. Tsai & O. W. D. Noise spectroscopy through dynamical decoupling with a superconducting flux qubit. *Nature Physics*, **7** 565 (2011). Cited on page 41.
- [Cahill69a] K. E. Cahill & R. J. Glauber. Density operators and quasiprobability distributions. *Phys. Rev.*, **177** 1882 (1969). Cited on page 53.
- [Cahill69b] K. E. Cahill & R. J. Glauber. Ordered expansions in boson amplitude operators. *Phys. Rev.*, **177** 1857 (1969). Cited on page 144.
- [Carmichael99] H. J. Carmichael. *Statistical Methods in Quantum Optics 1: Master Equations and Fokker-Planck Equations*. Springer-Verlag (1999). Cited on pages 38, 52 and 133.
- [Carmichael08] H. J. Carmichael. *Statistical Methods in Quantum Optics 2: Non-Classical Fields*. Springer-Verlag (2008). Cited on page 44.

- [Castellanos-Beltran07] M. A. Castellanos-Beltran & K. W. Lehnert. Widely tunable parametric amplifier based on a superconducting quantum interference device array resonator. *Appl. Phys. Lett.*, **91** 083509 (2007). Cited on pages 13 and 77.
- [Castellanos-Beltran08] M. A. Castellanos-Beltran, K. D. Irwin, G. C. Hilton, L. R. Vale & K. W. Lehnert. Amplification and squeezing of quantum noise with a tunable Josephson metamaterial. *Nat. Phys.*, **4** 929 (2008). Cited on pages 3, 37, 47, 61, 64, 77, 89, 104, 109, 114 and 120.
- [Catelani12] G. Catelani, S. E. Nigg, S. M. Girvin, R. J. Schoelkopf & L. I. Glazman. Decoherence of superconducting qubits caused by quasiparticle tunneling. *Phys. Rev. B*, **86** 184514 (2012). Cited on page 8.
- [Caves82] C. M. Caves. Quantum limits on noise in linear amplifiers. *Phys. Rev. D*, **26** 1817 (1982). Cited on pages 45, 46, 87 and 104.
- [Caves94] C. M. Caves & P. D. Drummond. Quantum limits on bosonic communication rates. *Rev. Mod. Phys.*, **66** 481 (1994). Cited on pages 45 and 47.
- [Chen11] Y.-F. Chen, D. Hover, S. Sendelbach, L. Maurer, S. T. Merkel, E. J. Pritchett, F. K. Wilhelm & R. McDermott. Microwave photon counter based on Josephson junctions. *Phys. Rev. Lett.*, **107** 217401 (2011). Cited on pages 3, 33, 37, 130 and 138.
- [Chiorescu03] I. Chiorescu, Y. Nakamura, C. J. P. M. Harmans & J. E. Mooij. Coherent quantum dynamics of a superconducting flux qubit. *Science*, **299** 1869 (2003). Cited on page 15.
- [Chiorescu04] I. Chiorescu, P. Bertet, K. Semba, Y. Nakamura, C. J. P. M. Harmans & J. E. Mooij. Coherent dynamics of a flux qubit coupled to a harmonic oscillator. *Nature*, **431** 159 (2004). Cited on page 2.
- [Chow12] J. M. Chow, J. M. Gambetta, A. D. Córcoles, S. T. Merkel, J. A. Smolin, C. Rigetti, S. Poletto, G. A. Keefe, M. B. Rothwell, J. R. Rozen, M. B. Ketchen & M. Steffen. Universal quantum gate set approaching fault-tolerant thresholds with superconducting qubits. *Phys. Rev. Lett.*, **109** 060501 (2012). Cited on pages 60 and 62.
- [Chuang98] I. L. Chuang, L. M. K. Vandersypen, X. Zhou, D. W. Leung & S. Lloyd. Experimental realization of a quantum algorithm. *Nature*, **393** 143 (1998). Cited on page 2.
- [Cirac97] J. I. Cirac, P. Zoller, H. J. Kimble & H. Mabuchi. Quantum state transfer and entanglement distribution among distant nodes in a quantum network. *Phys. Rev. Lett.*, **78** 3221 (1997). Cited on page 139.
- [Clerk10] A. A. Clerk, M. H. Devoret, S. M. Girvin, F. Marquardt & R. J. Schoelkopf. Introduction to quantum noise, measurement, and amplification. *Rev. Mod. Phys.*, **82** 1155 (2010). Cited on pages 34, 45, 77, 87 and 89.
- [daSilva10] M. P. da Silva, D. Bozyigit, A. Wallraff & A. Blais. Schemes for the observation of photon correlation functions in circuit QED with linear detectors. *Phys. Rev. A*, **82** 043804 (2010). Cited on pages 46, 56, 58, 67 and 125.
- [Davis95] K. B. Davis, M. O. Mewes, M. R. Andrews, N. J. van Druten, D. S. Durfee, D. M. Kurn & W. Ketterle. Bose-Einstein condensation in a gas of sodium atoms. *Phys. Rev. Lett.*, **75** 3969 (1995). Cited on page 1.
- [De Greve12] K. De Greve, L. Yu, P. L. McMahon, J. S. Pelc, C. M. Natarajan, N. Y. Kim, E. Abe, S. Maier, C. Schneider, M. Kamp, S. Hofling, R. H. Hadfield, A. Forchel, M. M. Fejer & Y. Yamamoto. Quantum-dot spin-photon entanglement via frequency downconversion to telecom wavelength. *Nature*, **491** 421 (2012). Cited on page 117.

- [Delbecq11] M. R. Delbecq, V. Schmitt, F. D. Parmentier, N. Roch, J. J. Viennot, G. Fève, B. Huard, C. Mora, A. Cottet & T. Kontos. Coupling a quantum dot, fermionic leads, and a microwave cavity on a chip. *Phys. Rev. Lett.*, **107** 256804 (2011). Cited on page 37.
- [Deleglise08] S. Deleglise, I. Dotsenko, C. Sayrin, J. Bernu, M. Brune, J.-M. Raimond & S. Haroche. Reconstruction of non-classical cavity field states with snapshots of their decoherence. *Nature*, **455** 510 (2008). Cited on pages 3 and 37.
- [Deppe08] F. Deppe, M. Mariani, E. P. Menzel, A. Marx, S. Saito, K. Kakuyanagi, H. Tanaka, T. Meno, K. Semba, H. Takayanagi, E. Solano & R. Gross. Two-photon probe of the Jaynes-Cummings model and controlled symmetry breaking in circuit QED. *Nat. Phys.*, **4** 686 (2008). Cited on page 2.
- [Deutsch85] D. Deutsch. Quantum theory, the Church-Turing principle and the universal quantum computer. *Proceedings of the Royal Society of London. Series A, Mathematical and Physical Sciences*, **400** 97 (1985). Cited on page 2.
- [Devoret85] M. H. Devoret, J. M. Martinis & J. Clarke. Measurements of macroscopic quantum tunneling out of the zero-voltage state of a current-biased Josephson junction. *Phys. Rev. Lett.*, **55** 1908 (1985). Cited on page 1.
- [Devoret97] M. H. Devoret. Quantum fluctuations in electrical circuits. In S. Reynaud, E. Giacobino & J. Zinn-Justin, eds., *Quantum Fluctuations: Les Houches Session LXIII*, pp. 351–386. Elsevier (1997). Cited on pages 9 and 11.
- [Devoret04] M. H. Devoret & J. M. Martinis. Implementing qubits with superconducting integrated circuits. *Quantum Information Processing*, **3** 163 (2004). Cited on page 13.
- [Devoret07] M. Devoret, S. Girvin & R. Schoelkopf. Circuit-QED: How strong can the coupling between a Josephson junction atom and a transmission line resonator be? *Annalen der Physik*, **16** 767 (2007). Cited on page 22.
- [Dewes12] A. Dewes, F. R. Ong, V. Schmitt, R. Lauro, N. Boulant, P. Bertet, D. Vion & D. Esteve. Characterization of a two-transmon processor with individual single-shot qubit readout. *Phys. Rev. Lett.*, **108** 057002 (2012). Cited on page 138.
- [Di Vincenzo95] D. P. Di Vincenzo. Quantum computation. *Science*, **270** 255 (1995). Cited on page 7.
- [DiCarlo09] L. DiCarlo, J. M. Chow, J. M. Gambetta, L. S. Bishop, B. R. Johnson, D. I. Schuster, J. Majer, A. Blais, L. Frunzio, S. M. Girvin & R. J. Schoelkopf. Demonstration of two-qubit algorithms with a superconducting quantum processor. *Nature*, **460** 240 (2009). Cited on page 3.
- [DiCarlo10] L. DiCarlo, M. D. Reed, L. Sun, B. R. Johnson, J. M. Chow, J. M. Gambetta, L. Frunzio, S. M. Girvin, M. H. Devoret & R. J. Schoelkopf. Preparation and measurement of three-qubit entanglement in a superconducting circuit. *Nature*, **467** 574 (2010). Cited on page 3.
- [Diedrich87] F. Diedrich & H. Walther. Nonclassical radiation of a single stored ion. *Phys. Rev. Lett.*, **58** 203 (1987). Cited on page 38.
- [Dirac27] P. Dirac. The quantum theory of the emission and absorption of radiation. *Proc. R. Soc. London*, **A 114** 243 (1927). Cited on page 1.
- [DiVincenzo06] D. P. DiVincenzo, F. Brito & R. H. Koch. Decoherence rates in complex Josephson qubit circuits. *Phys. Rev. B*, **74** 014514 (2006). Cited on page 8.
- [Dobek11] K. Dobek, M. Karpiński, R. Demkowicz-Dobrzański, K. Banaszek & P. Horodecki. Experimental extraction of secure correlations from a noisy private state. *Phys. Rev. Lett.*, **106** 030501 (2011). Cited on page 62.

- [Drummond80] P. D. Drummond & C. W. Gardiner. Generalised P-representations in quantum optics. *Journal of Physics A Mathematical General*, **13** 2353 (1980). Cited on pages 66, 67 and 68.
- [Duan01] L. M. Duan, J. I. Cirac & P. Zoller. Geometric manipulation of trapped ions for quantum computation. *Science*, **292** 1695 (2001). Cited on page 70.
- [Duan10] L.-M. Duan & C. Monroe. Colloquium: Quantum networks with trapped ions. *Rev. Mod. Phys.*, **82** 1209 (2010). Cited on page 139.
- [Dykman80] M. Dykman & M. Krivoglaz. Fluctuations in nonlinear systems near bifurcations corresponding to the appearance of new stable states. *Physica A: Statistical Mechanics and its Applications*, **104** 480 (1980). Cited on page 81.
- [Dyson49] F. J. Dyson. The radiation theories of Tomonaga, Schwinger, and Feynman. *Phys. Rev.*, **75** 486 (1949). Cited on page 1.
- [Eichler11a] C. Eichler, D. Bozyigit, C. Lang, M. Baur, L. Steffen, J. M. Fink, S. Filipp & A. Wallraff. Observation of two-mode squeezing in the microwave frequency domain. *Phys. Rev. Lett.*, **107** 113601 (2011). Cited on pages 3, 4, 37, 47, 54, 64, 77, 104 and 137.
- [Eichler11b] C. Eichler, D. Bozyigit, C. Lang, L. Steffen, J. Fink & A. Wallraff. Experimental state tomography of itinerant single microwave photons. *Phys. Rev. Lett.*, **106** 220503 (2011). Cited on pages 3, 4, 33, 37, 43, 44, 49, 50, 54, 55, 60, 61, 112, 118, 124 and 137.
- [Eichler12a] C. Eichler, D. Bozyigit & A. Wallraff. Characterizing quantum microwave radiation and its entanglement with superconducting qubits using linear detectors. *Phys. Rev. A*, **86** 032106 (2012). Cited on pages 3, 4, 27, 33, 125 and 137.
- [Eichler12b] C. Eichler, C. Lang, J. M. Fink, J. Govenius, S. Filipp & A. Wallraff. Observation of entanglement between itinerant microwave photons and a superconducting qubit. *Phys. Rev. Lett.*, **109** 240501 (2012). Cited on pages 3, 4, 27, 61 and 137.
- [Einstein05] A. Einstein. On a heuristic viewpoint concerning the production and transformation of light. *Annalen der Physik*, **17** 132 (1905). Cited on page 1.
- [Einstein35] A. Einstein, B. Podolsky & N. Rosen. Can quantum-mechanical description of physical reality be considered complete? *Phys. Rev.*, **47** 777 (1935). Cited on page 109.
- [Fedorov12] A. Fedorov, L. Steffen, M. Baur, M. P. da Silva & A. Wallraff. Implementation of a Toffoli gate with superconducting circuits. *Nature*, **481** 170 (2012). Cited on pages 3 and 138.
- [Ferguson13] D. G. Ferguson, A. A. Houck & J. Koch. Symmetries and collective excitations in large superconducting circuits. *Phys. Rev. X*, **3** 011003 (2013). Cited on page 97.
- [Feynman50] R. P. Feynman. Mathematical formulation of the quantum theory of electromagnetic interaction. *Phys. Rev.*, **80** 440 (1950). Cited on page 1.
- [Feynman82] R. P. Feynman. Simulating physics with computers. *Int. J. Theor. Phys.*, **21** 467 (1982). Cited on page 2.
- [Filipp09] S. Filipp, P. Maurer, P. J. Leek, M. Baur, R. Bianchetti, J. M. Fink, M. Göppl, L. Steffen, J. M. Gambetta, A. Blais & A. Wallraff. Two-qubit state tomography using a joint dispersive readout. *Phys. Rev. Lett.*, **102** 200402 (2009). Cited on page 2.
- [Filipp11] S. Filipp, M. Göppl, J. M. Fink, M. Baur, R. Bianchetti, L. Steffen & A. Wallraff. Multimode mediated qubit-qubit coupling and dark-state symmetries in circuit quantum electrodynamics. *Phys. Rev. A*, **83** 063827 (2011). Cited on page 23.
- [Filippov11] S. N. Filippov & V. I. Man'ko. Measuring microwave quantum states: Tomogram and moments. *Phys. Rev. A*, **84** 033827 (2011). Cited on page 47.

- [Fink08] J. M. Fink, M. Göppl, M. Baur, R. Bianchetti, P. J. Leek, A. Blais & A. Wallraff. Climbing the Jaynes-Cummings ladder and observing its nonlinearity in a cavity QED system. *Nature*, **454** 315 (2008). Cited on pages 2 and 26.
- [Fink10a] J. Fink. *Quantum nonlinearities in strong coupling circuit QED*. Ph.D. thesis, ETH Zurich (2010). Cited on pages 28 and 32.
- [Fink10b] J. M. Fink, L. Steffen, P. Studer, L. S. Bishop, M. Baur, R. Bianchetti, D. Bozyigit, C. Lang, S. Filipp, P. J. Leek & A. Wallraff. Quantum-to-classical transition in cavity quantum electrodynamics. *Physical Review Letters*, **105** 163601 (2010). Cited on pages 26, 55 and 114.
- [Flagg10] E. B. Flagg, A. Muller, S. V. Polyakov, A. Ling, A. Migdall & G. S. Solomon. Interference of single photons from two separate semiconductor quantum dots. *Phys. Rev. Lett.*, **104** 137401 (2010). Cited on page 70.
- [Flurin12] E. Flurin, N. Roch, F. Mallet, M. H. Devoret & B. Huard. Generating entangled microwave radiation over two transmission lines. *Phys. Rev. Lett.*, **109** 183901 (2012). Cited on pages 37, 58, 79, 104, 109, 118 and 138.
- [Fragner08] A. Fragner, M. Göppl, J. M. Fink, M. Baur, R. Bianchetti, P. J. Leek, A. Blais & A. Wallraff. Resolving vacuum fluctuations in an electrical circuit by measuring the Lamb shift. *Science*, **322** 1357 (2008). Cited on page 2.
- [Frey12] T. Frey, P. J. Leek, M. Beck, A. Blais, T. Ihn, K. Ensslin & A. Wallraff. Dipole coupling of a double quantum dot to a microwave resonator. *Phys. Rev. Lett.*, **108** 046807 (2012). Cited on pages 3, 37 and 137.
- [Friedman00] J. R. Friedman, V. Patel, W. Chen, S. K. Tolpygo & J. E. Lukens. Quantum superposition of distinct macroscopic states. *Nature*, **406** 43 (2000). Cited on page 15.
- [Furusawa98] A. Furusawa, J. L. Sørensen, S. L. Braunstein, C. A. Fuchs, H. J. Kimble & E. S. Polzik. Unconditional quantum teleportation. *Science*, **282** 706 (1998). Cited on page 109.
- [Gabelli04] J. Gabelli, L.-H. Reydellet, G. Feve, J.-M. Berroir, B. Placais, P. Roche & D. C. Glattli. Hanbury Brown–Twiss correlations to probe the population statistics of GHz photons emitted by conductors. *Phys. Rev. Lett.*, **93** 056801 (2004). Cited on page 66.
- [Gambetta06] J. Gambetta, A. Blais, D. I. Schuster, A. Wallraff, L. Frunzio, J. Majer, M. H. Devoret, S. M. Girvin & R. J. Schoelkopf. Qubit-photon interactions in a cavity: Measurement-induced dephasing and number splitting. *Phys. Rev. A*, **74** 042318 (2006). Cited on pages 25 and 134.
- [Gambetta07] J. Gambetta, W. A. Braff, A. Wallraff, S. M. Girvin & R. J. Schoelkopf. Protocols for optimal readout of qubits using a continuous quantum nondemolition measurement. *Phys. Rev. A*, **76** 012325 (2007). Cited on page 121.
- [Gambetta11] J. M. Gambetta, A. A. Houck & A. Blais. Superconducting qubit with Purcell protection and tunable coupling. *Phys. Rev. Lett.*, **106** 030502 (2011). Cited on page 39.
- [Gao12] W. B. Gao, P. Fallahi, E. Togan, J. Miguel-Sanchez & A. Imamoglu. Observation of entanglement between a quantum dot spin and a single photon. *Nature*, **491** 426 (2012). Cited on page 117.
- [Gardiner85] C. W. Gardiner & M. J. Collett. Input and output in damped quantum systems: Quantum stochastic differential equations and the master equation. *Phys. Rev. A*, **31** 3761 (1985). Cited on pages 19, 47, 82 and 131.
- [Gardiner91] C. W. Gardiner & P. Zoller. *Quantum Noise*. Springer (1991). Cited on page 21.

- [Geerlings12] K. Geerlings, S. Shankar, E. Edwards, L. Frunzio, R. J. Schoelkopf & M. H. Devoret. Improving the quality factor of microwave compact resonators by optimizing their geometrical parameters. *Applied Physics Letters*, **100** 192601 (2012). Cited on page 15.
- [Gerry05] C. Gerry & P. L. Knight. *Introductory Quantum Optics*. Cambridge University Press (2005). Cited on page 38.
- [Girvin11] S. M. Girvin. Superconducting qubits and circuits: Artificial atoms coupled to microwave photons (2011). Lectures delivered at Ecole d'Été Les Houches; To be published by Oxford University Press. Cited on pages 10 and 12.
- [Glauber63] R. J. Glauber. Coherent and incoherent states of the radiation field. *Phys. Rev.*, **131** 2766 (1963). Cited on pages 11 and 52.
- [Göppl08] M. Göppl, A. Fragner, M. Baur, R. Bianchetti, S. Filipp, J. M. Fink, P. J. Leek, G. Puebla, L. Steffen & A. Wallraff. Coplanar waveguide resonators for circuit quantum electrodynamics. *Journal of Applied Physics*, **104** 113904 (2008). Cited on pages 16, 85, 97 and 154.
- [Göppl09] M. Göppl. *Engineering Quantum Electronic Chips - Realization and Characterization of Circuit Quantum Electrodynamics Systems*. Ph.D. thesis, ETH Zurich (2009). Cited on page 28.
- [Gordon63] J. P. Gordon, W. H. Louisell & L. R. Walker. Quantum fluctuations and noise in parametric processes II. *Phys. Rev.*, **129** 481 (1963). Cited on page 77.
- [Govenius12] J. Govenius. *Single-Shot Qubit Readout in Circuit QED using Parametric Amplification*. Master's thesis, ETH Zurich (2012). Cited on page 150.
- [Gross82] M. Gross & S. Haroche. Superradiance: An essay on the theory of collective spontaneous emission. *Phys. Rep.*, **93** 301 (1982). Cited on page 137.
- [Grosshans03] F. Grosshans, G. Van Assche, J. Wenger, R. Brouri, N. J. Cerf & P. Grangier. Quantum key distribution using gaussian-modulated coherent states. *Nature*, **421** 238 (2003). Cited on page 109.
- [Grover96] L. K. Grover. A fast quantum mechanical algorithm for database search. In *Proceedings of the twenty-eighth annual ACM symposium on Theory of computing*, pp. 212–219. ACM, Philadelphia, Pennsylvania, United States (1996). Cited on page 2.
- [Guta12] M. Guta, T. Kypraios & I. Dryden. Rank-based model selection for multiple ions quantum tomography. *New Journal of Physics*, **14** 105002 (2012). Cited on page 61.
- [Hanson08] R. Hanson & D. D. Awschalom. Coherent manipulation of single spins in semiconductors. *Nature*, **453** 1043 (2008). Cited on page 2.
- [Haroche89] S. Haroche & D. Kleppner. Cavity quantum electrodynamics. *Phys. Today*, **42** 24 (1989). Cited on page 2.
- [Haroche06] S. Haroche & J.-M. Raimond. *Exploring the Quantum: Atoms, Cavities, and Photons*. Oxford University Press, Oxford (2006). Cited on pages 3, 22, 26, 59 and 118.
- [Hatridge11] M. Hatridge, R. Vijay, D. H. Slichter, J. Clarke & I. Siddiqi. Dispersive magnetometry with a quantum limited SQUID parametric amplifier. *Phys. Rev. B*, **83** 134501 (2011). Cited on pages 3, 37, 47, 64 and 77.
- [Hatridge13] M. Hatridge, S. Shankar, M. Mirrahimi, F. Schackert, K. Geerlings, T. Brecht, K. M. Sliwa, B. Abdo, L. Frunzio, S. M. Girvin, R. J. Schoelkopf & M. H. Devoret. Quantum back-action of an individual variable-strength measurement. *Science*, **339** 178 (2013). Cited on pages 130 and 131.

- [Haus62] H. A. Haus & J. A. Mullen. Quantum noise in linear amplifiers. *Phys. Rev.*, **128** 2407 (1962). Cited on page 45.
- [Heinzle12] L. Heinzle. *Pump cancellation for a parametric amplifier*. Semester thesis, Laboratory of solid state physics, ETH Zurich (2012). Cited on page 150.
- [Helmer09] F. Helmer, M. Mariantoni, E. Solano & F. Marquardt. Quantum nondemolition photon detection in circuit QED and the quantum Zeno effect. *Phys. Rev. A*, **79** 052115 (2009). Cited on page 95.
- [Helstrom76] C. W. Helstrom. *Quantum Detection and Estimation Theory*. Academic Press, New York (1976). Cited on page 63.
- [Herzog96] U. Herzog. Generating-function approach to the moment problem for the density matrix of a single mode. *Phys. Rev. A*, **53** 2889 (1996). Cited on page 57.
- [Ho Eom12] B. Ho Eom, P. K. Day, H. G. LeDuc & J. Zmuidzinas. A wideband, low-noise superconducting amplifier with high dynamic range. *Nat Phys*, **8** 623 (2012). Cited on pages 3 and 79.
- [Hofheinz08] M. Hofheinz, E. M. Weig, M. Ansmann, R. C. Bialczak, E. Lucero, M. Neeley, A. D. O'Connell, H. Wang, J. M. Martinis & A. N. Cleland. Generation of Fock states in a superconducting quantum circuit. *Nature*, **454** 310 (2008). Cited on pages 3 and 27.
- [Hofheinz09] M. Hofheinz, H. Wang, M. Ansmann, R. C. Bialczak, E. Lucero, M. Neeley, A. D. O'Connell, D. Sank, J. Wenner, J. M. Martinis & A. N. Cleland. Synthesizing arbitrary quantum states in a superconducting resonator. *Nature*, **459** 546 (2009). Cited on pages 3, 37 and 118.
- [Hofmann12] J. Hofmann, M. Krug, N. Ortegel, L. Gérard, M. Weber, W. Rosenfeld & H. Weinfurter. Herald entanglement between widely separated atoms. *Science*, **337** 72 (2012). Cited on page 70.
- [Hogan12] S. D. Hogan, J. A. Agner, F. Merkt, T. Thiele, S. Filipp & A. Wallraff. Driving Rydberg-Rydberg transitions from a coplanar microwave waveguide. *Physical Review Letters*, **108** 063004 (2012). Cited on page 37.
- [Hoi12] I.-C. Hoi, T. Palomaki, J. Lindkvist, G. Johansson, P. Delsing & C. M. Wilson. Generation of nonclassical microwave states using an artificial atom in 1D open space. *Phys. Rev. Lett.*, **108** 263601 (2012). Cited on pages 118 and 137.
- [Hong87] C. K. Hong, Z. Y. Ou & L. Mandel. Measurement of subpicosecond time intervals between two photons by interference. *Phys. Rev. Lett.*, **59** 2044 (1987). Cited on page 70.
- [Houck07] A. Houck, D. Schuster, J. Gambetta, J. Schreier, B. Johnson, J. Chow, L. Frunzio, J. Majer, M. Devoret, S. Girvin & R. Schoelkopf. Generating single microwave photons in a circuit. *Nature*, **449** 328 (2007). Cited on pages 37 and 118.
- [Houck08] A. A. Houck, J. A. Schreier, B. R. Johnson, J. M. Chow, J. Koch, J. M. Gambetta, D. I. Schuster, L. Frunzio, M. H. Devoret, S. M. Girvin & R. J. Schoelkopf. Controlling the spontaneous emission of a superconducting transmon qubit. *Phys. Rev. Lett.*, **101** 080502 (2008). Cited on pages 38, 43 and 44.
- [Houck12] A. A. Houck, H. E. Tureci & J. Koch. On-chip quantum simulation with superconducting circuits. *Nat. Phys.*, **8** 292 (2012). Cited on page 137.
- [Hradil97] Z. Hradil. Quantum-state estimation. *Phys. Rev. A*, **55** R1561 (1997). Cited on page 63.
- [Hradil04] Z. Hradil, J. Rehacek, J. Fiurasek & M. Jezek. Maximum-likelihood methods in quantum mechanics. In M. Paris & J. Rehacek, eds., *Quantum State Estimation*, Lecture Notes in Physics. Springer (2004). Cited on pages 60, 62 and 63.

- [Hradil06] Z. Hradil, D. Mogilevtsev & J. Řeháček. Biased tomography schemes: An objective approach. *Phys. Rev. Lett.*, **96** 230401 (2006). Cited on page 63.
- [Řeháček07] J. Řeháček, Z. c. v. Hradil, E. Knill & A. I. Lvovsky. Diluted maximum-likelihood algorithm for quantum tomography. *Phys. Rev. A*, **75** 042108 (2007). Cited on page 62.
- [Řeháček08] J. Řeháček, D. Mogilevtsev & Z. Hradil. Tomography for quantum diagnostics. *New Journal of Physics*, **10** 043022 (2008). Cited on page 62.
- [Imamoğlu97] A. Imamoğlu, H. Schmidt, G. Woods & M. Deutsch. Strongly interacting photons in a nonlinear cavity. *Phys. Rev. Lett.*, **79** 1467 (1997). Cited on pages 26 and 137.
- [Imoto85] N. Imoto, H. A. Haus & Y. Yamamoto. Quantum nondemolition measurement of the photon number via the optical Kerr effect. *Phys. Rev. A*, **32** 2287 (1985). Cited on page 95.
- [Ithier05] G. Ithier, E. Collin, P. Joyez, P. J. Meeson, D. Vion, D. Esteve, F. Chiarello, A. Shnirman, Y. Makhlin, J. Schrieffer & G. Schön. Decoherence in a superconducting quantum bit circuit. *Phys. Rev. B*, **72** 134519 (2005). Cited on pages 8 and 41.
- [Jahne07] K. Jahne, B. Yurke & U. Gavish. High-fidelity transfer of an arbitrary quantum state between harmonic oscillators. *Phys. Rev. A*, **75** 010301 (2007). Cited on page 139.
- [Jaynes63] E. Jaynes & F. Cummings. Comparison of quantum and semiclassical radiation theories with application to the beam maser. *Proceedings of the IEEE*, **51** 89 (1963). Cited on page 23.
- [Johansson09] J. R. Johansson, G. Johansson, C. M. Wilson & F. Nori. Dynamical Casimir effect in a superconducting coplanar waveguide. *Phys. Rev. Lett.*, **103** 147003 (2009). Cited on page 79.
- [Johnson10] B. R. Johnson, M. D. Reed, A. A. Houck, D. I. Schuster, L. S. Bishop, E. Ginossar, J. M. Gambetta, L. DiCarlo, L. Frunzio, S. M. Girvin & R. J. Schoelkopf. Quantum non-demolition detection of single microwave photons in a circuit. *Nat. Phys.*, **6** 663 (2010). Cited on pages 2 and 95.
- [Johnson12] J. E. Johnson, C. Macklin, D. H. Slichter, R. Vijay, E. B. Weingarten, J. Clarke & I. Siddiqi. Heralded state preparation in a superconducting qubit. *Phys. Rev. Lett.*, **109** 050506 (2012). Cited on page 77.
- [Josephson62] B. D. Josephson. Possible new effects in superconductive tunnelling. *Physics Letters*, **1** 251 (1962). Cited on page 12.
- [Kaltenbaek06] R. Kaltenbaek, B. Blauensteiner, M. Żukowski, M. Aspelmeyer & A. Zeilinger. Experimental interference of independent photons. *Phys. Rev. Lett.*, **96** 240502 (2006). Cited on page 70.
- [Kamal09] A. Kamal, A. Marblestone & M. Devoret. Signal-to-pump back-action and self-oscillation in double-pump Josephson parametric amplifier (2009). Cited on pages 77, 79, 89 and 109.
- [Kamal11] A. Kamal, J. Clarke & M. H. Devoret. Noiseless non-reciprocity in a parametric active device. *Nat Phys*, **7** 311 (2011). Cited on page 33.
- [Kiesel11] T. Kiesel, W. Vogel, B. Hage & R. Schnabel. Direct sampling of negative quasiprobabilities of a squeezed state. *Phys. Rev. Lett.*, **107** 113604 (2011). Cited on page 55.
- [Kim97] M. S. Kim. Quasiprobability functions measured by photon statistics of amplified signal fields. *Phys. Rev. A*, **56** 3175 (1997). Cited on page 54.
- [Kimble08] H. J. Kimble. The quantum internet. *Nature*, **453** 1023 (2008). Cited on pages 117 and 138.

- [Kinion08] D. Kinion & J. Clarke. Microstrip superconducting quantum interference device radio-frequency amplifier: Scattering parameters and input coupling. *Applied Physics Letters*, **92** 172503 (2008). Cited on pages 37 and 54.
- [Knill01] E. Knill, R. Laflamme & G. J. Milburn. A scheme for efficient quantum computation with linear optics. *Nature*, **409** 46 (2001). Cited on pages 38, 70 and 138.
- [Koch07] J. Koch, T. M. Yu, J. Gambetta, A. A. Houck, D. I. Schuster, J. Majer, A. Blais, M. H. Devoret, S. M. Girvin & R. J. Schoelkopf. Charge-insensitive qubit design derived from the Cooper pair box. *Phys. Rev. A*, **76** 042319 (2007). Cited on pages 3, 8, 13, 14, 23, 24, 39 and 41.
- [Kok02] P. Kok, H. Lee & J. P. Dowling. Creation of large-photon-number path entanglement conditioned on photodetection. *Phys. Rev. A*, **65** 052104 (2002). Cited on page 71.
- [Korotkov11] A. N. Korotkov. Quantum bayesian approach to circuit QED measurement. arXiv:1111.4016v1 [quant-ph] (2011). Cited on page 131.
- [Krauter11] H. Krauter, C. A. Muschik, K. Jensen, W. Wasilewski, J. M. Petersen, J. I. Cirac & E. S. Polzik. Entanglement generated by dissipation and steady state entanglement of two macroscopic objects. *Phys. Rev. Lett.*, **107** 080503 (2011). Cited on page 8.
- [Kubo10] Y. Kubo, F. R. Ong, P. Bertet, D. Vion, V. Jacques, D. Zheng, A. Dréau, J.-F. Roch, A. Auffeves, F. Jelezko, J. Wrachtrup, M. F. Barthe, P. Bergonzo & D. Esteve. Strong coupling of a spin ensemble to a superconducting resonator. *Phys. Rev. Lett.*, **105** 140502 (2010). Cited on page 37.
- [Kubo11] Y. Kubo, C. Grezes, A. Dewes, T. Umeda, J. Isoya, H. Sumiya, N. Morishita, H. Abe, S. Onoda, T. Ohshima, V. Jacques, A. Dréau, J.-F. Roch, I. Diniz, A. Auffeves, D. Vion, D. Esteve & P. Bertet. Hybrid quantum circuit with a superconducting qubit coupled to a spin ensemble. *Phys. Rev. Lett.*, **107** 220501 (2011). Cited on page 137.
- [Laflamme12] C. Laflamme & A. A. Clerk. Weak Qubit Measurement with a Nonlinear Cavity: Beyond Perturbation Theory. *Physical Review Letters*, **109** 123602 (2012). Cited on pages 26 and 136.
- [Lambert10] N. Lambert, Y.-N. Chen & F. Nori. Unified single-photon and single-electron counting statistics: From cavity QED to electron transport. *Phys. Rev. A*, **82** 063840 (2010). Cited on page 138.
- [Lang09] C. Lang. *Read-Out Strategies for Multi-Qubit States in Circuit Quantum Electrodynamics*. Diploma thesis, ETH Zurich and LMU Munich (2009). Cited on pages 34 and 35.
- [Lang11] C. Lang, D. Bozyigit, C. Eichler, L. Steffen, J. M. Fink, A. A. Abdumalikov Jr., M. Baur, S. Filipp, M. P. da Silva, A. Blais & A. Wallraff. Observation of resonant photon blockade at microwave frequencies using correlation function measurements. *Phys. Rev. Lett.*, **106** 243601 (2011). Cited on pages 3, 26, 37, 54, 61, 66, 67, 110 and 137.
- [Lang13] C. Lang, C. Eichler, L. Steffen, J. M. Fink, M. J. Woolley, A. Blais & A. Wallraff. Probing correlations, indistinguishability and entanglement in hong-ou-mandel experiments at microwave frequencies. *Nat. Phys.*, p. in print (2013). Cited on page 70.
- [Lee11] N. Lee, H. Benichi, Y. Takeno, S. Takeda, J. Webb, E. Huntington & A. Furusawa. Teleportation of nonclassical wave packets of light. *Science*, **332** 330 (2011). Cited on page 12.
- [Leek10] P. J. Leek, M. Baur, J. M. Fink, R. Bianchetti, L. Steffen, S. Filipp & A. Wallraff. Cavity quantum electrodynamics with separate photon storage and qubit readout modes. *Physical Review Letters*, **104** 100504 (2010). Cited on page 121.

- [Leibrandt09] D. R. Leibrandt, J. Labaziewicz, V. Vuletić & I. L. Chuang. Cavity sideband cooling of a single trapped ion. *Phys. Rev. Lett.*, **103** 103001 (2009). Cited on page 8.
- [Lenander11] M. Lenander, H. Wang, R. C. Bialczak, E. Lucero, M. Mariantoni, M. Neeley, A. D. O'Connell, D. Sank, M. Weides, J. Wenner, T. Yamamoto, Y. Yin, J. Zhao, A. N. Cleland & J. M. Martinis. Measurement of energy decay in superconducting qubits from nonequilibrium quasiparticles. *Phys. Rev. B*, **84** 024501 (2011). Cited on page 8.
- [Leonhardt93] U. Leonhardt & H. Paul. Realistic optical homodyne measurements and quasiprobability distributions. *Phys. Rev. A*, **48** 4598 (1993). Cited on page 54.
- [Leonhardt94] U. Leonhardt & H. Paul. High-accuracy optical homodyne detection with low-efficiency detectors: "preamplification" from antisqueezing. *Phys. Rev. Lett.*, **72** 4086 (1994). Cited on page 46.
- [Lettow10] R. Lettow, Y. L. A. Rezus, A. Renn, G. Zumofen, E. Ikonen, S. Götzinger & V. Sandoghdar. Quantum interference of tunably indistinguishable photons from remote organic molecules. *Phys. Rev. Lett.*, **104** 123605 (2010). Cited on page 70.
- [Lindblad76] G. Lindblad. On the generators of quantum dynamical semigroups. *Communications in Mathematical Physics*, **48** 119 (1976). Cited on page 21.
- [Loudon00] R. Loudon. *The Quantum Theory of Light*. Oxford U (2000). Cited on page 46.
- [Louisell60] W. H. Louisell. *Coupled mode and parametric electronics*. John Wiley, New York (1960). Cited on page 79.
- [Louisell61] W. H. Louisell, A. Yariv & A. E. Siegman. Quantum fluctuations and noise in parametric processes I. *Phys. Rev.*, **124** 1646 (1961). Cited on page 77.
- [Lounis05] B. Lounis & M. Orrit. Single-photon sources. *Rep. Prog. Phys.*, **68** 1129 (2005). Cited on page 38.
- [Lucero12] E. Lucero, R. Barends, Y. Chen, J. Kelly, M. Mariantoni, A. Megrant, P. O'Malley, D. Sank, A. Vainsencher, J. Wenner, T. White, Y. Yin, A. N. Cleland & J. M. Martinis. Computing prime factors with a Josephson phase qubit quantum processor. *Nat. Phys.*, **8** 719 (2012). Cited on page 3.
- [Lupaşcu07] A. Lupaşcu, S. Saito, T. Picot, P. C. de Groot, C. J. P. M. Harmans & J. E. Mooij. Quantum non-demolition measurement of a superconducting two-level system. *Nat. Phys.*, **3** 119 (2007). Cited on page 26.
- [Lvovsky04] A. I. Lvovsky. Iterative maximum-likelihood reconstruction in quantum homodyne tomography. *Journal of Optics B: Quantum and Semiclassical Optics*, **6** S556 (2004). Cited on pages 62 and 63.
- [Lvovsky09] A. I. Lvovsky & M. G. Raymer. Continuous-variable optical quantum-state tomography. *Rev. Mod. Phys.*, **81** 299 (2009). Cited on pages 45, 47, 62 and 63.
- [Mabuchi02] H. Mabuchi & A. C. Doherty. Cavity quantum electrodynamics: Coherence in context. *Science*, **298** 1372 (2002). Cited on page 2.
- [Majer07] J. Majer, J. M. Chow, J. M. Gambetta, J. Koch, B. R. Johnson, J. A. Schreier, L. Frunzio, D. I. Schuster, A. A. Houck, A. Wallraff, A. Blais, M. H. Devoret, S. M. Girvin & R. J. Schoelkopf. Coupling superconducting qubits via a cavity bus. *Nature*, **449** 443 (2007). Cited on pages 2 and 15.
- [Makhlin01] Y. Makhlin, G. Schön & A. Shnirman. Quantum-state engineering with Josephson-junction devices. *Rev. Mod. Phys.*, **73** 357 (2001). Cited on pages 2, 12 and 13.

- [Mallet09] F. Mallet, F. R. Ong, A. Palacios-Laloy, F. Nguyen, P. Bertet, D. Vion & D. Esteve. Single-shot qubit readout in circuit quantum electrodynamics. *Nat. Phys.*, **5** 791 (2009). Cited on pages 81 and 146.
- [Mallet11] F. Mallet, M. A. Castellanos-Beltran, H. S. Ku, S. Glancy, E. Knill, K. D. Irwin, G. C. Hilton, L. R. Vale & K. W. Lehnert. Quantum state tomography of an itinerant squeezed microwave field. *Phys. Rev. Lett.*, **106** 220502 (2011). Cited on pages 3, 37, 47, 54, 58, 107, 109 and 118.
- [Manucharyan09] V. E. Manucharyan, J. Koch, L. I. Glazman & M. H. Devoret. Fluxonium: Single cooper-pair circuit free of charge offsets. *Science*, **326** 113 (2009). Cited on page 15.
- [Mariantoni10] M. Mariantoni, E. P. Menzel, F. Deppe, M. A. Araque Caballero, A. Baust, T. Niemczyk, E. Hoffmann, E. Solano, A. Marx & R. Gross. Planck spectroscopy and quantum noise of microwave beam splitters. *Phys. Rev. Lett.*, **105** 133601 (2010). Cited on pages 11 and 66.
- [Mariantoni11a] M. Mariantoni, H. Wang, R. C. Bialczak, M. Lenander, E. Lucero, M. Neeley, A. D. O’Connell, D. Sank, M. Weides, J. Wenner, T. Yamamoto, Y. Yin, J. Zhao, J. M. Martinis & A. N. Cleland. Photon shell game in three-resonator circuit quantum electrodynamics. *Nat. Phys.*, **7** 287 (2011). Cited on page 138.
- [Mariantoni11b] M. Mariantoni, H. Wang, T. Yamamoto, M. Neeley, R. C. Bialczak, Y. Chen, M. Lenander, E. Lucero, A. D. O’Connell, D. Sank, M. Weides, J. Wenner, Y. Yin, J. Zhao, A. N. Korotkov, A. N. Cleland & J. M. Martinis. Implementing the quantum von Neumann architecture with superconducting circuits. *Science*, **334** 61 (2011). Cited on page 3.
- [Marquardt01] F. Marquardt & C. Bruder. Superposition of two mesoscopically distinct quantum states: Coupling a Cooper-pair box to a large superconducting island. *Phys. Rev. B*, **63** 054514 (2001). Cited on page 2.
- [Marthaler06] M. Marthaler & M. I. Dykman. Switching via quantum activation: A parametrically modulated oscillator. *Physical Review A (Atomic, Molecular, and Optical Physics)*, **73** 042108 (2006). Cited on page 81.
- [Martinis87] J. M. Martinis, M. H. Devoret & J. Clarke. Experimental tests for the quantum behavior of a macroscopic degree of freedom: The phase difference across a Josephson junction. *Phys. Rev. B*, **35** 4682 (1987). Cited on page 1.
- [Martinis02] J. M. Martinis, S. Nam, J. Aumentado & C. Urbina. Rabi oscillations in a large Josephson-junction qubit. *Phys. Rev. Lett.*, **89** 117901 (2002). Cited on page 15.
- [Menzel10] E. P. Menzel, F. Deppe, M. Mariantoni, M. A. Araque Caballero, A. Baust, T. Niemczyk, E. Hoffmann, A. Marx, E. Solano & R. Gross. Dual-path state reconstruction scheme for propagating quantum microwaves and detector noise tomography. *Phys. Rev. Lett.*, **105** 100401 (2010). Cited on pages 3, 37, 54, 55, 66 and 118.
- [Menzel12] E. P. Menzel, R. Di Candia, F. Deppe, P. Eder, L. Zhong, M. Ihmig, M. Haerberlein, A. Baust, E. Hoffmann, D. Ballester, K. Inomata, T. Yamamoto, Y. Nakamura, E. Solano, A. Marx & R. Gross. Path entanglement of continuous-variable quantum microwaves. *Phys. Rev. Lett.*, **109** 250502 (2012). Cited on pages 3, 109, 115 and 138.
- [Mikulin84] E. Mikulin, A. Tarasov & M. Shkrebyonock. Low temperature expansion pulse tubes. *Adv. Cryo. Eng.*, **29** 629 (1984). Cited on page 29.
- [Miller05] R. Miller, T. E. Northup, K. M. Birnbaum, A. Boca, A. D. Boozer & H. J. Kimble. Trapped atoms in cavity QED: coupling quantized light and matter. *Journal of Physics B: Atomic, Molecular and Optical Physics*, **38** S551 (2005). Cited on page 2.

- [Mlynek12] J. A. Mlynek, A. A. Abdumalikov, J. M. Fink, L. Steffen, M. Baur, C. Lang, A. F. van Loo & A. Wallraff. Demonstrating W-type entanglement of Dicke states in resonant cavity quantum electrodynamics. *Phys. Rev. A*, **86** 053838 (2012). Cited on pages 3 and 137.
- [Moehring04] D. L. Moehring, M. J. Madsen, B. B. Blinov & C. Monroe. Experimental bell inequality violation with an atom and a photon. *Phys. Rev. Lett.*, **93** 090410 (2004). Cited on page 117.
- [Moehring07] D. L. Moehring, P. Maunz, S. Olmschenk, K. C. Younge, D. N. Matsukevich, L. M. Duan & C. Monroe. Entanglement of single-atom quantum bits at a distance. *Nature*, **449** 68 (2007). Cited on pages 70, 117 and 139.
- [Mogilevtsev07] D. Mogilevtsev, J. Řeháček & Z. Hradil. Objective approach to biased tomography schemes. *Phys. Rev. A*, **75** 012112 (2007). Cited on page 63.
- [Mollow67] B. R. Mollow & R. J. Glauber. Quantum theory of parametric amplification I. *Phys. Rev.*, **160** 1076 (1967). Cited on page 77.
- [Mooij99] J. E. Mooij, T. Orlando, L. Levitov, L. Tian, C. H. van der Wal & S. Lloyd. Josephson persistent-current qubit. *Science*, **285** 1036 (1999). Cited on page 2.
- [Motzoi09] F. Motzoi, J. M. Gambetta, P. Rebentrost & F. K. Wilhelm. Simple pulses for elimination of leakage in weakly nonlinear qubits. *Phys. Rev. Lett.*, **103** 110501 (2009). Cited on page 39.
- [Murch12] K. W. Murch, S. J. Weber, E. M. Levenson-Falk, R. Vijay & I. Siddiqi. $1/f$ noise of Josephson-junction-embedded microwave resonators at single photon energies and millikelvin temperatures. *Applied Physics Letters*, **100** 142601 (2012). Cited on page 8.
- [Nakamura97] Y. Nakamura, C. D. Chen & J. S. Tsai. Spectroscopy of energy-level splitting between two macroscopic quantum states of charge coherently superposed by Josephson coupling. *Phys. Rev. Lett.*, **79** 2328 (1997). Cited on page 2.
- [Nakamura99] Y. Nakamura, Y. A. Pashkin & J. S. Tsai. Coherent control of macroscopic quantum states in a single-Cooper-pair box. *Nature*, **398** 786 (1999). Cited on page 2.
- [Nataf10] P. Nataf & C. Ciuti. No-go theorem for superradiant quantum phase transitions in cavity QED and counter-example in circuit QED. *Nat Commun*, **1** 72 (2010). Cited on page 9.
- [Nguyen12] F. Nguyen, E. Zakka-Bajjani, R. W. Simmonds & J. Aumentado. Quantum interference between two single photons of different microwave frequencies. *Phys. Rev. Lett.*, **108** 163602 (2012). Cited on page 3.
- [Nielsen00] M. A. Nielsen & I. L. Chuang. *Quantum Computation and Quantum Information*. Cambridge University Press (2000). Cited on page 62.
- [Nigg12] S. E. Nigg, H. Paik, B. Vlastakis, G. Kirchmair, S. Shankar, L. Frunzio, M. H. Devoret, R. J. Schoelkopf & S. M. Girvin. Black-box superconducting circuit quantization. *Phys. Rev. Lett.*, **108** 240502 (2012). Cited on pages 9 and 11.
- [Noh91] J. W. Noh, A. Fougères & L. Mandel. Measurement of the quantum phase by photon counting. *Phys. Rev. Lett.*, **67** 1426 (1991). Cited on page 45.
- [O'Brien09] J. L. O'Brien, A. Furusawa & J. Vučković. Photonic quantum technologies. *Nat. Photon.*, **3** 687 (2009). Cited on pages 2 and 38.
- [Olmschenk09] S. Olmschenk, D. N. Matsukevich, P. Maunz, D. Hayes, L.-M. Duan & C. Monroe. Quantum teleportation between distant matter qubits. *Science*, **323** 486 (2009). Cited on page 117.

- [Ou92] Z. Y. Ou, S. F. Pereira, H. J. Kimble & K. C. Peng. Realization of the Einstein-Podolsky-Rosen paradox for continuous variables. *Phys. Rev. Lett.*, **68** 3663 (1992). Cited on page 109.
- [Paik11] H. Paik, D. I. Schuster, L. S. Bishop, G. Kirchmair, G. Catelani, A. P. Sears, B. R. Johnson, M. J. Reagor, L. Frunzio, L. I. Glazman, S. M. Girvin, M. H. Devoret & R. J. Schoelkopf. Observation of high coherence in Josephson junction qubits measured in a three-dimensional circuit QED architecture. *Phys. Rev. Lett.*, **107** 240501 (2011). Cited on pages 3 and 15.
- [Park09] Y.-S. Park & H. Wang. Resolved-sideband and cryogenic cooling of an optomechanical resonator. *Nat. Phys.*, **5** 489 (2009). Cited on page 8.
- [Pauli40] W. Pauli. The connection between spin and statistics. *Phys. Rev.*, **58** 716 (1940). Cited on page 1.
- [Peropadre11] B. Peropadre, G. Romero, G. Johansson, C. M. Wilson, E. Solano & J. J. García-Ripoll. Approaching perfect microwave photodetection in circuit QED. *Phys. Rev. A*, **84** 063834 (2011). Cited on pages 3 and 138.
- [Planck01] M. Planck. On the law of distribution of energy in the normal spectrum. *Annalen der Physik*, **4** 553 (1901). Cited on page 1.
- [Plastina03] F. Plastina & G. Falci. Communicating Josephson qubits. *Phys. Rev. B*, **67** 224514 (2003). Cited on page 2.
- [Pobell06] F. Pobell. *Matter and Methods at Low Temperatures*. Springer, 3rd edition, (2006). Cited on pages 8, 29 and 30.
- [Poudel12] A. Poudel, R. McDermott & M. G. Vavilov. Quantum efficiency of a microwave photon detector based on a current-biased Josephson junction. *Phys. Rev. B*, **86** 174506 (2012). Cited on pages 3 and 138.
- [Poazar93] D. M. Pozar. *Microwave Engineering*. Addison-Wesley Publishing Company (1993). Cited on pages 18, 19, 34, 70, 71 and 94.
- [Puebla-Hellmann12] G. Puebla-Hellmann & A. Wallraff. Realization of gigahertz-frequency impedance matching circuits for nano-scale devices. *Applied Physics Letters*, **101** 053108 (2012). Cited on pages 3 and 137.
- [Reed10] M. D. Reed, L. DiCarlo, B. R. Johnson, L. Sun, D. I. Schuster, L. Frunzio & R. J. Schoelkopf. High-fidelity readout in circuit quantum electrodynamics using the Jaynes-Cummings nonlinearity. *Phys. Rev. Lett.*, **105** 173601 (2010). Cited on page 26.
- [Reed12] M. D. Reed, L. DiCarlo, S. E. Nigg, L. Sun, L. Frunzio, S. M. Girvin & R. J. Schoelkopf. Realization of three-qubit quantum error correction with superconducting circuits. *Nature*, **482** 382 (2012). Cited on pages 3 and 138.
- [Reid88] M. D. Reid & P. D. Drummond. Quantum correlations of phase in nondegenerate parametric oscillation. *Phys. Rev. Lett.*, **60** 2731 (1988). Cited on page 109.
- [Riedmatten03] H. d. Riedmatten, I. Marcikic, W. Tittel, H. Zbinden & N. Gisin. Quantum interference with photon pairs created in spatially separated sources. *Phys. Rev. A*, **67** 022301 (2003). Cited on page 70.
- [Rigetti12] C. Rigetti, J. M. Gambetta, S. Poletto, B. L. T. Plourde, J. M. Chow, A. D. Córcoles, J. A. Smolin, S. T. Merkel, J. R. Rozen, G. A. Keefe, M. B. Rothwell, M. B. Ketchen & M. Steffen. Superconducting qubit in a waveguide cavity with a coherence time approaching 0.1 ms. *Phys. Rev. B*, **86** 100506 (2012). Cited on pages 3 and 15.

- [Ristè12a] D. Ristè, C. C. Bultink, K. W. Lehnert & L. DiCarlo. Feedback control of a solid-state qubit using high-fidelity projective measurement. *Phys. Rev. Lett.*, **109** 240502 (2012). Cited on page 3.
- [Riste12b] D. Riste, C. C. Bultink, M. J. Tiggelman, R. N. Schouten, K. W. Lehnert & L. DiCarlo. Millisecond charge-parity fluctuations and induced decoherence in a superconducting qubit. *arXiv:1212.5459* (2012). Cited on page 138.
- [Ristè12c] D. Ristè, J. G. van Leeuwen, H.-S. Ku, K. W. Lehnert & L. DiCarlo. Initialization by measurement of a superconducting quantum bit circuit. *Phys. Rev. Lett.*, **109** 050507 (2012). Cited on pages 8 and 77.
- [Ritter12] S. Ritter, C. Nolleke, C. Hahn, A. Reiserer, A. Neuzner, M. Uphoff, M. Mücke, E. Figueroa, J. Bochmann & G. Rempe. An elementary quantum network of single atoms in optical cavities. *Nature*, **484** 195 (2012). Cited on pages 117 and 138.
- [Roch12] N. Roch, E. Flurin, F. Nguyen, P. Morfin, P. Campagne-Ibarcq, M. H. Devoret & B. Huard. Widely tunable, nondegenerate three-wave mixing microwave device operating near the quantum limit. *Phys. Rev. Lett.*, **108** 147701 (2012). Cited on page 79.
- [Romero09] G. Romero, J. J. García-Ripoll & E. Solano. Microwave photon detector in circuit QED. *Phys. Rev. Lett.*, **102** 173602 (2009). Cited on pages 3, 37 and 138.
- [Sanders89] B. C. Sanders & G. J. Milburn. Complementarity in a quantum nondemolition measurement. *Phys. Rev. A*, **39** 694 (1989). Cited on page 95.
- [Santamore04] D. H. Santamore, H.-S. Goan, G. J. Milburn & M. L. Roukes. Anharmonic effects on a phonon-number measurement of a quantum-mesoscopic-mechanical oscillator. *Phys. Rev. A*, **70** 052105 (2004). Cited on page 95.
- [Sayrin11] C. Sayrin, I. Dotsenko, X. Zhou, B. Peaudecerf, T. Rybarczyk, S. Gleyzes, P. Rouchon, M. Mirrahimi, H. Amini, M. Brune, J.-M. Raimond & S. Haroche. Real-time quantum feedback prepares and stabilizes photon number states. *Nature*, **477** 73 (2011). Cited on page 37.
- [Schliesser08] A. Schliesser, R. Riviere, G. Anetsberger, O. Arcizet & T. J. Kippenberg. Resolved-sideband cooling of a micromechanical oscillator. *Nat Phys*, **4** 415 (2008). Cited on page 8.
- [Schoelkopf08] R. J. Schoelkopf & S. M. Girvin. Wiring up quantum systems. *Nature*, **451** 664 (2008). Cited on page 2.
- [Schreier08] J. Schreier, A. Houck, J. Koch, D. I. Schuster, B. Johnson, J. Chow, J. Gambetta, J. Majer, L. Frunzio, M. Devoret, S. Girvin & R. Schoelkopf. Suppressing charge noise decoherence in superconducting charge qubits. *Phys. Rev. B*, **77** 180502 (2008). Cited on page 14.
- [Schuster05] D. I. Schuster, A. Wallraff, A. Blais, L. Frunzio, R.-S. Huang, J. Majer, S. M. Girvin & R. J. Schoelkopf. AC Stark shift and dephasing of a superconducting qubit strongly coupled to a cavity field. *Physical Review Letters*, **94** 123602 (2005). Cited on pages 2 and 151.
- [Schuster07] D. I. Schuster, A. A. Houck, J. A. Schreier, A. Wallraff, J. M. Gambetta, A. Blais, L. Frunzio, J. Majer, B. Johnson, M. H. Devoret, S. M. Girvin & R. J. Schoelkopf. Resolving photon number states in a superconducting circuit. *Nature*, **445** 515 (2007). Cited on page 2.
- [Schuster10] D. I. Schuster, A. Fragner, M. I. Dykman, S. A. Lyon & R. J. Schoelkopf. Proposal for manipulating and detecting spin and orbital states of trapped electrons on helium using cavity quantum electrodynamics. *Phys. Rev. Lett.*, **105** 040503 (2010). Cited on page 37.

- [Scully97] M. O. Scully & M. S. Zubairy. *Quantum Optics*. Cambridge University Press (1997). Cited on page 45.
- [Shor94] P. W. Shor. Algorithms for quantum computation: Discrete logarithms and factoring. In *Proceedings, 35th Annual Symposium on Foundations of Computer Science, Santa Fe*, p. 124. IEEE Computer Society Press (1994). Cited on page 2.
- [Siddiqi04] I. Siddiqi, R. Vijay, F. Pierre, C. M. Wilson, M. Metcalfe, C. Rigetti, L. Frunzio & M. H. Devoret. RF-driven Josephson bifurcation amplifier for quantum measurement. *Phys. Rev. Lett.*, **93** 207002 (2004). Cited on pages 3 and 81.
- [Siewert04] J. Siewert & T. Brandes. Applications of adiabatic passage in solid-state devices. In B. Kramer, ed., *Advances in Solid State Physics*, vol. 44, pp. 181–190. Springer Berlin Heidelberg (2004). Cited on page 139.
- [Sillanpää07] M. A. Sillanpää, J. I. Park & R. W. Simmonds. Coherent quantum state storage and transfer between two phase qubits via a resonant cavity. *Nature*, **449** 438 (2007). Cited on page 2.
- [Simon00] R. Simon. Peres-Horodecki separability criterion for continuous variable systems. *Phys. Rev. Lett.*, **84** 2726 (2000). Cited on page 114.
- [Simons01] R. N. Simons. *Coplanar waveguide circuits, components and systems*. Wiley Series in Microwave and Optical Engineering. Wiley Inter-Science (2001). Cited on page 16.
- [Slusher85] R. E. Slusher, L. W. Hollberg, B. Yurke, J. C. Mertz & J. F. Valley. Observation of squeezed states generated by four-wave mixing in an optical cavity. *Phys. Rev. Lett.*, **55** 2409 (1985). Cited on pages 77 and 78.
- [Steffen06] M. Steffen, M. Ansmann, R. McDermott, N. Katz, R. C. Bialczak, E. Lucero, M. Neeley, E. M. Weig, A. N. Cleland & J. M. Martinis. State tomography of capacitively shunted phase qubits with high fidelity. *Phys. Rev. Lett.*, **97** 050502 (2006). Cited on page 2.
- [Stute12] A. Stute, B. Casabone, P. Schindler, T. Monz, P. O. Schmidt, B. Brandstatter, T. E. Northup & R. Blatt. Tunable ion-photon entanglement in an optical cavity. *Nature*, **485** 482 (2012). Cited on page 117.
- [Suchoi10] O. Suchoi, B. Abdo, E. Segev, O. Shtempluck, M. P. Blencowe & E. Buks. Intermode dephasing in a superconducting stripline resonator. *Phys. Rev. B*, **81** 174525 (2010). Cited on page 95.
- [Teufel11] J. D. Teufel, T. Donner, D. Li, J. W. Harlow, M. S. Allman, K. Cicak, A. J. Sirois, J. D. Whittaker, K. W. Lehnert & R. W. Simmonds. Sideband cooling of micromechanical motion to the quantum ground state. *Nature*, **475** 359 (2011). Cited on pages 8, 77 and 137.
- [Tholén07] E. Tholén, A. Ergül, E. Doherty, F. Weber, F. Grégis & D. Haviland. Nonlinearities and parametric amplification in superconducting coplanar waveguide resonators. *Appl. Phys. Lett.*, **90** 253509 (2007). Cited on page 77.
- [Tholén09] E. A. Tholén, A. Ergül, K. Stannigel, C. Hutter & D. B. Haviland. Parametric amplification with weak-link nonlinearity in superconducting microresonators. *Physica Scripta Volume T*, **137** 014019 (2009). Cited on page 3.
- [Thompson92] R. J. Thompson, G. Rempe & H. J. Kimble. Observation of normal-mode splitting for an atom in an optical cavity. *Phys. Rev. Lett.*, **68** 1132 (1992). Cited on page 12.
- [Tinkham96] M. Tinkham. *Introduction to Superconductivity*. McGraw-Hill International Editions (1996). Cited on pages 12 and 13.

- [Tipsmark11] A. Tipsmark, R. Dong, A. Laghaout, P. Marek, M. Ježek & U. L. Andersen. Experimental demonstration of a Hadamard gate for coherent state qubits. *Phys. Rev. A*, **84** 050301 (2011). Cited on page 63.
- [Togan10] E. Togan, Y. Chu, A. S. Trifonov, L. Jiang, J. Maze, L. Childress, M. V. G. Dutt, A. S. Sørensen, P. R. Hemmer, A. S. Zibrov & M. D. Lukin. Quantum entanglement between an optical photon and a solid-state spin qubit. *Nature*, **466** 730 (2010). Cited on page 117.
- [Usuga10] M. A. Usuga, C. R. Muller, C. Wittmann, P. Marek, R. Filip, C. Marquardt, G. Leuchs & U. L. Andersen. Noise-powered probabilistic concentration of phase information. *Nat Phys*, **6** 767 (2010). Cited on page 63.
- [Vandenbergh96] L. Vandenberghe & S. Boyd. Semidefinite programming. *SIAM Review*, **38** 49 (1996). Cited on page 60.
- [Vandersypen04] L. M. K. Vandersypen & I. L. Chuang. NMR techniques for quantum control and computation. *Rev. Mod. Phys.*, **76** 1037 (2004). Cited on page 2.
- [Vasilyev00] M. Vasilyev, S.-K. Choi, P. Kumar & G. M. D'Ariano. Tomographic measurement of joint photon statistics of the twin-beam quantum state. *Phys. Rev. Lett.*, **84** 2354 (2000). Cited on page 109.
- [Vidal02] G. Vidal & R. F. Werner. Computable measure of entanglement. *Phys. Rev. A*, **65** 032314 (2002). Cited on pages 74 and 125.
- [Viehmann11] O. Viehmann, J. von Delft & F. Marquardt. Superradiant phase transitions and the standard description of circuit qed. *Phys. Rev. Lett.*, **107** 113602 (2011). Cited on page 9.
- [Vijay09] R. Vijay, M. H. Devoret & I. Siddiqi. Invited review article: The Josephson bifurcation amplifier. *Rev. Sci. Instrum.*, **80** 111101 (2009). Cited on pages 81 and 110.
- [Vijay11] R. Vijay, D. H. Slichter & I. Siddiqi. Observation of quantum jumps in a superconducting artificial atom. *Phys. Rev. Lett.*, **106** 110502 (2011). Cited on pages 3, 54 and 146.
- [Vijay12] R. Vijay, C. Macklin, D. H. Slichter, S. J. Weber, K. W. Murch, R. Naik, A. N. Korotkov & I. Siddiqi. Stabilizing Rabi oscillations in a superconducting qubit using quantum feedback. *Nature*, **490** 77 (2012). Cited on pages 3, 77 and 138.
- [Vion02] D. Vion, A. Aassime, A. Cottet, P. Joyez, H. Pothier, C. Urbina, D. Esteve & M. H. Devoret. Manipulating the quantum state of an electrical circuit. *Science*, **296** 886 (2002). Cited on pages 2 and 15.
- [Vogel00] W. Vogel. Nonclassical states: An observable criterion. *Phys. Rev. Lett.*, **84** 1849 (2000). Cited on page 55.
- [Volz06] J. Volz, M. Weber, D. Schlenk, W. Rosenfeld, J. Vrana, K. Saucke, C. Kurtsiefer & H. Weinfurter. Observation of entanglement of a single photon with a trapped atom. *Phys. Rev. Lett.*, **96** 030404 (2006). Cited on page 117.
- [Voss81] R. F. Voss & R. A. Webb. Macroscopic quantum tunneling in 1- μm Nb Josephson junctions. *Phys. Rev. Lett.*, **47** 265 (1981). Cited on page 1.
- [Wahyu Utami08] D. Wahyu Utami & A. A. Clerk. Entanglement dynamics in a dispersively coupled qubit-oscillator system. *Phys. Rev. A*, **78** 042323 (2008). Cited on page 132.
- [Wallquist06] M. Wallquist, V. S. Shumeiko & G. Wendin. Selective coupling of superconducting charge qubits mediated by a tunable stripline cavity. *Phys. Rev. B*, **74** 224506 (2006). Cited on pages 90, 92 and 93.

- [Wallraff04] A. Wallraff, D. I. Schuster, A. Blais, L. Frunzio, R.-S. Huang, J. Majer, S. Kumar, S. M. Girvin & R. J. Schoelkopf. Strong coupling of a single photon to a superconducting qubit using circuit quantum electrodynamics. *Nature*, **431** 162 (2004). Cited on pages 2, 15, 22 and 134.
- [Wallraff05] A. Wallraff, D. I. Schuster, A. Blais, L. Frunzio, J. Majer, S. M. Girvin & R. J. Schoelkopf. Approaching unit visibility for control of a superconducting qubit with dispersive readout. *Phys. Rev. Lett.*, **95** 060501 (2005). Cited on pages 24, 25, 39, 40, 121 and 146.
- [Walls94] D. F. Walls & G. J. Milburn. *Quantum Optics*. Springer Verlag, Berlin (1994). Cited on pages 19, 20, 47 and 82.
- [Walther06] H. Walther, B. T. H. Varcoe, B.-G. Englert & T. Becker. Cavity quantum electrodynamics. *Reports on Progress in Physics*, **69** 1325 (2006). Cited on pages 2 and 12.
- [Wang09] H. Wang, M. Hofheinz, M. Ansmann, R. C. Bialczak, E. Lucero, M. Neeley, A. D. O'Connell, D. Sank, M. Weides, J. Wenner, A. N. Cleland & J. M. Martinis. Decoherence dynamics of complex photon states in a superconducting circuit. *Phys. Rev. Lett.*, **103** 200404 (2009). Cited on page 37.
- [Wang11] H. Wang, M. Mariantoni, R. C. Bialczak, M. Lenander, E. Lucero, M. Neeley, A. D. O'Connell, D. Sank, M. Weides, J. Wenner, T. Yamamoto, Y. Yin, J. Zhao, J. M. Martinis & A. N. Cleland. Deterministic entanglement of photons in two superconducting microwave resonators. *Phys. Rev. Lett.*, **106** 060401 (2011). Cited on pages 3 and 37.
- [Wellstood04] F. Wellstood, C. Urbina & J. Clarke. Flicker 1/f noise in the critical current of Josephson junctions at 0.09-4.2 K. *Appl. Phys. Lett.*, **85** 5296 (2004). Cited on page 8.
- [Welsch99] D.-G. Welsch, W. Vogel & T. Opatrny. Homodyne detection and quantum-state reconstruction. vol. 39 of *Progress in Optics*, pp. 63 – 211. Elsevier (1999). Cited on page 45.
- [Wenner11] J. Wenner, M. Neeley, R. C. Bialczak, M. Lenander, E. Lucero, A. D. O'Connell, D. Sank, H. Wang, M. Weides, A. N. Cleland & J. M. Martinis. Wirebond crosstalk and cavity modes in large chip mounts for superconducting qubits. *Supercond. Sci. Technol.*, **24** 065001 (2011). Cited on page 28.
- [Wilk07] T. Wilk, S. C. Webster, A. Kuhn & G. Rempe. Single-atom single-photon quantum interface. *Science*, **317** 488 (2007). Cited on page 117.
- [Wilson11] C. M. Wilson, G. Johansson, A. Pourkabirian, M. Simoen, J. R. Johansson, T. Duty, F. Nori & P. Delsing. Observation of the dynamical Casimir effect in a superconducting circuit. *Nature*, **479** 376 (2011). Cited on pages 79 and 118.
- [Wineland79] D. J. Wineland & W. M. Itano. Laser cooling of atoms. *Phys. Rev. A*, **20** 1521 (1979). Cited on page 8.
- [Wiseman10] H. Wiseman & G. Milburn. *Quantum Measurement and Control*. Cambridge University Press (2010). Cited on pages 8, 77 and 131.
- [Wu86] L.-A. Wu, H. J. Kimble, J. L. Hall & H. Wu. Generation of squeezed states by parametric down conversion. *Phys. Rev. Lett.*, **57** 2520 (1986). Cited on page 77.
- [Wu10] H. Wu, R. E. George, J. H. Wesenberg, K. Mølmer, D. I. Schuster, R. J. Schoelkopf, K. M. Itoh, A. Ardavan, J. J. L. Morton & G. A. D. Briggs. Storage of multiple coherent microwave excitations in an electron spin ensemble. *Phys. Rev. Lett.*, **105** 140503 (2010). Cited on page 137.
- [Wunsche91] A. Wunsche. Displaced fock states and their connection to quasiprobabilities. *Quantum Optics: Journal of the European Optical Society Part B*, **3** 359 (1991). Cited on page 65.

- [Yamamoto08] T. Yamamoto, K. Inomata, M. Watanabe, K. Matsuba, T. Miyazaki, W. D. Oliver, Y. Nakamura & J. S. Tsai. Flux-driven Josephson parametric amplifier. *Appl. Phys. Lett.*, **93** 042510 (2008). Cited on pages 3, 77 and 79.
- [Yang03] C.-P. Yang, S.-I. Chu & S. Han. Possible realization of entanglement, logical gates, and quantum-information transfer with superconducting-quantum-interference-device qubits in cavity QED. *Phys. Rev. A*, **67** 042311 (2003). Cited on page 2.
- [Yin13] Y. Yin, Y. Chen, D. Sank, P. J. J. O'Malley, T. C. White, R. Barends, J. Kelly, E. Lucero, M. Mariantoni, A. Megrant, C. Neill, A. Vainsencher, J. Wenner, A. N. Korotkov, A. N. Cleland & J. M. Martinis. Catch and release of microwave photon states. *Phys. Rev. Lett.*, **110** 107001 (2013). Cited on page 139.
- [Yonezawa07] H. Yonezawa, S. L. Braunstein & A. Furusawa. Experimental demonstration of quantum teleportation of broadband squeezing. *Phys. Rev. Lett.*, **99** 110503 (2007). Cited on page 109.
- [Yoshida92] K. Yoshida, M. S. Hossain, T. Kisu, K. Enpuku & K. Yamafuji. Modeling of kinetic-inductance coplanar stripline with NbN thin films. *Japanese Journal of Applied Physics*, **31** 3844 (1992). Cited on page 11.
- [Yuan08] Z.-S. Yuan, Y.-A. Chen, B. Zhao, S. Chen, J. Schmiedmayer & J.-W. Pan. Experimental demonstration of a BDCZ quantum repeater node. *Nature*, **454** 1098 (2008). Cited on page 117.
- [Yuen80] H. Yuen & J. Shapiro. Optical communication with two-photon coherent states—part iii: Quantum measurements realizable with photoemissive detectors. *Information Theory, IEEE Transactions on*, **26** 78 (1980). Cited on page 45.
- [Yurke84] B. Yurke & J. S. Denker. Quantum network theory. *Phys. Rev. A*, **29** 1419 (1984). Cited on pages 11 and 16.
- [Yurke87] B. Yurke. Squeezed-state generation using a Josephson parametric amplifier. *J. Opt. Soc. Am. B*, **4** 1551 (1987). Cited on pages 37, 47, 77 and 81.
- [Yurke88] B. Yurke, P. G. Kaminsky, R. E. Miller, E. A. Whittaker, A. D. Smith, A. H. Silver & R. W. Simon. Observation of 4.2-K equilibrium-noise squeezing via a Josephson-parametric amplifier. *Phys. Rev. Lett.*, **60** 764 (1988). Cited on pages 3 and 77.
- [Yurke06] B. Yurke & E. Buks. Performance of cavity-parametric amplifiers, employing Kerr nonlinearities, in the presence of two-photon loss. *J. Lightwave Technol.*, **24** 5054 (2006). Cited on pages 3, 37, 46, 77, 82 and 110.

List of Publications

1. C. Eichler, N. Hasselmann, and P. Kopietz. “Condensate density of interacting bosons: A functional renormalization group approach.” *Phys. Rev. E.*, **80**, 051129 (2009)
2. D. Bozyigit, C. Lang, L. Steffen, J. M. Fink, C. Eichler, M. Baur, R. Bianchetti, P. J. Leek, S. Filipp, M. P. da Silva, A. Blais, and A. Wallraff. “Antibunching of Microwave Frequency Photons observed in Correlation Measurements using Linear Detectors.” *Nat. Phys.*, **7**, 154-158 (2011)
3. D. Bozyigit, C. Lang, L. Steffen, J. M. Fink, C. Eichler, M. Baur, R. Bianchetti, P. J. Leek, S. Filipp, M. P. da Silva, A. Blais, and A. Wallraff. “Correlation Measurements of Individual Microwave Photons Emitted from a Symmetric Cavity.” *J. Phys.: Conf. Ser.*, **264**, 012024 (2011)
4. C. Eichler, D. Bozyigit, C. Lang, L. Steffen, J. M. Fink, and A. Wallraff. “Experimental State Tomography of Itinerant Single Microwave Photons.” *Phys. Rev. Lett.*, **106**, 220503 (2011)
5. C. Eichler, D. Bozyigit, C. Lang, M. Baur, L. Steffen, J. M. Fink, S. Filipp, and A. Wallraff. “Observation of Two-Mode Squeezing in the Microwave Frequency Domain.” *Phys. Rev. Lett.*, **107**, 113601 (2011)
6. C. Lang, D. Bozyigit, C. Eichler, L. Steffen, J. M. Fink, A. A. Abdumalikov, M. Baur, S. Filipp, M. P. da Silva, A. Blais and A. Wallraff. “Observation of Resonant Photon Blockade at Microwave Frequencies using Correlation Function Measurements.” *Phys. Rev. Lett.*, **106**, 243601 (2011)
7. C. Eichler, D. Bozyigit, and A. Wallraff. “Characterizing quantum microwave radiation and its entanglement with superconducting qubits using linear detectors.” *Phys. Rev. A.*, **86**, 032106 (2012)

8. C. Eichler, C. Lang, J. M. Fink, J. Govenius, S. Filipp and A. Wallraff. “Observation of Entanglement between Itinerant Microwave Photons and a Superconducting Qubit.” *Phys. Rev. Lett.*, **109**, 240501 (2012)
9. C. Eichler, D. Bozyigit, C. Lang, L. Steffen, J. M. Fink, and A. Wallraff. “Tomography schemes for characterizing itinerant microwave photon fields” (2012). Lectures delivered at Ecole d’Eté Les Houches; To be published by Oxford University Press.
10. C. Lang, C. Eichler, L. Steffen, J. M. Fink, M. J. Woolley, A. Blais, A. Wallraff, “Probing Correlations, Indistinguishability and Entanglement in Hong-Ou-Mandel Experiments at Microwave Frequencies”, *Nat. Phys.* , in print (2013)

Credits

Die vorliegende Arbeit entstand aus der fruchtbaren Zusammenarbeit mit Freunden und Kollegen heraus und wäre nicht möglich gewesen ohne die vielseitige Unterstützung, die ich während meiner gesamten Ausbildungszeit erfahren habe. Stellvertretend für alljene, die mich auf dem Weg hierhin begleitet haben, möchte ich insbesondere den Menschen Dank sagen, die in den drei letzten Jahren zum Entstehen der Doktorarbeit beigetragen haben.

Besonderer Dank gilt zunächst meinem Doktorvater Andreas Wallraff, der mich während meiner gesamten Forschungszeit intensiv unterstützt, motiviert und gefördert hat. Seine Begeisterungsfähigkeit für die Wissenschaft, sein tiefes Verständnis für experimentelle Zusammenhänge und sein hoher Anspruch an eine durchsichtige Darstellung physikalischer Sachverhalte waren prägend. Weiterhin danke ich Atac Imamoglu für die Begutachtung meiner Doktorarbeit und für die inspirierende und erhellende Vorlesung zur Quantenoptik, mit der er mir keinen besseren Einstieg ins Doktoratsstudium hätte ermöglichen können.

Gebührlichen Dank möchte ich außerdem allen Kollegen vom *Qudev* Team zollen, die für eine so angenehme Laboratmosphäre gesorgt haben und deren Mitarbeit entscheidend bei der Realisierung von allen Experimenten war. Diskussions- und Hilfsbereitschaft habe ich durchweg von allen Seiten verspürt. Besonders hervorheben möchte ich Christian Lang und Deniz Bozyigit, mit denen mich eine enge, stets vom Teamgeist geprägte Zusammenarbeit an den Photonkorrelationsmessungen verbindet. Darüber hinaus möchte ich Lars Steffen, Johannes Fink und Matthias Baur für deren Hilfe und Anleitung bei der Probenfabrikation danken. Großer Dank geht auch an Stefan Filipp für seine Freundschaft, viele inspirierende Physikdiskussionen und gemeinsame Familienausflüge, sowie für sein gewissenhaftes Kommentieren meiner Doktorarbeit. Weiterhin möchte ich allen Physikkollegen danken, die mich während der letzten Jahre durch stimulierende Fragen, anregende Diskussionen und hilfreiche Hinweise weitergebracht und mein Interesse an der Forschung wachgehalten haben.

Meinen Eltern und meiner Familie möchte ich tiefen Dank aussprechen für alles was sie mir mit auf den Weg gegeben haben und für ihre bedingungslose Unterstützung. Von Herzen danke ich Heike für ihre Liebe, ihre unermessliche Ausdauer und ihren Optimismus. Sie hat diese Arbeit mitgetragen und zusammen mit unseren beiden Töchtern Ella und Noemi für drei unvergessliche Jahre in Zürich gesorgt.

Curriculum Vitae

Personal

Name: Christopher Eichler
Contact: Erlenstrasse 10, 8048 Zürich, Switzerland. eichlerc@phys.ethz.ch
Date of birth: 19th of December 1983 in Kirchheimbolanden, Germany

Education

2003 Abitur, Elisabeth-Langässer-Gymnasium Alzey.
2004 - 2009 Studies of physics at the 'Goethe-Universität' and studies of music at the 'Hochschule für Musik und darstellende Kunst' in Frankfurt/Main. Semesters abroad at UPMC in Paris and at UnB in Brasilia.
2009 Graduation in physics (Dipl.-Phys.) with Prof. Peter Kopietz at 'Goethe-Universität' Frankfurt. Thesis: 'Wechselwirkende Bosegase – Ein funktionaler Renormierungsgruppenansatz'.
2009 - 2012 Doctoral research in the quantum device lab at the physics department of ETH Zurich.
2012 Graduation in music (Dipl.-Mus.) at HfMdK Frankfurt.

Employments

2003 - 2004 Military service in the military orchestra Karlsruhe.
2005 -2006 Research and development for Probeam Munich and IFSW Stuttgart (6 month).
2006-2009 Teaching assistance at the 'Goethe-Universität' Frankfurt (4 terms).
2009-2012 Research and teaching assistance at ETH Zurich.

Scholarships

2007 DAAD Free Mover exchange fellowship.
2007-2009 Fellow of the 'Studienstiftung des deutschen Volkes'.